



Calhoun: The NPS Institutional Archive
DSpace Repository

Theses and Dissertations

1. Thesis and Dissertation Collection, all items

2010

High spatial resolution bidirectional retrieval using satellite data

McConnon, Cecelia L.

Monterey, California. Naval Postgraduate School

<http://hdl.handle.net/10945/5102>

This publication is a work of the U.S. Government as defined in Title 17, United States Code, Section 101. Copyright protection is not available for this work in the United States.

Downloaded from NPS Archive: Calhoun



Calhoun is the Naval Postgraduate School's public access digital repository for research materials and institutional publications created by the NPS community. Calhoun is named for Professor of Mathematics Guy K. Calhoun, NPS's first appointed -- and published -- scholarly author.

Dudley Knox Library / Naval Postgraduate School
411 Dyer Road / 1 University Circle
Monterey, California USA 93943

<http://www.nps.edu/library>



NAVAL POSTGRADUATE SCHOOL

MONTEREY, CALIFORNIA

THESIS

**HIGH SPATIAL RESOLUTION BIDIRECTIONAL
REFLECTANCE RETRIEVAL USING SATELLITE DATA**

by

Cecelia L. McConnon

December 2010

Thesis Advisor:
Second Reader:

R. C. Olsen
J. H. Newman

Approved for public release; distribution is unlimited

THIS PAGE INTENTIONALLY LEFT BLANK

REPORT DOCUMENTATION PAGE			<i>Form Approved OMB No. 0704-0188</i>	
Public reporting burden for this collection of information is estimated to average 1 hour per response, including the time for reviewing instruction, searching existing data sources, gathering and maintaining the data needed, and completing and reviewing the collection of information. Send comments regarding this burden estimate or any other aspect of this collection of information, including suggestions for reducing this burden, to Washington headquarters Services, Directorate for Information Operations and Reports, 1215 Jefferson Davis Highway, Suite 1204, Arlington, VA 22202-4302, and to the Office of Management and Budget, Paperwork Reduction Project (0704-0188) Washington DC 20503.				
1. AGENCY USE ONLY (Leave blank)		2. REPORT DATE December 2010	3. REPORT TYPE AND DATES COVERED Master's Thesis	
4. TITLE AND SUBTITLE High Spatial Resolution Bidirectional Reflectance Retrieval Using Satellite Data			5. FUNDING NUMBERS	
6. AUTHOR(S) Cecelia L. McConnon				
7. PERFORMING ORGANIZATION NAME(S) AND ADDRESS(ES) Naval Postgraduate School Monterey, CA 93943-5000			8. PERFORMING ORGANIZATION REPORT NUMBER	
9. SPONSORING /MONITORING AGENCY NAME(S) AND ADDRESS(ES) N/A			10. SPONSORING/MONITORING AGENCY REPORT NUMBER	
11. SUPPLEMENTARY NOTES The views expressed in this thesis are those of the author and do not reflect the official policy or position of the Department of Defense or the U.S. Government. IRB Protocol number: N/A.				
12a. DISTRIBUTION / AVAILABILITY STATEMENT Approved for public release; distribution is unlimited.			12b. DISTRIBUTION CODE	
13. ABSTRACT (maximum 200 words) Worldview-2 spectral imagery acquired over Duck, NC and Pendleton, CA were analyzed to extract Bidirectional Reflectance Distribution Functions (BRDF) for 8 spectral bands. Spectral data in the visible and near-infrared bands were acquired for 15 azimuth/elevation values during the Duck NC orbit pass; data were collected at ten-second intervals. Ten images were acquired over Pendleton. Orthoready images were coregistered using first-order polynomials for the two image sequences. BRDF profiles have been created for scene elements: vegetation, asphalt, sand, and water. These data allowed for unique high-spatial resolution BRDF profiles, which can be used to inform terrain classification and target detection in satellite imagery.				
14. SUBJECT TERMS Remote Sensing, Multispectral, 8-color, ENVI, BRDF, Bidirectional Reflectance Distribution Function, MISR, Worldview-2, Pendleton, CA, Duck, NC			15. NUMBER OF PAGES 173	
			16. PRICE CODE	
17. SECURITY CLASSIFICATION OF REPORT Unclassified	18. SECURITY CLASSIFICATION OF THIS PAGE Unclassified	19. SECURITY CLASSIFICATION OF ABSTRACT Unclassified	20. LIMITATION OF ABSTRACT UU	

NSN 7540-01-280-5500

Standard Form 298 (Rev. 2-89)
Prescribed by ANSI Std. Z39-18

THIS PAGE INTENTIONALLY LEFT BLANK

Approved for public release; distribution is unlimited

**HIGH SPATIAL RESOLUTION BIDIRECTIONAL REFLECTANCE
RETRIEVAL USING SATELLITE DATA**

Cecelia L. McConnon
Lieutenant, United States Navy
B.S., United States Naval Academy, 2002

Submitted in partial fulfillment of the
requirements for the degree of

MASTER OF SCIENCE IN SPACE SYSTEMS OPERATIONS

from the

**NAVAL POSTGRADUATE SCHOOL
December 2010**

Author: Cecelia L. McConnon

Approved by: Richard C. Olsen
Thesis Advisor

James H. Newman
Second Reader

Rudolf Panholzer
Chair, Space Systems Academic Group

THIS PAGE INTENTIONALLY LEFT BLANK

ABSTRACT

Worldview-2 spectral imagery acquired over Duck, NC, and Pendleton, CA, were analyzed to extract Bidirectional Reflectance Distribution Functions (BRDF) for 8 spectral bands. Spectral data in the visible and near-infrared bands were acquired for 15 azimuth/elevation values during the Duck NC orbit pass; data were collected at ten-second intervals. Ten images were acquired over Pendleton. Orthorectified images were coregistered using first-order polynomials for the two image sequences. BRDF profiles have been created for scene elements: vegetation, asphalt, sand, and water. These data allowed for unique high-spatial resolution BRDF profiles, which can be used to inform terrain classification and target detection in satellite imagery.

THIS PAGE INTENTIONALLY LEFT BLANK

TABLE OF CONTENTS

I.	INTRODUCTION.....	1
II.	BACKGROUND	3
A.	REMOTE SENSING	3
B.	PHYSICS OF LIGHT	5
	1. Interactions With Matter	6
	2. Solid Angle.....	8
	3. Foreshortening	10
	4. Irradiance	11
	5. Radiance.....	11
	6. Bidirectional Reflectance Distribution Function	12
	7. Anisotropy	14
C.	GROUND-BASED SENSORS.....	16
D.	SPACE-BORNE SENSORS: MULTI-ANGLE AND MULTIPLE ANGLE SATELLITES	20
	1. Multi-angle Imaging SpectroRadiometer (MISR).....	21
	2. Polarization and Directionality of the Earth's Reflectances (POLDER)	24
	3. Compact High Resolution Imaging Spectrometer (CHRIS).....	27
E.	BRDF MODELS	29
	1. Lambertian Model	30
	2. Rahman-Pinty-Verstraete Model	31
	3. Ross-Thick Li-Sparse Model.....	32
	4. Torrance-Sparrow Model	32
	5. Oren-Nayar Model.....	33
III.	EXPERIMENTAL APPROACH	35
A.	PROBLEM DEFINITION	35
B.	EQUIPMENT	35
	1. Worldview-2	35
	2. The Environment for Visualizing Images 4.7 (ENVI [®])	38
IV.	METHODOLOGY	41
A.	PRODUCT.....	41
B.	IMAGE PREPARATION	45
C.	REGIONS OF INTEREST	49
D.	IMAGE RATIOING.....	54
V.	OBSERVATIONS AND ANALYSIS.....	57
A.	CALCULATIONS	57
B.	EFFECTS OF LIMITED IMAGERY PROCESSING	57
C.	MISR DATA.....	58
D.	SHIFT IN DIGITAL NUMBER OBSERVED OVER SEQUENCE OF IMAGES	64

E.	IMAGE RATIO ANALYSIS	65
1.	Images	65
2.	Terrain Effects in Spatial Profiles	70
F.	BRDF SHIFT BETWEEN REGIONS OF INTEREST (DUCK, NC)	72
G.	BRDF SHIFT BETWEEN BANDS	73
H.	IMAGE RATIO DISPLAYING WAVELENGTH DEPENDENCE IN REGIONS OF INTEREST BY BAND	74
I.	BRDF RESULTS BY SEPARATION ANGLE FOR REGIONS OF INTEREST	76
VI.	SUMMARY	79
VII.	CONCLUSIONS AND FUTURE WORK	81
	LIST OF REFERENCES	83
	APPENDIX: CHARTS AND GRAPHS	89
A.	WORLDVIEW-2 GAIN, OFFSET VALUES*, ABSOLUTE CALIBRATION FACTOR AND EFFECTIVE BANDWIDTH	89
B.	SPECTRAL IRRADIANCE	89
C.	MISR PRODUCTS UTILIZED	90
D.	HISTOGRAM SHIFT WITH VIEW ANGLE BY BAND (DUCK, NC)	91
E.	HISTOGRAM SHIFT WITH VIEW ANGLE BY BAND (PENDLETON, CA)	99
F.	SPECTRAL RADIANCE DISPLAYING VARIANCE WITH WAVELENGTH AND VIEW ANGLE (DUCK, NC)	107
G.	SPECTRAL RADIANCE DISPLAYING VARIANCE WITH WAVELENGTH AND VIEW ANGLE (PENDLETON, CA)	119
H.	BRDF RESULTS BY SEPARATION ANGLE FOR REGIONS OF INTEREST (DUCK, NC)	129
I.	BRDF RESULTS BY SEPARATION ANGLE FOR REGIONS OF INTEREST (PENDLETON, CA)	141
	INITIAL DISTRIBUTION LIST	151

LIST OF FIGURES

Figure 1.	Camp Randall Field, Madison, WI, Spatial Resolution of 30m, 10m, and 1m (Image: University of Wisconsin, Institute for Environmental Studies)	3
Figure 2.	Differences between Multi-spectral imagery and Hyperspectral imagery	4
Figure 3.	The Electromagnetic Spectrum.....	5
Figure 4.	Electromagnetic Radiation Interactions with Matter [2]	7
Figure 5.	Solid angle, Ω	9
Figure 6.	(a) Radian defined (b) Steradian defined	9
Figure 7.	Foreshortening [3].....	11
Figure 8.	Reflection Geometry used in the definition of the BRDF	13
Figure 9.	Anisotropic nature of Finished Wood.....	14
Figure 10.	Anisotropy of Natural Features. Top: Soybean Field, Bottom: Black Spruce Forest, Left: Backscattering (sun behind observer), Right: forwardscattering (sun opposite observer), Photograph by Don Deering.....	15
Figure 11.	Murray-Coleman and Smith's Gonioreflectometer (1990).....	17
Figure 12.	Lawrence Berkeley Laboratory's Gonioreflectometer (1992) [9].....	17
Figure 13.	Incidence-plane BRDF of rough aluminum surface for several incidence angles, θ_i [10].....	18
Figure 14.	Portable Apparatus or Rapid Acquisitions of Bidirectional Observations of Land and Atmosphere (PARABOLA) Ground Sensor [11]	19
Figure 15.	Reflectance values for multiple solar zenith angles in Red (Top) and NIR (Bottom) bands of PARABOLA and Chen-Leblanc's radiative transfer model are compared.....	19
Figure 16.	Terra Spacecraft with 5 Climate-Monitoring Sensors: MODIS, MISR, ASTER, MOPITT, and CERES.....	21
Figure 17.	Multi-angle Imaging SpectroRadiometer (MISR) observes the Earth simultaneously with nine discrete cameras from $\pm 70.5^\circ$ in four spectral bands [14].....	22
Figure 18.	Mean and hot spot root mean squared error (RMSE) statistics displaying accuracy of RPV and Ross-Li model inversions	23
Figure 19.	Illustration of the POLDER's rotating polarizing wheel. Scanned bands are in the VNIR bands ($\lambda=443, 490, 564, 670, 763, 765, 865, \text{ and } 910 \text{ nm}$)...25	25
Figure 20.	Sample BRDF product derived from the space-borne POLDER instrument. The angular space, annotated ϕ , represents the azimuthal delta between the sun and the viewing direction. BRDF is at a maximum in the backscattering direction (hotspot, $\phi=0^\circ$) and at a minimum in the forward scattering direction ($\phi=180^\circ$) [22]	26
Figure 21.	Reflectance values for sample region, Tree cover, broadleaved, evergreen, acquired by space-borne POLDER instrument [22]	27
Figure 22.	Compact High Resolution Imaging Spectrometer (CHRIS) [23]	28
Figure 23.	Reflectance data derived from CHRIS/PROBA over a range of zenith angles [25].....	29

Figure 24.	Explanation of Lambert's Cosine Law. I_0 represents the observed radiance.	30
Figure 25.	Laboratory-based BRDF of whole, 4-, and 2-mm cut poplar leaves at (a) normal incidence and 340 nm and (b) 67° incidence and 860 nm [28]	31
Figure 26.	Various BRDF models plotted against a Reference Image [32]	33
Figure 27.	Oren-Nayar Model for Rough Surfaces. Note the improved accuracy of the model over that of the Lambertian model.	34
Figure 28.	Artist rendering of Worldview-2 Satellite	36
Figure 29.	Worldview-2 Bands and Relative Spectral Radiance Response	37
Figure 30.	The reference image (left) and warp image (right) require the selection of a large number of tie points for accurate registration.	46
Figure 31.	(a) A flat surface viewed from directly overhead (Nadir) (b) The same surface viewed with 30°-Off-nadir Roll (c) Surface with 30° Off-Nadir Roll and 60° Off-Nadir Pitch (d) Additional 30° Yaw Introduced	48
Figure 32.	Displacement effect on imagery due to terrain	49
Figure 33.	The initial 11 ROIs at Duck.	50
Figure 34.	ROIs displayed in n-D visualizer	51
Figure 35.	The n-D visualizer display. Left: Sand ROI in (Band 1 & 7), Center: Two identified clumps (Bands 1 & 7), Right: Two clumps in Band 5 & 7, which introduces more separate in the clumps	52
Figure 36.	Left: Sandy area, Center: Initial Sand ROI which encompasses wet and dry sand, Right: The result of n-D visualizer. The original Sand ROI is divided into 2 different ROIs, wet and dry.	52
Figure 37.	(Left) Several of Duck, NC, original ROIs. (Right) n-D visualizer has removed the pixels that displayed differing DN's from the majority over several considered bands, representing cars in a parking lot (Red ROI), an island in a pond (Blue ROI) and structures/objects on a roof (Pink ROIs)	53
Figure 38.	Image Ratioing Interactive Data Language Code	54
Figure 39.	Image Ratio of Duck, NC, Image P006/P011 (Band 2: 450-510 nm)	55
Figure 40.	Image Ratio of Duck, NC, Image P006/P011 (Bands 2: 450-510, Band 5: 630-690, and Band 8: 860-1040 nm)	56
Figure 41.	Illustration of Solar Zenith Angle, Viewing Zenith Angle, and Calculated Separation Angle [36]	57
Figure 42.	Pendleton Overflight by Terra/MISR (Path 41) on the WRS-2 Map (Worldwide Reference System)	59
Figure 43.	MISR Radiance Image: ROI for comparison with Worldview-2 (Camera: AN, Red Band)	59
Figure 44.	MISR Radiance Image: Zoom of ROI for comparison with Worldview-2 (Camera: AN, Red Band)	61
Figure 45.	Worldview-2 Image: ROI for Comparison with MISR (Image P009, Band 5: 630-690 nm)	61
Figure 46.	MISR Radiance Plot in Red Channel (672 nm) by Camera and Zenith Angle: Pendleton, CA	62
Figure 47.	Worldview-2 Radiance Plot in Band 5 (630-690 nm) by Time and Zenith Angle: Pendleton, CA	62

Figure 48.	MISR Brightness Variance in Red Channel (672 nm) with respect to Elevation Angle (Camera): Pendleton, CA.....	63
Figure 49.	Worldview-2 Brightness Variance in Band 5 (630–690 nm) with respect to Elevation Angle (Time): Pendleton, CA.....	63
Figure 50.	Worldview-2 Brightness Variance in Band 8 (860–1040 nm) with respect to Elevation Angle (Time): Duck, NC.....	65
Figure 51.	Duck Image Ratio, Image P006/P011 (Bands 2: 450–510, Band 5: 630–690, and Band 8: 860–1040 nm).....	66
Figure 52.	Pendleton Image Ratio, Image P009/P010 (Bands 2: 450–510, Band 5: 630–690, and Band 8: 860–1040 nm).....	66
Figure 53.	Pendleton Image Ratio: ROIs annotated (Band 3: 510–580 nm)	67
Figure 54.	Chip of Pendleton Image Ratio: Field (Veg) and Soil ROIs annotated.....	68
Figure 55.	Relative Ratio of Pendleton Image Ratio: Field (Veg) and Soil ROIs	69
Figure 56.	Google maps true-color image of Pendleton Spatial Profiles’ Regions	70
Figure 57.	Pendleton Image Ratio Spatial Profiles (Band 3: 510–580 nm).....	70
Figure 58.	Pendleton Image Ratio Spatial Profile #1 (Band 3: 510–580 nm)	71
Figure 59.	Pendleton Image Ratio Spatial Profile #2 (Band 3: 510–580 nm)	72
Figure 60.	BRDF ROI Comparison wrt Satellite Position for Duck ROIs: Left: Soil (Wet), Right: Soil (Dry) (Band 7: 770–895 nm).....	73
Figure 61.	BRDF Band Comparison wrt Satellite Position for Duck ROI: Soil (Dry) Band 7 and 8 (Band 7: 770–895 nm, Band 8: 860–1040 nm)	73
Figure 62.	Image Ratio done for All Regions of Interest in all Worldview-2 Bands (Duck, NC).....	74
Figure 63.	Image Ratio done for All Regions of Interest in all Worldview-2 Bands (Pendleton, CA)	75
Figure 64.	BRDF Results by Separation Angle for Ocean vs. Harbor (Pendleton, CA) ..	76
Figure 65.	BRDF Results by Separation Angle for Field (Veg) (Pendleton, CA)	77
Figure 66.	BRDF Results by Separation Angle for man-made materials	77
Figure 67.	BRDF Results by Separation Angle for Excellent and Poor IR Reflectors.....	78
Figure 68.	Histogram Shift with View Angle: Duck, NC (Band 1).....	91
Figure 69.	Histogram Shift with View Angle: Duck, NC (Band 2).....	92
Figure 70.	Histogram Shift with View Angle: Duck, NC (Band 3).....	93
Figure 71.	Histogram Shift with View Angle: Duck, NC (Band 4).....	94
Figure 72.	Histogram Shift with View Angle: Duck, NC (Band 5).....	95
Figure 73.	Histogram Shift with View Angle: Duck, NC (Band 6).....	96
Figure 74.	Histogram Shift with View Angle: Duck, NC (Band 7).....	97
Figure 75.	Histogram Shift with View Angle: Duck, NC (Band 8).....	98
Figure 76.	Histogram Shift with View Angle: Pendleton, CA (Band 1).....	99
Figure 77.	Histogram Shift with View Angle: Pendleton, CA (Band 2).....	100
Figure 78.	Histogram Shift with View Angle: Pendleton, CA (Band 3).....	101
Figure 79.	Histogram Shift with View Angle: Pendleton, CA (Band 4).....	102
Figure 80.	Histogram Shift with View Angle: Pendleton, CA (Band 5).....	103
Figure 81.	Histogram Shift with View Angle: Pendleton, CA (Band 6).....	104
Figure 82.	Histogram Shift with View Angle: Pendleton, CA (Band 7).....	105
Figure 83.	Histogram Shift with View Angle: Pendleton, CA (Band 8).....	106

Figure 84.	Spectral Radiance Displaying Variance with Wavelength and View Angle: Duck, NC (Ocean ROI).....	107
Figure 85.	Spectral Radiance Displaying Variance with Wavelength and View Angle: Duck, NC (Pond ROI).....	108
Figure 86.	Spectral Radiance Displaying Variance with Wavelength and View Angle: Duck, NC (Soil (Dry) ROI)	109
Figure 87.	Spectral Radiance Displaying Variance with Wavelength and View Angle: Duck, NC (Soil (Wet) ROI).....	110
Figure 88.	Spectral Radiance Displaying Variance with Wavelength and View Angle: Duck, NC (Forest ROI).....	111
Figure 89.	Spectral Radiance Displaying Variance with Wavelength and View Angle: Duck, NC (Golf Course ROI)	112
Figure 90.	Spectral Radiance Displaying Variance with Wavelength and View Angle: Duck, NC (Baseball Field ROI).....	113
Figure 91.	Spectral Radiance Displaying Variance with Wavelength and View Angle: Duck, NC (Parking Lot ROI).....	114
Figure 92.	Spectral Radiance Displaying Variance with Wavelength and View Angle: Duck, NC (Parking Lot 2 ROI).....	115
Figure 93.	Spectral Radiance Displaying Variance with Wavelength and View Angle: Duck, NC (Roof Top ROI)	116
Figure 94.	Spectral Radiance Displaying Variance with Wavelength and View Angle: Duck, NC (Roof Top 2 ROI)	117
Figure 95.	Spectral Radiance Displaying Variance with Wavelength and View Angle: Duck, NC (Roof Top 3 ROI)	118
Figure 96.	Spectral Radiance Displaying Variance with Wavelength and View Angle: Pendleton, CA (Ocean ROI)	119
Figure 97.	Spectral Radiance Displaying Variance with Wavelength and View Angle: Pendleton, CA (Harbor ROI)	120
Figure 98.	Spectral Radiance Displaying Variance with Wavelength and View Angle: Pendleton, CA (Marsh (Veg) ROI).....	121
Figure 99.	Spectral Radiance Displaying Variance with Wavelength and View Angle: Pendleton, CA (Field (Veg) ROI).....	122
Figure 100.	Spectral Radiance Displaying Variance with Wavelength and View Angle: Pendleton, CA (Soil (Wet) ROI).....	123
Figure 101.	Spectral Radiance Displaying Variance with Wavelength and View Angle: Pendleton, CA (Soil (Dry) ROI)	124
Figure 102.	Spectral Radiance Displaying Variance with Wavelength and View Angle: Pendleton, CA (Sand ROI)	125
Figure 103.	Spectral Radiance Displaying Variance with Wavelength and View Angle: Pendleton, CA (Sand 2 ROI)	126
Figure 104.	Spectral Radiance Displaying Variance with Wavelength and View Angle: Pendleton, CA (Sand 3 ROI)	127
Figure 105.	Spectral Radiance Displaying Variance with Wavelength and View Angle: Pendleton, CA (Tarmac ROI)	128
Figure 106.	BRDF Results by Separation Angle: Duck, NC (Ocean ROI)	129

Figure 107.	BRDF Results by Separation Angle: Duck, NC (Pond ROI)	130
Figure 108.	BRDF Results by Separation Angle: Duck, NC (Soil (Dry) ROI)	131
Figure 109.	BRDF Results by Separation Angle: Duck, NC (Soil (Wet) ROI).....	132
Figure 110.	BRDF Results by Separation Angle: Duck, NC (Forest ROI).....	133
Figure 111.	BRDF Results by Separation Angle: Duck, NC (Golf Course ROI).....	134
Figure 112.	BRDF Results by Separation Angle: Duck, NC (Baseball Field ROI).....	135
Figure 113.	BRDF Results by Separation Angle: Duck, NC (Parking Lot ROI).....	136
Figure 114.	BRDF Results by Separation Angle: Duck, NC (Parking Lot 2 ROI).....	137
Figure 115.	BRDF Results by Separation Angle: Duck, NC (Roof Top ROI)	138
Figure 116.	BRDF Results by Separation Angle: Duck, NC (Roof Top 2 ROI)	139
Figure 117.	BRDF Results by Separation Angle: Duck, NC (Roof Top 3 ROI)	140
Figure 118.	BRDF Results by Separation Angle: Pendleton, CA (Ocean ROI).....	141
Figure 119.	BRDF Results by Separation Angle: Pendleton, CA (Harbor ROI)	142
Figure 120.	BRDF Results by Separation Angle: Pendleton, CA (Marsh (Veg) ROI)....	143
Figure 121.	BRDF Results by Separation Angle: Pendleton, CA (Field (Veg) ROI).....	144
Figure 122.	BRDF Results by Separation Angle: Pendleton, CA (Soil (Wet) ROI)	145
Figure 123.	BRDF Results by Separation Angle: Pendleton, CA (Soil (Dry) ROI).....	146
Figure 124.	BRDF Results by Separation Angle: Pendleton, CA (Sand ROI)	147
Figure 125.	BRDF Results by Separation Angle: Pendleton, CA (Sand 2 ROI)	148
Figure 126.	BRDF Results by Separation Angle: Pendleton, CA (Sand 3 ROI)	149
Figure 127.	BRDF Results by Separation Angle: Pendleton, CA (Tarmac ROI).....	150

THIS PAGE INTENTIONALLY LEFT BLANK

LIST OF TABLES

Table 1.	Visible and Infrared Bands defined by Wavelength	6
Table 2.	Units of Radiometric Terms.....	13
Table 3.	MISR Spectral Bands.....	22
Table 4.	The Spectral Bands of Worldview-2 [34]	38
Table 5.	DigitalGlobe Satellites' Panchromatic and Multispectral Ground Sample Distance (GSD) Resolution.....	38
Table 6.	Duck, NC, Worldview-2 Imagery data (March 24, 2010).....	42
Table 7.	Pendleton, CA, worldview-2 Imagery data (March 24, 2010)	43
Table 8.	Satellite and Solar Azimuthal Angles, Elevation Angles, and Overall Separation Angles, Left: Pendleton, CA, Right: Duck, NC.....	44

THIS PAGE INTENTIONALLY LEFT BLANK

LIST OF ACRONYMS AND ABBREVIATIONS

ADEOS	Advanced Earth Observing Satellite
ASDC	Atmospheric Science and Data Center
ASTER	Advanced Spaceborne Thermal Emission and Reflection Radiometer
AVHRR	Advanced Very High Resolution Radiometer
BRDF	Bidirectional Reflectance Distribution Function
CHRIS	Compact High Resolution Imaging Spectrometer
DEM	Digital Elevation Model
DN	Digital Number
ENVI	Environment for Visualizing Images
EO	Earth Observing
EOS	Earth Observing System
ESA	European Space Agency
FIR	Far Infrared
FOV	Field of View
FPC	Foliage Projective Cover
FZA	Fly-by Zenith Angle
GCP	Ground Control Points
GSD	Ground Sample Distance
HSI	Hyperspectral Imagery
IDL	Interactive Data Language
JPL	Jet Propulsion Laboratory
LWIR	Long-wave Infrared
MWIR	Mid-wave Infrared
MISR	Multi-angle Imaging Spectroradiometer
MODIS	Moderate Resolution Imaging Spectroradiometer
MSI	Multispectral Imagery
NASA	National Aeronautics and Space Administration
NIR	Near Infrared
NOAA	National Oceanic and Atmospheric Administration
NPS	Naval Postgraduate School

OR2A	Ortho-Ready Standard 2A
PARABOLA	Portable Apparatus or Rapid Acquisitions of Bidirectional Observations of Land and Atmosphere
POLDER	Polarization and Directionality of the Earth's Reflectances
PROBA	Project for On Board Autonomy
ROI	Region of Interest
RPV	Rahman-Pinty-Verstraete
RTA	Radiative Transfer Algorithms
SWIR	Short-wave Infrared
TIF	Tagged Image Format
UTM	Universal Transverse Mercator
VNIR	Visible and Near Infrared
WRS	Worldwide Reference System

ACKNOWLEDGMENTS

I am very thankful for the opportunity to complete this thesis as part of my master's degree at the Naval Postgraduate School. It has been an amazing tour. I would like to thank Dr. Olsen for his confidence in my eventual completion of this thesis and his enthusiasm in the topic. Thank you to Dr. Newman for agreeing to critique this work. Last and most importantly, thanks to my family. The arrival of our first son called in to question whether I would have the time and motivation to complete this, but my husband ensured I had at least the time!

THIS PAGE INTENTIONALLY LEFT BLANK

I. INTRODUCTION

Classical remote sensing systems have viewed the earth from a perspective, which has been limited to a single view, generally in a near-nadir configuration. Of necessity, variations in reflectance with illumination angle and view angle have been ignored. LANDSAT is a classic illustration of this in Earth resource systems. Variations in reflectance with angles are quantified by the BiDirectional Reflectance Distribution Function, abbreviated “BRDF”. This quantity has been measured in laboratory settings, and is just starting to be observed from airborne and satellite systems. Satellites offer the best way to make regular and frequent BRDF measurements on a large scale. With a large number of observations, it is possible to accurately model the global BRDF. This could provide benefits to applications such as terrain mapping. This thesis addresses BRDF observations obtained over Duck, NC and Pendleton, CA, utilizing successive images taken by the Worldview-2 commercial satellite imaging system. The advantages of Worldview-2 over its predecessors are vastly improved spectral and spatial resolution and a high revisit time, which serve to provide more data points to the model. This thesis displays the improvements in BRDF observations on a small-scale.

THIS PAGE INTENTIONALLY LEFT BLANK

II. BACKGROUND

A. REMOTE SENSING

Remote sensing involves the collection of data from sensors, which are not in direct contact with the object being observed. Platforms such as airplanes, buoys, and satellites are ideal candidates for remote sensing instruments.

Radiometry is the field concerned with the measurement of the electromagnetic spectrum. Radiometry deals in absolute power, unlike the field of photometry, which measures brightness/intensity as perceived by the human eye. Radiometers are the most common remote sensing instrument and are used to measure the radiant flux, or power, of electromagnetic radiation. Common radiometry terms are explained in the next section of this chapter.

Many products are derived from remote sensing instruments, and resolution properties can vary widely between acquired imagery. Spatial, spectral, radiometric, and temporal resolution are limiting features of the specific instruments used to obtain imagery.

Spatial resolution involves a sensor's ability to distinguish physical separation of two objects viewed. In the remote sensing community, low spatial resolution is defined as 30 m or greater, medium ranges from 4-30 m, and high resolution imagery is less than 4 m. Excellent satellite imagery is currently on the order of 0.5 m spatial resolution.



Figure 1. Camp Randall Field, Madison, WI, Spatial Resolution of 30m, 10m, and 1m (Image: University of Wisconsin, Institute for Environmental Studies)

Spectral resolution typically refers to the number of bands over the spectral range of measured frequencies. For example, if an instrument had only one spectral band over the visible spectrum, a photon of red light ($\sim 700\text{nm}$) observed by the instrument would be indistinguishable from a measured photon of green light ($\sim 500\text{nm}$). Panchromatic imagers are an example of single-band imagers. However, if an instrument had numerous incremental bands, then the instrument could distinguish between the visible colors. Multispectral imaging (MSI) and hyperspectral imaging (HSI) refers to the level of spectral resolution. This concept is illustrated in Figure 2.

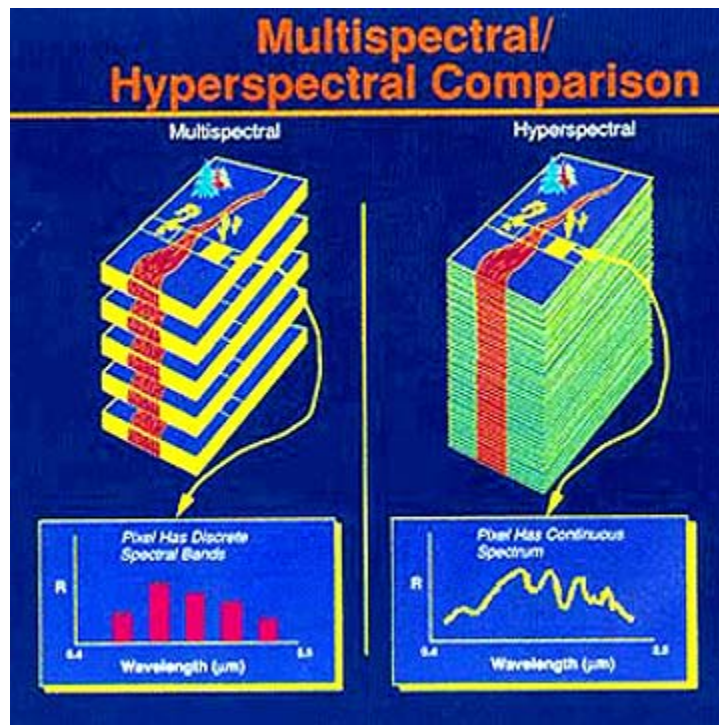


Figure 2. Differences between Multi-spectral imagery and Hyperspectral imagery

Radiometric resolution is the number of different intensities the sensor can detect. Greater resolution allows for finer distinguishability between intensities. It is typically limited by the available number of bits. For example, an eight digit binary string might be capable of defining 256 shades of gray; however, the limiting factor on radiometric resolution is often noise in the system.

The final type of resolution, temporal resolution, is a description of how often a sensor can obtain imagery of a region of interest (ROI), also known as its revisit time. It is useful for change detection in imagery. For example, deforestation studies do not require a high temporal resolution, as change occurs over a long period of time, whereas the intelligence community requires high temporal resolution as well as low.

B. PHYSICS OF LIGHT

While the term ‘light’ may sometimes be used interchangeably with ‘visible’, ‘light’ is a general term for all wavelengths and frequencies in the electromagnetic spectrum. The spectrum is illustrated in Figure 3. The visible portion of the spectrum refers to the wavelengths visible to the human eye, approximately 400-700 nm. All wavelengths/frequencies possess defining characteristics of intensity, polarization, and phase, and where necessary, the author will refer to wavelengths by their general category (i.e., visible, near-infrared (NIR), ultraviolet, etc.). The general definitions of these categories are delineated in Table 1.

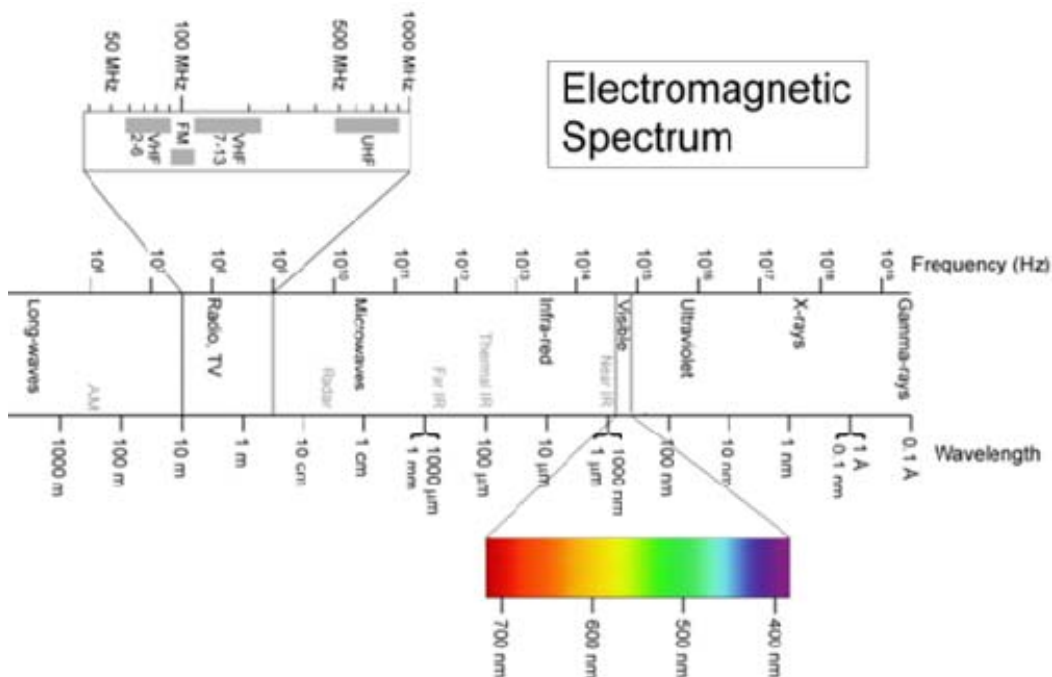


Figure 3. The Electromagnetic Spectrum

Name	Wavelength (μm)
Visible	0.38 - 0.75
Red	0.62 - 0.75
Orange	0.59 - 0.62
Yellow	0.57 - 0.59
Green	0.495 - 0.57
Cyan	0.476 - 0.495
Blue	0.45 – 0.475
Violet	0.38 – 0.45
NIR	0.75 – 1.4
SWIR	1.4 – 3.0
MWIR	3.0 – 8.0
LWIR	8.0 – 15.0
FIR	14.0 – 1000

Table 1. Visible and Infrared Bands defined by Wavelength

1. Interactions With Matter

Light can be considered as radiated or irradiated. These terms refer to the source and destination of energy. Radiation refers to the emission of energy from an object, while irradiation refers to the interaction of radiated energy upon a surface. A prime example of a radiator is the Sun, while the Earth, interacting with the Sun's emitted energy, would be considered irradiated by the energy. Electromagnetic radiation interacts with matter in one of four ways: scattering, transmission, absorption, and reflection. How light behaves upon striking a medium depends upon the characteristics of the medium, the angle of incidence, and the characteristics of the light itself [1].

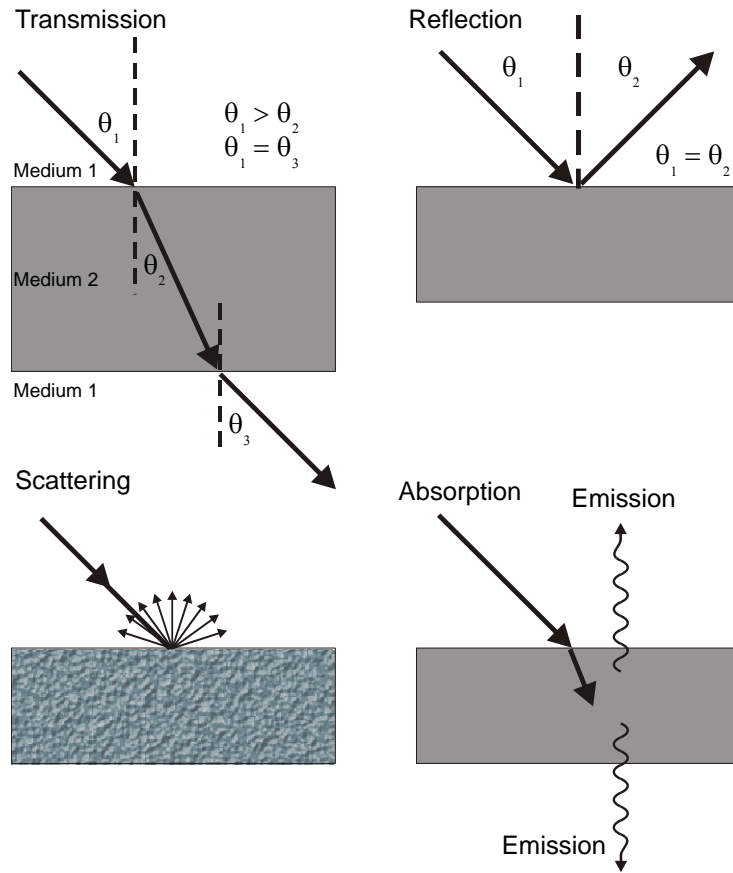


Figure 4. Electromagnetic Radiation Interactions with Matter [2]

Scattering does not change the energy of the electromagnetic wave but changes the direction of the wave. The interaction causes the wave to be redirected in a myriad of directions, maintaining wavelength, but with each resulting wave at a reduced intensity of the original.

Transmission is the process of an energy wave passing through a medium. It is dependent upon the properties of the medium the energy wave is passing from, properties of the medium it is entering into, and the angle of incidence between the two. Transmission describes how a wave's angle of incidence, θ_1 , referenced from the normal, is affected due to a velocity change caused by its passage from one medium to another. It results in a velocity and direction change of the wave, called refraction. This concept can be illustrated mathematically. Each medium has an intrinsic property, called an index of refraction, η , which is described in Equation (1):

$$\eta = \frac{c}{v} \quad (1)$$

The index of refraction is the ratio of the velocity of the radiation in a vacuum, c , to the velocity in a medium, v . As the energy passes from one medium to the next, the interaction is described by Snell's Law, summarized as follows:

$$\frac{\sin \theta_1}{\sin \theta_2} = \frac{v_1}{v_2} = \frac{n_2}{n_1} \quad (2)$$

The resulting angle of refraction is θ_2 , which is also referenced from the normal.

Absorption occurs when the irradiated object does not allow transmission through the material, but instead the energy is converted into internal heat that is then reemitted as thermal radiation.

Specular reflection involves the bounce back of electromagnetic radiation by a surface upon which the radiation is incident. The law of reflection defines a plane, the plane of incidence, in which the incident wave, reflected wave, and surface normal lie. This law assumes a smooth surface, which results in a specular reflection, and the angle of incidence equals the angle of reflectance. The reflective nature of a surface is summarized by the equation:

$$R = \left(\frac{v_1 - v_2}{v_1 + v_2} \right)^2 = \left(\frac{\eta_2 - \eta_1}{\eta_2 + \eta_1} \right)^2 \quad (3)$$

Where again v is the velocity in a medium and η is the index of refraction. The reflectivity of the air-water interface results in a value of approximately 0.02, or 2%. This means, 2% of the energy is reflected back and 98% of the energy is transmitted through the water.

2. Solid Angle

Solid angles, quantified by the definition of steradians, are useful when describing properties and behavior of light. A solid angle, Ω , refers to the cone of angles which subtend an area on the surface of a sphere, the area of which is equal to the area occupied by an object. Mathematically, solid angles are defined by Equation (4). The concept is illustrated by Figure 5.

$$\Omega = \frac{A}{R^2} \quad (4)$$

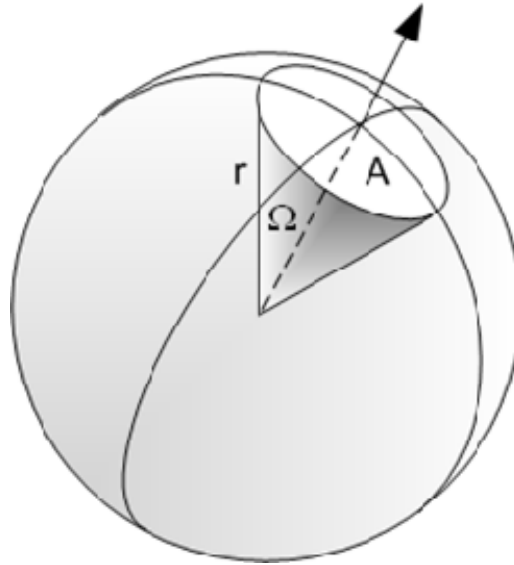


Figure 5. Solid angle, Ω

While a radian is defined in 2-D, a steradian is a 3-D concept. Steradian, meaning solid radian, allows solid angles to be quantified. A steradian is defined on a sphere of radius, R . It is the solid angle required to subtend an area equal to R^2 ($A = R^2$). When substituted into Equation (4), the equation evaluates to 1.

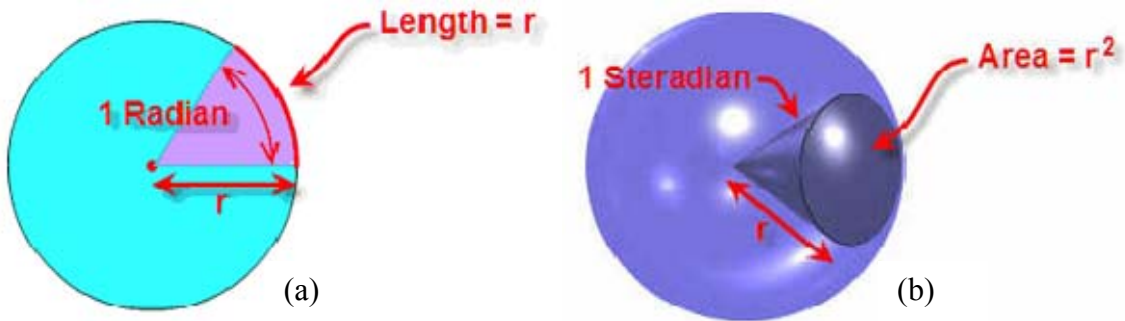


Figure 6. (a) Radian defined (b) Steradian defined

The surface area of a sphere is $4\pi R^2$, regardless of the size of the sphere. Utilizing Equation (4), the solid angle of any sphere is calculated as

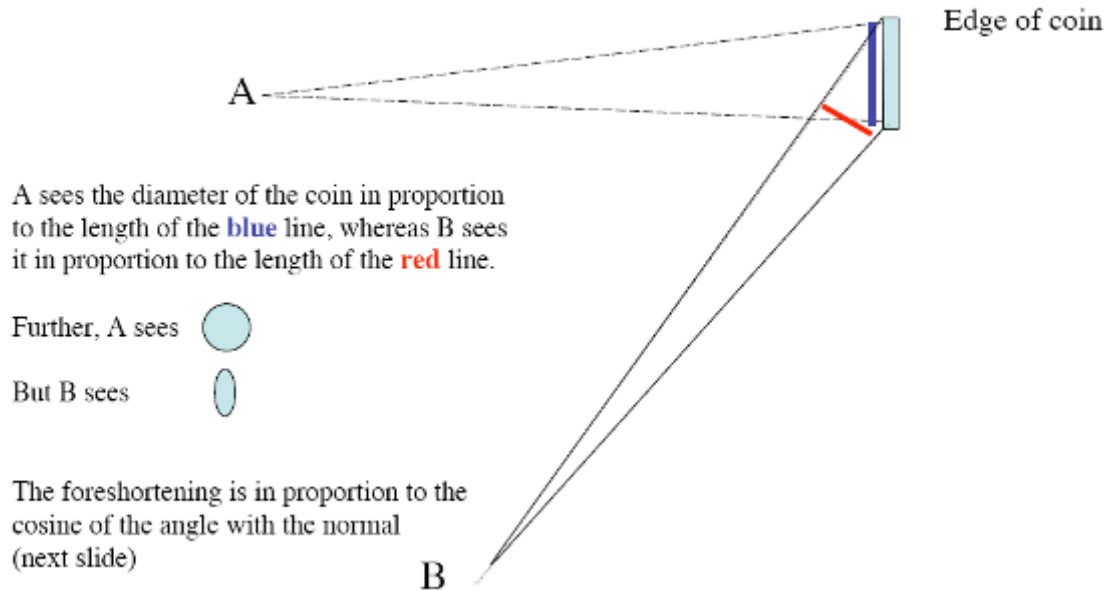
$$\Omega = \frac{4\pi R^2}{R^2} = 4\pi \text{ [sr]} \quad (5)$$

Calculating steradians removes the sphere's radius from consideration. Steradians quantify the relative amount of the sphere surrounding a point that is occupied by an object when viewed from the center of the sphere. An object that obscures the entire region surrounding a point would be said to occupy 4π steradians. Conversely, an object that appears to cover only half of the viewable sphere, a hemisphere, occupies 2π [sr]. Note that the steradian is a dimensionless quantity, and [sr] or the term 'steradian', are included solely for clarity. For clarification, when an object subtends only a portion of a given sphere, Equation (4) is rewritten as

$$d\Omega = \frac{dA}{R^2} \quad (6)$$

3. Foreshortening

An understanding of foreshortening is necessary to understand the subtle differences in radiometric terms. This concept is clearly explained in Figure 7.



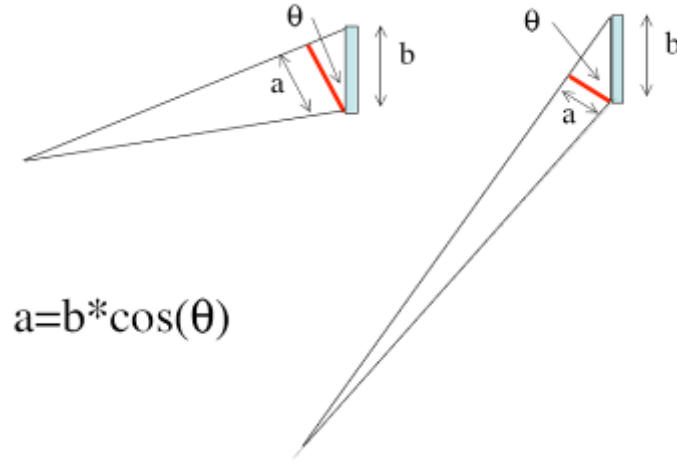


Figure 7. Foreshortening [3]

Foreshortening is a term frequently used in graphic design, and it describes how an image's appearance varies with the viewer's perspective.

4. Irradiance

Irradiance is the flux per unit area onto a surface and is defined as

$$E = \frac{d\Phi}{dA} \text{ [Wm}^{-2}\text{]} \quad (7)$$

where Φ is the radiant flux, or power. It is not foreshortened. Irradiance implies directionality, typically power inbound to a surface [4].

5. Radiance

Radiant intensity describes the flux per unit solid angle from a point source into a particular direction. It provides directional information but no spatial information, and it is defined as

$$I = \frac{d\Phi}{d\Omega} \text{ [Wsr}^{-1}\text{]} \quad (8)$$

where $d\Omega$ is the element of solid angle. Radiance, L , introduces the spatial element [4]. It is the flux per unit projected area per unit solid angle. As it deals with the amount of

energy passing through a specific solid angle and onto an area, it requires the introduction of the concept of foreshortening.

$$L = \frac{d\Phi}{d\Omega dA \cos \theta} \text{ [Wsr}^{-1}\text{m}^{-2}\text{]} \quad (9)$$

Manipulating Equations (7),(8), and (9)

$$L = \frac{d\Phi}{d\Omega dA \cos \theta} = \frac{\frac{d\Phi}{dA}}{\cos \theta d\Omega} = \frac{dE}{\cos \theta d\Omega} \quad (10)$$

Radiance is not identical across all wavelengths; therefore, a term is needed to describe the differing quantity with respect to wavelength. Introduction of the term, spectral radiance, L_λ , allows for this differentiation.

6. Bidirectional Reflectance Distribution Function

The Bidirectional reflectance distribution function (BRDF) describes the scattering characteristics of a material or object by describing how light from a source, incident on a target, is reflected in a given direction. The BRDF equation is the ratio of the energy scattered by the target in a particular direction, dependent upon wavelength, over the energy that was incident on the target from a particular direction (BR) integrated for all combinations of inbound and outbound energy directions (DF). BRDF is dependent on both the angle of incidence and on the angle of reflectance. These angles are defined in a Cartesian coordinate system by a polar angle, θ , measured from the surface normal, and an azimuthal angle, ϕ , measured from the x-axis. The geometry is defined in Figure 8.

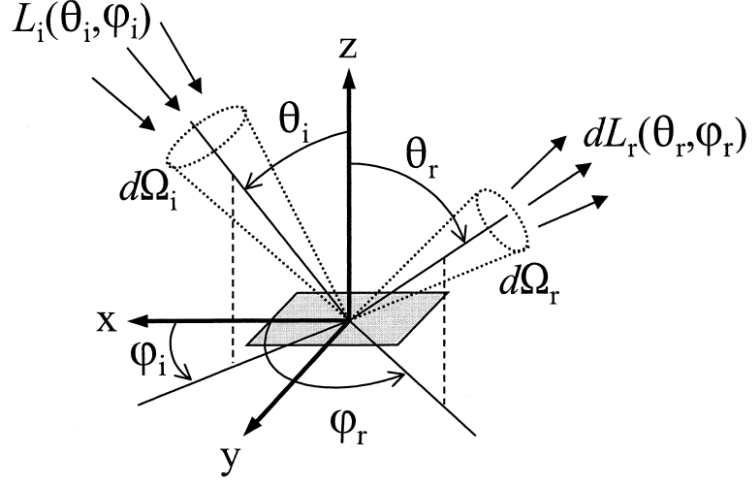


Figure 8. Reflection Geometry used in the definition of the BRDF

Symbol	Name	Unit
E_i, E_r	Irradiance	$\frac{W}{m^2}$
L_i, L_r	Radiance	$\frac{W}{m^2 sr}$
$L_{\lambda,i}, L_{\lambda,r}$	Spectral radiance	$\frac{W}{m^3 sr}$
f_r	BRDF	$\frac{1}{sr}$

Table 2. Units of Radiometric Terms

The BRDF equation is [4][5][6]:

$$f_r(\lambda, \theta_i, \phi_i, \theta_r, \phi_r) = \frac{dL_{\lambda,r}(\lambda, \theta_r, \phi_r)}{dE_{\lambda,i}(\lambda, \theta_i, \phi_i)} [sr^{-1}] \quad (11)$$

Here, $dE_{\lambda,i}(\lambda, \theta_i, \phi_i)$ is the incident spectral irradiance and $dL_{\lambda,r}(\lambda, \theta_r, \phi_r)$ is the reflected spectral radiance with regards to wavelength. This equation assumes uniform irradiance over a large area of a uniform, flat, and isotropic surface. Wavelength is disregarded to simplify the equation. Now the equation is written in terms of the incident irradiance and reflected radiance.

$$f_r(\theta_i, \phi_i, \theta_r, \phi_r) = \frac{dL_r(\theta_r, \phi_r)}{dE_i(\theta_i, \phi_i)} [sr^{-1}] \quad (12)$$

Radiance, unlike irradiance, does not involve a surface, only energy at a point. This allows it to interchangeably represent energy inbound or outbound. To elaborate, radiance leaving a point, p , in the direction of a point, q , is the same as radiance arriving at q from p . This concept allows the BRDF equation, Equation (11), to be put solely in terms of radiance. The process is begun by manipulating Equation (10),

$$dE = L \cos \theta d\Omega \quad (13)$$

Then Equation (13) is rewritten with the appropriate reference angles

$$dE_i(\theta_i, \phi_i) = L_i(\theta_i, \phi_i) \cos \theta_i d\Omega_i \quad (14)$$

And substituted into Equation (12)

$$f_r(\theta_i, \phi_i, \theta_r, \phi_r) = \frac{dL_r(\theta_r, \phi_r)}{L_i(\theta_i, \phi_i) \cos \theta_i d\Omega_i} [\text{sr}^{-1}] \quad (15)$$

Equation (15), another way of expressing the BRDF equation, now relates solely to radiance.

7. Anisotropy

Anisotropy is the property of being directionally dependent. In contrast, an isotropic surface displays a property identically in all directions. The study of BRDF is concerned with the property of reflectance. An example of an isotropic reflector is unfinished wood, as it appears the same from all viewing angles, while finished wood displays anisotropic reflection. The anisotropic nature of finished wood is displayed in Figure 9.



Figure 9. Anisotropic nature of Finished Wood

Most land surfaces are strongly anisotropic reflectors in the optical to thermal wavelengths. The main source of this anisotropic nature is the three-dimensional character of a surface. Shadowing and image obstruction are typical reasons an object differs in its appearance when viewed from different angles. This manifests in changes in surface radiance. An accurate BRDF is the appropriate method for capturing and expressing this anisotropic nature.

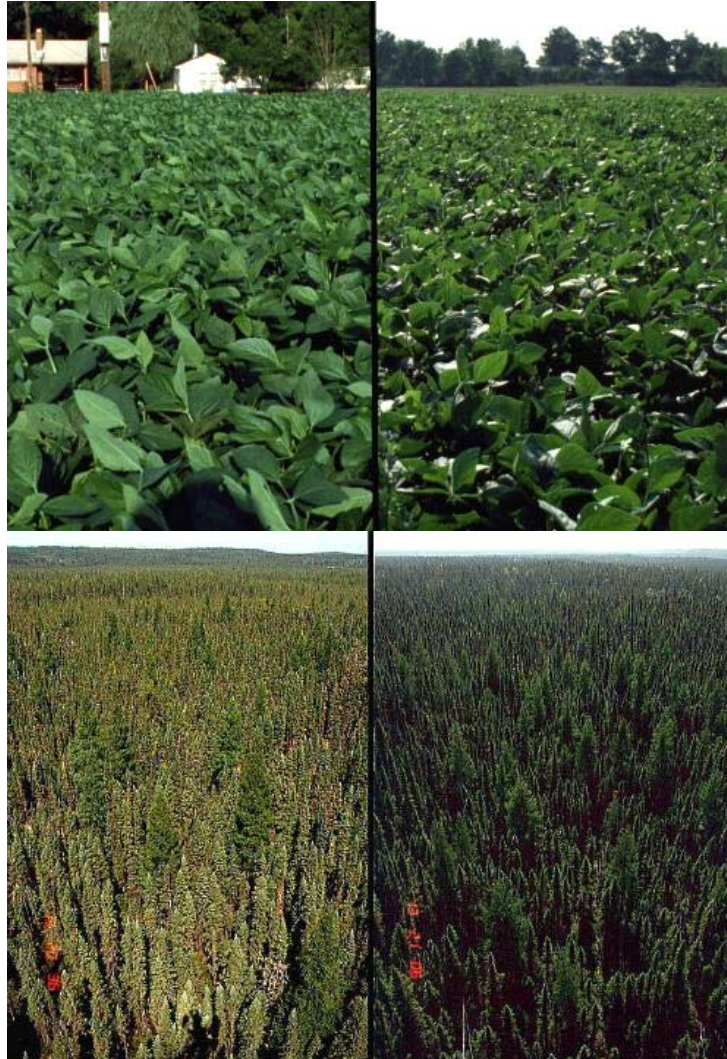


Figure 10. Anisotropy of Natural Features. Top: Soybean Field, Bottom: Black Spruce Forest, Left: Backscattering (sun behind observer), Right: forwardscattering (sun opposite observer), Photograph by Don Deering.

The images in Figure 10. , were taken as part of the Goddard Space Flight Center's PARABOLA experiment, and display how the sun angle, with respect to the observer, causes a difference in the appearance of the object, illustrating its anisotropic nature. Backscattering, when the sun is behind the observer, for example, causes a hot-spot effect, which hides all shadows. Forwardscattering, where the sun is opposite the observer, shows effects such as specular reflection and increased shadowing [7].

C. GROUND-BASED SENSORS

Ground-based sensors are required to measure surface BRDF and validate the results of the space-borne sensors. Gonioreflectometers are a type of ground measurement tools, while the PARABOLA is a unique system designed with the mission of surface BRDF measurements.

A gonioreflectometer, as the name implies, was designed to measure the angles of incident and reflected light. It provides more control over measurements taken in situ as it consists of a light source, the material to be observed, and a sensor to measure the reflected light. As BRDF is a four-dimensionally-dependent concept, the original gonioreflectometer, proposed in Murray-Coleman and Smith's 1990 article for the Journal of the Illuminating Engineering Society, provided four degrees of mechanical freedom. Gonioreflectometers have provided enormous amounts of data as they present a way to accurately, though not expeditiously, measure the BRDF over a large combination of angles [8].

The first major renovation to the original design was proposed by the Lawrence Berkeley Laboratory in 1992. It differed from the original design as it incorporated a hemispherical mirror and a fish-eye lens, which allowed for simultaneous measurement of all angles of reflected energy at a given incident angle without movement of the camera. Though a dramatic simplification of the BRDF measurement collection process, the design was not without its own flaws, such as distortion caused by the fish eye lens and unintended re-illumination of the sample.

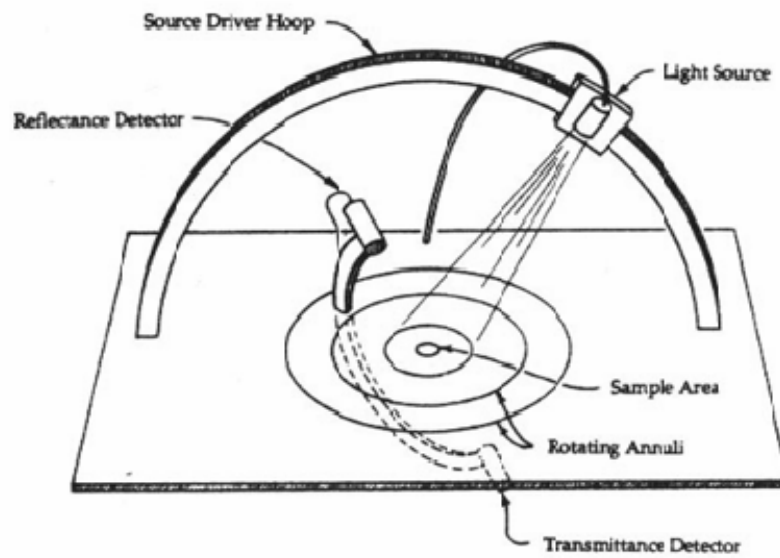


Figure 11. Murray-Coleman and Smith's Gonioreflectometer (1990)

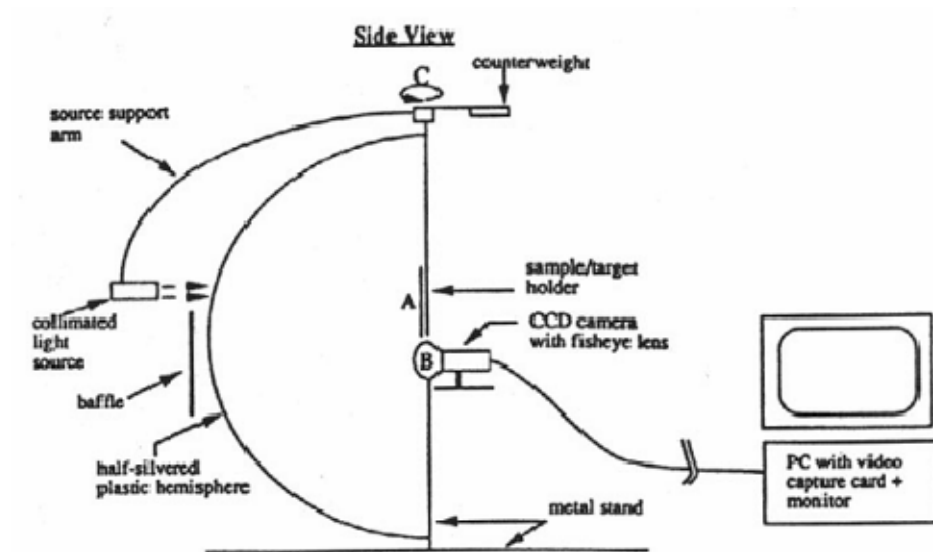


Figure 12. Lawrence Berkeley Laboratory's Gonioreflectometer (1992) [9]

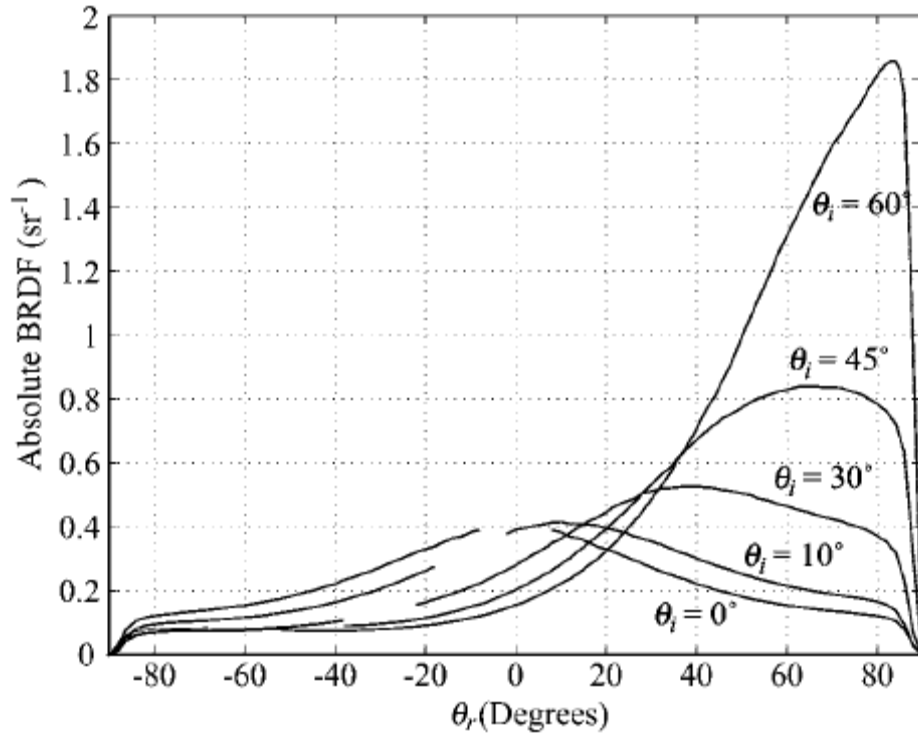


Figure 13. Incidence-plane BRDF of rough aluminum surface for several incidence angles, θ_i [10]

Figure 13. displays a sample of measurements taken from the results of a study into automation of a three-axis gonioreflectometer. The figure is taken from a full hemispherical dataset. It displays a rise in the BRDF value when the incident angle and the reflected angle coincide [10].

PARABOLA, the Portable Apparatus or Rapid Acquisitions of Bidirectional Observations of Land and Atmosphere, is a three channel, rotating head radiometer. It has three detectors, two silicon and one germanium solid state, with filters corresponding to the spectral bands, 630–690, 760–900, and 1550–1750 nm, respectively. The two-axis, two-motor rotation of the head enables a near-complete sampling of the entire sky/ground sphere with a FOV of 15° . During its 3-minute cycle it measures 72 azimuthal and 37 elevation positions, generating radiance measurements for both the ground and sky. Its primary purpose is to research the nature of BRDF and was designed to provide in-field verification of MISR data.



Figure 14. Portable Apparatus or Rapid Acquisitions of Bidirectional Observations of Land and Atmosphere (PARABOLA) Ground Sensor [11]

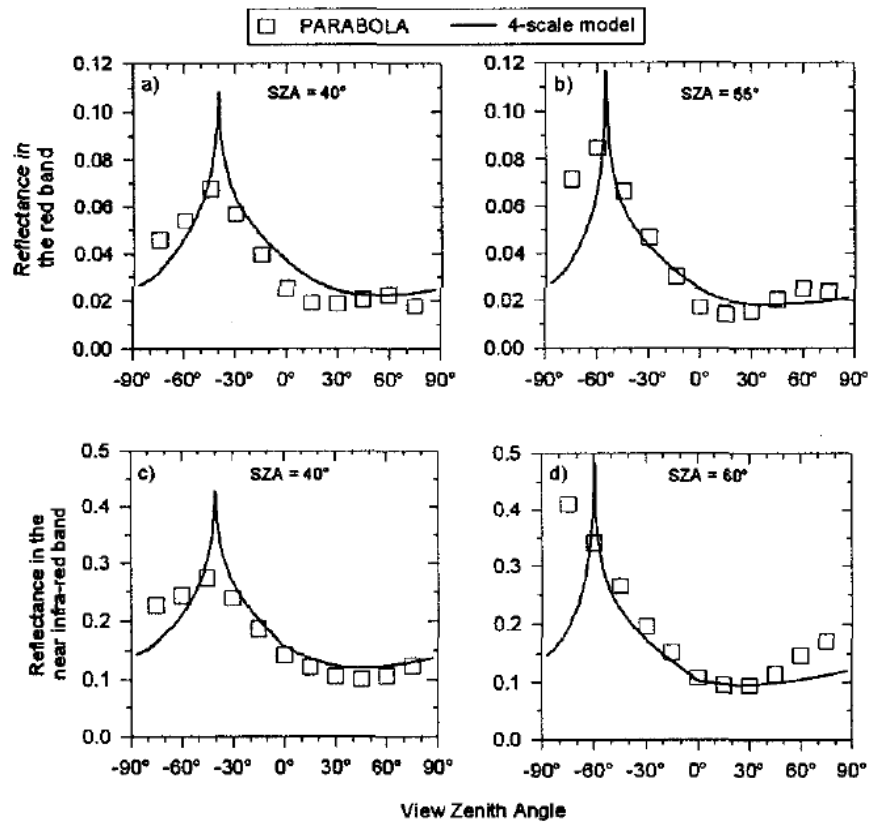


Figure 15. Reflectance values for multiple solar zenith angles in Red (Top) and NIR (Bottom) bands of PARABOLA and Chen-Leblanc's radiative transfer model are compared

Experiments were done in the forests in Saskatchewan, Canada, utilizing PARABOLA. PARABOLA data was compared to results calculated by a geometric optical model radiative-transfer model. As Figure 15. shows, the model tested simulates the measurements closely, with the exception of at large view zenith angles on the backscattering side [12].

D. SPACE-BORNE SENSORS: MULTI-ANGLE AND MULTIPLE ANGLE SATELLITES

Satellites have long been used to make measurements of the Earth. The NASA concept called the Earth Observing System (EOS) consists of a series of coordinated polar and low-inclination satellites designed for global observations. Most of these satellites are not in a position to make BRDF measurements, as they generally offer only a nadir view. A small number of sensors have begun to offer routine multiple angle views. The advent of IKONOS in 1999 allowed for significant off-nadir collection. This raises issues on how to deal with off-nadir views in the analysis of spectral data. These satellites aid in atmospheric corrections as they make timely and successive, and in the case of multi-angle, simultaneous measurements of the atmospheric aerosols which informs and improves atmospheric modeling [13]. The use of cross-track and along-track instruments counters the narrow field of view (FOV) argument and allows for an increase in the range of angular observations that can be made.

Multi-angle satellites acquire multiple images of the same object at differing angles through the simultaneous employment of multiple sensors. These systems allow for instantaneous sampling of BRDF. Multiple angle satellites acquire multiple images of the same object at differing angles through use of a single sensor over a period of time. MISR and POLDER are examples of multi-angle systems, while PROBA/CHRIS is a multiple angle imager. MISR was originally launched aboard the Terra (EOS AM) satellite. Images from multi-angle and multiple angle satellites are advantageous to the study of BRDF as they can be used to validate models or be coupled with models to provide a more accurate picture of BRDF.

1. Multi-angle Imaging SpectroRadiometer (MISR)

The Jet Propulsion Laboratory (JPL) designed the MISR sensor, which was launched on NASA's EOS flagship satellite, Terra, in December of 1999. MISR has nine cameras that simultaneously image the Earth at nine discrete angles. Cameras point forward and aftward of the local vertical at 26.1° , 45.6° , 60.0° , and 70.5° , and at Nadir. MISR images in the blue, green, red, and near-infrared spectral bands, and its spatial resolution ranges from 1 km in its normal operating mode to 275 m in local mode. MISR is a pushbroom sensor, also called a cross-track imager, which means its image is obtained through the motion of the satellite itself. The counter type, a whiskbroom sensor or along-track imager, acquires its images through the additional side-to-side sweeping motion of the sensor [e.g., MODIS].

The multi-angle capability of MISR aids in furthering understanding of how sunlight is scattered under varying conditions. Also, it provides information regarding monthly, seasonal, and long-term trends different types of clouds, aerosol particles, and surfaces. More specifically, it allowed for advanced study of the amount, type, and source of aerosol particles; characteristics of clouds; and land cover distribution.

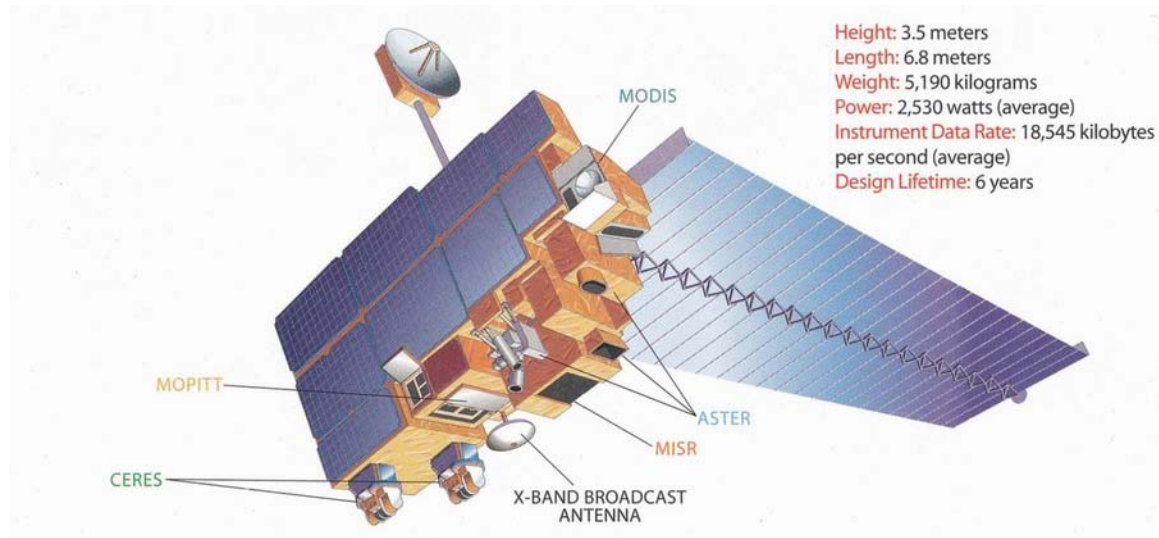


Figure 16. Terra Spacecraft with 5 Climate-Monitoring Sensors: MODIS, MISR, ASTER, MOPITT, and CERES

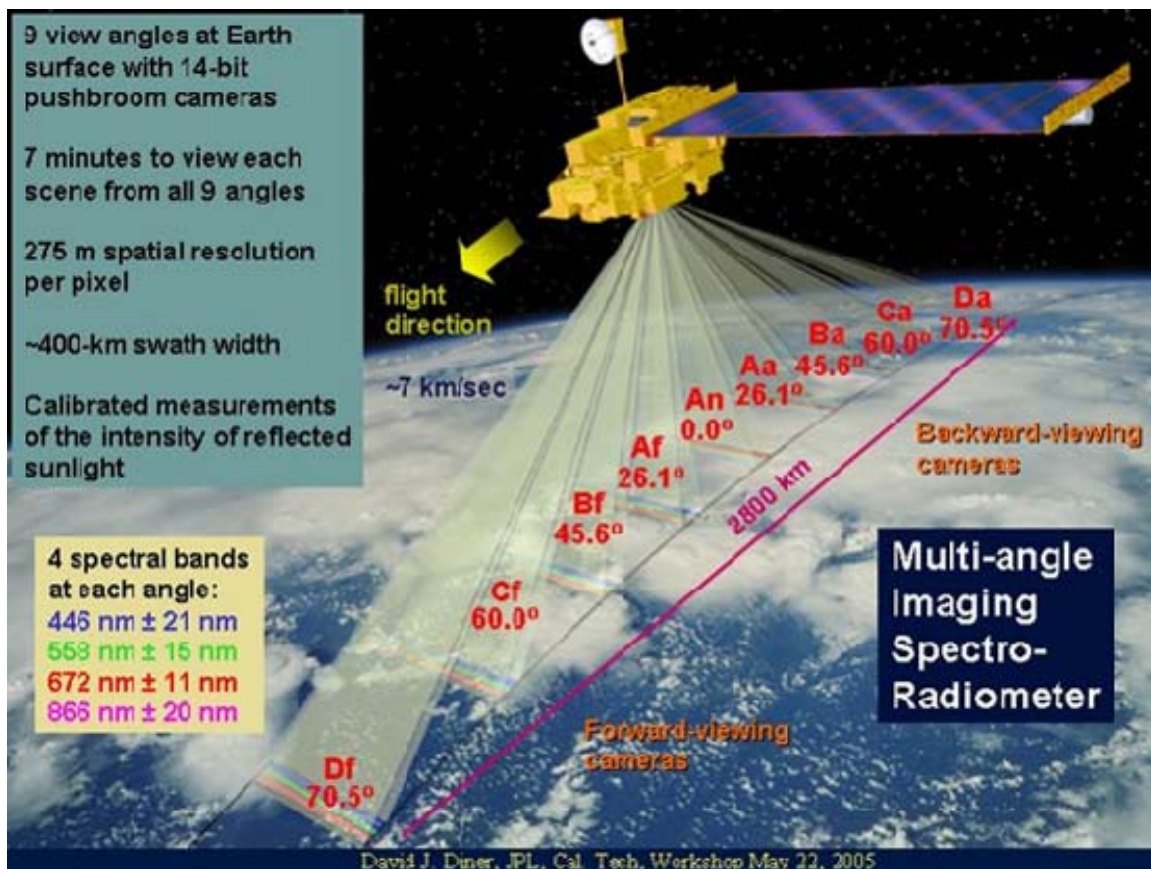


Figure 17. Multi-angle Imaging SpectroRadiometer (MISR) observes the Earth simultaneously with nine discrete cameras from $\pm 70.5^\circ$ in four spectral bands [14]

Table 3. MISR Spectral Bands

Name	Center Wavelength (nm)
Blue	446
Green	558
Red	672
NIR	867

Numerous studies have been done into the use of MISR data in the mapping of BRDF. The improved spatial resolution in local mode and the multi-angle viewing

capabilities have proven beneficial. In a study over the Queensland, Australia, the non-linear Rahman-Pinty-Verstraete (RPV) model and the linear Ross-Thick Li-Sparse Reciprocal (Ross-Li) model were compared using local mode MISR data. These models are further explained in the next section.

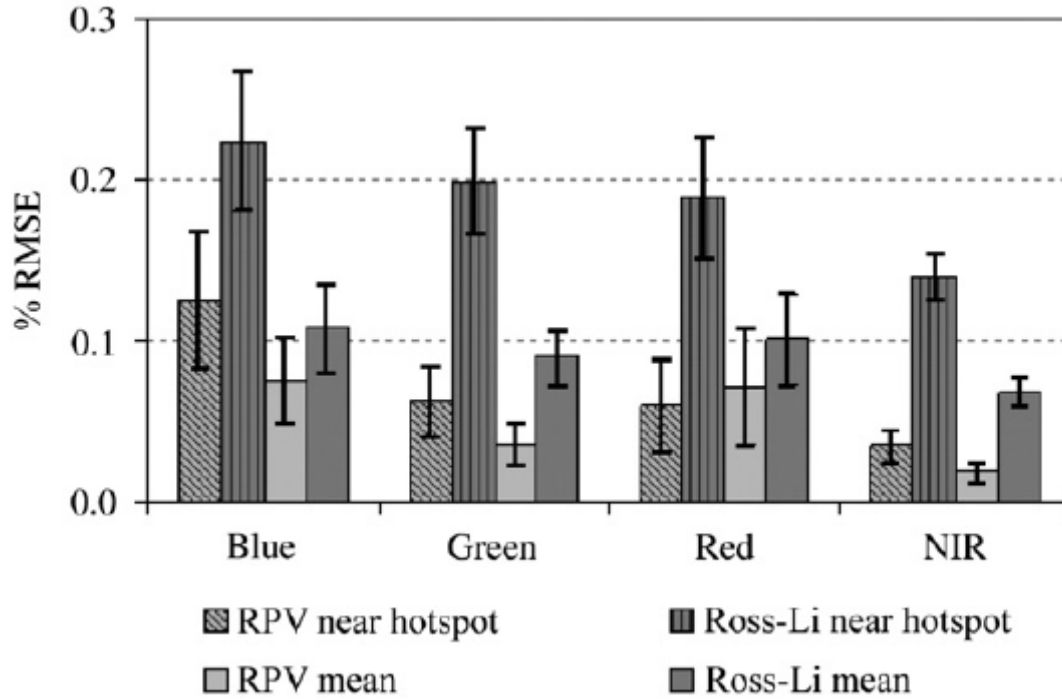


Figure 18. Mean and hot spot root mean squared error (RMSE) statistics displaying accuracy of RPV and Ross-Li model inversions

Finding the RPV model a better fit, it was compared to the foliage projective cover (FPC) and it was assessed that the resulting BRDF model were sufficient to map the vegetation in the grassland and woodland region of the Southern Brigalow Belt. The study concludes that the use of Local MISR data removes the need to use complex atmospheric radiative transfer algorithms (RTAs) within the scope of the limited geographic region [15]. It was proposed that MISR data could be used to improve the BRDF and albedo products created by the Moderate Resolution Imaging SpectroRadiometer (MODIS) instrument, also onboard the Terra satellite. Preliminary

work showed a reduction in bidirectional reflectance factors (BRF) by 10% in the red and green, when compared to MODIS-only data [16].

2. Polarization and Directionality of the Earth's Reflectances (POLDER)

POLDER was launched aboard the sun-synchronous, polar-orbiting Advanced Earth Observing Satellite (ADEOS) in August of 1996 and POLDER II was launched on ADEOS II in December of 2002, which flew until 2003. ADEOS and its instruments were also part of NASA's EOS mission. The POLDER instruments were important to the study of BRDF measurements as they provided the first opportunity to sample the BRDF of every point on Earth for viewing zenith angles up to 60° for the full azimuth range, at a spatial resolution of approximately 6 km. This was accomplished through the use of a wide FOV lens and a rotating filter and polarizing wheel [17][18].

The lens allowed for a maximum FOV of 114° , specifically $\pm 43^\circ$ along track and $\pm 51^\circ$ across track. The polarizing wheel rotated and scanned eight narrow spectral bands in the visible and NIR in 4.9 seconds. The surface target was viewed up to 14 times during the satellite overpass with various viewing angles. Over successive days, with the assumption of cloud-free days, orbital shifts allowed a sampling of the BRDF over the whole instrument field of view.

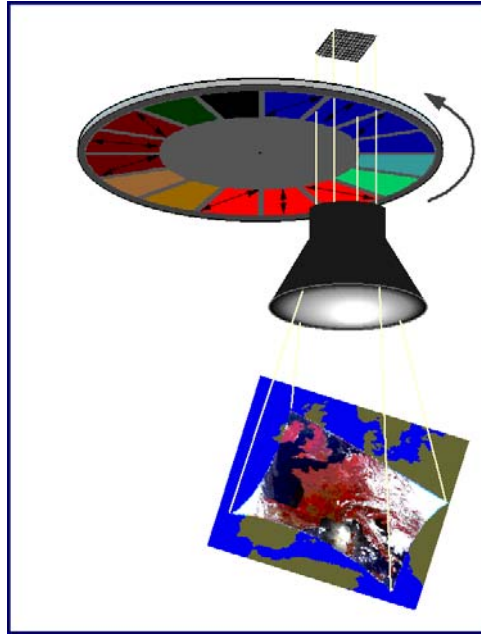


Figure 19. Illustration of the POLDER's rotating polarizing wheel. Scanned bands are in the VNIR bands ($\lambda=443, 490, 564, 670, 763, 765, 865$, and 910 nm).

POLDER filled the polarized reflectance observation need. An additional benefit of POLDER and ADEOS was that they did not operate solely cross-track, as previous satellites had. This allowed for less restrictive BRDF measurements. The processing of POLDER's data was improved as well. POLDER's scientists used a corrected Rayleigh scattering and an improved atmospheric scattering model, which no longer relied on a simple Lambertian surface. Analysis of the data in follow-on reports ([19][20][21]), showed that the imaging systems captured the hot spot and specular features well.

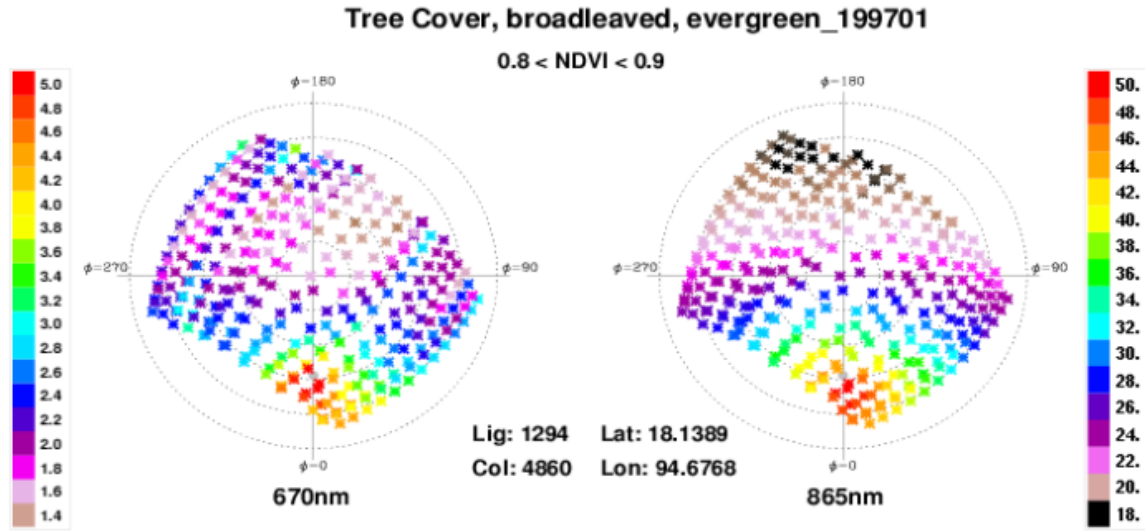


Figure 20. Sample BRDF product derived from the space-borne POLDER instrument. The angular space, annotated ϕ , represents the azimuthal delta between the sun and the viewing direction. BRDF is at a maximum in the backscattering direction (hotspot, $\phi=0^\circ$) and at a minimum in the forward scattering direction ($\phi=180^\circ$) [22]

As shown in Figure 20. , BRDF is plotted for two wavelengths, 670 nm and 867 nm. The BRDF peaks when the sun and viewing directions coincide. This is evident in the principle plane displayed in Figure 21.

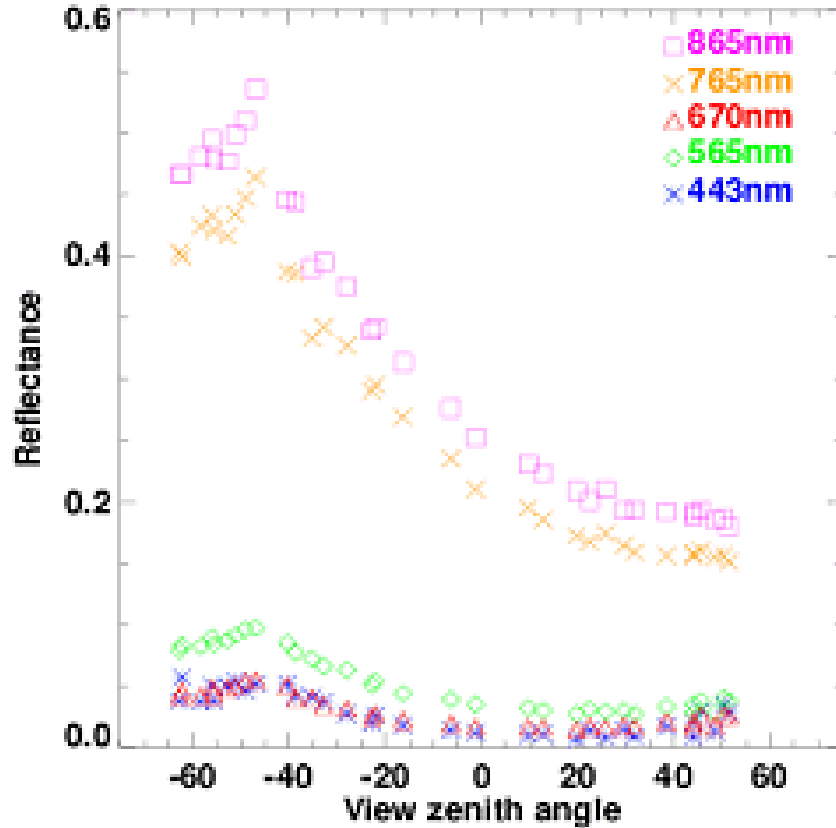


Figure 21. Reflectance values for sample region, Tree cover, broadleaved, evergreen, acquired by space-borne POLDER instrument [22]

3. Compact High Resolution Imaging Spectrometer (CHRIS)

The European Space Agency (ESA) launched CHRIS aboard the ‘Project for On-Board Autonomy’ (PROBA-1) satellite in 2001. The instrument provides large images, 13 km x 13 km, at medium resolution, 17 m, in 13 narrow spectral bands. When resolution is reduced to 34 m, it is capable of imaging in 62 spectral bands. The sensor is deemed ‘multiple angle’ because the satellite has four reaction wheels. These reaction wheels allow PROBA-1 to slew along-track, which gives CHRIS the ability to image a site five times during a single pass, and across-track, which reduces its revisit time of a ROI to less than a week. The high spatial resolution of CHRIS allowed for validation of other space-borne sensors such as POLDER, MODIS, and MISR.

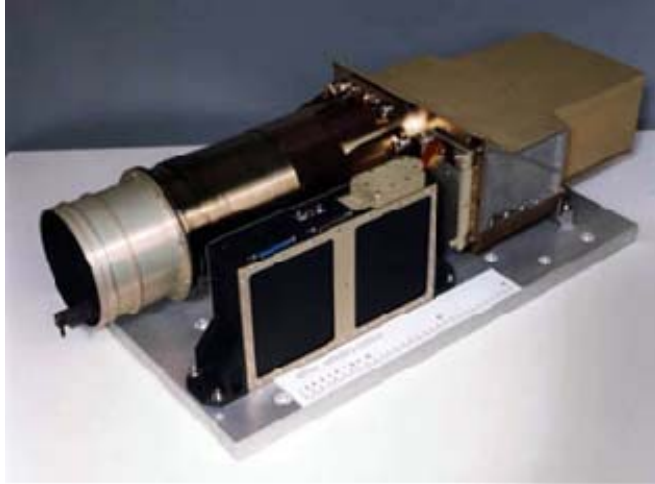


Figure 22. Compact High Resolution Imaging Spectrometer (CHRIS) [23]

Research has suggested the usefulness of CHRIS in deriving leaf area indices from BRDF model inversion [24]. Additional research into the usefulness of automatic land cover mapping products generated from CHRIS-derived BRDF data utilizing neural network algorithms has proven promising [25], and improvements to fitting the retrieved CHRIS data have been proposed through the use of an atmospheric correction algorithm specific for PROBA/CHRIS over land [26].

Figure 23. displays reflectance data acquired by PROBA/CHRIS. It displays the reflectance characteristics of four different regions over five different angles, with vegetated areas depicted in the left two charts, and man-made materials in the two charts on the right. The vegetation IR ledge can be clearly observed over all angles in the cornfield. The four charts illustrate the varying dependence of the materials on the fly-by zenith angle (FZA), the viewing angle. The curves are also flatter across the man-made materials, indicating a lesser dependence on wavelength. The multiple angles plotted reveal the dependence of the material on viewing angle. Each of the four regions displays different angle-dependency.

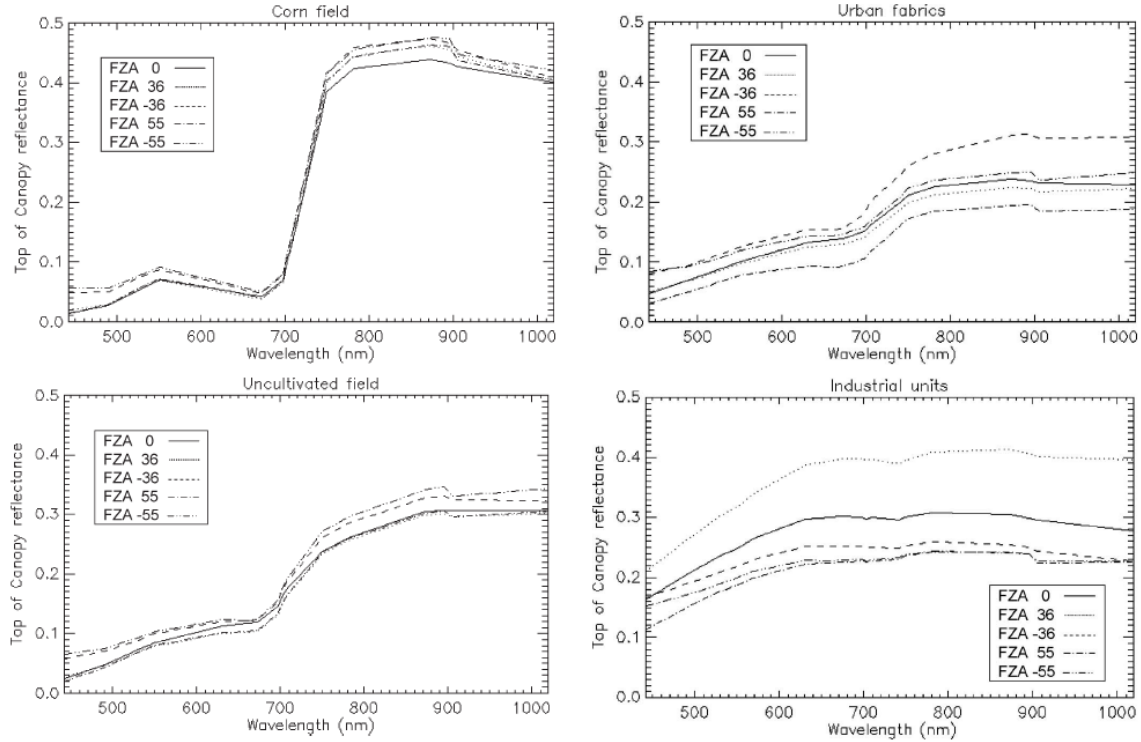


Figure 23. Reflectance data derived from CHRIS/PROBA over a range of zenith angles [25]

E. BRDF MODELS

Given the complex nature of measuring BRDF, approximations have been made in the past through the use of models. These models have been extensively developed for use in 3-D graphics and modeling [27]. These models are also tools used by scientists to improve the accuracy of calculations and to provide insight into affects seen in acquired imagery. These models are constantly being updated as the communities understanding of BRDF increases. Newer models are inherently more complex. Some attempt to account for more variables, while others focus on better modeling smaller regions of interest. The Lambertian model was among the first BRDF models. Torrance-Sparrow and Oren-Nayar are other follow-on models that attempt to better model surface BRDFs.

1. Lambertian Model

The Lambertian model is one of the earliest and simplest models. It was derived by Johann Lambert in 1760. The Lambertian model assumes that the surface is perfectly isotropic and therefore the apparent radiance is the same when viewed from any angle. Rough surfaces are often approximated as Lambertian surfaces. Lambert's cosine law, also known as the cosine emission law or Lambert's emission law, is the mathematical explanation for this postulation. It assumes that the radiant intensity, I , from an isotropic reflector is directly proportional to the cosine of the angle between the observer's line of sight and the surface normal. The radiance is constant because as the intensity is reduced as the distance increases, so too does the observed area. See Figure 24. This model is for a perfectly diffused object. It is often used to represent the diffuse element in newer, more complex models. The BRDF of a Lambertian surface is a constant.

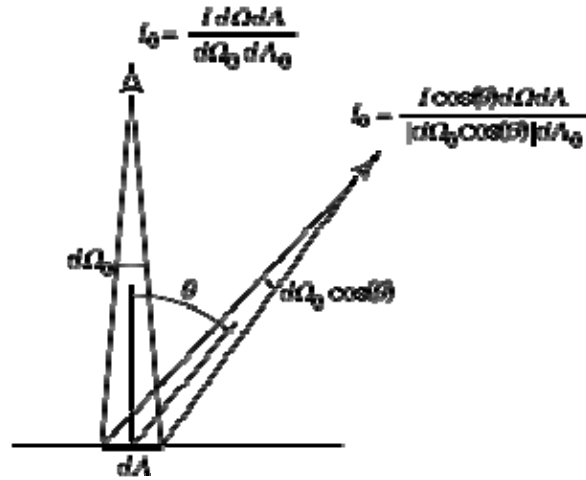


Figure 24. Explanation of Lambert's Cosine Law. I_0 represents the observed radiance.

In an experiment done on South African savanna vegetation, researchers found that a leaf, when intact displayed specular reflection, but when crushed more closely resembled a diffuse surface. As the particle size decreased with further crushing, the BRDF of the leaf flattened toward a constant, displaying a BRDF of a near-Lambertian surface. This is displayed in Figure 25.

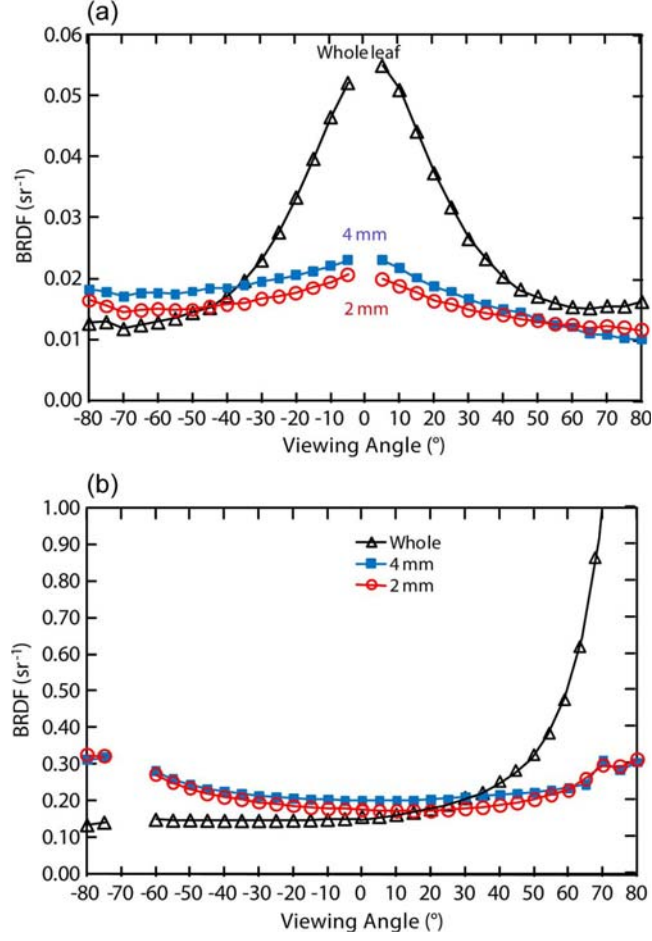


Figure 25. Laboratory-based BRDF of whole, 4-, and 2-mm cut poplar leaves at (a) normal incidence and 340 nm and (b) 67° incidence and 860 nm [28]

2. Rahman-Pinty-Verstraete Model

The semi-empirical RPV model is dependent on three terms, ρ_0 , k , and Θ , described by the function:

$$\rho_s(\theta_i, \varphi_i; \theta_r, \varphi_r; \lambda) = \rho_0 * M(\theta_i, \theta_r, k) * F(g) * [1 + R(G)] \quad (16)$$

where ρ_0 , the intensity of the surface reflectance, and k , the level of anisotropy of the surface, are empirical surface parameters, and Θ controls the function $F(g)$ and

influences the relative forward and backscattering. The model expresses the reflectance ρ_s , in terms of illumination from a direction, θ_i and ϕ_i , and the direction of observation, θ_r and ϕ_r [29].

3. Ross-Thick Li-Sparse Model

The Ross-Li model is a linear, kernel-driven model where BRDF is expressed as a sum of theoretically constructed kernel functions, dependent upon solar zenith angle, θ_s , viewing zenith angle, θ_v , and relative azimuth angle, ϕ , between the sun and viewer planes. The equation describing the model is:

$$\rho(\theta_s, \theta_v, \phi) = a_0 + a_1 * f_1(\theta_s, \theta_v, \phi) + a_2 * f_2(\theta_s, \theta_v, \phi) \quad (17)$$

The two kernels that make up the sum represent single scattering from a dense leaf canopy (f_1) and sparse surface objects with geometric-optical mutual shadowing (f_2). Also included are coefficients that represent isotropic, volumetric and geometric reflectance a_0 , a_1 , and a_2 [30].

4. Torrance-Sparrow Model

The Torrance-Sparrow model was created in 1967. It was one of the first models to capture off-specular peak. It also introduced the geometric attenuation factor, G , which allowed for masking and shadowing [31][8].

As the model was based in geometrical optics, the physics of light's motion was simplified to consider light moving as a ray, vice the true wave nature of light. This assumption requires the size of the wavelength to be significantly smaller than the matter it is interacting with. The model surface was made up of many microfaceted surfaces, considered to be perfect specular reflectors, with differing normals. The normals followed a Gaussian probability distribution. The model assumed the diffuse element was due to internal scattering and multiple microfacet reflections. The format of the model's specular element was derived using Fresnel reflectance and it was summed with the diffuse element to achieve the end equation.

The model fit the data well, however, to do so, it was necessary to input several constants. Its simplified physics and the necessity of these constants are the major shortcomings of the model.

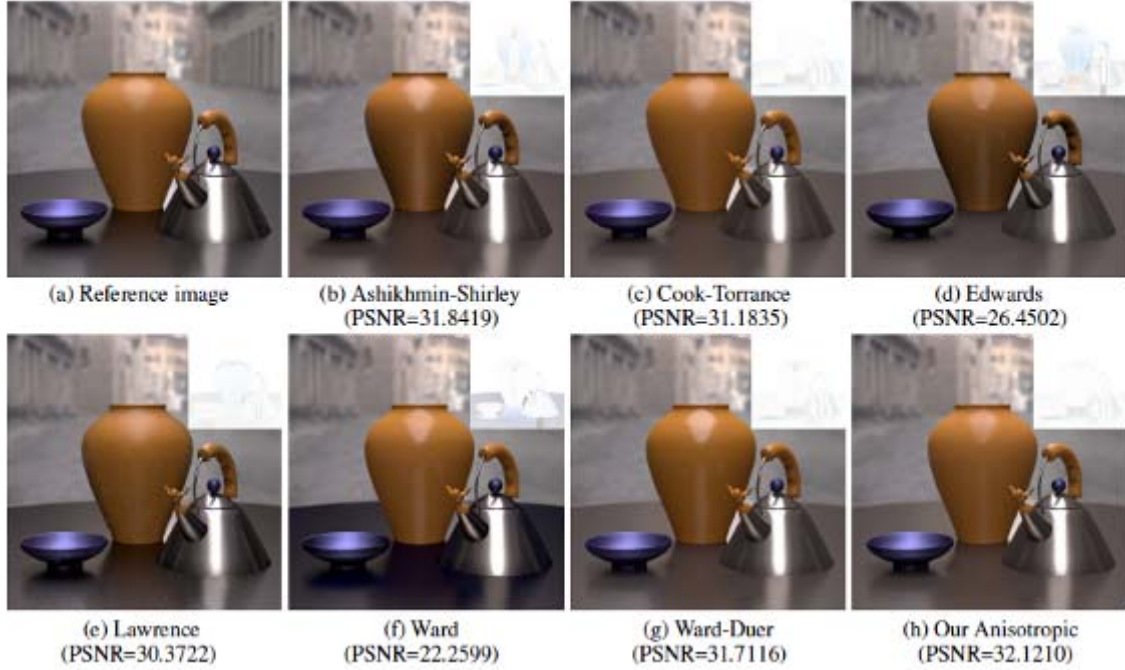


Figure 26. Various BRDF models plotted against a Reference Image [32]

A follow on model, the Cook-Torrance model was developed from the Torrance-Sparrow model, and offered improvement through the accountability of wavelength and color shifting. Various models are plotted against a reference image in Figure 26. The Cook-Torrance model is depicted in part (c) of the figure. The intensity of the insets represents disparity between the model and the reference image.

5. Oren-Nayar Model

This model is similar to the Torrance-Sparrow model in that it uses a microfaceted surface; however, it differs because it assumes these microfacets are perfectly diffuse vice perfectly specular. The Oren-Nayar model was created in 1993, and its main advantage was an improvement over the Lambertian technique for modeling rough, diffuse surfaces. Lambert's model does not account for surface roughness. Rough

surfaces have varying normals across the surface and therefore foreshortening occurs disproportionately between the intensity and area. This means the radiance is not held constant as it is in the Lambertian model [33].



Figure 27. Oren-Nayar Model for Rough Surfaces. Note the improved accuracy of the model over that of the Lambertian model.

III. EXPERIMENTAL APPROACH

A. PROBLEM DEFINITION

An area that has had limited research attention involves the accurate calculation and modeling of bidirectional reflectance. The difficult and specific nature of the calculations has driven researchers to labor to improve models to fit the limited amount of data. The calculation of BRDF is extremely difficult because it requires individual measurements of all combinations of direction of incoming irradiance from a source and the subsequent outgoing radiance from a target over a broad spectrum of wavelengths. Measurements have been done in the field, which have provided precise information regarding a few specific surfaces. From such measurements, models have been created, which may provide a workable representation of the BRDF under similar conditions of material and terrain. Tradeoffs are made in accuracy in an effort to simplify analysis, as calculating BRDF for each experiment would be tedious and time consuming. This is an acceptable solution for some but a poor solution for others. Further work is needed in finding an expeditious and cost-effective method to retrieve the bidirectional reflectance over a broad spectrum of wavelengths, angles, and geography.

The goal of this thesis is to illustrate the use of Worldview-2, specifically the advantage provided by its contribution to the library of BRDF data, through its generation of high spatial resolution data in eight wavelengths.

B. EQUIPMENT

1. Worldview-2

The data for analysis was collected by the Worldview-2 satellite. The Worldview-2 satellite was launched by DigitalGlobe in 2009. The addition of this satellite added unique remote sensing capabilities that were previously unavailable.



Figure 28. Artist rendering of Worldview-2 Satellite

Four spectral bands are typically provided in multispectral imagery. These include bands in the red, green, blue and near-infrared spectrum. These bands are provided by Worldview-2 and by its predecessor, Quickbird, which is also a multispectral imager. Worldview-2 differs because it is capable of imaging in four new bands. A visual and numerical definition of these bands is provided in Figure 29. and Table 4. , respectively. The first new band, ‘coastal blue’, with wavelength limits of 400–450 nm, offers improved bathymetry, vegetation, and atmospheric correction study. The second additional band is a yellow band, with a range of 585–625 nm, which aids in creating true-color images and improves target characteristics important in vegetation analysis. The third band is a red-edge band. Imaging from 705–745 nm, this band is useful for evaluating the health of vegetation and the production of chlorophyll. Finally, Worldview-2 provides a second near-infrared band, capable of viewing wavelengths from 860–1040 nm. This band provides an overlap in the original near-infrared band, and is less susceptible to atmospheric effects.

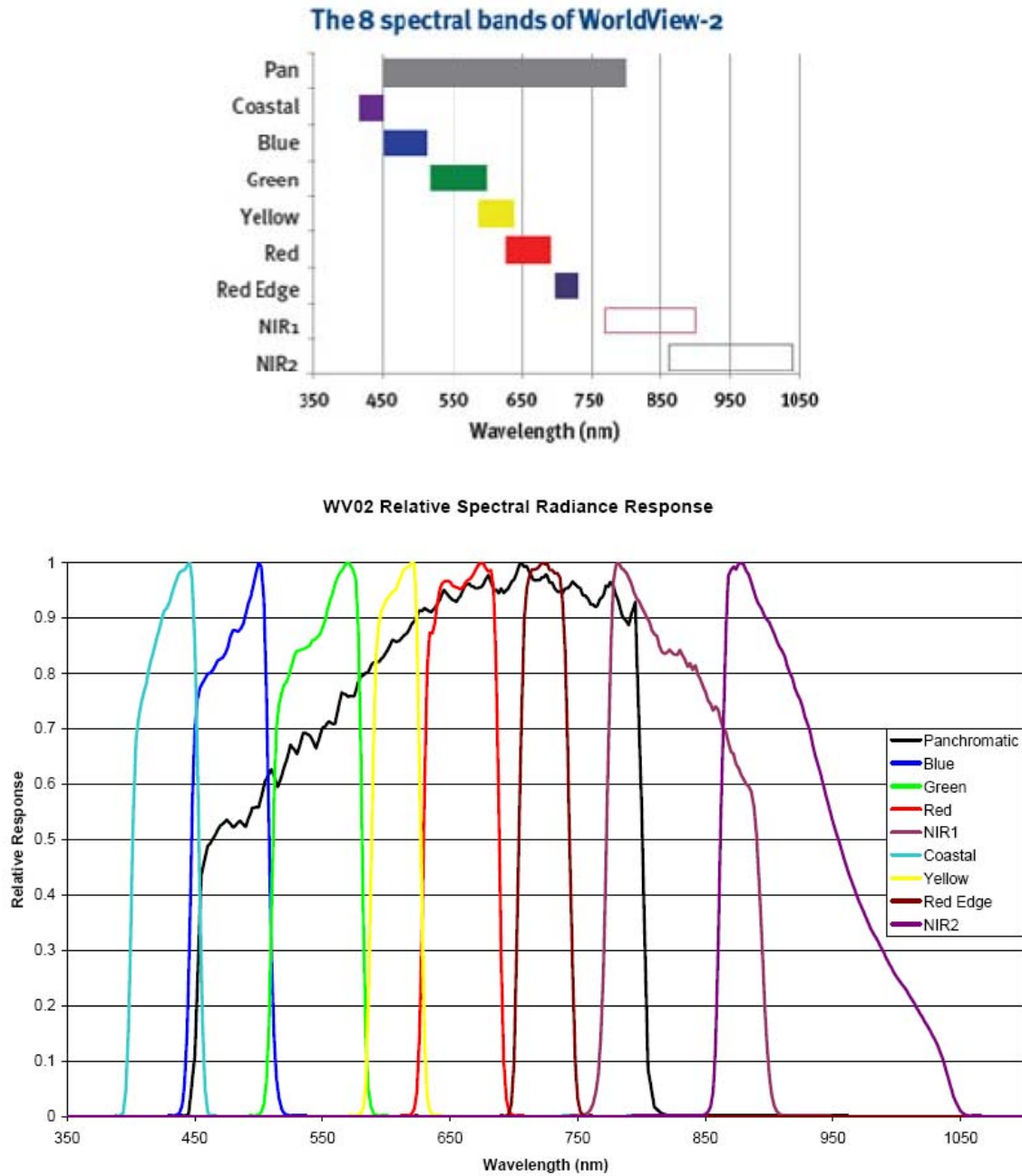


Figure 29. Worldview-2 Bands and Relative Spectral Radiance Response

Table 4. The Spectral Bands of Worldview-2 [34]

Band	Center (nm)	Min (nm)	Max (nm)	Name
PAN	632	464	801	Panchromatic
1	427	400	450	Coastal Blue
2	478	450	510	Blue
3	546	510	580	Green
4	608	585	625	Yellow
5	659	630	690	Red
6	724	705	745	Red-Edge
7	831	770	895	NIR1
8	908	860	1040	NIR2

An additional benefit of Worldview-2 over DigitalGlobe's previous spectral imagery satellite, Quickbird, is improved spatial resolution. Worldview-2 provides a nominal 0.5 m panchromatic and 2.0 m multispectral imagery.

Satellite	Panchromatic GSD (m)		Multispectral GSD (m)	
	Nadir	Off-Nadir	Nadir	Off-Nadir
Quickbird	0.61	0.72 (25°)	2.44	2.88 (25°)
Worldview-1	0.50	0.55 (20°)	N/A	N/A
Worldview-2	0.46	0.52 (20°)	1.80	2.40 (20°)

Table 5. DigitalGlobe Satellites' Panchromatic and Multispectral Ground Sample Distance (GSD) Resolution

2. The Environment for Visualizing Images 4.7 (ENVI[®])

A number of different tools are available to process and analyze geospatial imagery. Image processing done in support of this thesis was done using ITT Visual Information Solution's ENVI[®] software. The integrated Interactive Data Language (IDL) software was utilized to process and analyze the 25 multispectral image products received.

ENVI provides preprocessing software for Worldview-2 imagery. This software allows conversion of digital numbers, which relate relative brightness throughout the image, into radiance. This is done with a known gain and offset correction, embedded

within the imagery files. Alignment and spatial correction of the image is done through use of ENVI's mosaicing and registration tools. Analysis tools, such as the Region of Interest tool and the Spatial Profile tool were also used to extract information from the imagery. Further explanation of the employment of these tools is provided in the Methodology chapter.

THIS PAGE INTENTIONALLY LEFT BLANK

IV. METHODOLOGY

A. PRODUCT

Multi-angle data were acquired as part of an experiment in bathymetry derivation obtained from observing wave motion [35]. Sites were chosen for advantageous access and topography. The utility for our purposes was serendipitous. Two locations were imaged: Pendleton, CA, and Duck, NC. The latter site is advantageous for our work because of very low relief, simplifying registration.

Imaging by Worldview-2 was done over both locations on March 24, 2010. Ten images were taken over Pendleton, CA, and 15 over Duck, NC, by both the panchromatic imager and the multispectral imager. The multispectral data is the focus of analysis in this thesis.

Name	Acquisition Time (GMT)	Mean Satellite Azimuth (deg)	Mean Satellite Elevation (deg)
1/P006	15:41:35	57.9	46.9
2/P004	15:41:46	63.4	49.4
3/P005	15:41:57	69.8	51.6
4/P013	15:42:08	77	53.5
5/P009	15:42:18	85	54.9
6/P003	15:42:29	93.8	55.8
7/P008	15:42:40	102.9	56
8/P010	15:42:51	112	55.4
9/P012	15:43:01	120.4	54.3
10/P014	15:43:12	128.1	52.6
11/P001	15:43:22	134.8	50.6
12/P015	15:43:33	140.5	48.3
13/P011	15:43:43	145.3	46
14/P002	15:43:53	149.5	43.7
15/P007	15:44:03	153	41.3

Name	Solar Azimuth (deg)	Solar Elevation (deg)	Solar Zenith Angle (deg)	Separation Angle (deg)
1/P006	144.5	50.1	39.9	66.61301
2/P004	144.5	50.1	39.9	62.23531
3/P005	144.6	50.1	39.9	57.37138
4/P013	144.7	50.1	39.9	51.97498
5/P009	144.7	50.2	39.8	45.93798
6/P003	144.8	50.2	39.8	39.38992
7/P008	144.8	50.2	39.8	32.51828
8/P010	144.9	50.2	39.8	25.67801
9/P012	145	50.2	39.8	19.3063
10/P014	145	50.3	39.7	13.3248
11/P001	145.1	50.3	39.7	8.153563
12/P015	145.2	50.3	39.7	3.835664
13/P011	145.2	50.3	39.7	-1.84744
14/P002	145.3	50.3	39.7	-4.48537
15/P007	145.3	50.4	39.6	-7.53443

Table 6. Duck, NC, Worldview-2 Imagery data (March 24, 2010)

Name	Acquisition Time (GMT)	Mean Satellite Azimuth (deg)	Mean Satellite Elevation (deg)
1/P002	19:03:32	277.8	61.2
2/P007	19:03:42	267.1	60.1
3/P009	19:03:53	257.6	58.2
4/P006	19:04:04	249.5	55.8
5/P008	19:04:15	242.9	53.1
6/P004	19:04:26	237.3	50.1
7/P010	19:04:36	232.9	47.2
8/P005	19:04:47	229.2	44.4
9/P003	19:04:57	226.2	41.6
10/P001	19:05:08	223.6	39.1

Name	Solar Azimuth (deg)	Solar Elevation (deg)	Solar Zenith Angle (deg)	Separation Angle (deg)
1/P002	155.9	56.2	33.8	-83.3647
2/P007	156	56.2	33.8	-77.9109
3/P009	156.1	56.2	33.8	-72.7192
4/P006	156.2	56.3	33.7	-68.0675
5/P008	156.2	56.3	33.7	-64.2788
6/P004	156.3	56.3	33.7	-61.0071
7/P010	156.4	56.3	33.7	-58.464
8/P005	156.5	56.3	33.7	-56.3613
9/P003	156.5	56.3	33.7	-54.8343
10/P001	156.6	56.3	33.7	-53.4706

Table 7. Pendleton, CA, worldview-2 Imagery data (March 24, 2010)

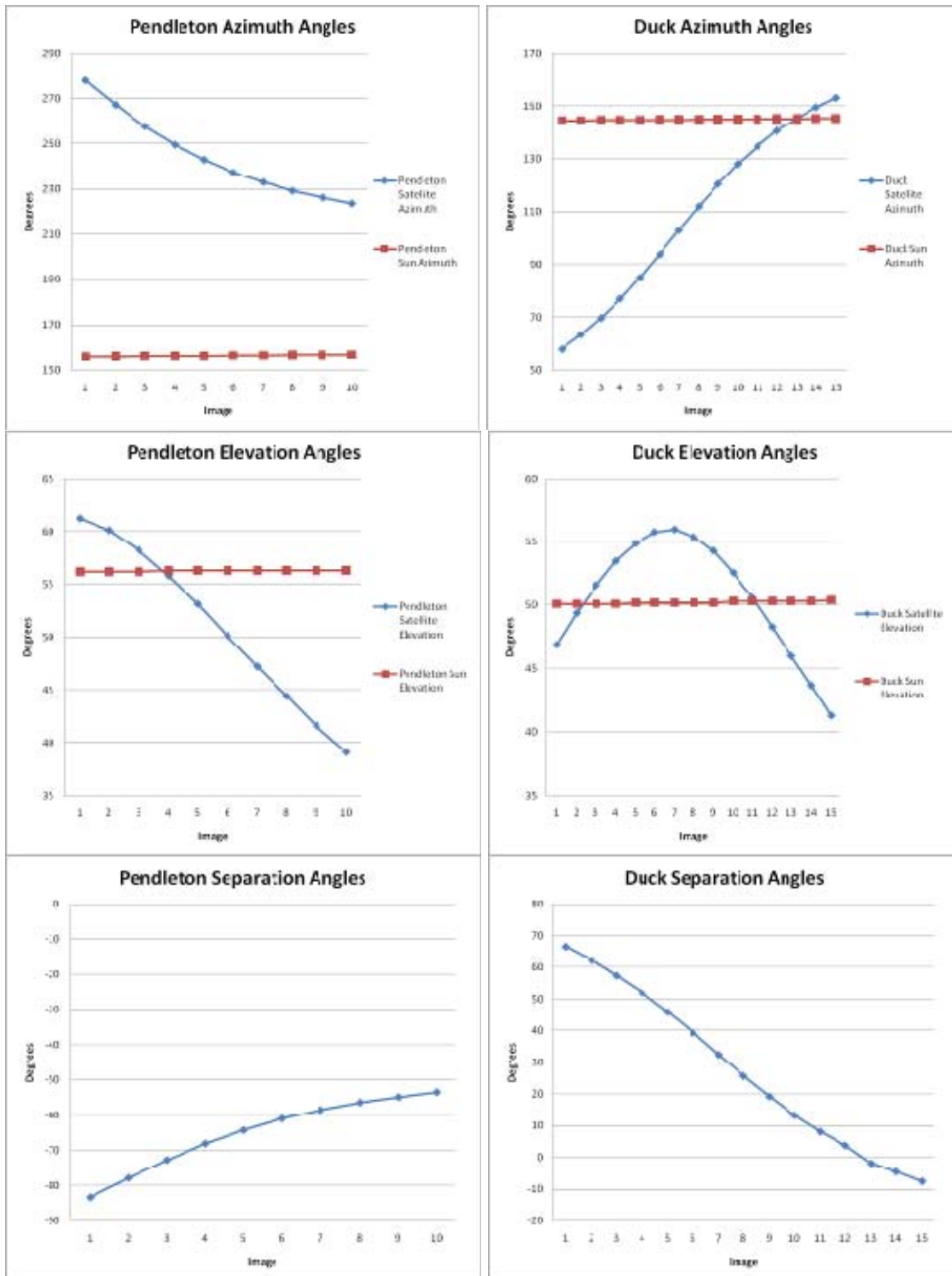


Table 8. Satellite and Solar Azimuthal Angles, Elevation Angles, and Overall Separation Angles, Left: Pendleton, CA, Right: Duck, NC

B. IMAGE PREPARATION

DigitalGlobe processes imagery as requested by the customer. Three levels are available and specific options may also be available within the level. These levels include:

- Level 1: Basic 1B or Basic Stereo Pairs
- Level 2: Standard (2A) or Ortho-Ready Standard (OR2A)
- Level 3: Ortho-rectified (DigitalGlobe or Custom)

Level 1 processing is done on all Level 2 processed images, to include radiometric and sensor correction. Radiometric correction is necessary to reduce the effects of noise in the imagery. Noise can originate from the atmosphere, the sun-sensor geometry, or the sensor itself. Radiometric correction provides two key benefits to this research. The first allows mosaicing of images. The second advantage is image consistency, which accommodates work involving temporal data. The additional level of processing involved in Standard 2A and OR2A processing provides uniform GSD throughout the image and projects the image on a plane using the customer's selected map projection and datum. Map projection options include Geographic (latitude/longitude), Universal Transverse Mercator (UTM), and a customer defined State Plane. Standard 2A applies a coarse digital elevation model (DEM), while OR2A is projected to an average elevation, but has no topographic relief applied. OR2A stands ready for custom ortho-rectification, providing flexibility to the customer. Increased processing comes at an increase price to the consumer. With Level 3 processing, the image is ortho-rectified. Ortho-rectification applies a fine DEM using map projection and the customer's requested datum. The DEM can be provided by DigitalGlobe or the customer. Mosaicing is also available at the highest level of processing.

The imagery used in this thesis underwent Ortho-Ready Standard, a level 2 process. Each image over Duck, NC, and Pendleton, CA, was received in three separate tagged image format (TIF) files. TIF files are a standard imagery format as they allow lossless imagery storage and can be edited and resaved without degradation of the image.

Basic registration processes came first. As the pass over Duck, NC, and Pendleton, CA, resulted in 15 and 10 images, respectively, registration was required. Registration is the process of correcting a reference (warp) image to match base image geometry, using tie points between the two images. While the registration process is tedious, it is necessary. Errors arise due to different satellite viewpoints that cause differences in acquisition and cause the images to be misaligned. In this analysis, the chronological-center image was selected as the base image to minimize the differences between the base image and the warp images. While often called ground control points (GCPs), the more accurate term is tie points. Tie points refer to points selected within the base and warp image and indicate a single feature identified in both images. GCPs are used to relate a point in a remote sensing image to a geographic point on the earth. Registration allows the Geographic projections done on each image to be aligned with the Geographic projection of the reference image. The ENVI program refers to tie points and GCPs synonymously. To achieve a well-registered image, approximately 70 points were referenced to the base image. An illustration of this process is captured in Figure 30.

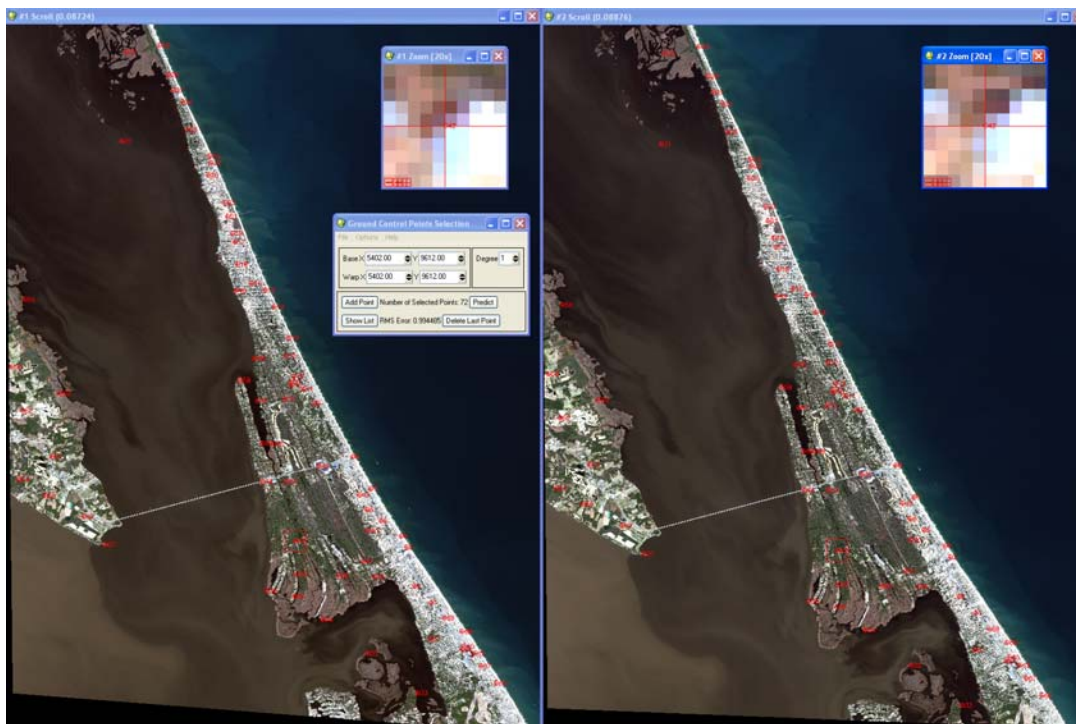


Figure 30. The reference image (left) and warp image (right) require the selection of a large number of tie points for accurate registration.

When using off-nadir imagery, the Geographic projection done by Level 2 processing does not result in an accurate projection of latitude and longitude, regardless of the image selected as the registration reference. If accurate latitude and longitudes are required, they are accomplished with ortho-rectification. Ortho-rectification removes the effects of terrain relief displacement, lens distortion, and camera tilt. Ortho-rectification creates uniform scale and true geometry within imagery and allows measurement of true distances, as an ortho-rectified image accurately represents the Earth's surface. This correction is necessary when using off-nadir imagery and in topographically diverse landscape. As a satellite overflies a ground point, it images at differing angles and subsequently returns different views of the same object. This occurs because as the view angle changes, the distance from the object also changes. The same effect occurs when the surface viewed is not flat, and the effect becomes more pronounced as the diversity of the terrain increases. To correct for terrain changes, an accurate DEM is required. Figure 31. illustrates how errors are introduced in satellite imagery due to off-nadir imaging. Figure 32. illustrates how terrain elevation affects images.

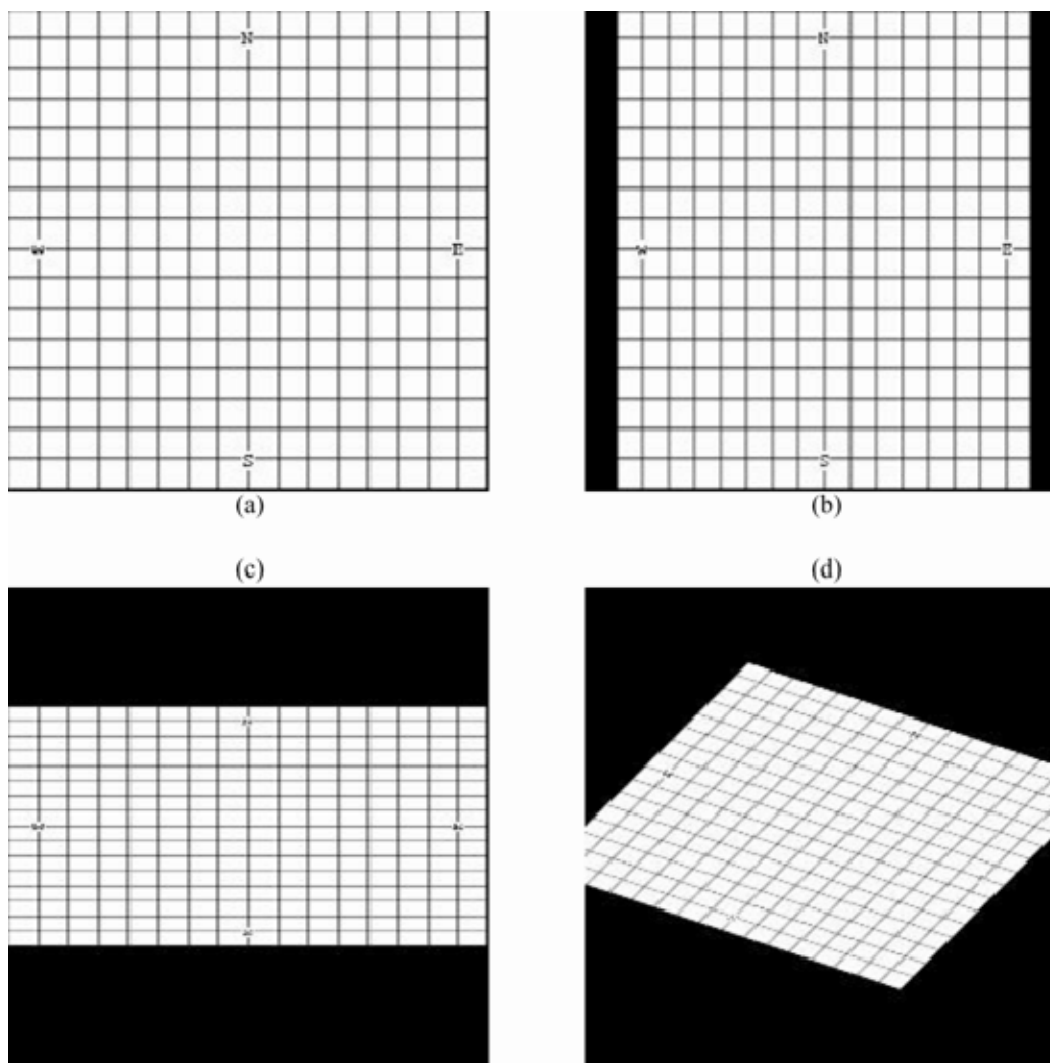


Figure 31. (a) A flat surface viewed from directly overhead (Nadir) (b) The same surface viewed with 30°-Off-nadir Roll (c) Surface with 30° Off-Nadir Roll and 60° Off-Nadir Pitch (d) Additional 30° Yaw Introduced

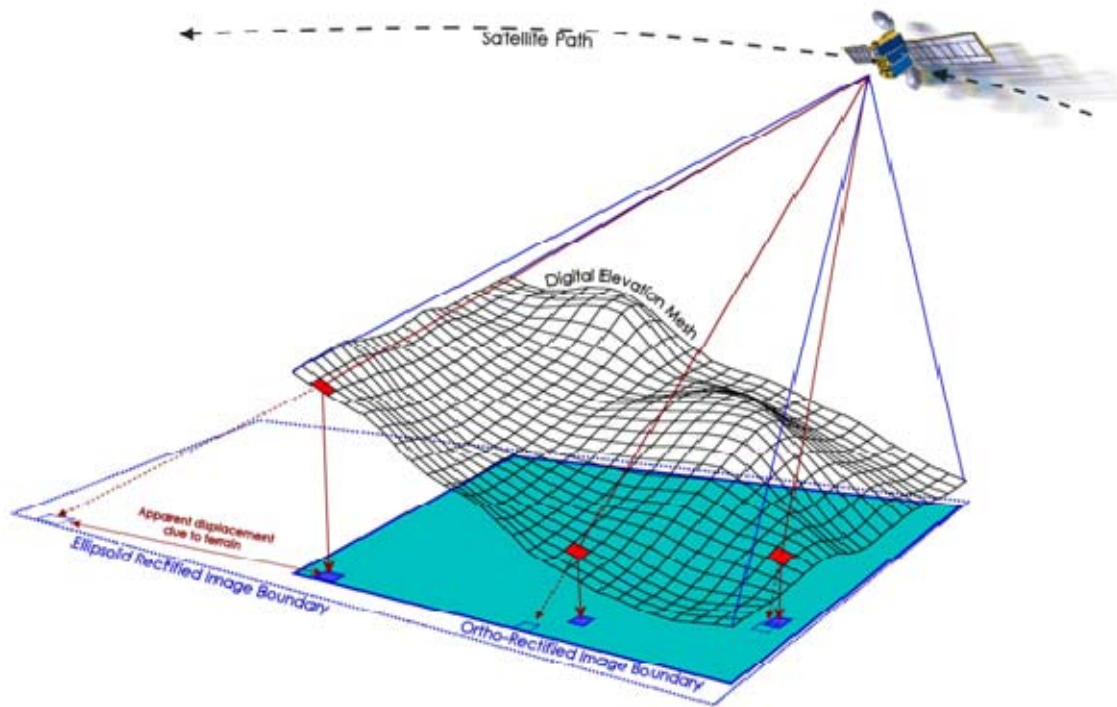


Figure 32. Displacement effect on imagery due to terrain

As the scope of this thesis did not require an accurate map of the location, ortho-rectification was not required. Registration of the images was the furthest step taken and was done by the staff of the Naval Postgraduate School.

Following image registration, the images were chipped to display smaller regions. Analysis was done on the full image and the smaller chips.

C. REGIONS OF INTEREST

Regions of Interest allow the selection of an area of pixels and allow them to be grouped for processing with ENVI. ROIs are typically a group of pixels with similar characteristics. ROIs were selected for Duck and Pendleton. To begin, a general area of terrain is selected. In Duck, an initial 11 regions were created. This eventually became 12 as the process revealed two types of sand within one ROI. In Pendleton, 10 regions were selected. The ROIs were titled as follows:

<u>Duck, NC</u>	<u>Pendleton, CA</u>
Forest	Field (Veg)
Pond	Harbor
Roof Top (x3)	Tarmac
Baseball Outfield	Sand (x3)
Soil (Dry)	Soil (Wet)
Soil (Wet)	Soil (Dry)
Ocean	Ocean
Golf Course	Marsh (Veg)
Parking Lot (x2)	



Figure 33. The initial 11 ROIs at Duck.

As the ROIs are initially selected by a general area, there are inherently some dissimilar pixels within the region. The n-D visualizer allows exclusion of these pixels to maintain a homogenous ROI.

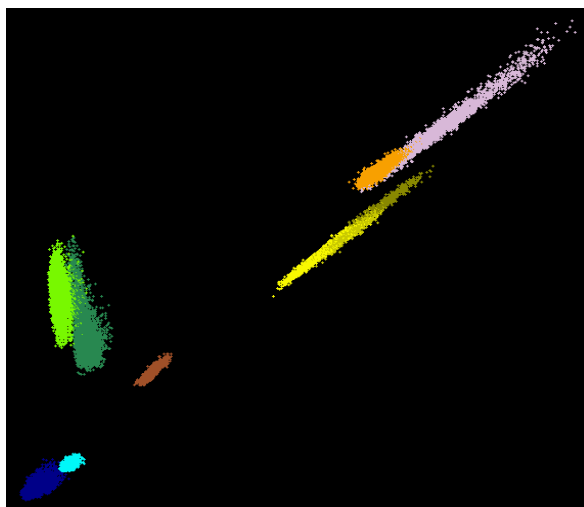


Figure 34. ROIs displayed in n-D visualizer

The n-D visualizer plots all pixels within the ROIs. Pixel color corresponds with the corresponding color of the ROI. As depicted in Figure 34. , the axes are digital number (DN) in selected bands, with the bottom left corner representing (0,0) and increasing as you move up and right. In this figure, the x-axis is Band 5 (Red), and the y-axis is Band 6 (Red-edge). Note the relative brightness of the vegetation ROIs (green pixels) in the Red-edge band and the relative darkness in the Red band. The tarmac (pink pixels) is bright in both bands.

The outlier pixels are represented by their separation from the major grouping of pixels in each ROI. To remove these from further ENVI processing, the user manually highlights a group of outliers and opts to remove them from the group. Often, the n-D visualizer illustrates clear differences between two or more materials within the same group, which are not easily discerned by the naked eye. ENVI provides the option of splitting the ROI into two or more new ROIs, as illustrated with Figure 35. When one goes to edit the Sand ROI, Figure 35. shows a pixel clump. In Band 1 and Band 7, it is not very clear that there are two discernible clumps. In Band 5 and Band 7, it becomes clearer. Rather than removing one of the pixel clumps, a second ROI is created. The ROI, Sand, is split into Sand (Dry) and Sand (Wet). Once this process is complete, the ROIs are updated accordingly. The whittled-down ROIs are displayed in Figure 37.

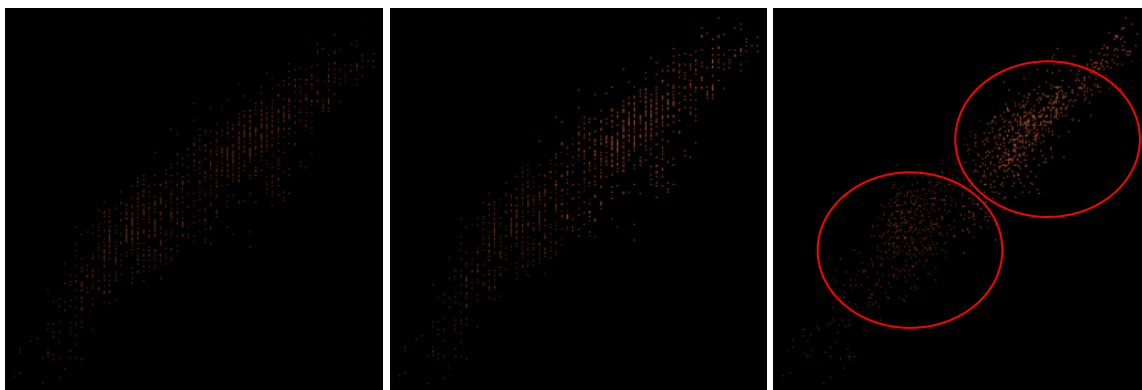


Figure 35. The n-D visualizer display. Left: Sand ROI in (Band 1 & 7), Center: Two identified clumps (Bands 1 & 7), Right: Two clumps in Band 5 & 7, which introduces more separate in the clumps

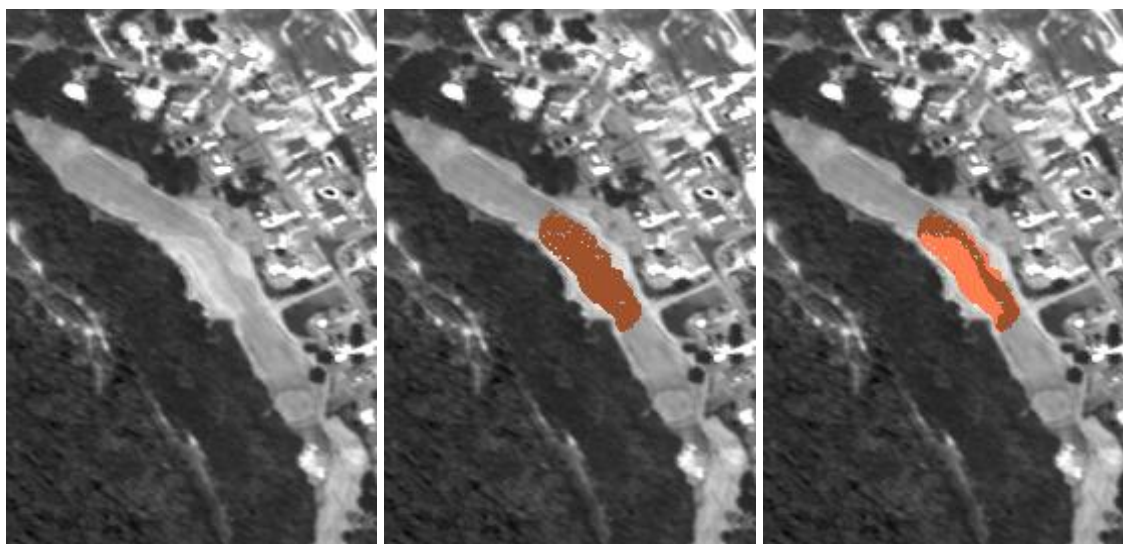


Figure 36. Left: Sandy area, Center: Initial Sand ROI which encompasses wet and dry sand, Right: The result of n-D visualizer. The original Sand ROI is divided into 2 different ROIs, wet and dry.

These pixels typically represent differing materials within the terrain such as a road cutting through a field or a car in a parking lot. By removing these from processing, a homogenous ROI can be obtained for analysis.

While at DigitalGlobe, the product underwent processing that made use of the gain and offset numbers provided in the Appendix. These numbers were retrieved from

the .imd files provided along with the imagery. The end result delivered to the customer transformed the raw image digital number values into radiometrically corrected image pixels, $q_{\text{pixel}, \text{band}}$. The calibration factor applied can also be found in the Appendix.

Statistics were run on the ROIs. Worldview-2 DNs were converted to absolute radiance utilizing the following equations:

$$DN \equiv q_{\text{pixel}, \text{band}} \text{ [counts]} \quad (18)$$

$$L_{\text{pixel}, \text{band}} = \text{abscalfactor}_{\text{band}} * q_{\text{pixel}, \text{band}} \text{ [Wm}^{-2}\text{sr}^{-1}] \quad (19)$$

$$L_{\lambda, \text{pixel}, \text{band}} = \frac{L_{\text{pixel}, \text{band}}}{\Delta\lambda_{\text{band}}} \text{ [Wm}^{-2}\text{sr}^{-1}\mu\text{m}] \quad (20)$$

where $q_{\text{pixel}, \text{band}}$ are radiometrically corrected image pixels, $L_{\text{pixel}, \text{band}}$ is top-of-atmosphere band integrated radiance image pixels, and $L_{\lambda, \text{pixel}, \text{band}}$ is top-of-atmosphere band-averaged spectral radiance image pixels. Following this, statistical analyses were then done on the homogeneous ROIs utilizing ENVI, and the radiance values were analyzed.

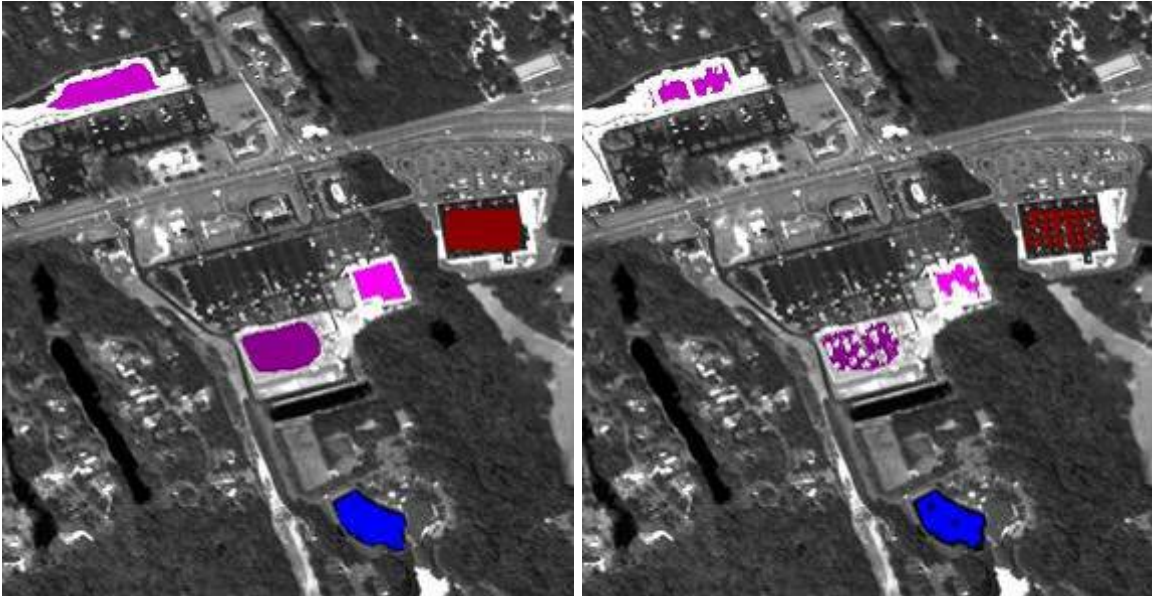


Figure 37. (Left) Several of Duck, NC, original ROIs. (Right) n-D visualizer has removed the pixels that displayed differing DNs from the majority over several considered bands, representing cars in a parking lot (Red ROI), an island in a pond (Blue ROI) and structures/objects on a roof (Pink ROIs)

D. IMAGE RATIOING

Image ratioing offers the benefit of removing or minimizing many of the errors previously mentioned. Image ratioing is the process of dividing an image by another image, pixel by pixel. The process was done using the ENVI-compatible IDL workbench and was performed across all inputted wavelengths.

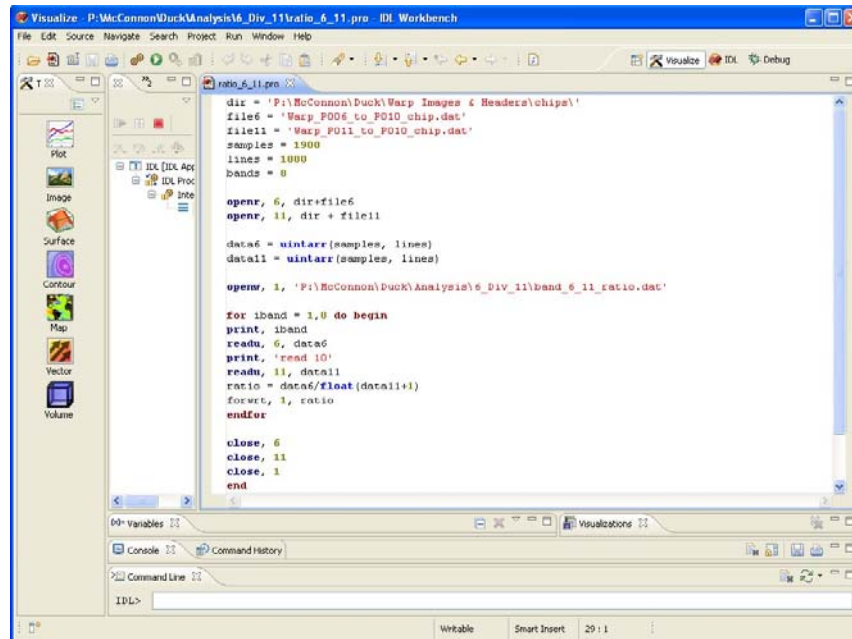


Figure 38. Image Ratioing Interactive Data Language Code

In image ratioing, the brighter image is divided into the darker image to ensure the resulting image is scaled so that all pixels hold a value between 0 and 1. This was done for both sets of imagery. In the Pendleton imagery, image P009 was divided by P010, and in the Duck imagery P006 was divided by P011. In both cases, the brightest image, placed in the denominator, corresponded to the up-sun, or on-axis, image where the satellite elevation most closely matched the solar elevation. Coincidentally, the brightest image was the latter image taken. The resulting ratio represents congruity between the initial two images. Zero represents dissimilar pixels, such as a saturated pixel contrasted with a dark pixel, while a value of 1 represents identical pixels. Values lying between represent some disparity in pixel value. This concept is illustrated in

Figure 39. Note the boat traveling south down the coast. It appears bright in contrast with the surrounding ocean- a high DN value in contrast with a low DN. As mentioned previously, the brighter image happened to be the second image taken and was used in the denominator. At the boat's position in the first image, its high value is placed in the numerator. At that same location in the second image, there is only dark-pixelated ocean, which is placed in the denominator. This results in a value near 1. The values are reversed at the boat's second position, resulting in a value near 0.



Figure 39. Image Ratio of Duck, NC, Image P006/P011 (Band 2: 450-510 nm)

The grayscale image displays information for only one band. Figure 40. displays information for three bands and the use of color in the image allows for the presentation of a greater depth of information. As in the grayscale image, white and black represent total similarity and total dissimilarity, respectively; however, in the color image the range of gray now displays *equal* change between the three represented bands. Gray is useful for displaying the level of view-angle dependence of reflectance. Color is used to illustrate *unequal* change between the bands and illustrates both view-angle dependence and wavelength dependence of reflectance. The color image of Duck, NC, is displayed in Figure 40.



Figure 40. Image Ratio of Duck, NC, Image P006/P011 (Bands 2: 450–510, Band 5: 630–690, and Band 8: 860–1040 nm)

Image ratioing, in addition to allowing the presentation of information in a concentrated form, offers the benefit of a reduction in severity of numerous undesirable effects. The images were taken in close sequential order, with the solar zenith angle nearly identical; therefore, there is similar shadowing between the images. Ratioing removes a large amount of this shadowing, and presents the shadowed regions in a manner that is more consistent with the sunlit regions. Additionally, the satellite views the target through the Earth's atmosphere. The atmosphere has major effects on imagery, and not all affect different wavelengths equally. Scattering is one such affect, which causes shorter wavelengths to be scattered more than longer wavelengths. For example, the majority of atmospheric effects are cancelled out by ratioing. Some effects remain due to the satellite's motion, which causes the view angle, and subsequently the path length, to change. Furthermore, in our analysis, accurate in situ solar irradiation measurements were not taken. These measurements are part of the BRDF calculation, and their removal through ratioing allows the comparison of radiance to more accurately scale to the BRDF. Analysis on these images is done in the next chapter.

V. OBSERVATIONS AND ANALYSIS

A. CALCULATIONS

Calculations were done using the information regarding the satellite's and the sun's positions when the imagery was acquired. The separation angle between the incident angle (the sun's position) and the reflected angle (the satellite's position) were calculated to allow comparison between images. This information is available in the Appendix.

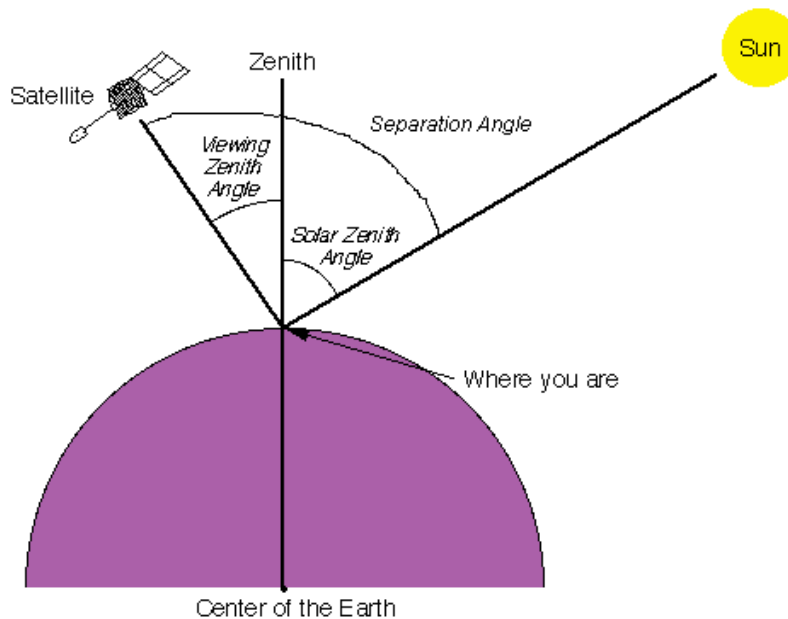


Figure 41. Illustration of Solar Zenith Angle, Viewing Zenith Angle, and Calculated Separation Angle [36]

B. EFFECTS OF LIMITED IMAGERY PROCESSING

The raw imagery used in this research is subject to many effects that must be accounted for in order to derive quantitative data. Limited processing was performed on the imagery, and many of these effects remain. Processing limitations must be accurately annotated to ensure inaccurate analysis is not obtained or assumed. Initial processing was

done by DigitalGlobe prior to its dissemination to the customer. Upon receipt of the imagery at the Naval Postgraduate School, all image processing was done utilizing the ENVI software. Processing tools used consisted of the Worldview 2 Calibrated Utility preprocessing tool, Georeferenced mosaicing, and Image-to-Image registration. No further processing tools were applied to the imagery prior to follow-on analysis. Therefore, it can be assumed that all effects not corrected for by these tools, remain. Specifically, effects imparted due to atmospheric conditions are not removed. Additionally, orthorectification was not performed on the imagery, and the spatial processing done, registration, does not accurately allow for accurate DEM integration.

C. MISR DATA

A comparable data set was obtained for Pendleton from MISR. MISR data were requested and received from the EOS data gateway at NASA Langley's Atmospheric Science and Data Center (ASDC). As MISR images a geographic area approximately once every 16 days, the imagery requested was taken on March 26, 2010. This corresponded to Terra orbit 54,630 and path 41, as depicted in Figure 42. This data was selected because it was the timeliest for comparison with the imagery taken by Worldview-2 on March 24, 2010.

The product received was Level 1B1 Radiance Data in Global mode for each of MISR's 9 cameras. The level of processing included DN's radiometrically-scaled to radiance with no geometric resampling or registration. Following receipt, the product was processed using ENVI and chipped to the desired region. The image was relatively cloud free in the region of interest.

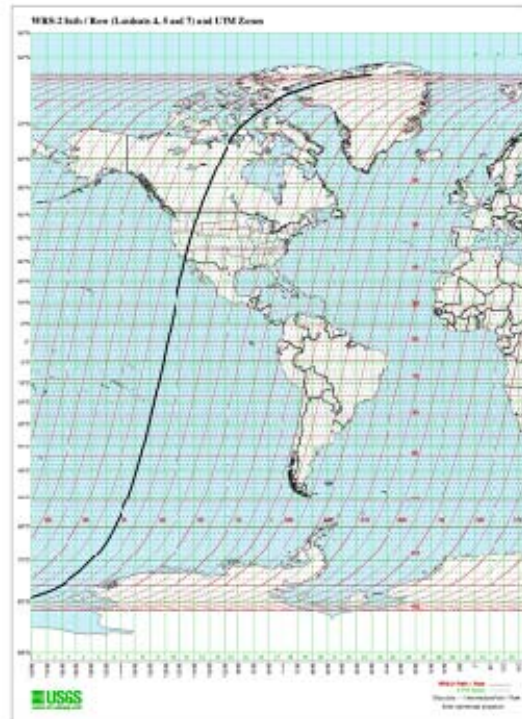


Figure 42. Pendleton Overflight by Terra/MISR (Path 41) on the WRS-2 Map (Worldwide Reference System)

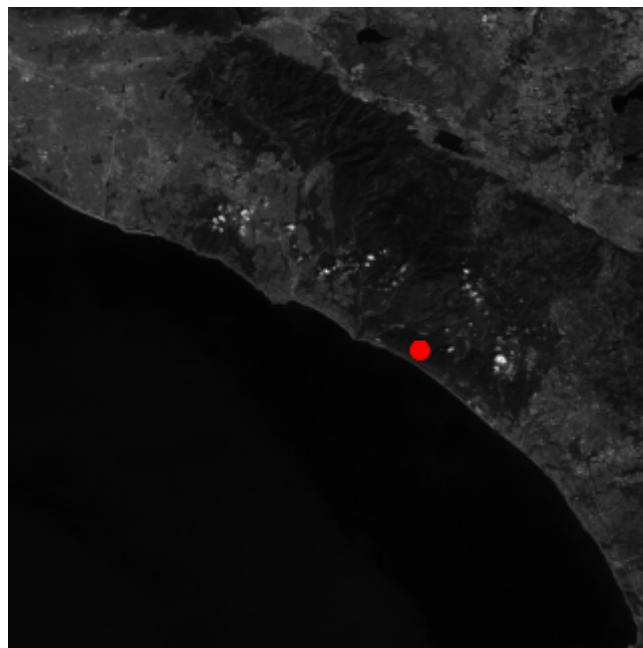


Figure 43. MISR Radiance Image: ROI for comparison with Worldview-2 (Camera: AN, Red Band)

Comparison between the Worldview-2 and MISR were done utilizing a ROI generated in the coastal hills in the vicinity of Pendleton. While the spatial size of the image was similar, approximately 125 km², the spatial resolution of each image resulted in a marked difference in pixels for analysis. In global mode, spatial resolution for MISR is approximately 1 km for all channels except the Red channel, which is 275 m, while Worldview-2's spatial resolution is 2.4 m (off-nadir). Analysis was done on MISR's scaled red channel and Band 5 of Worldview-2. The MISR red channel was selected due to its high spatial resolution in contrast with the other three bands.

While the MISR product returned scaled radiance values, the Worldview-2 data underwent conversion from DN to radiance utilizing the process describe in the Region of Interest Section of this chapter. The trends are presented for comparison.

Figure 46. shows a decrease in radiance as the zenith angle decreases. This is in contrast with measurements made by systems such as Chen-Leblanc's gonireflectometer, PARABOLA, and POLDER (Figure 13. , Figure 15. , Figure 21. , respectively). While most plots show a comparison of the incident and viewing angles, an estimate of the sun's position and the corresponding separation angle were made. This does not appear to provide an explanation for the difference; however, the data does not appear to be erroneous as the right half of Figure 47. displays a similar trend to the MISR data in Figure 46. The cause for the difference in the region is unknown; however, the region is large and diverse, and it can be assumed that the materials present in the region are varied. As illustrated in the PROBA/CHRIS data of Figure 23. , different materials display different angle-dependency trends, and this is one possible explanation for the unexpected radiance-vs.-angle curves.

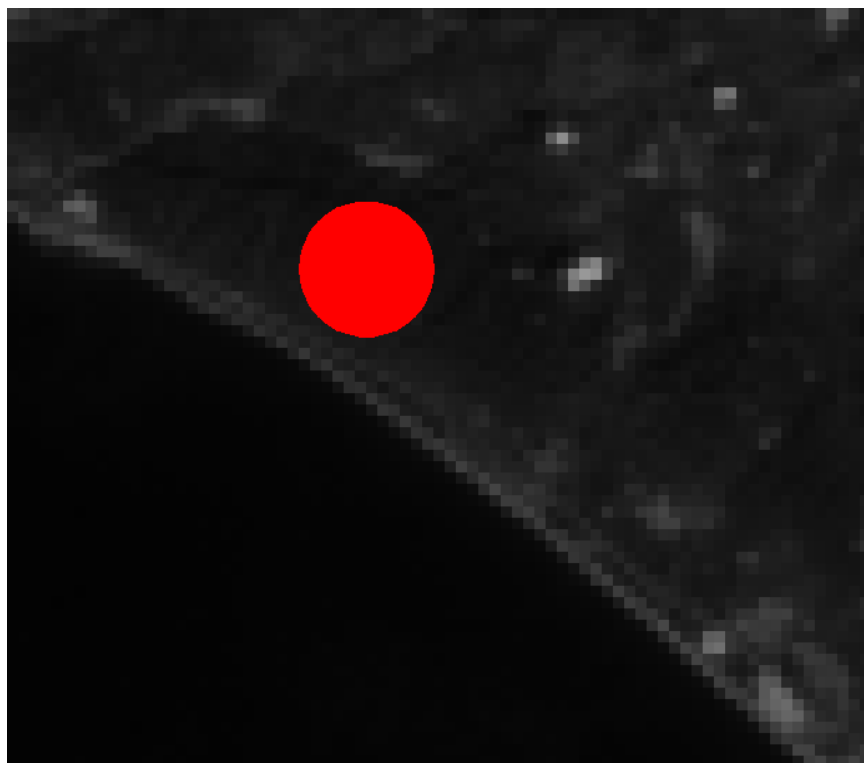


Figure 44. MISR Radiance Image: Zoom of ROI for comparison with Worldview-2 (Camera: AN, Red Band)



Figure 45. Worldview-2 Image: ROI for Comparison with MISR (Image P009, Band 5: 630–690 nm)

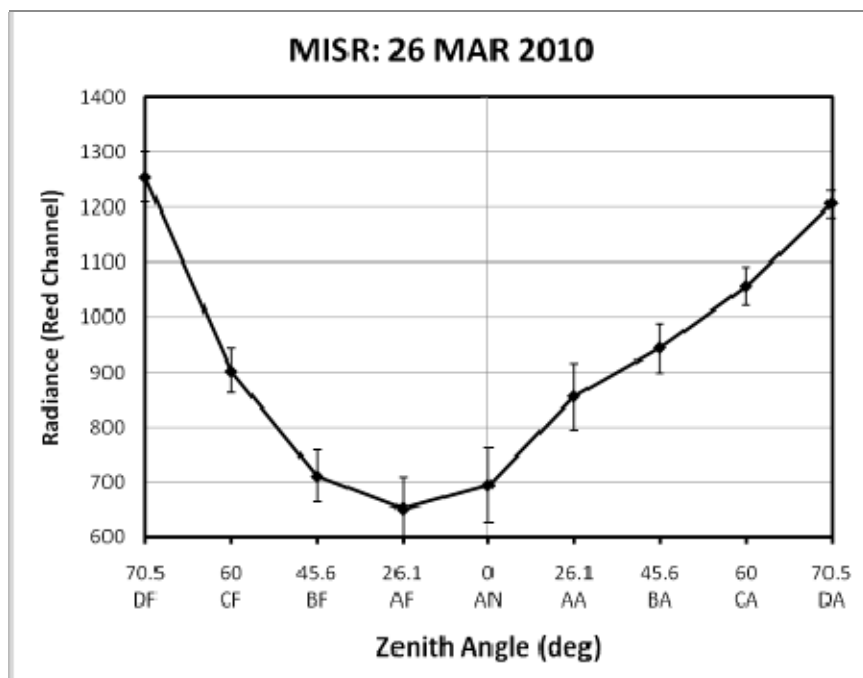


Figure 46. MISR Radiance Plot in Red Channel (672 nm) by Camera and Zenith Angle: Pendleton, CA

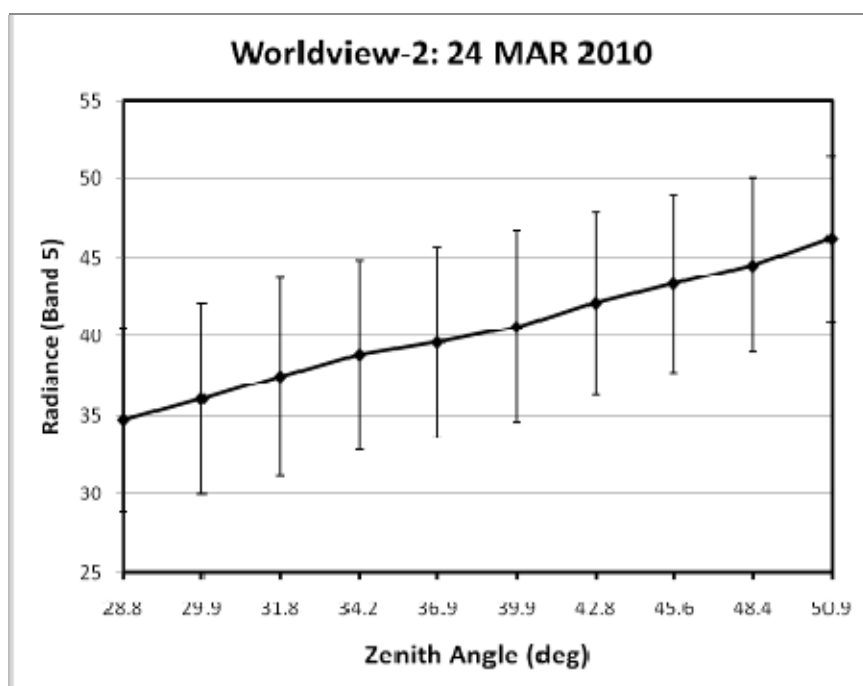


Figure 47. Worldview-2 Radiance Plot in Band 5 (630–690 nm) by Time and Zenith Angle: Pendleton, CA

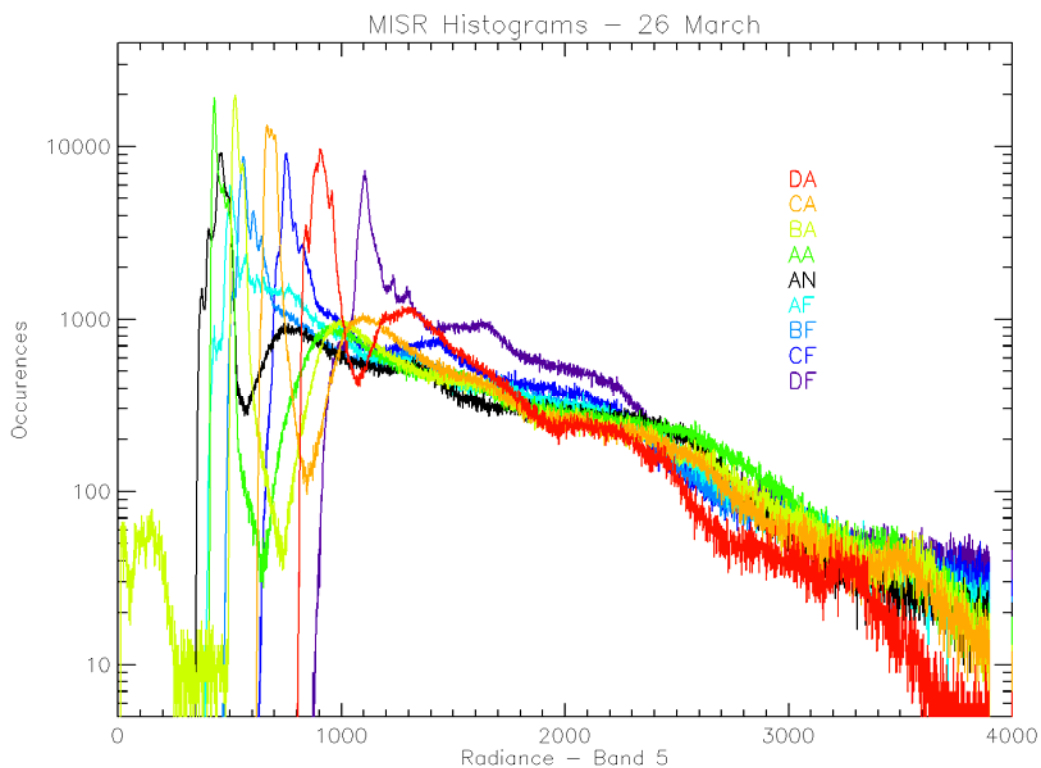


Figure 48. MISR Brightness Variance in Red Channel (672 nm) with respect to Elevation Angle (Camera): Pendleton, CA

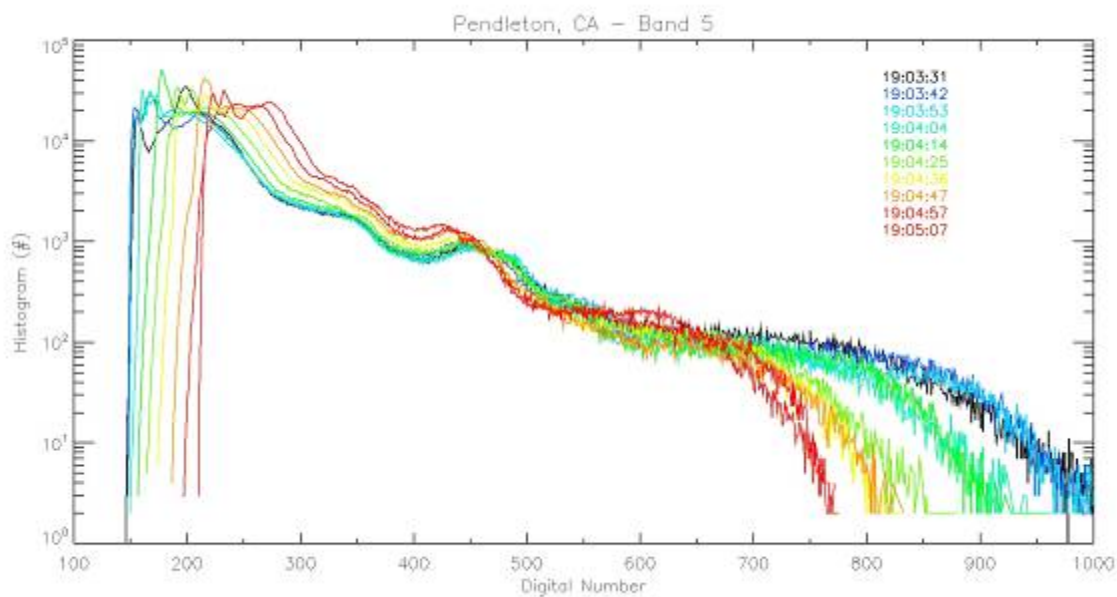


Figure 49. Worldview-2 Brightness Variance in Band 5 (630–690 nm) with respect to Elevation Angle (Time): Pendleton, CA

It is difficult to accurately compare individual ROIs given the enormous spatial scale difference between the systems. We approach the data globally, therefore, by using scene histograms, as shown in Figure 48. and Figure 49. Figure 48. shows how the 672 nm MISR data vary for the image chip shown in Figure 43. as the view angle varies. The nadir view has the dark peak, the most oblique views are the brightest. The peak is largely the dark water which dominates the scene. The ROI was evaluated in the red channel of each of the nine images, and the radiance values were plotted. Radiance shows a decrease with increasing elevation angle. This is also shown in the whole image histogram plotted in Figure 48. In the latter figure, the radiance curve shows a leftward shift until reaching nadir, after which it shifts back to the right. The images were acquired around noon over Pendleton, CA. Figure 49. shows the same sort of shift in the ‘water’ peak, but also a contraction in the dynamic range, which is so far unexplained.

D. SHIFT IN DIGITAL NUMBER OBSERVED OVER SEQUENCE OF IMAGES

Analysis was done on the imagery of Duck, NC, and Pendleton, CA. The large spike in the data in the low DNs is the water in the scene. The ocean is a poor reflector of energy, especially in the NIR bands. Conversely, plants are excellent NIR reflectors and this is captured in the spike at the DN 1400 count. The tail of the curve (>1400 counts) represents the extremely reflective nature of man-made materials within the image.

A brightness shift across all bands was observed. This observed shift, represented in the figure, qualitatively represents the BRDF of the scene. As the images progress chronologically, represented by an inverse rainbow scheme, there is an observed shift to the right of DN through the first 13 images, followed by a shift back to the left for the last 2 images. Graphs of all eight bands for both Duck and Pendleton can be found in the Appendix.

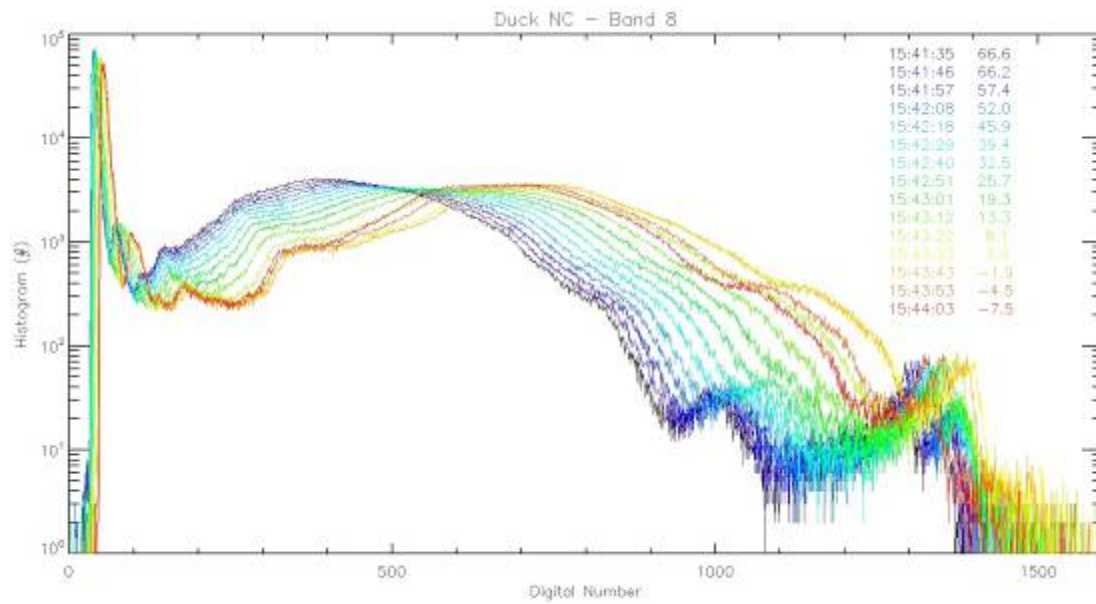


Figure 50. Worldview-2 Brightness Variance in Band 8 (860–1040 nm) with respect to Elevation Angle (Time): Duck, NC

E. IMAGE RATIO ANALYSIS

1. Images

Figure 51. is a full image ratio of Duck, NC, in the Worldview-2 bands 2, 5, and 8. Figure 52. is a full image ratio of the Pendleton scene in the same bands. While the images acquired over Duck appear relatively cloud-free, there is a large amount of cloud cover within the Pendleton images, which affects the BRDF values.



Figure 51. Duck Image Ratio, Image P006/P011 (Bands 2: 450–510, Band 5: 630–690, and Band 8: 860–1040 nm)

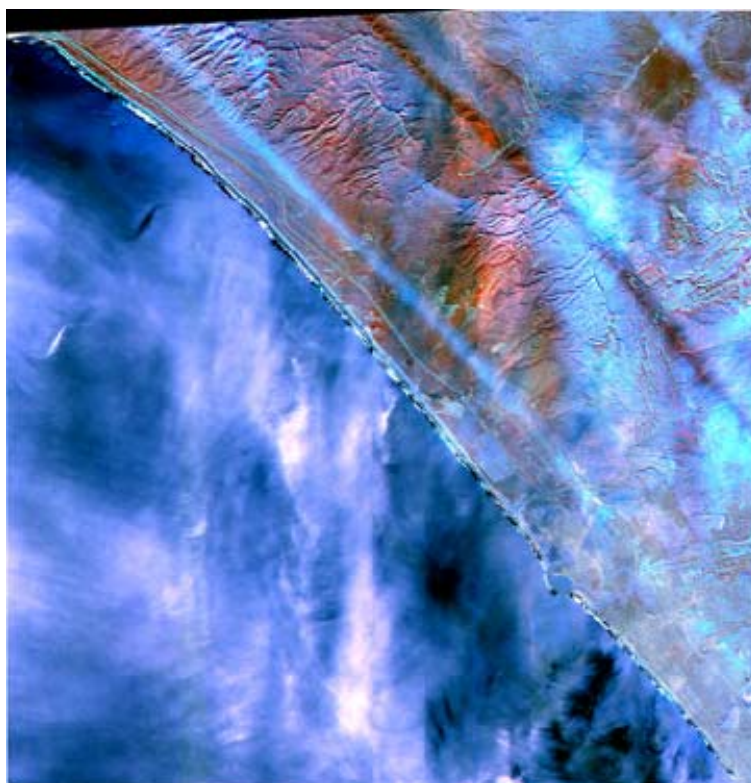


Figure 52. Pendleton Image Ratio, Image P009/P010 (Bands 2: 450–510, Band 5: 630–690, and Band 8: 860–1040 nm)

The full Pendleton scene was then chipped down to display interesting regions, as is the case in Figure 53. and Figure 54. These figures, as well as Figure 55. , display how BRDF varies over view-angle and wavelength despite similar terrain. Three fields of differing make up are viewed in the figures. In the first image, a gray-scale color ramp shows the range of ratio values within the image in Band 3. Darker regions indicate a greater difference between the compared images, and therefore a greater dependence on view angle. In the second image, the same concept is captured through the representation of differing colors; however, the image also illustrates the BRDF dependence on wavelength.



Figure 53. Pendleton Image Ratio: ROIs annotated (Band 3: 510–580 nm)

Further analysis of this was done on selected ROIs. A better understanding of the colors observed in Figure 54. can be achieved through observing the ratio changes annotated in Figure 55. As none of the regions have a flat line on the relative ratio chart, each region has an element of color. The wet and dry soils have similar wavelength-dependent BRDF shifts across all wavelengths, represented by the two curves approximately paralleling each other. If the ratios moved in lock step, the areas would

differ only in the brightness of color. They differ slightly in color, however, because the curves differ more than by solely a y-axis displacement. As it can be observed in Figure 55. , the two regions are more similar than the third region, the Field (Veg). The relative ratio of the vegetated field ticks up closer to 1 in the longer wavelengths. This allows one to conclude that vegetation has a reduction in angular dependence in these wavelengths. The marked shift between the bands results in a brightly colored region. All 3 ROIs move from the bottom left to the top right. This indicates that Band 8 appears to be the least affected by changes in the view angle.

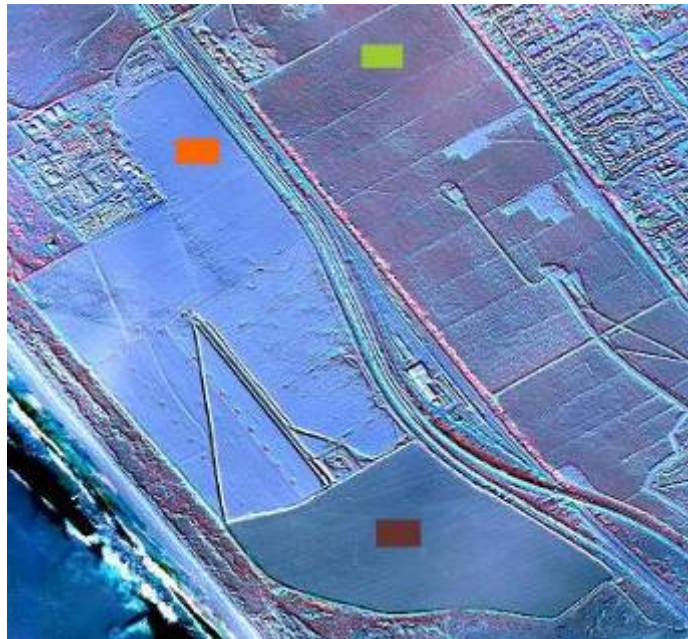


Figure 54. Chip of Pendleton Image Ratio: Field (Veg) and Soil ROIs annotated

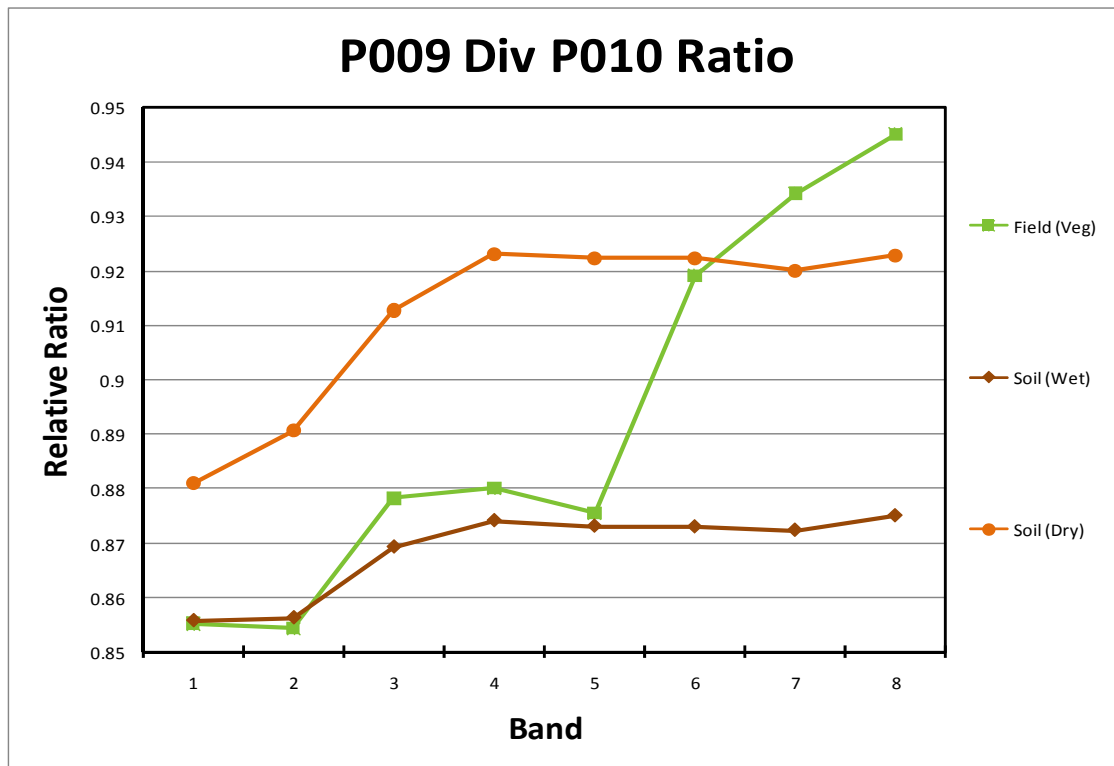


Figure 55. Relative Ratio of Pendleton Image Ratio: Field (Veg) and Soil ROIs

2. Terrain Effects in Spatial Profiles



Figure 56. Google maps true-color image of Pendleton Spatial Profiles' Regions

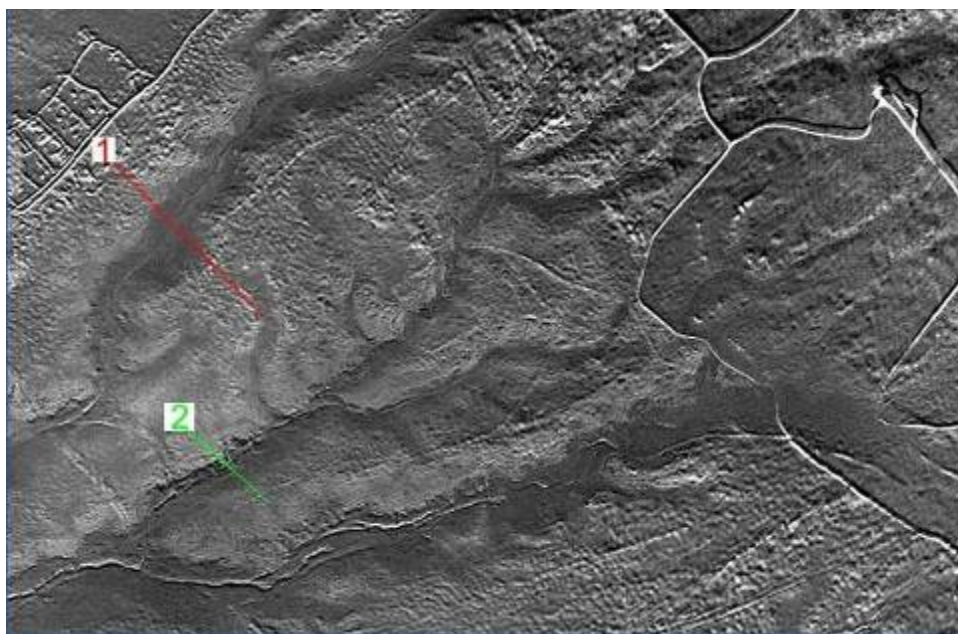


Figure 57. Pendleton Image Ratio Spatial Profiles (Band 3: 510–580 nm)

Figure 56. and Figure 57. are images of an area in the Pendleton scene. Figure 56. is a true-color image acquired through Google maps, while Figure 57. is a chip from the image ratio of P009 and P010 in Band 3. Spatial profiles were created within these images. They sample the value of pixels along the line. They were drawn with the intent of spanning a region of changing elevation and terrain. Profile 1 spans a valley, and this valley can be seen in the approximate locations of 50–100 in Figure 58.

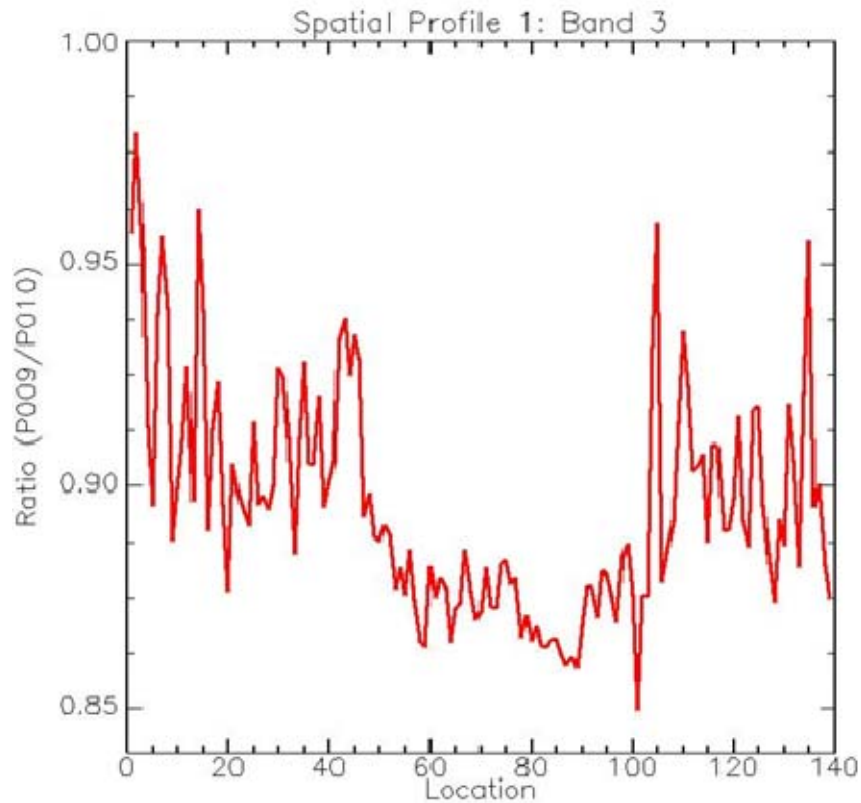


Figure 58. Pendleton Image Ratio Spatial Profile #1 (Band 3: 510–580 nm)

Profile 2 is across a mountain range, with the left side, 0-40, corresponding to a westerly facing slope, and the right side facing east, displayed in Figure 59. These profiles represent how BRDF changes while the ground angle changes, therefore, the exitance angle is changing, but the viewing angle remains fixed.

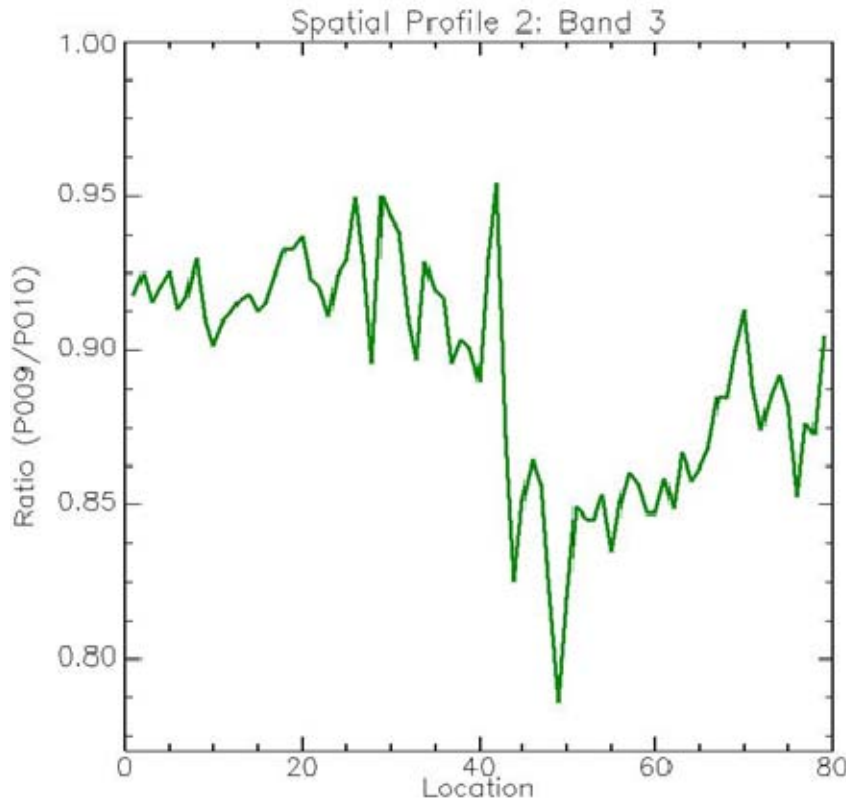


Figure 59. Pendleton Image Ratio Spatial Profile #2 (Band 3: 510–580 nm)

F. BRDF SHIFT BETWEEN REGIONS OF INTEREST (DUCK, NC)

The sun and the satellite's position relative to the sun are plotted in Figure 60. The series of separation angles are depicted with an arc with plus marks at each specific angle. These plus marks are colored to reflect the relative BRDF value and the color ramp provides the key.

Wet and dry soil in band 7, the NIR band, is compared in Figure 60. The materials are similar, therefore the differences are subtle, but it can be observed that the dry soil exhibits a generally higher BRDF for all plotted angles. This is consistent with general spectral measurements of soil. Soil reflectivity is largely dependent on six variables: moisture content, organic matter content, particle size distribution, iron oxide

content, soil mineralogy, and soil structure, with moisture content having the largest impact. This suggests the difference between the two is caused by the additional absorption by the water in the wet soil.

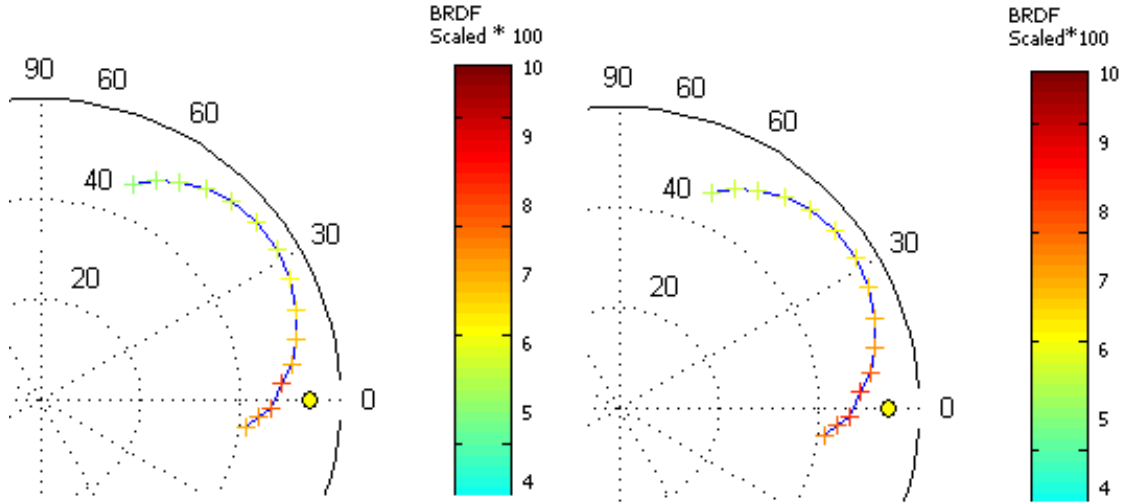


Figure 60. BRDF ROI Comparison wrt Satellite Position for Duck ROIs:
Left: Soil (Wet), Right: Soil (Dry) (Band 7: 770–895 nm)

G. BRDF SHIFT BETWEEN BANDS

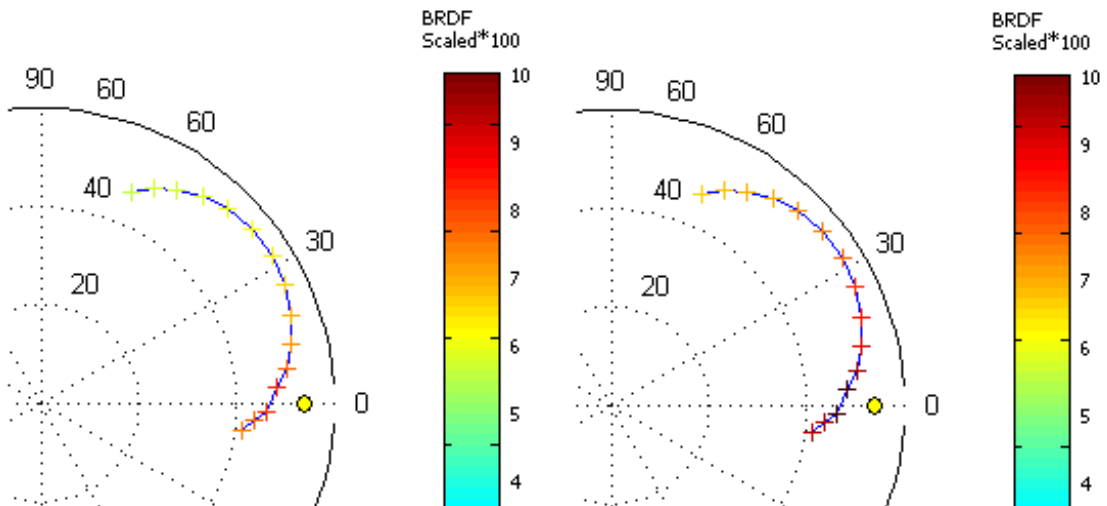


Figure 61. BRDF Band Comparison wrt Satellite Position for Duck ROI:
Soil (Dry) Band 7 and 8 (Band 7: 770–895 nm, Band 8: 860–1040 nm)

Another set of BRDFs are compared in Figure 61. This time the difference in BRDF across different bands is explored. Dry soil is plotted in the figure with band 7 BRDFs on the left and band 8 BRDFs on the right. The figure on the right displays a higher BRDF value across all separation angles. This is also consistent with soil studies, which show reflectance increasing until the SWIR band [37].

H. IMAGE RATIO DISPLAYING WAVELENGTH DEPENDENCE IN REGIONS OF INTEREST BY BAND

The plot of image ratio relative ratios for Duck, NC, and Pendleton, CA, are depicted in Figure 62. and Figure 63. , respectively.

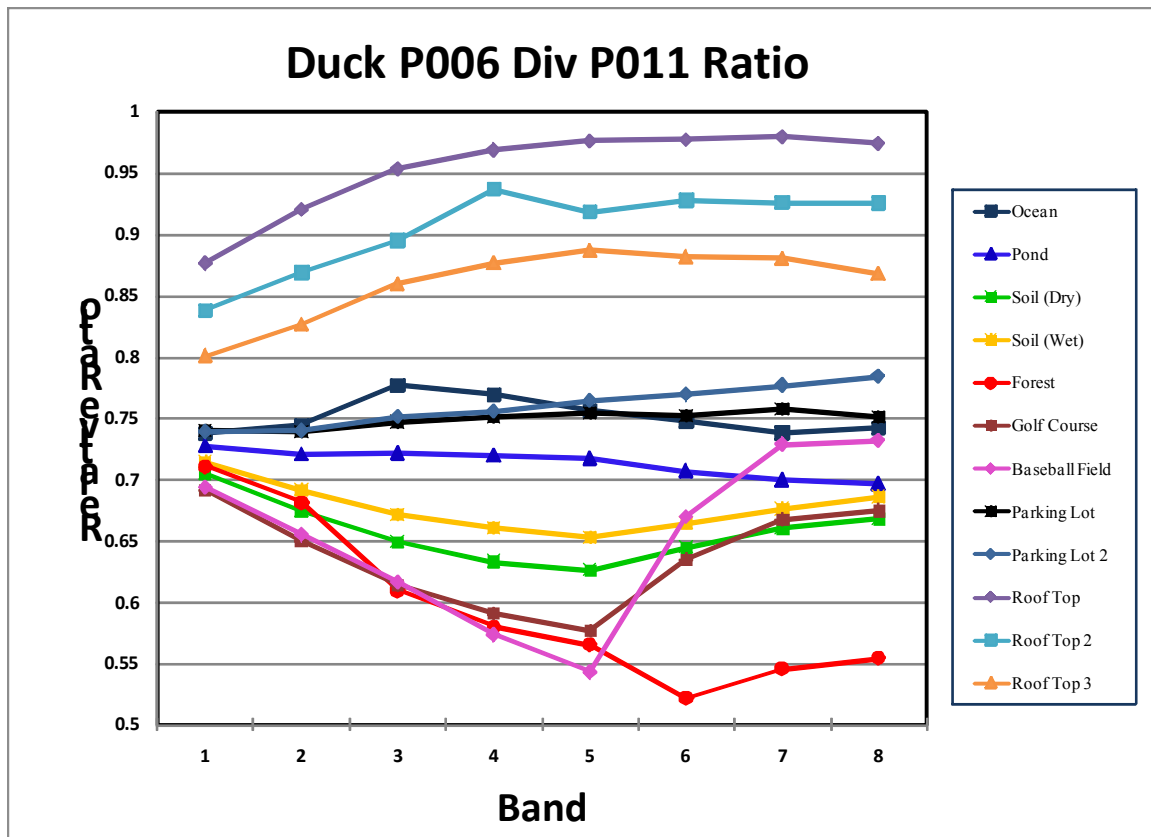


Figure 62. Image Ratio done for All Regions of Interest in all Worldview-2 Bands (Duck, NC)

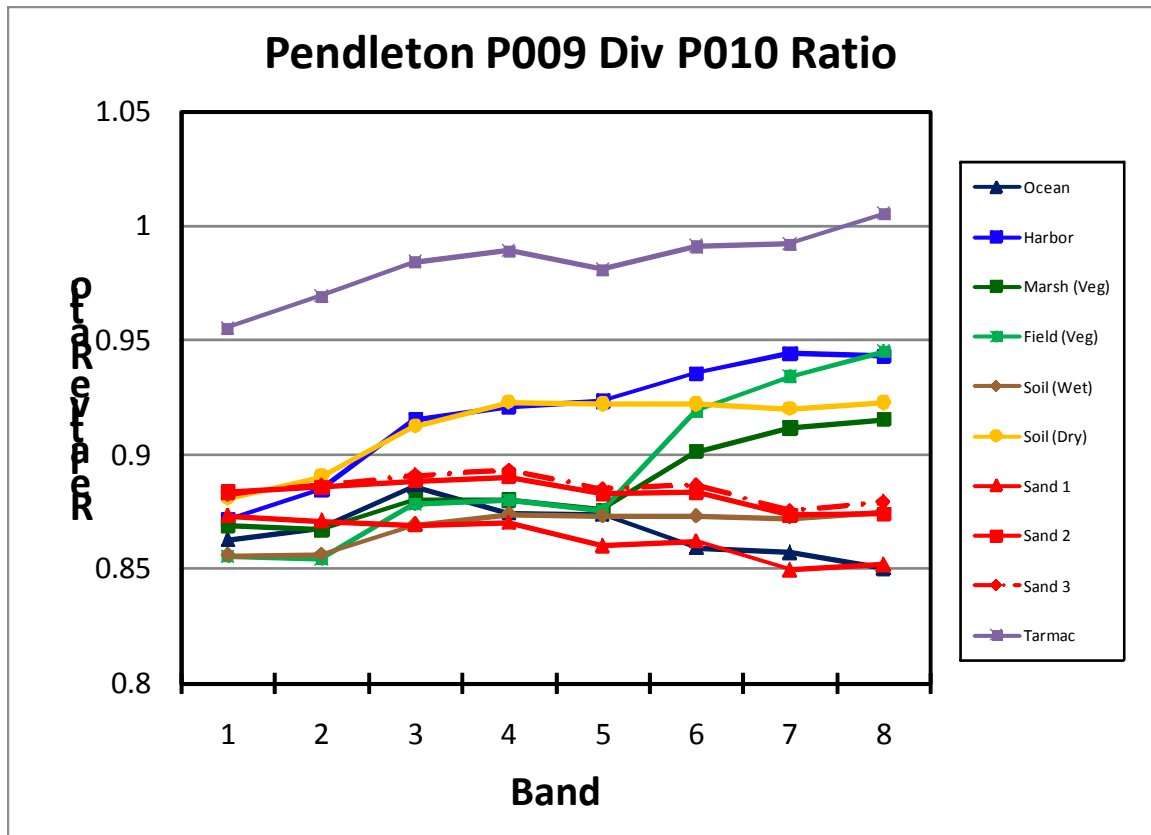


Figure 63. Image Ratio done for All Regions of Interest in all Worldview-2 Bands (Pendleton, CA)

Numerous material characteristics can be extracted from the charts. ROI curves that are flat indicate that there is not a large dependency on wavelength (Duck: Parking Lot, Pendleton: Sand 1, 2, and 3). Flat curves close to 1 also indicate a low dependency on angle. If the curve moves dramatically across wavelengths, this reflects a wavelength dependency of the BRDF (Duck: Baseball Field, Pendleton: Field (Veg)). Ratio values approaching a value of 1 are indicative of similarity between the two input images and low dependence on angle (Duck: Roof Top), while low-value ratios convey that the input images are dissimilar in the respective band due to the viewing angle (Duck: Forest).

I. BRDF RESULTS BY SEPARATION ANGLE FOR REGIONS OF INTEREST

When displayed by separation angle, a clear pattern in the radiance and subsequently the BRDF is observed. Studying the charts in the appendix reveals information about the surfaces within the ROIs. No surfaces in nature are a perfect example of a specular or diffuse reflector and are instead less-idealized versions of the two. A less-idealized surface may appear brighter in the specular and backscatter directions and darker when viewed at grazing angles. The chopiness of water affects its reflective characteristics.

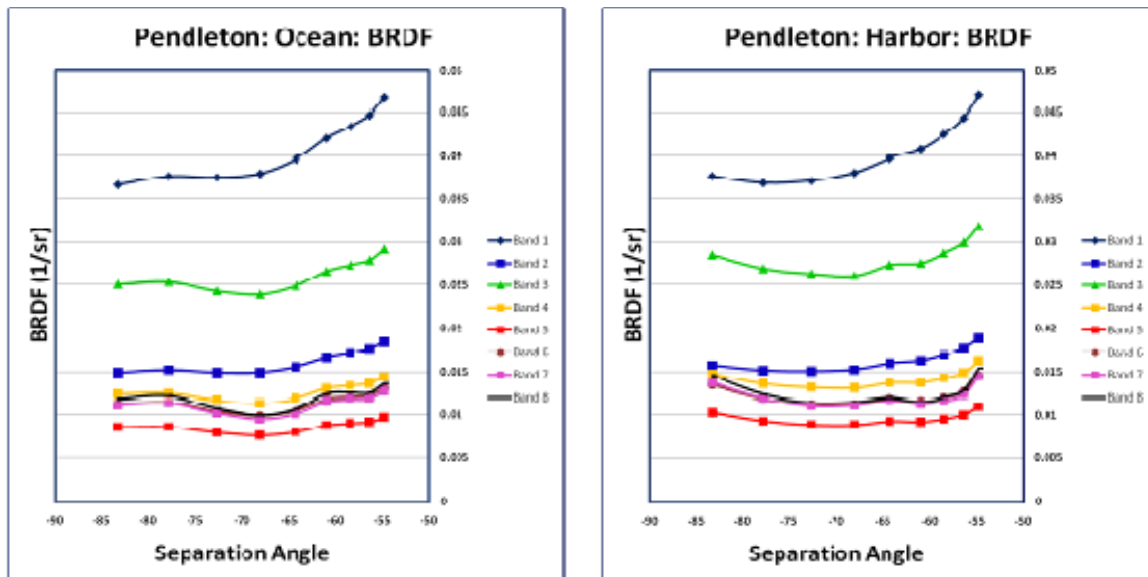


Figure 64. BRDF Results by Separation Angle for Ocean vs. Harbor (Pendleton, CA)

As observed in Figure 64. , the ocean is presumably rougher than the inland harbor and therefore it exhibits less specular traits. The BRDF of the harbor rises in the specular direction and again as the angle decreases toward the backscatter direction. Spectral trends can be observed, for example, water reflects similarly in both the near-IR and the red bands, seen in Figure 64. Another spectral effect is seen in Figure 65. Vegetation is highly reflective in the IR and absorbs strongly in the red, which can be clearly seen in the figure Band 5 and Band 8 curves. Vegetation is an example of a rough

surface and typically has a strong return from the backscatter direction, called the hot spot. This effect can be seen in Figure 65. It does not show a specular component in the forward-scatter direction, but rises as the separation angle decreases.

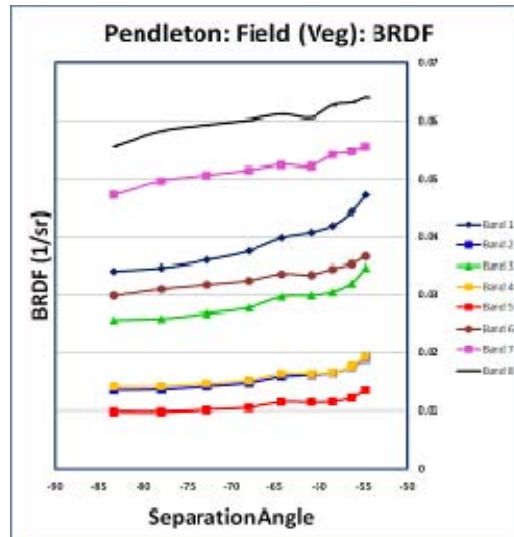


Figure 65. BRDF Results by Separation Angle for Field (Veg) (Pendleton, CA)

Figure 66. displays the highly reflective nature of man-made materials. These materials are reflective across all wavelengths, and display nearly diffuse characteristics, corresponding to a high BRDF in all wavelengths and across all angles.

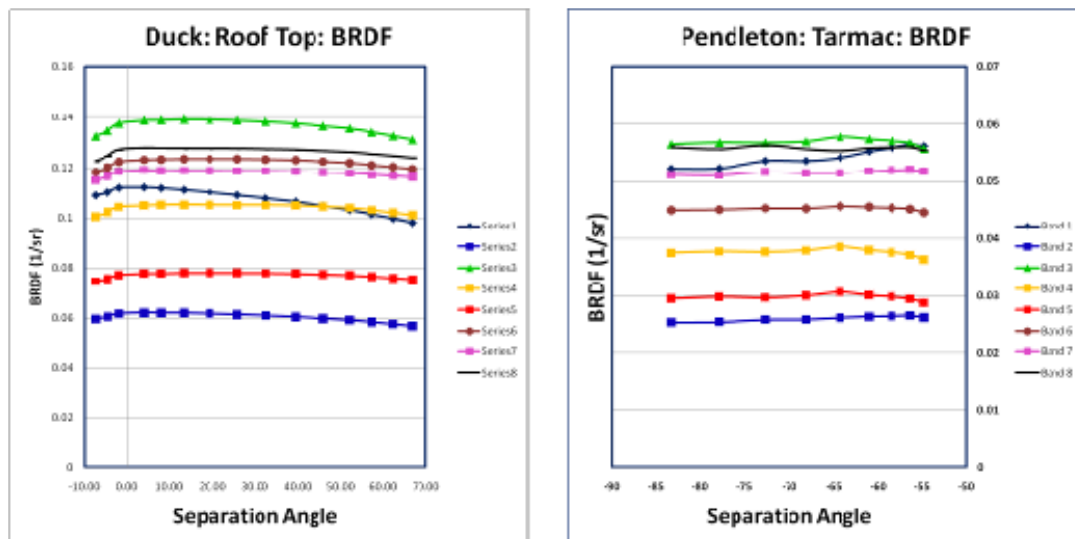


Figure 66. BRDF Results by Separation Angle for man-made materials

Some materials reflect IR energy better than others. This can be seen in Figure 67. Water is inherently a poor reflector, and this is particularly true in the near-IR and IR bands. Vegetation exhibits the opposite effect in the near-IR and IR.

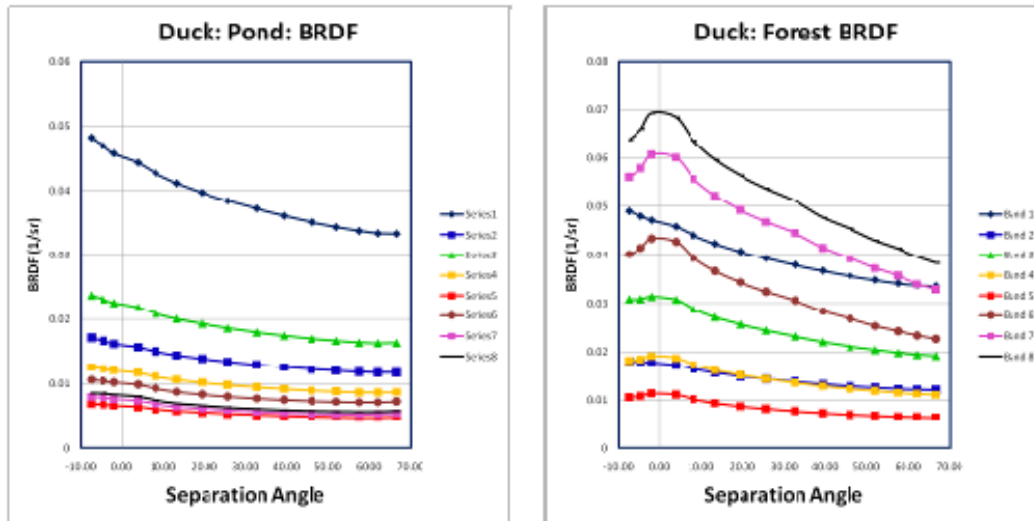


Figure 67. BRDF Results by Separation Angle for Excellent and Poor IR Reflectors

VI. SUMMARY

Bidirectional Reflectance Distribution Function (BRDF) trends were derived from the 8 spectral bands of Worldview-2 imagery, taken over Duck, NC, and Pendleton, CA, on March 24, 2010. Twenty-five Level OR2A images were retrieved from DigitalGlobe, after which they underwent co-registration and processing utilizing the ENVI software.

ENVI tools provided the means to analyze the imagery. Histograms of the images were generated. From these charts, BRDF shifts were visually apparent and could be compared. Analysis of the data also included the use of ENVI's ROI tool and the n-D visualize tool. With these tools, numerous areas were highlighted and refined for examination. These regions represented a variety of diverse terrains, to include: vegetation, asphalt, sand, and water. Image ratioing was completed on select images utilizing the compatible IDL program, which allowed the removal of many undesired imagery effects. Spatial profiles were generated from the created image ratios. ENVI's pre-processing tool allowed the conversion of DN to radiance values, which scaled the observed values to allow reasonable BRDF values to be generated; however, the values contained within this document are not independently meaningful, but instead the trends they display and the methods of retrieval examined are valuable.

Separation angles between the inbound, solar zenith angle and the outbound reflectance angle were calculated for comparison. Plotted against these numbers, BRDF shifts across wavelengths and regions of interest were examined.

Data was pulled from NASA Langley's ASDC from March 26, 2010 for a rough comparison over Pendleton, CA. Level 1B1 Radiance products from MISR's 9 multi-angle cameras were downloaded and chipped for further evaluation with ENVI. Within the MISR data and the Worldview-2 data, a common ROI was generated and the accompanying statistics scrutinized.

THIS PAGE INTENTIONALLY LEFT BLANK

VII. CONCLUSIONS AND FUTURE WORK

Worldview-2 is an important tool in the expanding field of global bidirectional reflectance distribution function mapping, with applications in areas like terrain mapping [38].

Worldview-2 provides spatial resolution at a level that had previously not been obtainable by on-orbit remote sensors. Aerial photography allows for a similar spatial resolution, however, satellites provide high revisit times that would be cost prohibitive to the aerial imagery community. Worldview-2 provides images at a spectral resolution that is beneficial to the BRDF study. While Worldview-2's multispectral imager does not offer the large set of spectral data that a hyperspectral imager would, its use is advantageous. On-orbit hyperspectral sensors are disadvantageous as they increase processing and increase the complexity and cost of the satellite's operation; however, DigitalGlobe's judicious selection of 8 bands provides access to beneficial data at key wavelengths. Based on the results of numerous aerial hyperspectral studies, 8 spectral bands at wavelengths critical in the study of change detection were selected.

This thesis delineates a technique to further the growth of the library of BRDF measurements, and utilizes tools capable of extracting these measurements.

Future work on this subject should first focus on improving the process of extracting reflectance data from satellite imagery. ENVI provides an ortho-rectification tool, which was not utilized in this thesis; exploring its use could prove beneficial. Imagery was obtained from multiple space-borne sensors but was not coordinated to be obtained simultaneously. Advanced coordination between ground and space-borne assets could provide corroboration for data. Processing the data was time intensive and therefore this thesis utilized only 25 data points. To obtain a comprehensive view of the reflectance environment, it is necessary to model the BRDF with significantly more data points. With the more expeditious processing technique of ortho-rectification, substantially more data could be handled. With the process improved, a real contribution of data of high-spatial resolution in 8-bands could be submitted to the BRDF library.

THIS PAGE INTENTIONALLY LEFT BLANK

LIST OF REFERENCES

- [1] T. E. Avery and G. L. Berlin, *Fundamentals of Remote Sensing and Airphoto Interpretation*, Macmillan Publishing Company, New York, 1992.
- [2] R. C. Olsen, *Remote Sensing from Air and Space*, Bellingham, Washington: SPIE Press, 2007.
- [3] K. Barnard, *The Bidirectional Reflectance Distribution Function*, Supplemental Lectures, Computer Vision, University of Arizona, Tucson, AZ, Spring 2010. Available: http://www.cs.arizona.edu/classes/cs477/spring10/ua_cs_only/lectures/BRDF.pdf
- [4] J. R. Schott, *Remote Sensing: The Image Chain Approach*, 2nd ed., New York, New York: Oxford University Press, 2007.
- [5] F. E. Nicodemus, J. C. Richmond, J. J. Hsia, I. W. Ginsburg, and T. Limperis, *Geometrical considerations and nomenclature for reflectance*, NBS Monograph 160, National Bureau of Standards, 1977.
- [6] M. F. Modest, *Radiative Heat Transfer*, New York, New York: McGraw-Hill, 1993.
- [7] W. Lucht and C. Schaaf, Boston University Department of Geography: BRDF Explained, [Online], Jul 2006, [cited 2010 Oct 1], Available: <http://www-modis.bu.edu/brdf/brdfexpl.html>
- [8] J. Radloff, *A Literature Review of Reflectance Measurement and its Application in the Realistic Rendering of Surfaces*, Technical Report Literature Review, Virtual Reality Special Interest Group, Computer Science Department, Rhodes University, Grahamstown, South Africa, June 2004. Available: <http://delta.ru.ac.za/vrsig/pastprojects/051btf/paper02.pdf>
- [9] G. J. Ward, *Measuring and Modeling Anisotropic Reflection*, Computer Graphics, vol. 26, no. 2: 265–272, 1992. Available: <http://delivery.acm.org/10.1145/140000/134078/p265-ward.pdf?key1=134078&key2=0118149821&coll=DL&dl=ACM&CFID=113441722&CFTOKEN=35183827>
- [10] H. Li, S. Foo, K. E. Torrance, and S. H. Westin, *Automated three-axis gonireflectometer for computer graphics applications*, Optical Engineering, vol. 45, no. 4, 2006. Available: http://www.graphics.cornell.edu/~westin/SPIE_5878-29_Gonio.pdf

- [11] (2010) Jet Propulsion Laboratory's MISR: Multi-angle Imaging SpectroRadiometer Validation website, [Online], [cited 2010 Oct 1]. Available: <http://misr.jpl.nasa.gov/Mission/validation/instruments/>
- [12] J. M. Chen, S. G. Leblanc, J. Cihlar, P. Bicheron, M. Leroy, D. Deering and T. Eck, *Studies of BRDF in conifer and deciduous boreal forests using the 4-Scale model and airborne POLDER and ground-based PARABOLA measurements*, Proceedings of IGARSS'97, 1997. Available: <http://ieeexplore.ieee.org/stamp/stamp.jsp?arnumber=00615828>
- [13] K. Khlopenkov and A. P. Trishchenko, *Analysis of BRDF and Albedo Properties of Pure and Mixed Surface Types from Terra MISR Using Landsat High-Resolution Land Cover and Angular Unmixing Technique*, Fourteenth ARM Science Team Meeting Proceedings, Albuquerque, New Mexico, March 22-26, 2004. Available: http://www.arm.gov/publications/proceedings/conf14/extended_abs/trishchenko-ap.pdf
- [14] (2010) Jet Propulsion Laboratory's MISR: Multi-angle Imaging SpectroRadiometer website, [Online], [cited 2010 Oct 1]. Available: <http://misr.jpl.nasa.gov/>
- [15] J. D. Armston, P. F. Scarth, S. R. Phinn, and T. J. Danaher, *Analysis of multi-date MISR measurements for forest and woodland communities, Queensland, Australia*, Science Direct Remote Sensing of Environment Journal, vol. 107: 287–298, 2007. Available: http://www.sciencedirect.com/science?_ob=MImg&_imagekey=B6V6V-4MP5KVM-2-R&_cdi=5824&_user=3326500&_pii=S0034425706004482&_origin=search&_coverDate=03%2F15%2F2007&_sk=998929998&view=c&wchp=dGLbVIW-zSkzk&md5=8babccbfa73692a8c1879464e8c1ce1d&ie=/sdarticle.pdf
- [16] Y. Jin, F. Gao, C. B. Schaaf, X. Li, A. H. Strahler, C. J. Bruegge, and J. V. Martonchik, *Improving MODIS surface BRDF/Albedo retrieval with MISR multiangle observations*, Geoscience and Remote Sensing, vol. 40, no. 7: 1593–1604, 2002. Available: <http://ieeexplore.ieee.org/stamp/stamp.jsp?tp=&arnumber=1542362&tag=1>
- [17] (2010) Centre National d'Études Spatiales: POLDER website. [Online]. [cited 2010 Oct 7], Available: <http://smsc.cnes.fr/POLDER/>
- [18] *ADEOS II: Advanced Earth Observing Satellite II*, NASA Earth Science Reference Handbook, Available: http://eosps.gsfc.nasa.gov/eos_homepage/mission_profiles/docs/ADEOSII.pdf

- [19] P. Y. Deschamps, F. M. Breon, M. Leroy, A. Podaire, A. Bricaud, J. C. Buriez, and G. Seze, *The POLDER Mission: Instrument characteristics and scientific objectives*, IEEE Transactions on Geoscience and Remote Sensing, vol. 32, no. 3: 598–615, 1994.
Available:
<http://ieeexplore.ieee.org/stamp/stamp.jsp?tp=&arnumber=297978&tag=1>
- [20] S. Bouffières, F. M. Bréon, and D. Tanré, *Atmospheric water vapor estimate by a differential absorption technique with the POLDER instrument*, Journal of Geophysical Research, vol. 102, no. D3: 3831–3841, 1997.
- [21] O. Hautecoeur, M. M. Leroy, *Surface Bidirectional Reflectance Distribution Function observed at global scaled by POLDER/ADEOS*, Geophysical Research Letters, vol. 25, no. 22: 4197–4200, 1998. Available:
<http://www.gps.caltech.edu/~vijay/Papers/BRDF/hautecoeur-leroy-98.pdf>
- [22] Lacaze, R., J.M. Chen, J.L. Roujean and S.G. Leblanc, *Retrieval of vegetation clumping index using hot spot signatures measured by POLDER instrument*, Remote Sensing of Environment, vol. 79: 84–95, 2002.
- [23] (2010) European Space Agency’s Earthnet Online PROBA website, [Online], [cited 2010 Oct 7], Available: <http://earth.esa.int/proba>
- [24] A. M. Smith, G. Bourgeois, R. de Jong, C. Nadeau, J. Freemantle, P. M. Teillet, A. Chichagov, G. Gedosejevs, H. When, and A. Shankaie, *Remote Sensing Derived Leaf Area Index and Potential Applications for Crop Modeling*, Geoscience and Remote Sensing Symposium: 2088–2091, 2006. Available:
<http://ieeexplore.ieee.org/stamp/stamp.jsp?tp=&arnumber=4241687>
- [25] R. Duca and F. Del Frate, *Hyperspectral and Multiangle CHRIS-PROBA Images for the Generation of Land Cover Maps*, Geoscience and Remote Sensing, vol. 46, no. 10: 2857–2866, 2008. Available:
<http://ieeexplore.ieee.org/stamp/stamp.jsp?tp=&arnumber=4637938>
- [26] L. Guanter, L. Alonso, and J. Moreno, *A Method for the surface reflectance retrieval from PROBA/CHRIS data over land: application to ESA SPARC campaigns*, Geoscience and Remote Sensing, vol. 43, no. 12: 2908–2917, 2005. Available:
<http://ieeexplore.ieee.org/stamp/stamp.jsp?tp=&arnumber=1542362&tag=1>
- [27] J. D. Foley, A. van Dam, S. K. Feiner, and J. F. Hughes, *Computer Graphics: Principles and Practice*, 2nd Edition: Addison-Wesley, 1996.
- [28] G. T. Georgiev, C. K. Gatebe, J. J. Butler, and M. D. King, *BRDF Analysis of Savanna Vegetation and Salt-Pan Samples*, IEEE Transactions on Geoscience and

- Remote Sensing, vol. 47, no. 8: 2546–2556, August 2009. Available: [http://modis-atmos.gsfc.nasa.gov/reference/docs/Georgiev_et_al._\(2009\).pdf](http://modis-atmos.gsfc.nasa.gov/reference/docs/Georgiev_et_al._(2009).pdf)
- [29] D. Biliouris, D. van der Zande, W. W. Verstraeten, J. Stuckens, B. Muys, P. Dutre, and P. Coppin, *RPV Model parameters based on Hyperspectral Bidirectional Reflectance Measurements of Fagus sylvatica L. Leaves*, MDPI.com Remote Sensing open-access journal, nol. 1: 92–106, 2009. Available: <http://www.mdpi.com/2072-4292/1/2/92/pdf>
- [30] A. P. Trishchenko, A. Jevtic, K. Khlopenkov, V. Korolevich, R. Latifovic, J. Chen, W. Park, S. Wang, and A. Davidson, *Surface albedo and radiation budget datasets over Canada from remote sensing observations and modeling for climate change impact studies*, Canada Earth Sciences website [Online], [cited 2010 Dec 13], Available: http://ess.nrcan.gc.ca/2002_2006/rcvcc/pdf/j28_albedoandradbudget.pdf
- [31] J. R. Schott, *Fundamentals of Polarimetric Remote Sensing*, Bellingham, Washington: SPIE Press, 2009.
- [32] M. Kurt, L. Szirmay-Kalos, and J. Krivanek, *An Anisotropic BRDF Model for Fitting and Monte Carlo Rendering*, ACM SIGGRAPH Computer Graphics Newsletter, vol. 44, no. 1, February 2010. Available: <http://delivery.acm.org/10.1145/1730000/1722996/a3-kurt.pdf?key1=1722996&key2=1618581921&coll=DL&dl=ACM&CFID=998154&CFTOKEN=29684535>
- [33] M. Oren and S. K. Nayar, *Generalization of the Lambertian Model and Implications for Machine Vision*, International Journal of Computer Vision, vol. 14, no. 3, 1992. Available: http://www1.cs.columbia.edu/CAVE/publications/pdfs/Nayar_IJCV95.pdf
- [34] *White Paper: The Benefits of the 8 Spectral Bands of WorldView-2*, DigitalGlobe, August 2009, Available: http://worldview2.digitalglobe.com/docs/WorldView-2_8-Band_Applications_Whitepaper.pdf
- [35] B. L. McCarthy, *Coastal Bathymetry Using 8-Color Multispectral Satellite Observations of Wave Motion*, MS thesis Naval Postgraduate School, Monterey, CA, 2010.
- [36] (2010) National Aeronautics and Space Administration S'COOL website, [Online], [cited 2010 Dec 6], Available: <http://asd-www.larc.nasa.gov/SCOOOL/definition.html>

- [37] S. Farooq, *Spectral Reflectance of Land Covers*, Lecture Notes, Department of Geology, Aligarh Muslim University, Aligarh, India, 2010. Available: <http://www.cps-amu.org/sf/notes/mlr-1-8.htm>
- [38] L. Su, Y. Huang, M. J. Chopping, A. Rango, J. V. Martonchik, *An empirical study on the utility of BRDF model parameters and topographic parameters for mapping vegetation in a semi-arid region with MISR imagery*, International Journal of Remote Sensing, vol. 30, no. 13, January 2009. Available: http://pdfserve.informaworld.com/530247_731493268_913270864.pdf

THIS PAGE INTENTIONALLY LEFT BLANK

APPENDIX: CHARTS AND GRAPHS

A. WORLDVIEW-2 GAIN, OFFSET VALUES*, ABSOLUTE CALIBRATION FACTOR AND EFFECTIVE BANDWIDTH

Band	Gain	Absolute Calibration Factor	Effective Bandwidth (μm)
1	1.85415428e-002	9.295654e-003	4.73e-002
2	9.81118344e-003	1.260825e-002	5.43e-002
3	1.55439861e-002	9.713071e-003	6.30e-002
4	1.07401758e-002	5.101088e-003	3.74e-002
5	1.07401758e-002	1.103623e-002	5.74e-002
6	1.07401758e-002	4.539619e-003	3.93e-002
7	1.07401758e-002	1.224380e-002	9.89e-002
8	1.07401758e-002	9.042234e-003	9.96e-002

*Offset for all bands equaled zero

B. SPECTRAL IRRADIANCE

Band	Spectral Irradiance ($\text{W}/(\text{m}^2 \cdot \text{sr} \cdot \text{nm})$)
1	1.88489
2	2.05999
3	2.09716
4	2.00309
5	1.8758
6	1.68533
7	1.36722
8	1.16124

*Generated by www.spectralcalc.com (T = 5250 C, $\epsilon=1$)

C. MISR PRODUCTS UTILIZED

Type	Identifier	Start Time (GMT)	End Time (GMT)
MI1B1	MISR_AM1_RP_GM_P041_O054630_DF_F03_0024.hdf	18:25:12.000000	19:15:09.160000
MI1B1	MISR_AM1_RP_GM_P041_O054630_CF_F03_0024.hdf	18:26:13.440000	19:16:10.600000
MI1B1	MISR_AM1_RP_GM_P041_O054630_BF_F03_0024.hdf	18:27:07.712000	19:17:04.872000
MI1B1	MISR_AM1_RP_GM_P041_O054630_AF_F03_0024.hdf	18:27:54.816000	19:17:51.976000
MI1B1	MISR_AM1_RP_GM_P041_O054630_AN_F03_0024.hdf	18:28:41.920000	19:18:39.080000
MI1B1	MISR_AM1_RP_GM_P041_O054630_AA_F03_0024.hdf	18:29:29.024000	19:19:26.184000
MI1B1	MISR_AM1_RP_GM_P041_O054630_BA_F03_0024.hdf	18:30:16.128000	19:20:13.288000
MI1B1	MISR_AM1_RP_GM_P041_O054630_CA_F03_0024.hdf	18:31:10.400000	19:21:07.560000
MI1B1	MISR_AM1_RP_GM_P041_O054630_DA_F03_0024.hdf	18:32:11.840000	19:22:09.000000

*Data acquired on March 26, 2010. Provided by EOS data gateway at NASA Langley's Atmospheric Science and Data Center.

Key

MI = MISR

1B1 = Level 1B1 Product

MISR = Instrument Name

AM1 = Satellite Name

(G)RP = (Georectified) Radiance Product

GM = Global Mode

Pxxx = Path Number

Oxxxxxx = Orbit Number

XX = Camera

Fnn = Format version of the product

nnnn = Product Version number

D. HISTOGRAM SHIFT WITH VIEW ANGLE BY BAND (DUCK, NC)

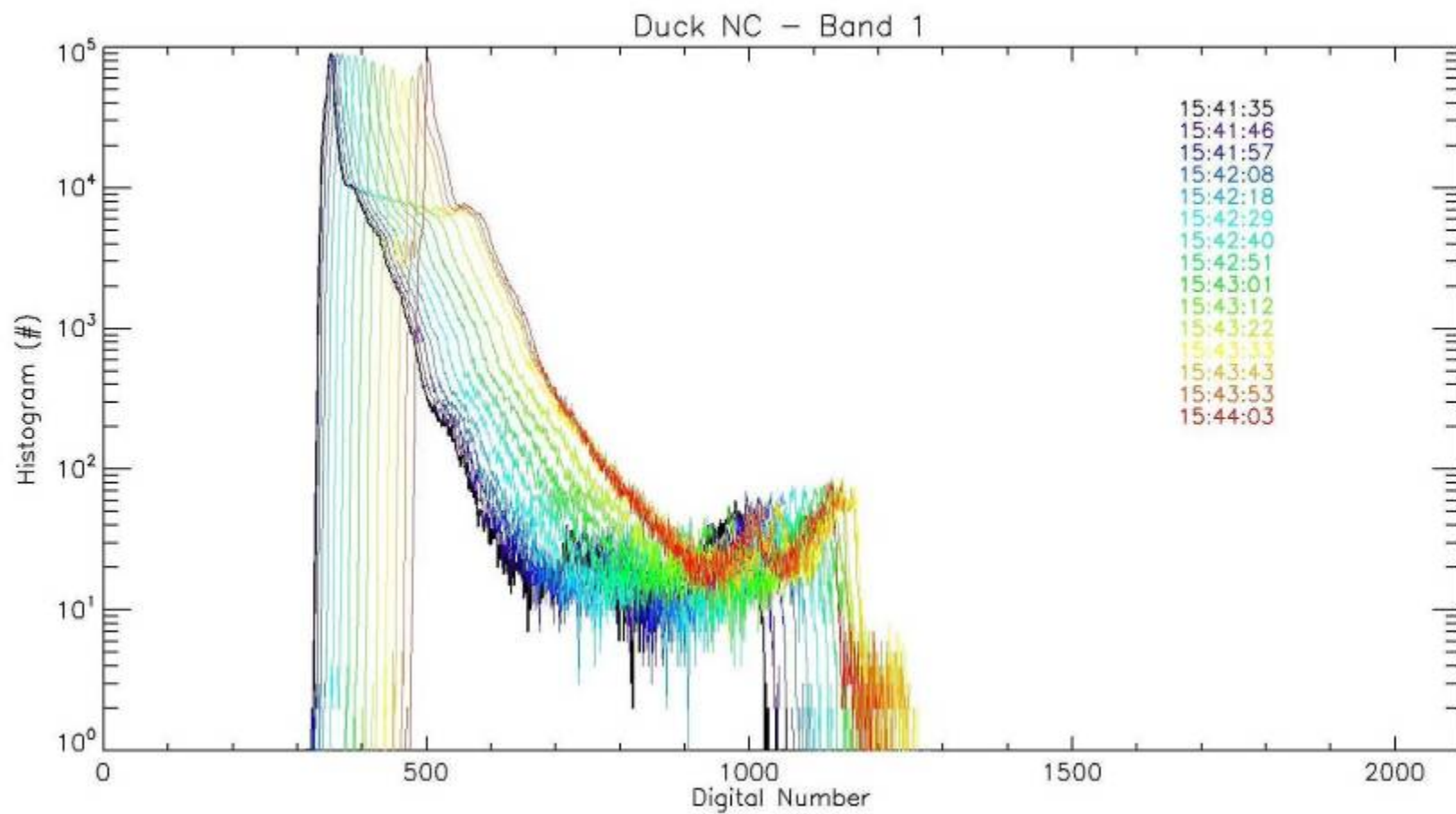


Figure 68. Histogram Shift with View Angle: Duck, NC (Band 1)

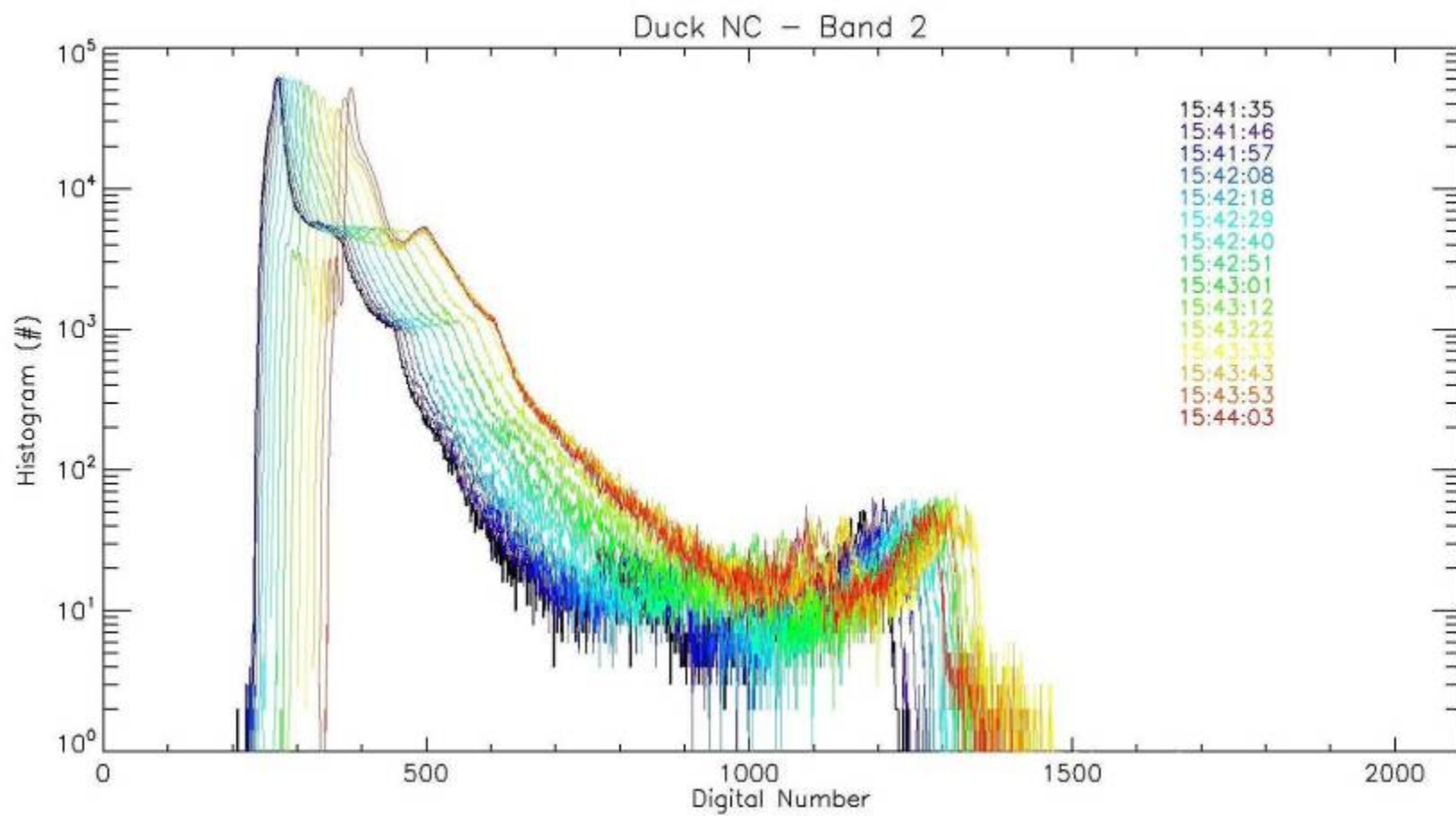


Figure 69. Histogram Shift with View Angle: Duck, NC (Band 2)

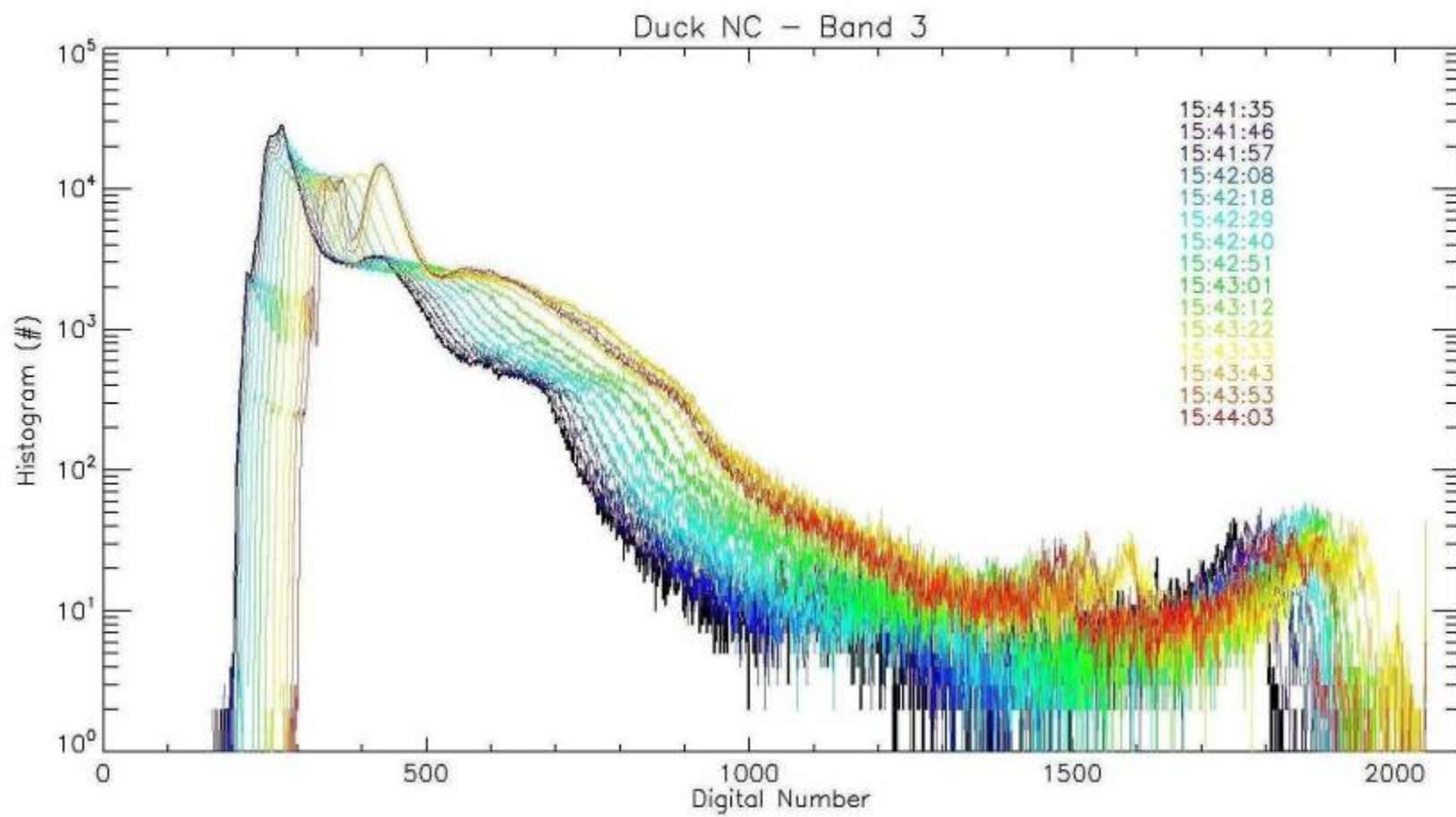


Figure 70. Histogram Shift with View Angle: Duck, NC (Band 3)

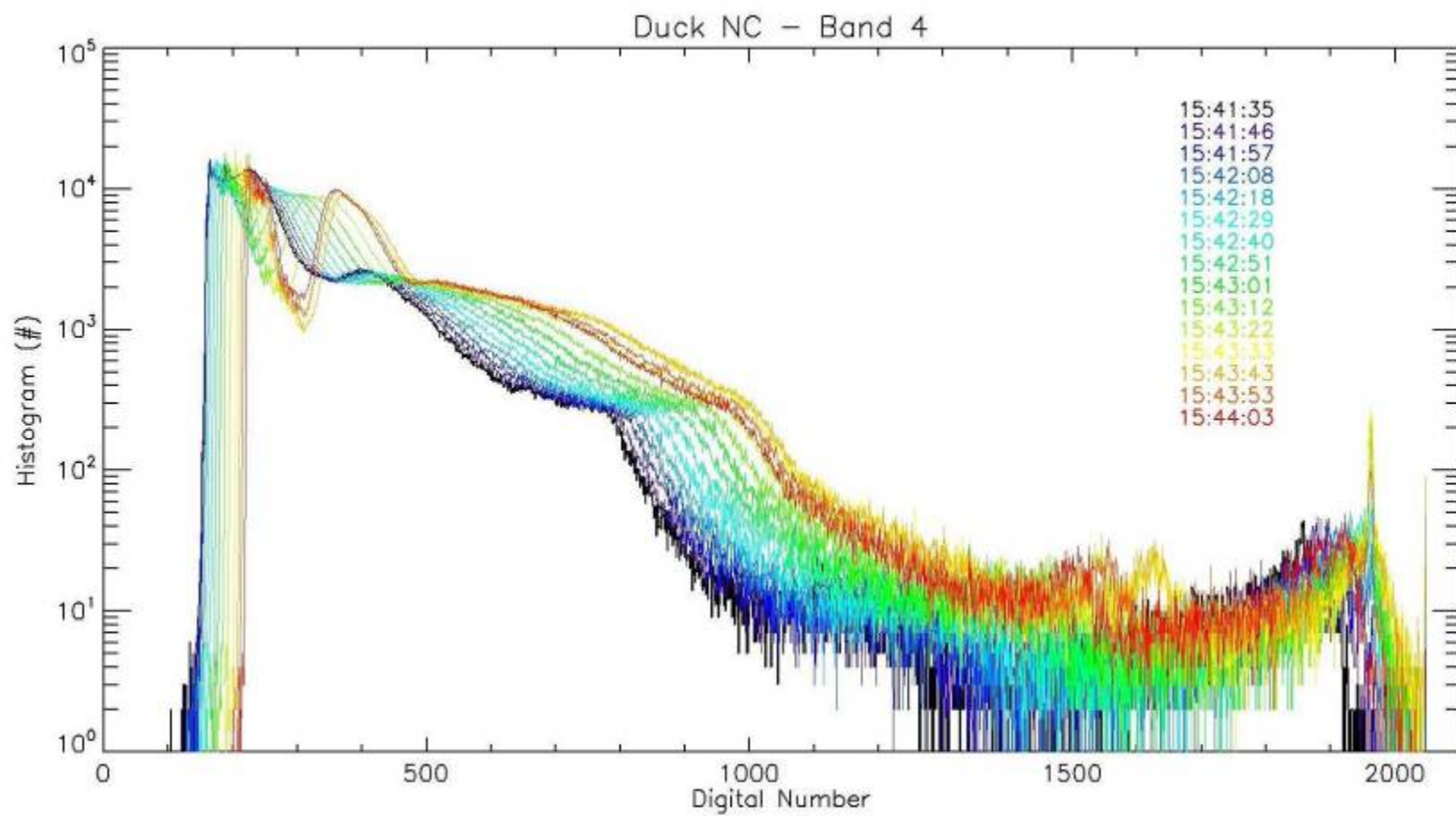


Figure 71. Histogram Shift with View Angle: Duck, NC (Band 4)

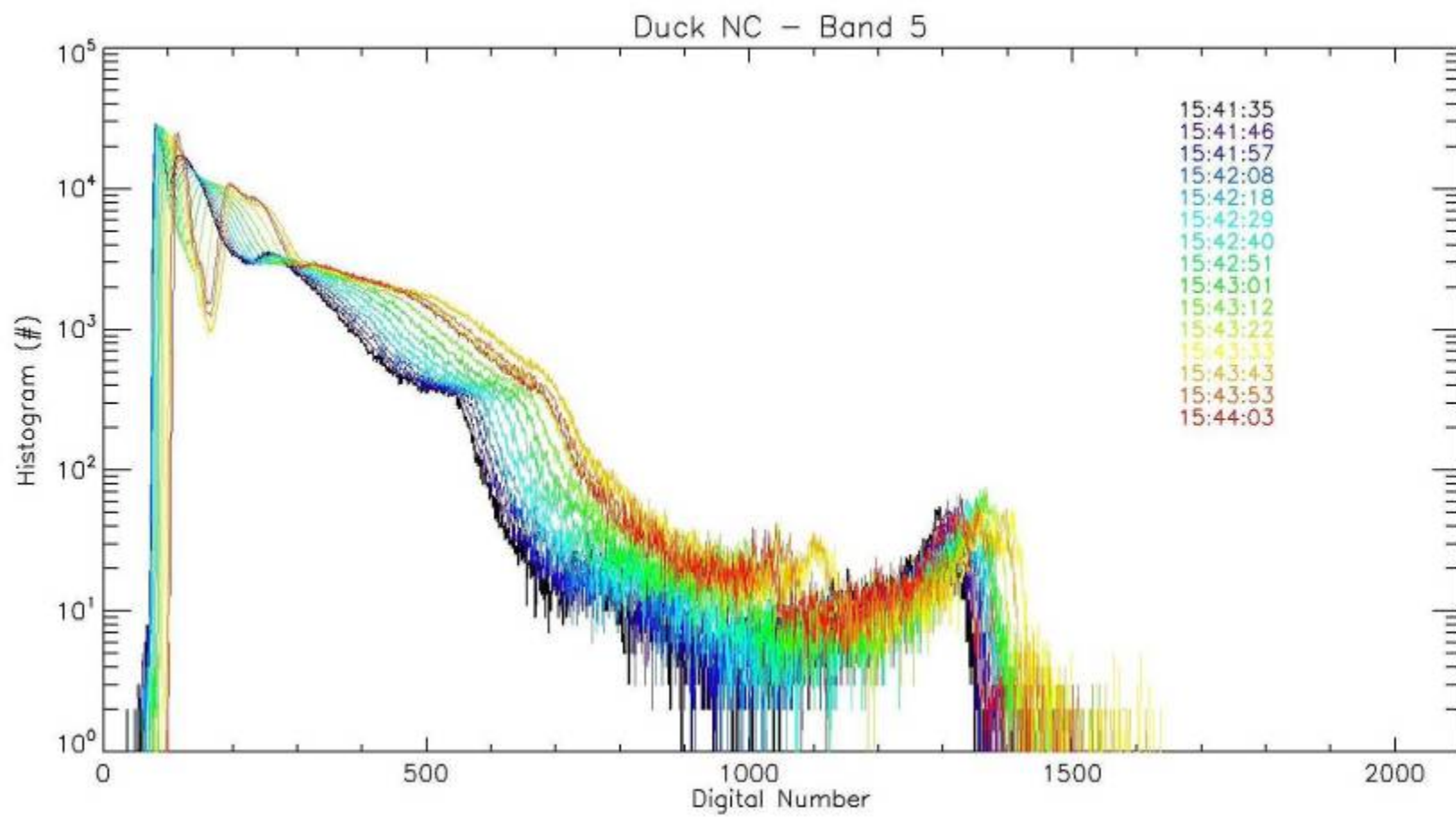


Figure 72. Histogram Shift with View Angle: Duck, NC (Band 5)

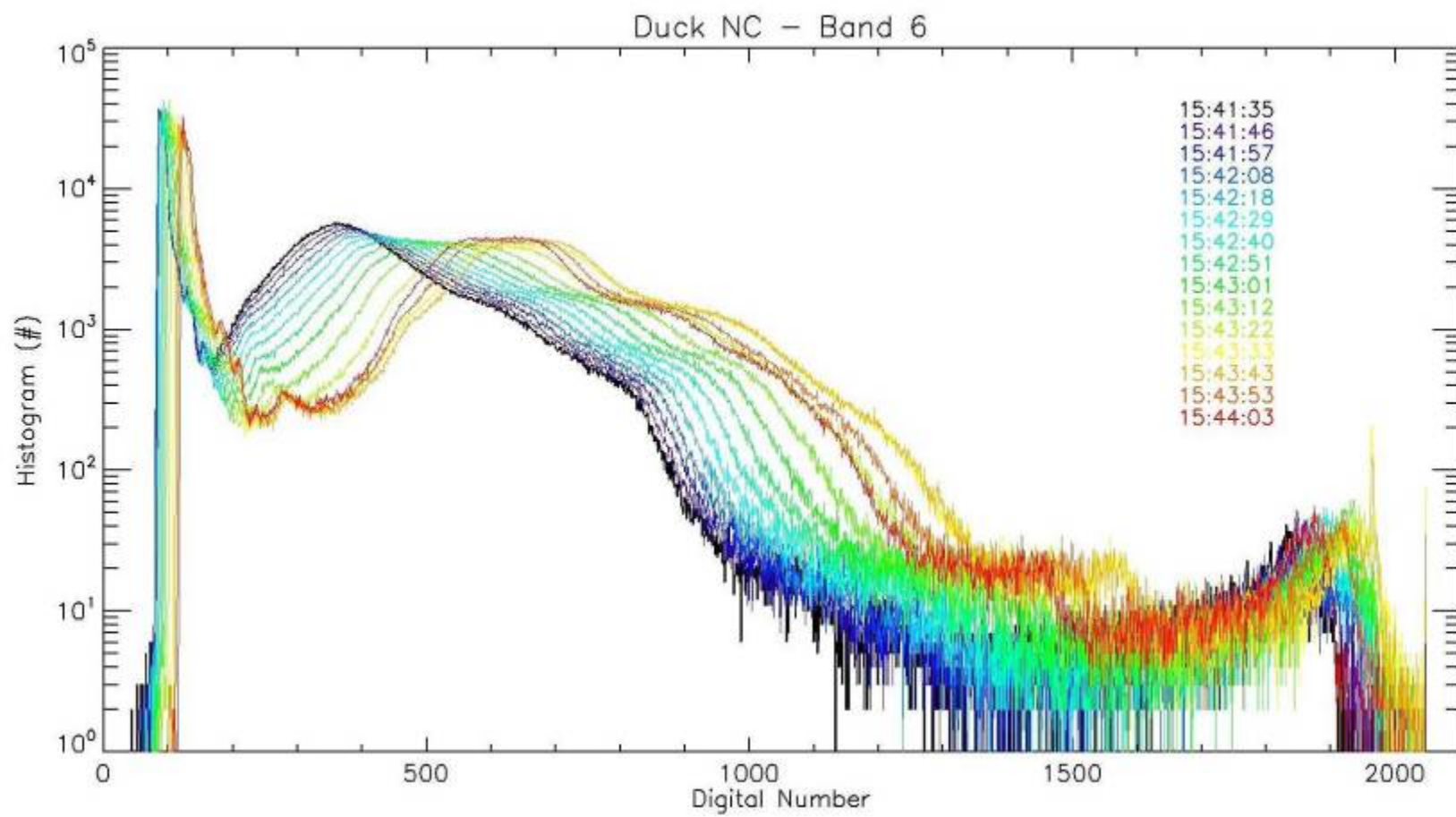


Figure 73. Histogram Shift with View Angle: Duck, NC (Band 6)

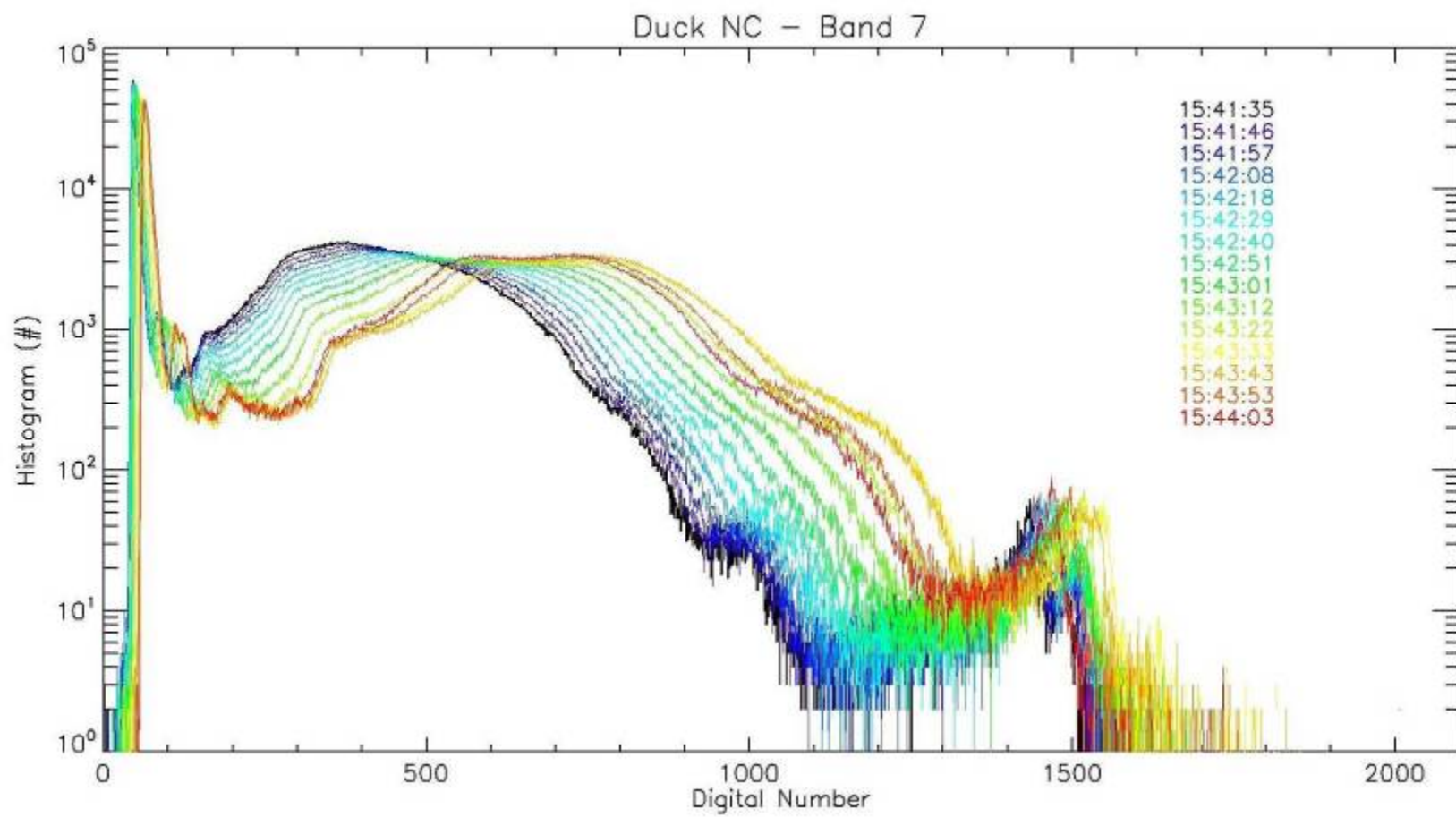


Figure 74. Histogram Shift with View Angle: Duck, NC (Band 7)

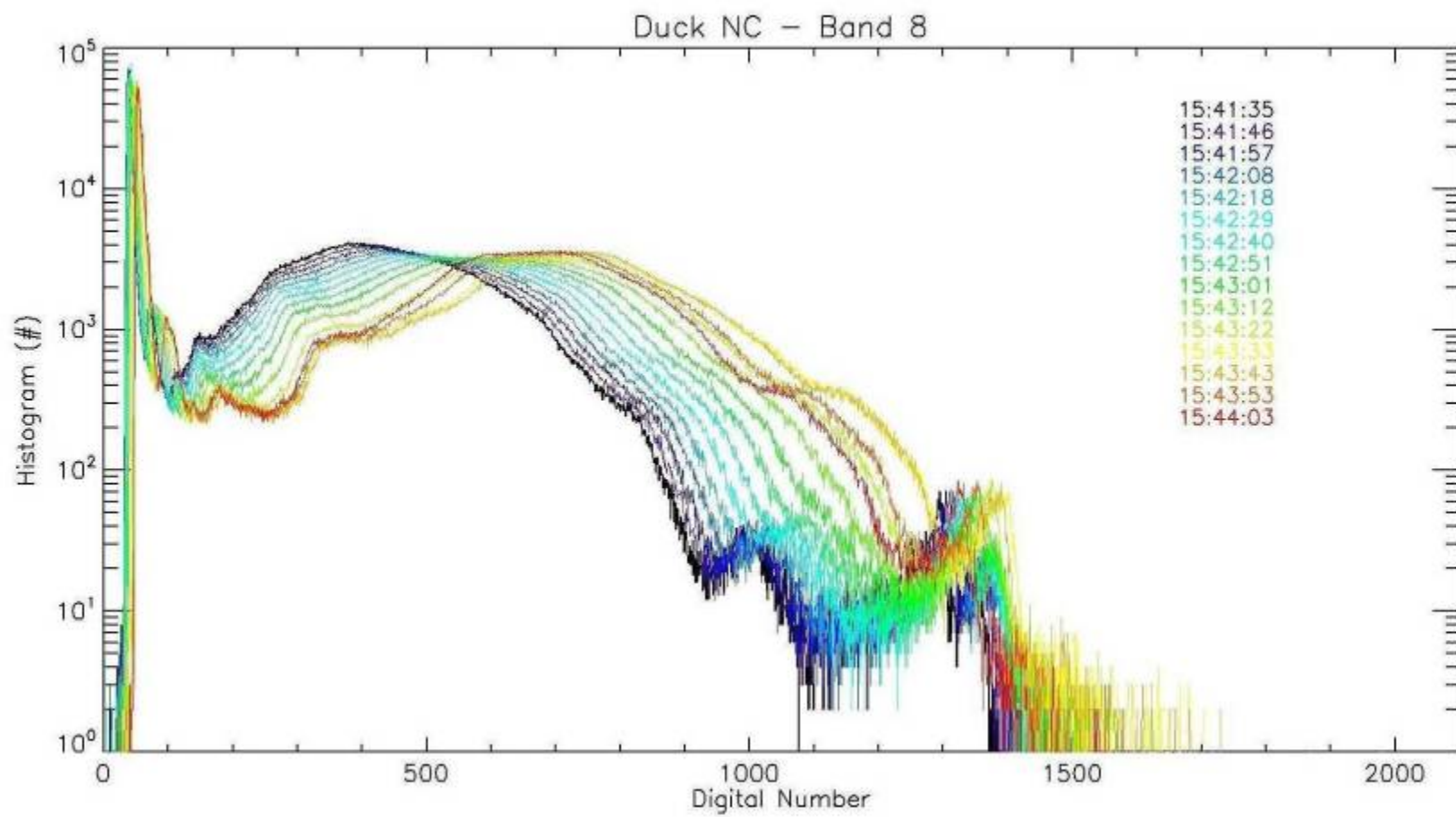


Figure 75. Histogram Shift with View Angle: Duck, NC (Band 8)

E. HISTOGRAM SHIFT WITH VIEW ANGLE BY BAND (PENDLETON, CA)

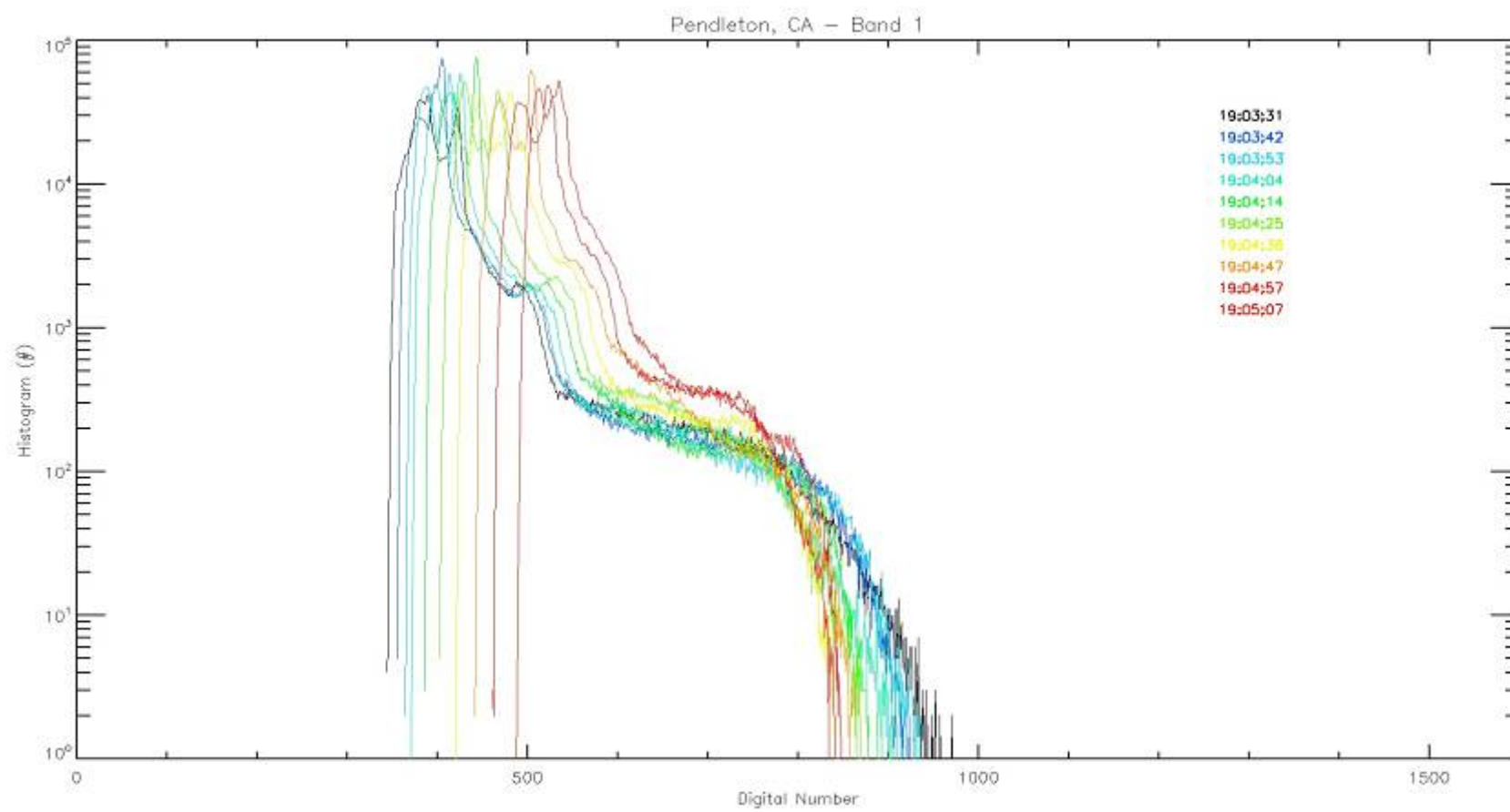


Figure 76. Histogram Shift with View Angle: Pendleton, CA (Band 1)

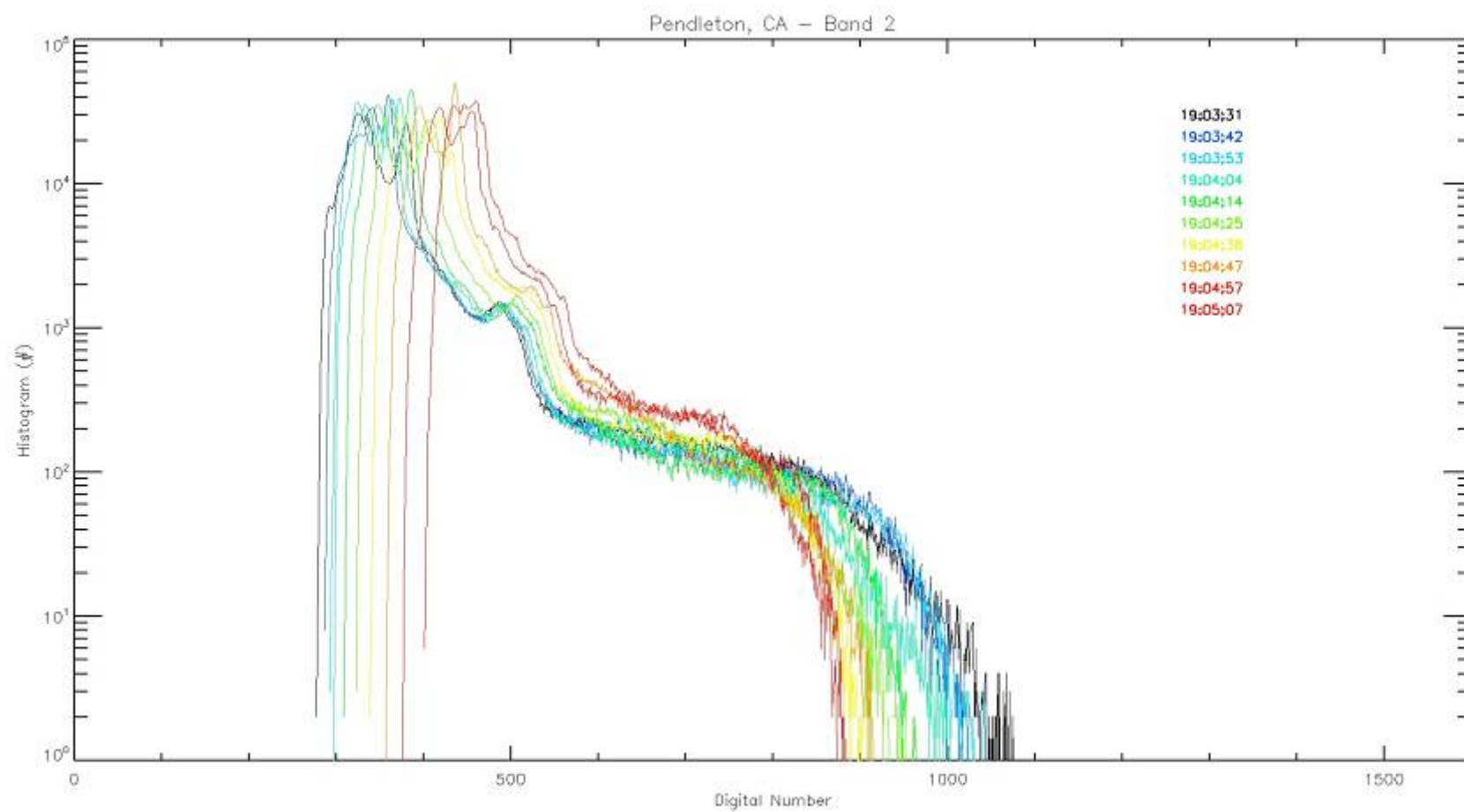


Figure 77. Histogram Shift with View Angle: Pendleton, CA (Band 2)

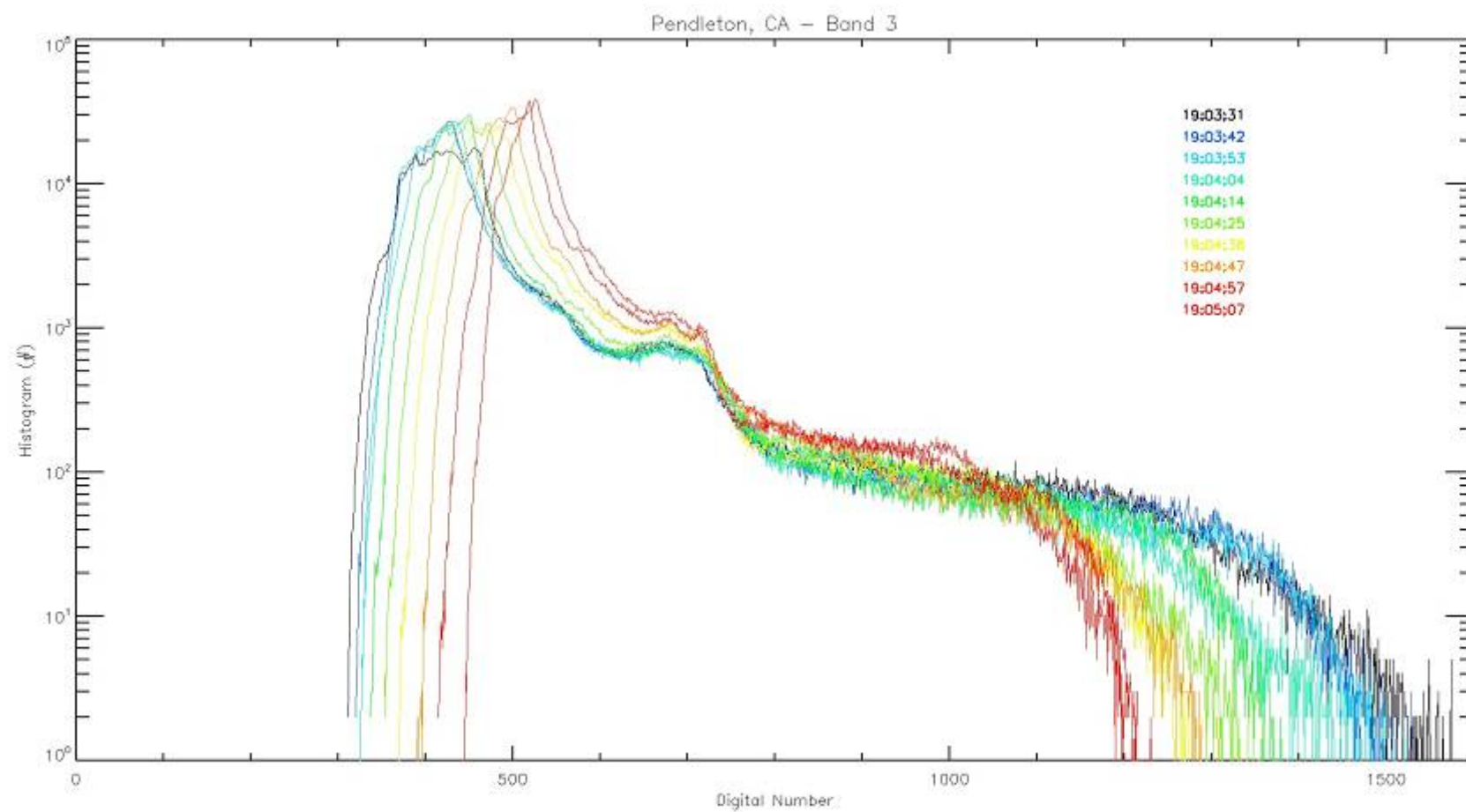


Figure 78. Histogram Shift with View Angle: Pendleton, CA (Band 3)

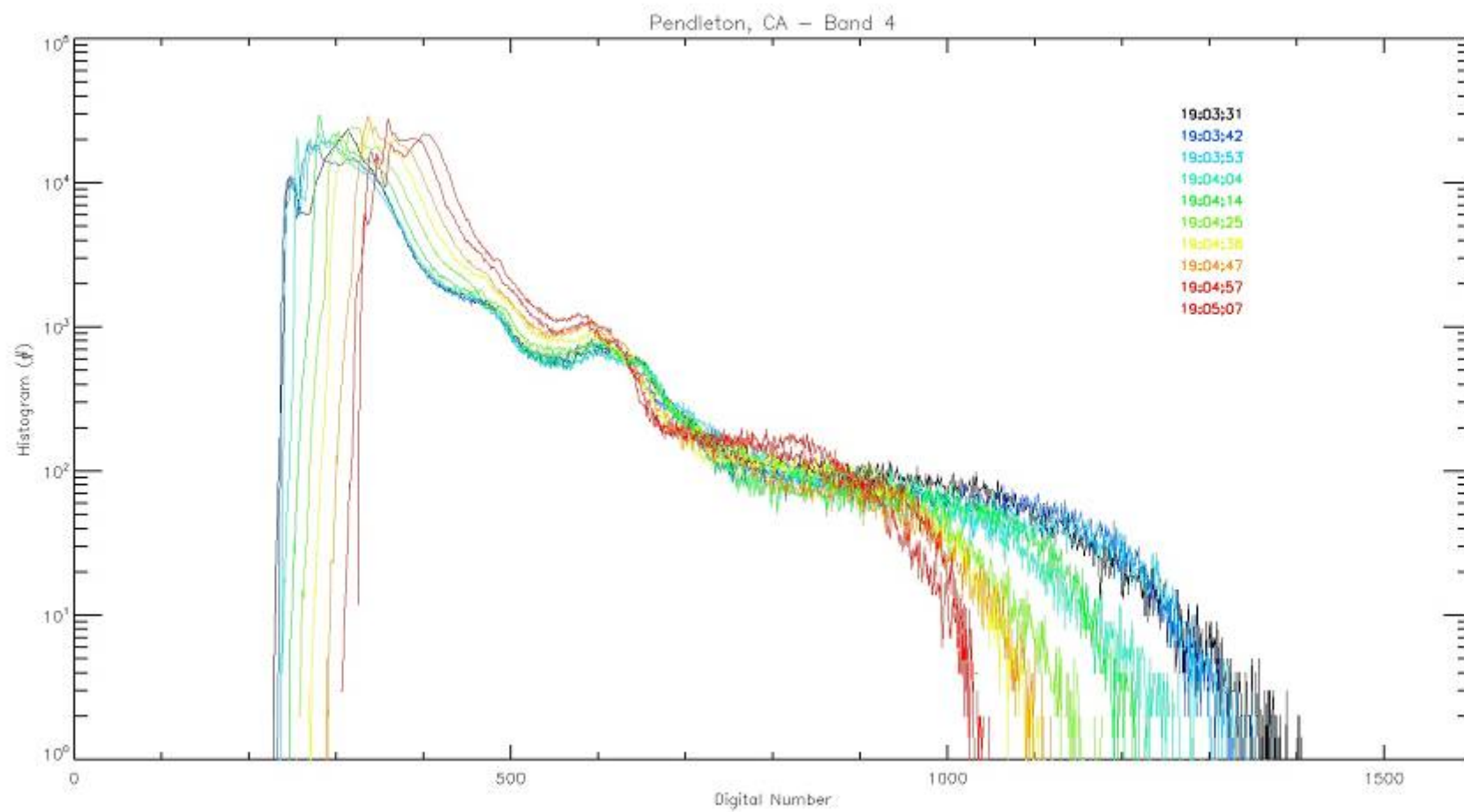


Figure 79. Histogram Shift with View Angle: Pendleton, CA (Band 4)

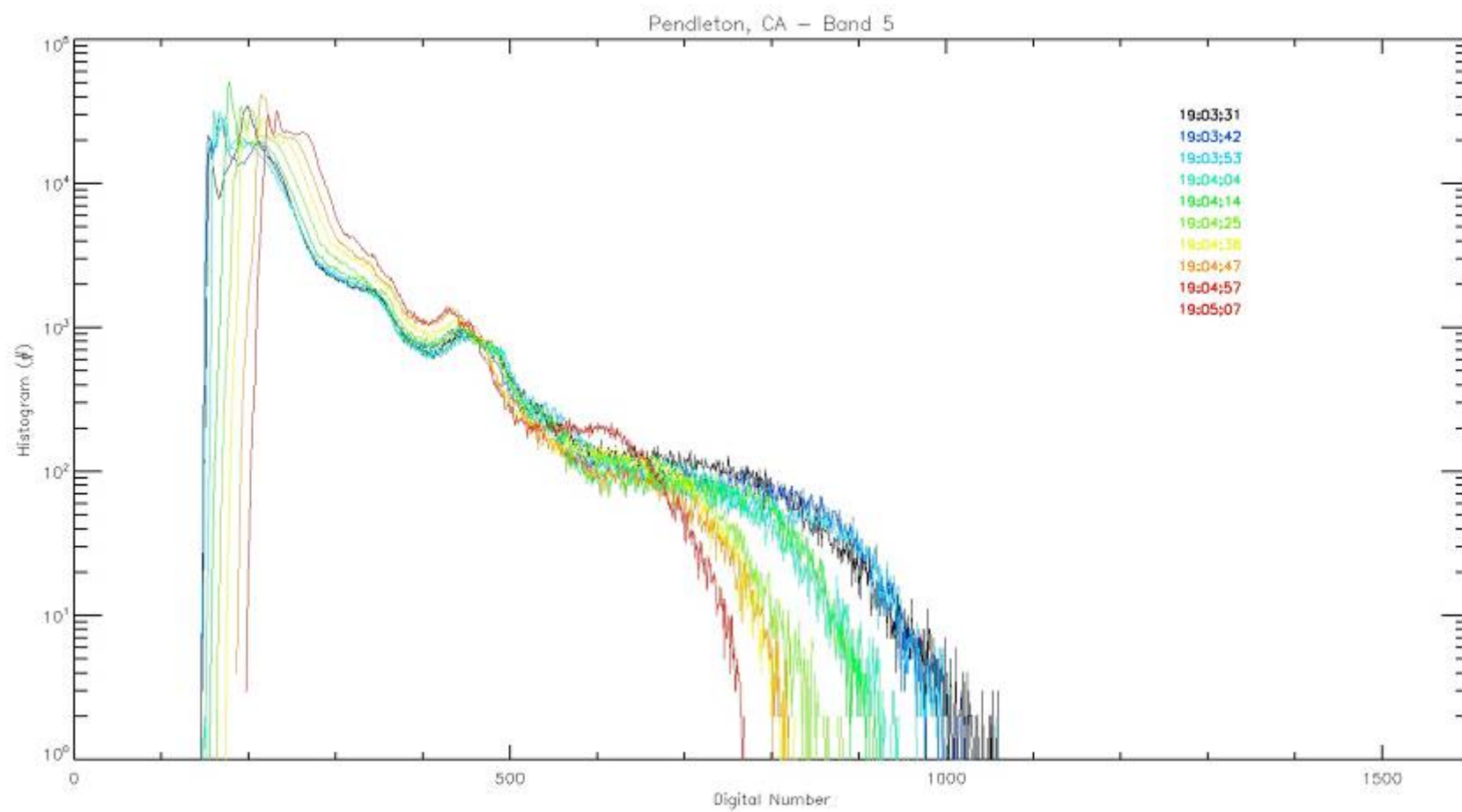


Figure 80. Histogram Shift with View Angle: Pendleton, CA (Band 5)

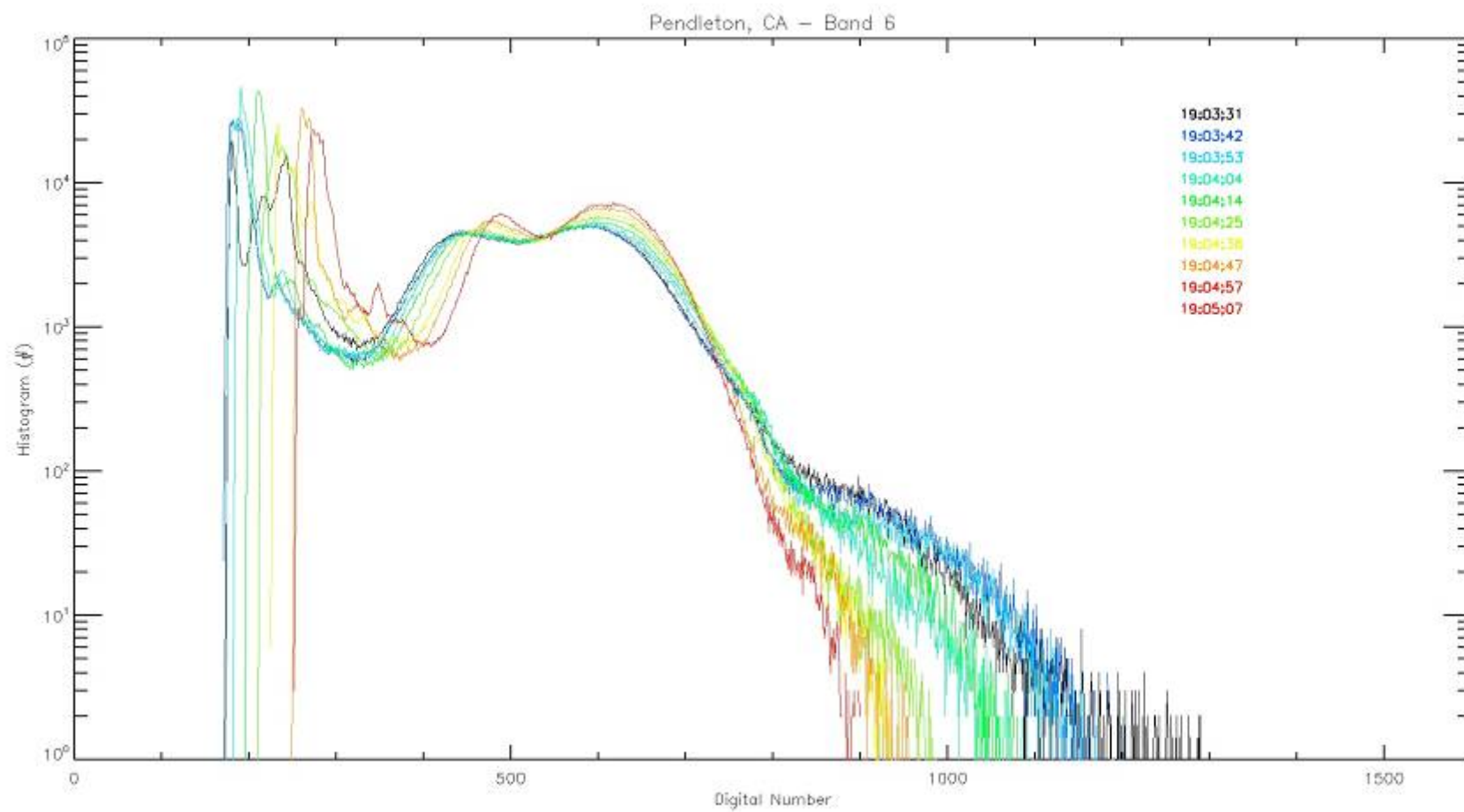


Figure 81. Histogram Shift with View Angle: Pendleton, CA (Band 6)

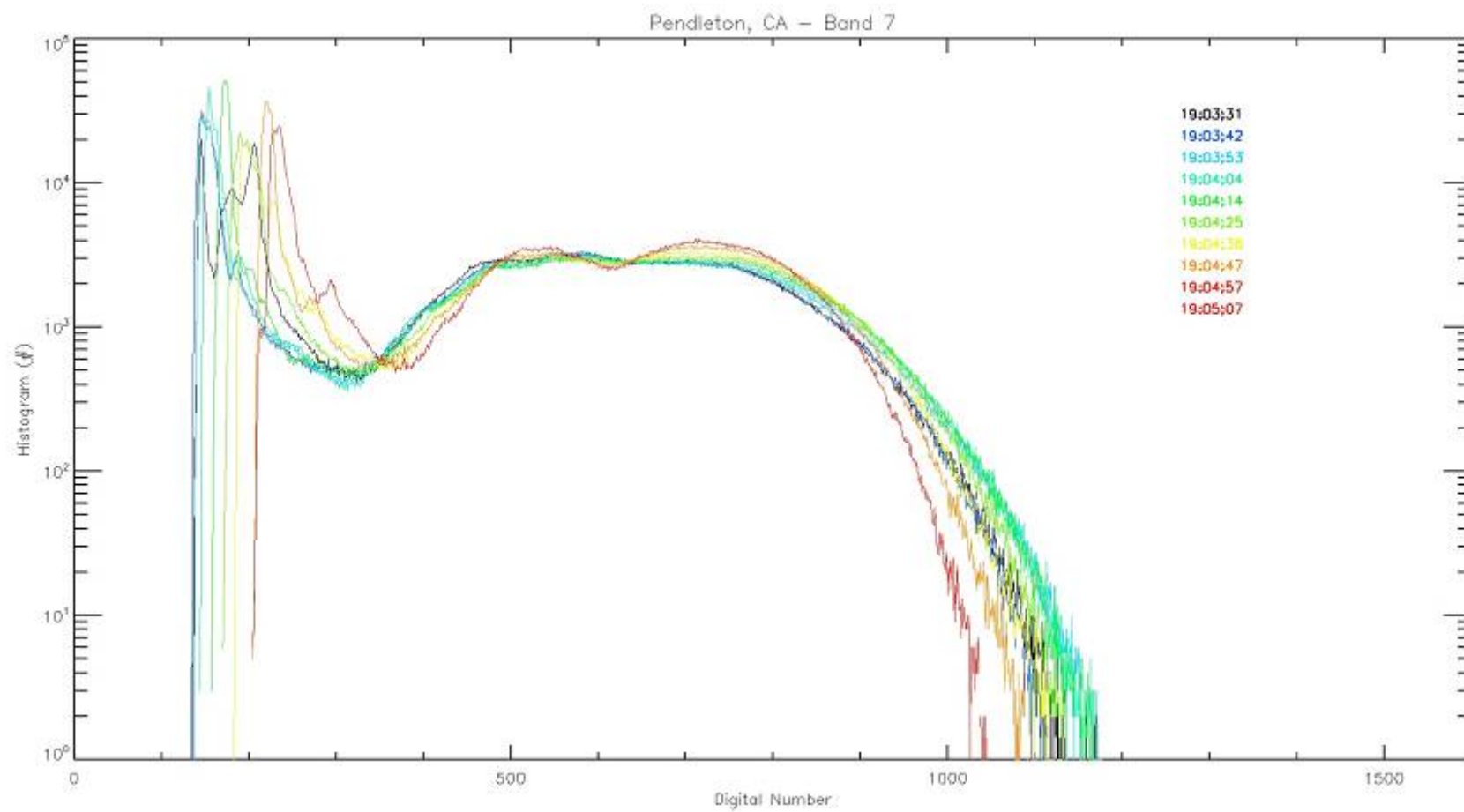


Figure 82. Histogram Shift with View Angle: Pendleton, CA (Band 7)

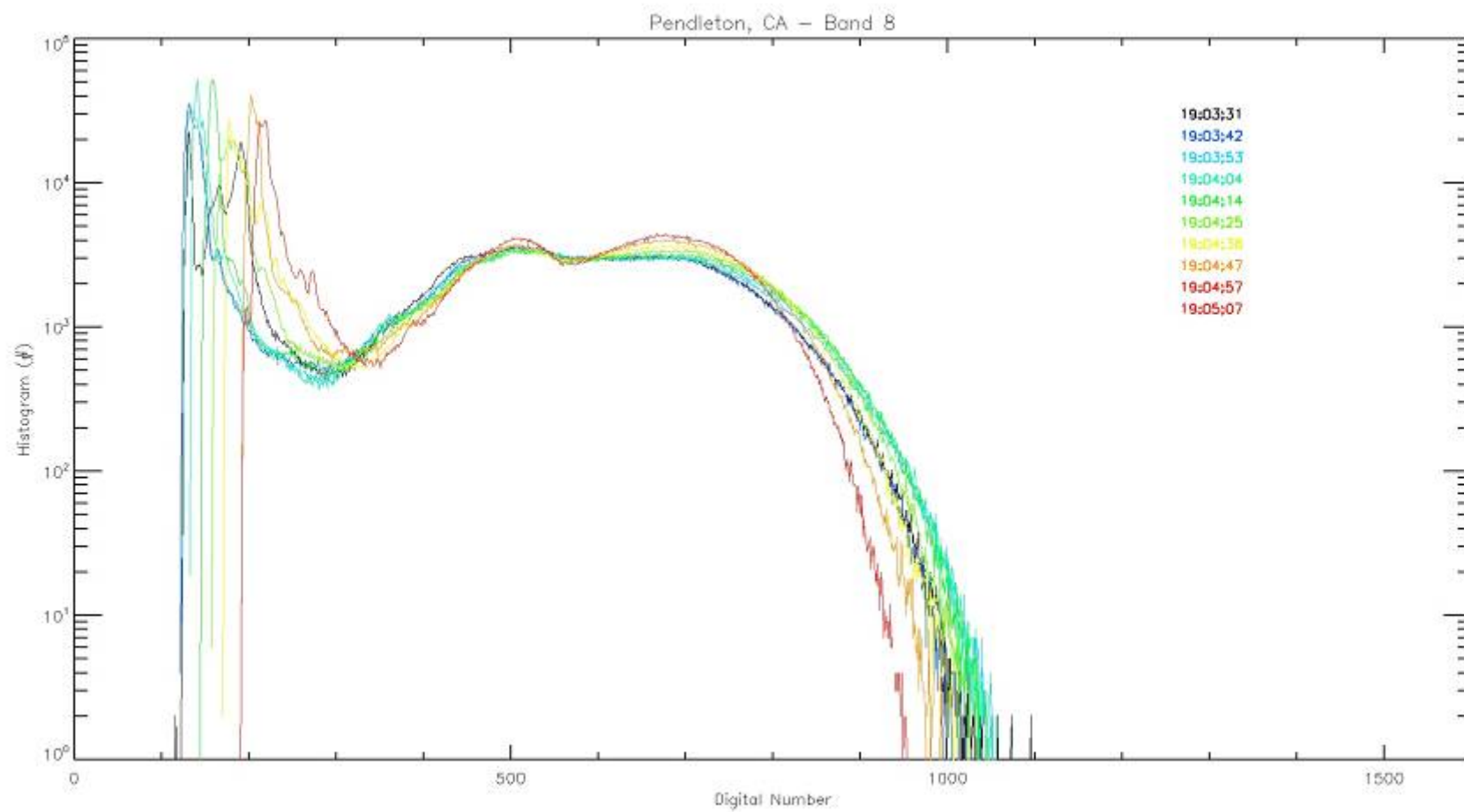


Figure 83. Histogram Shift with View Angle: Pendleton, CA (Band 8)

F. SPECTRAL RADIANCE DISPLAYING VARIANCE WITH WAVELENGTH AND VIEW ANGLE (DUCK, NC)

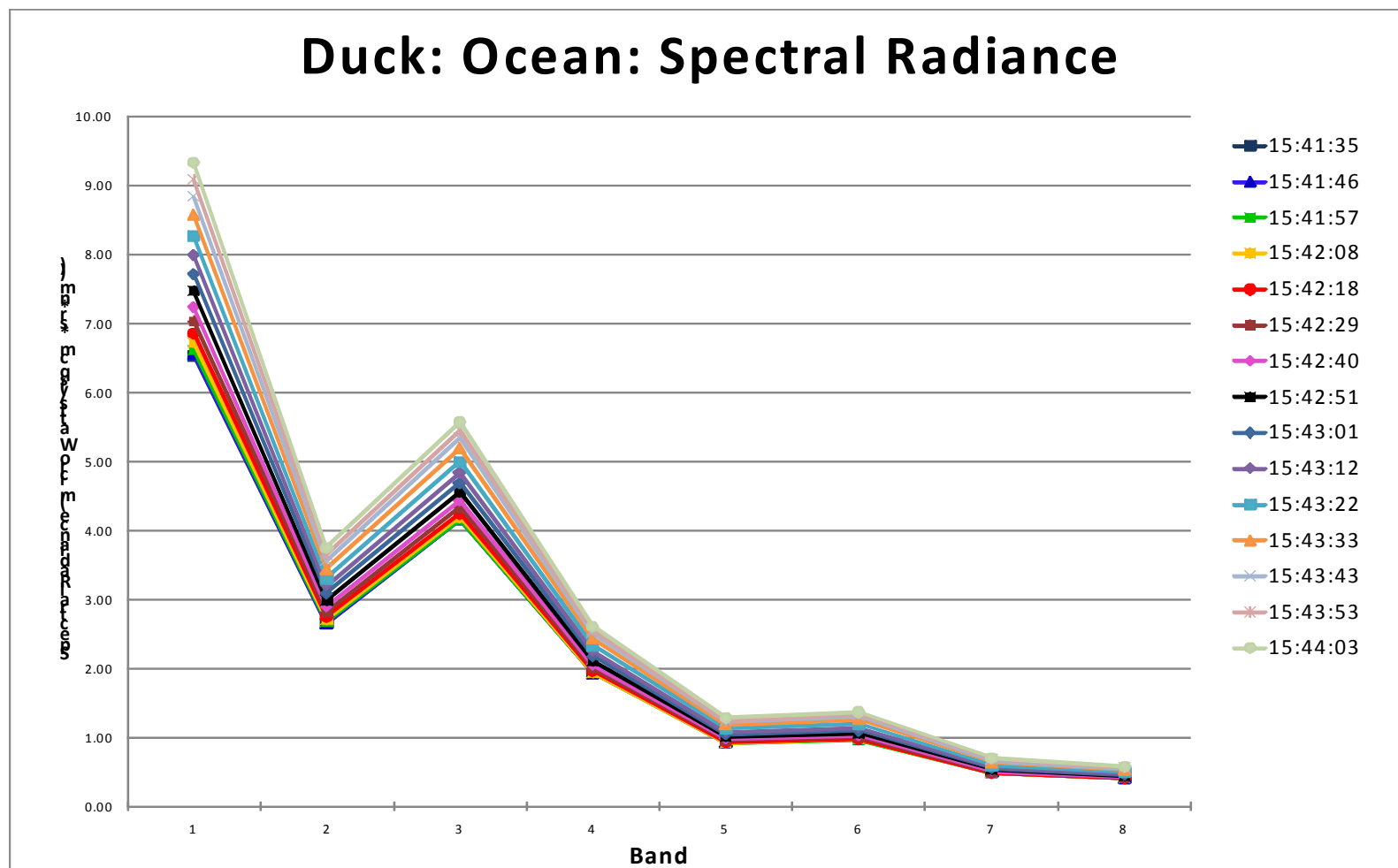


Figure 84. Spectral Radiance Displaying Variance with Wavelength and View Angle: Duck, NC (Ocean ROI)

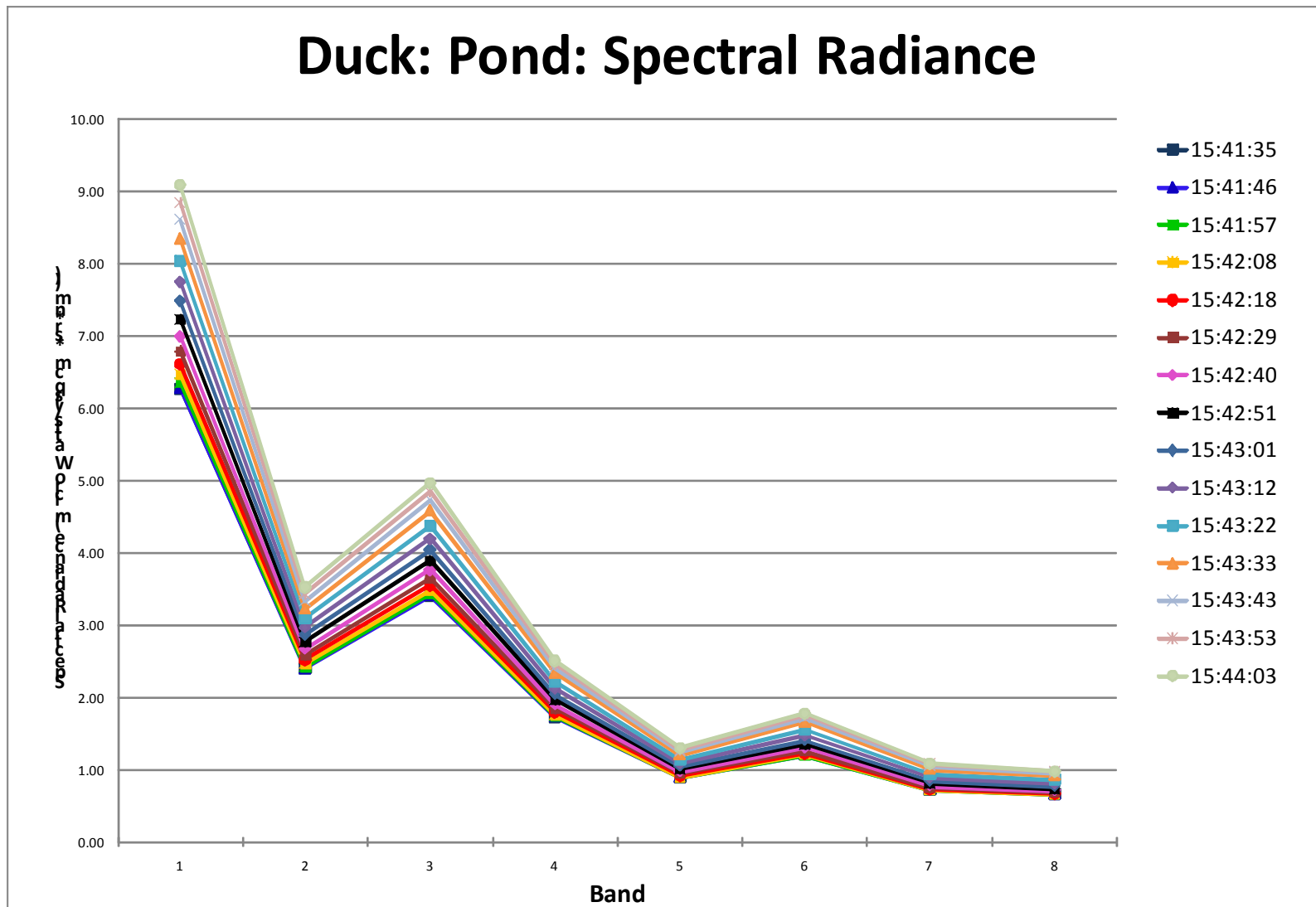


Figure 85. Spectral Radiance Displaying Variance with Wavelength and View Angle: Duck, NC (Pond ROI)

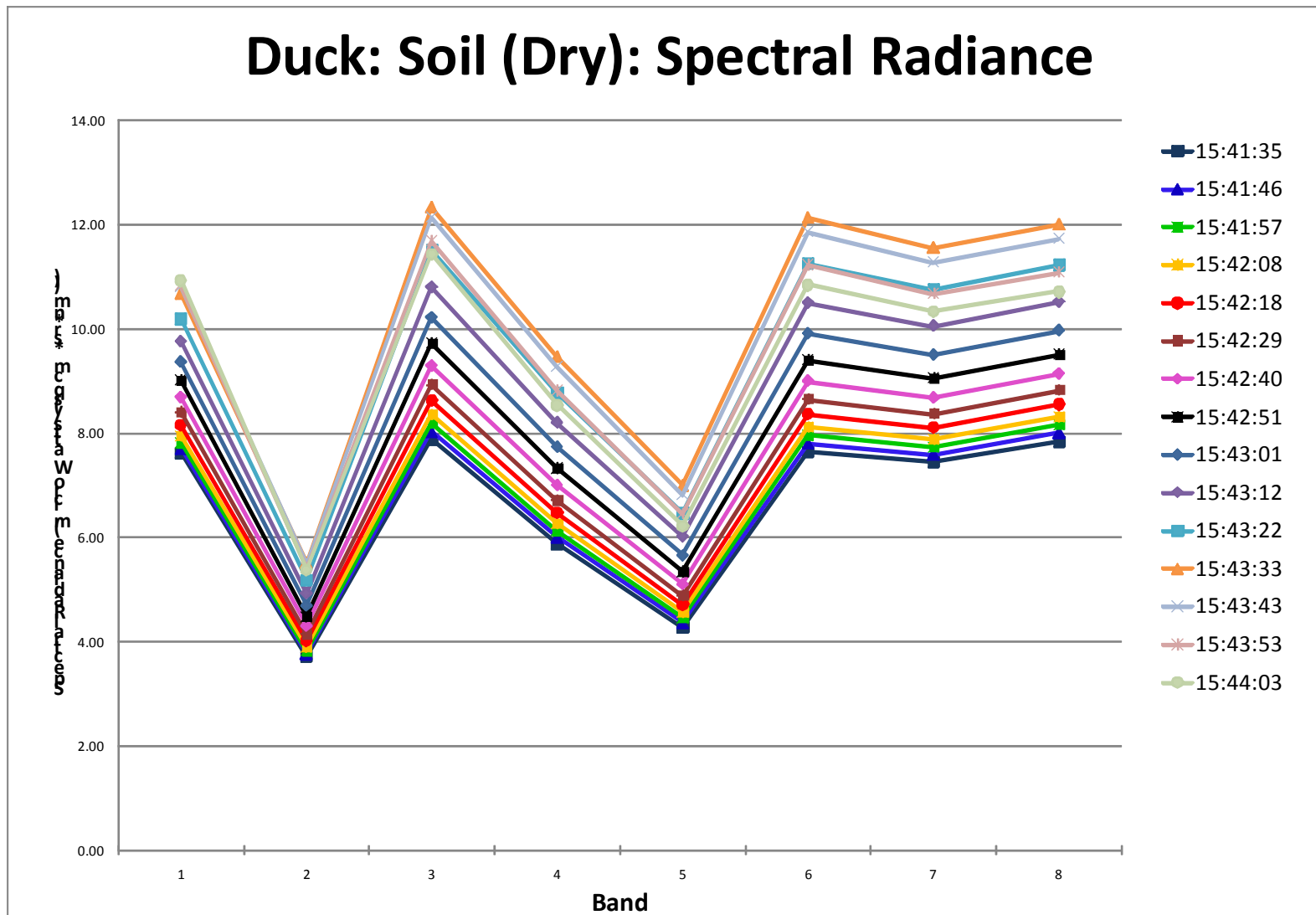


Figure 86. Spectral Radiance Displaying Variance with Wavelength and View Angle: Duck, NC (Soil (Dry) ROI)

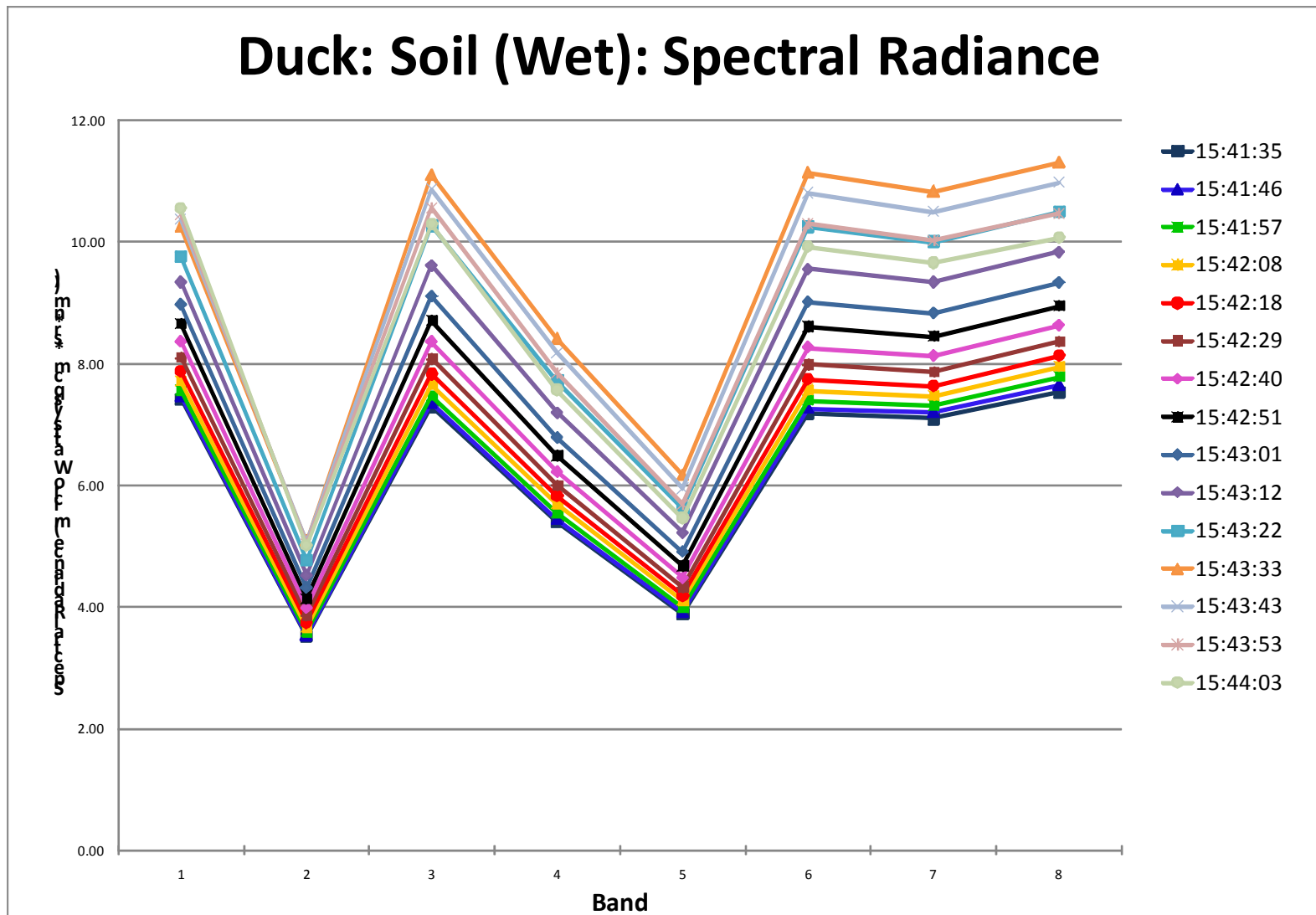


Figure 87. Spectral Radiance Displaying Variance with Wavelength and View Angle: Duck, NC (Soil (Wet) ROI)

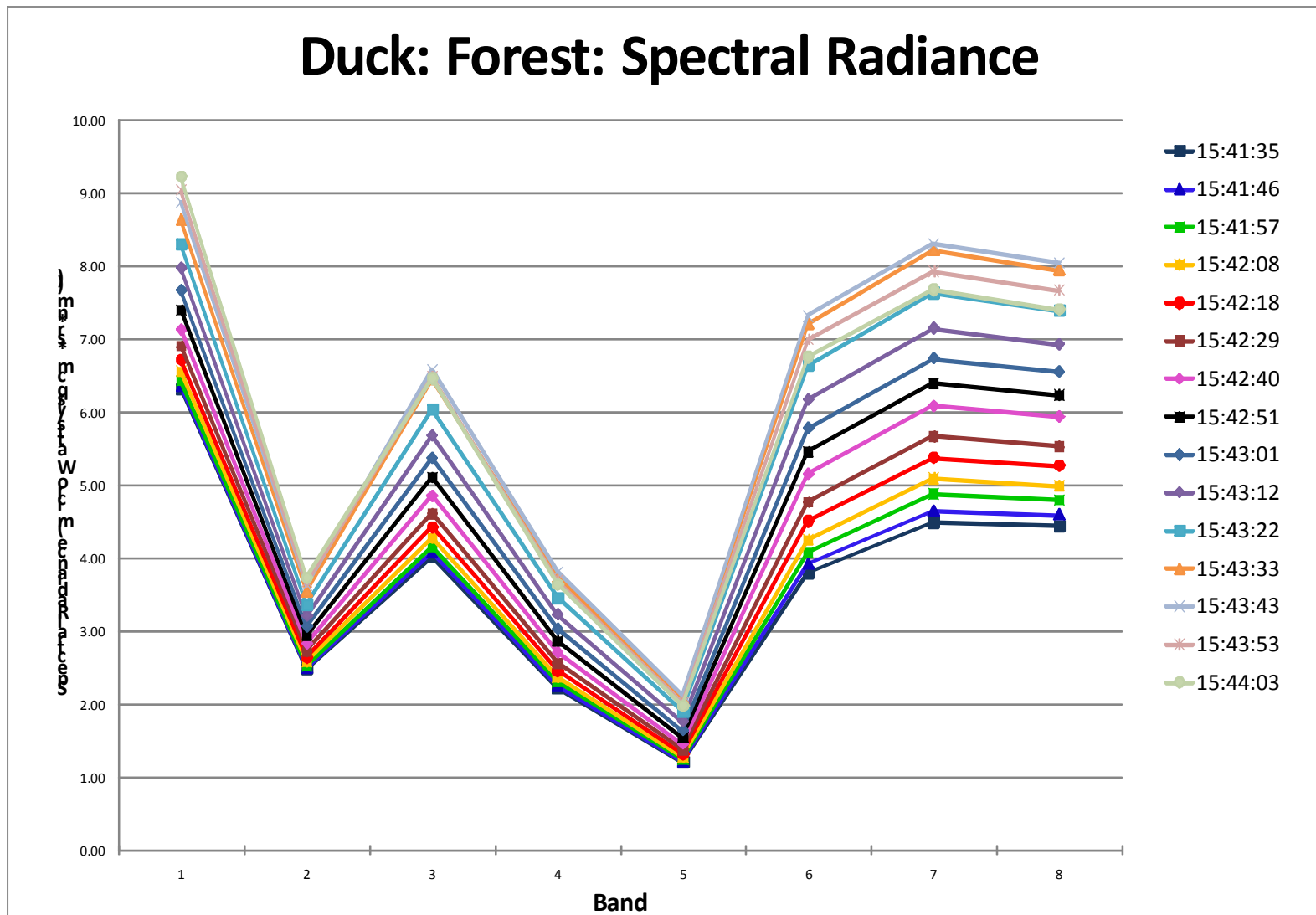


Figure 88. Spectral Radiance Displaying Variance with Wavelength and View Angle: Duck, NC (Forest ROI)

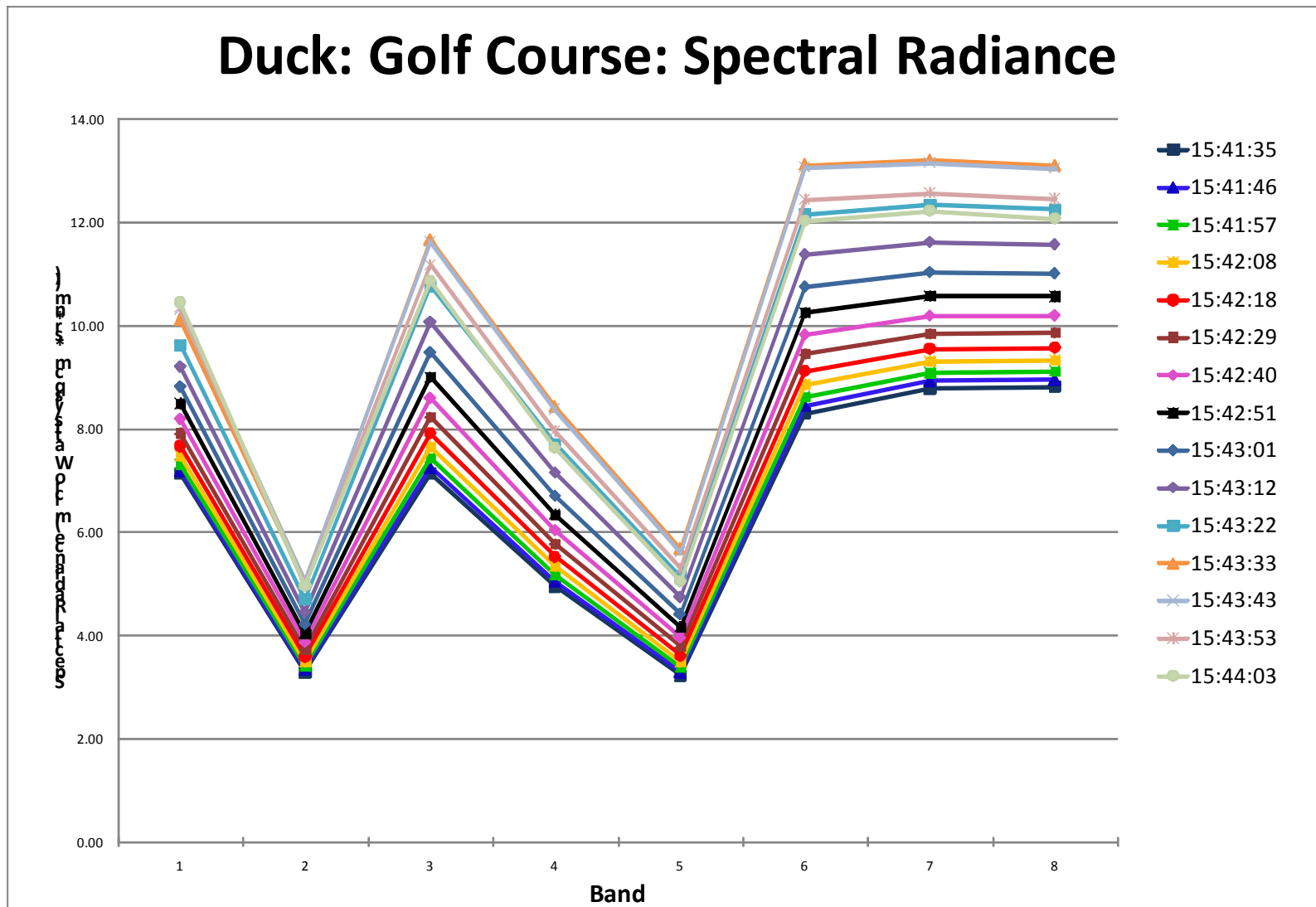


Figure 89. Spectral Radiance Displaying Variance with Wavelength and View Angle: Duck, NC (Golf Course ROI)

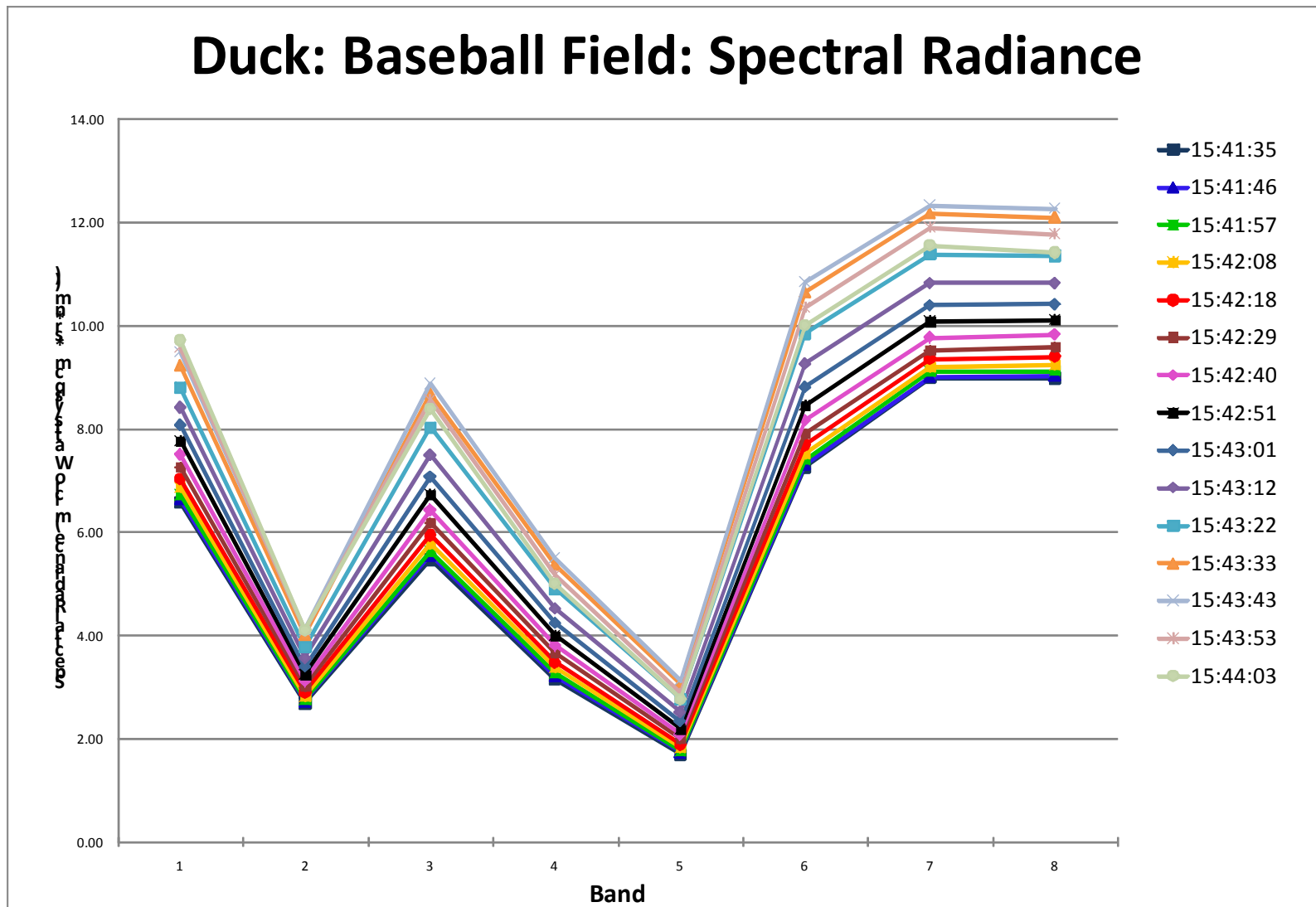


Figure 90. Spectral Radiance Displaying Variance with Wavelength and View Angle: Duck, NC (Baseball Field ROI)

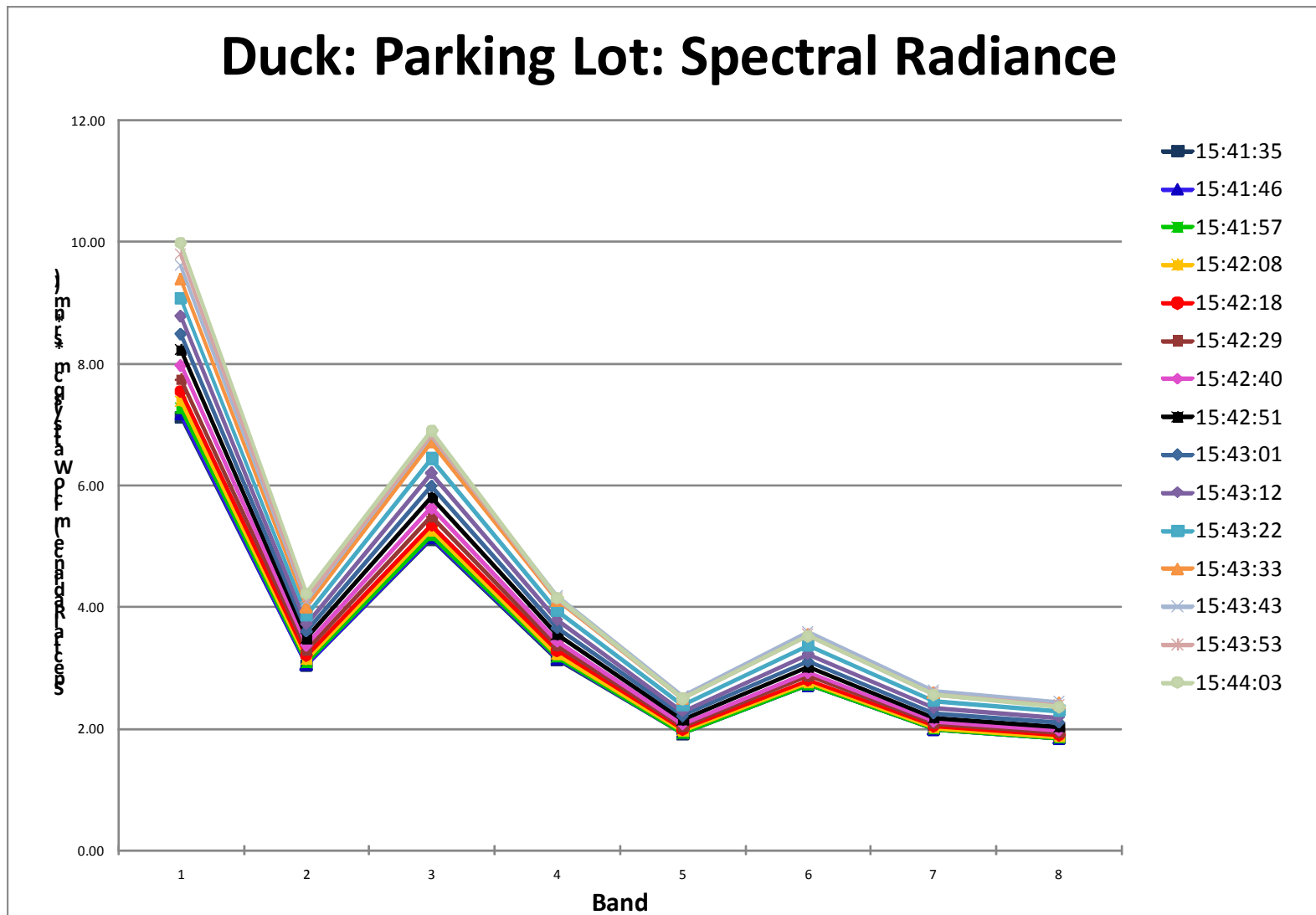


Figure 91. Spectral Radiance Displaying Variance with Wavelength and View Angle: Duck, NC (Parking Lot ROI)

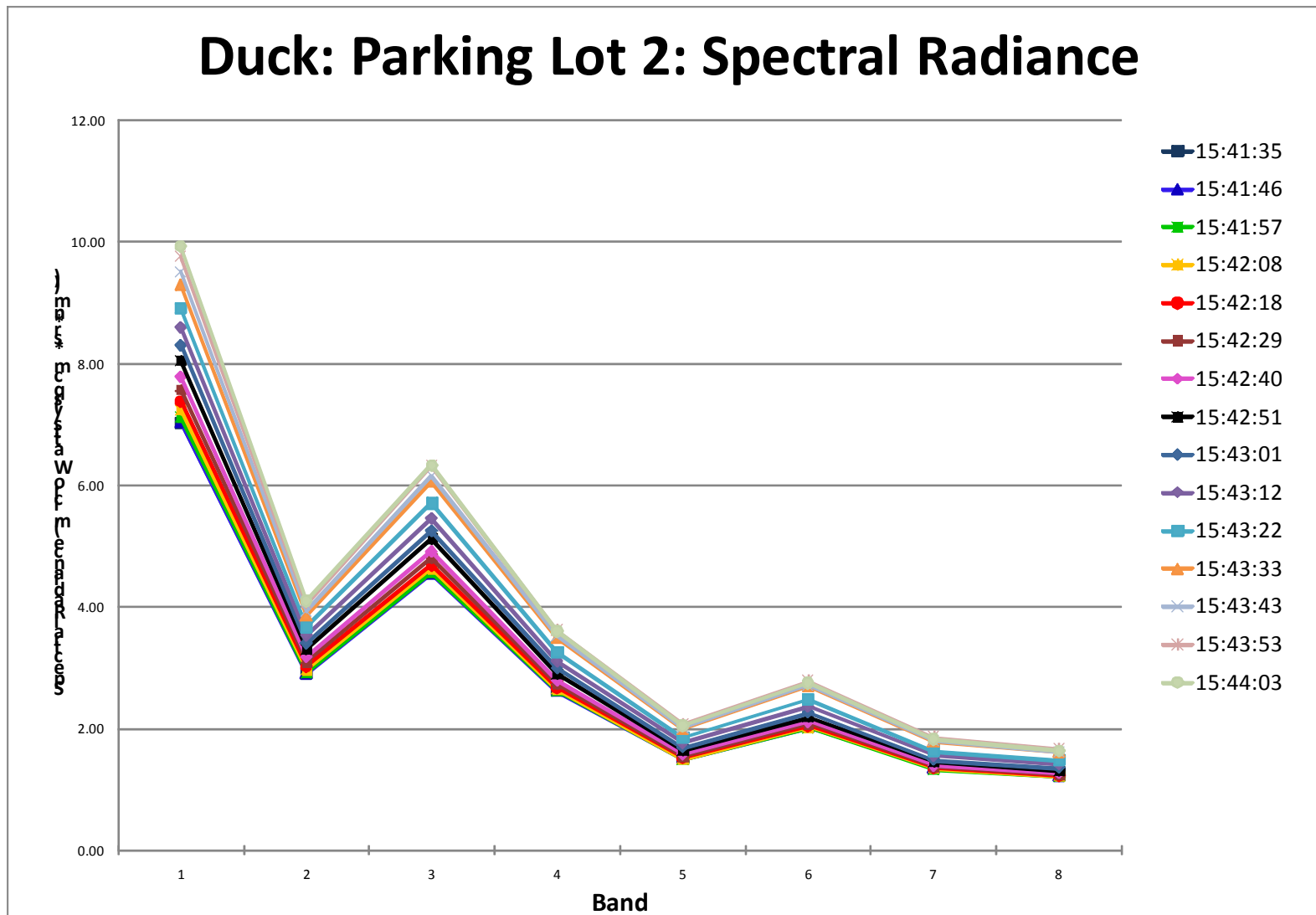


Figure 92. Spectral Radiance Displaying Variance with Wavelength and View Angle: Duck, NC (Parking Lot 2 ROI)

Duck: Roof Top: Spectral Radiance

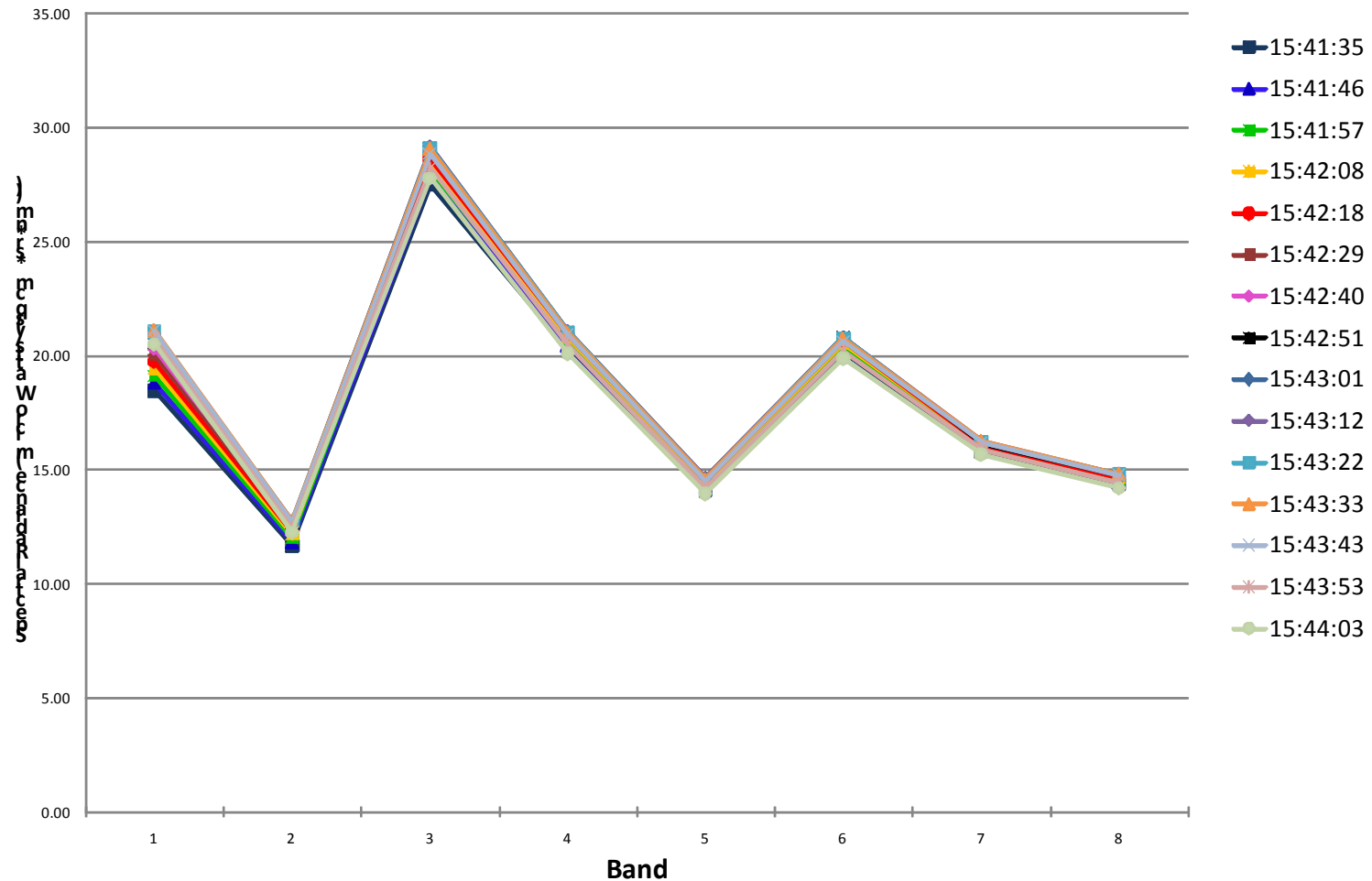


Figure 93. Spectral Radiance Displaying Variance with Wavelength and View Angle: Duck, NC (Roof Top ROI)

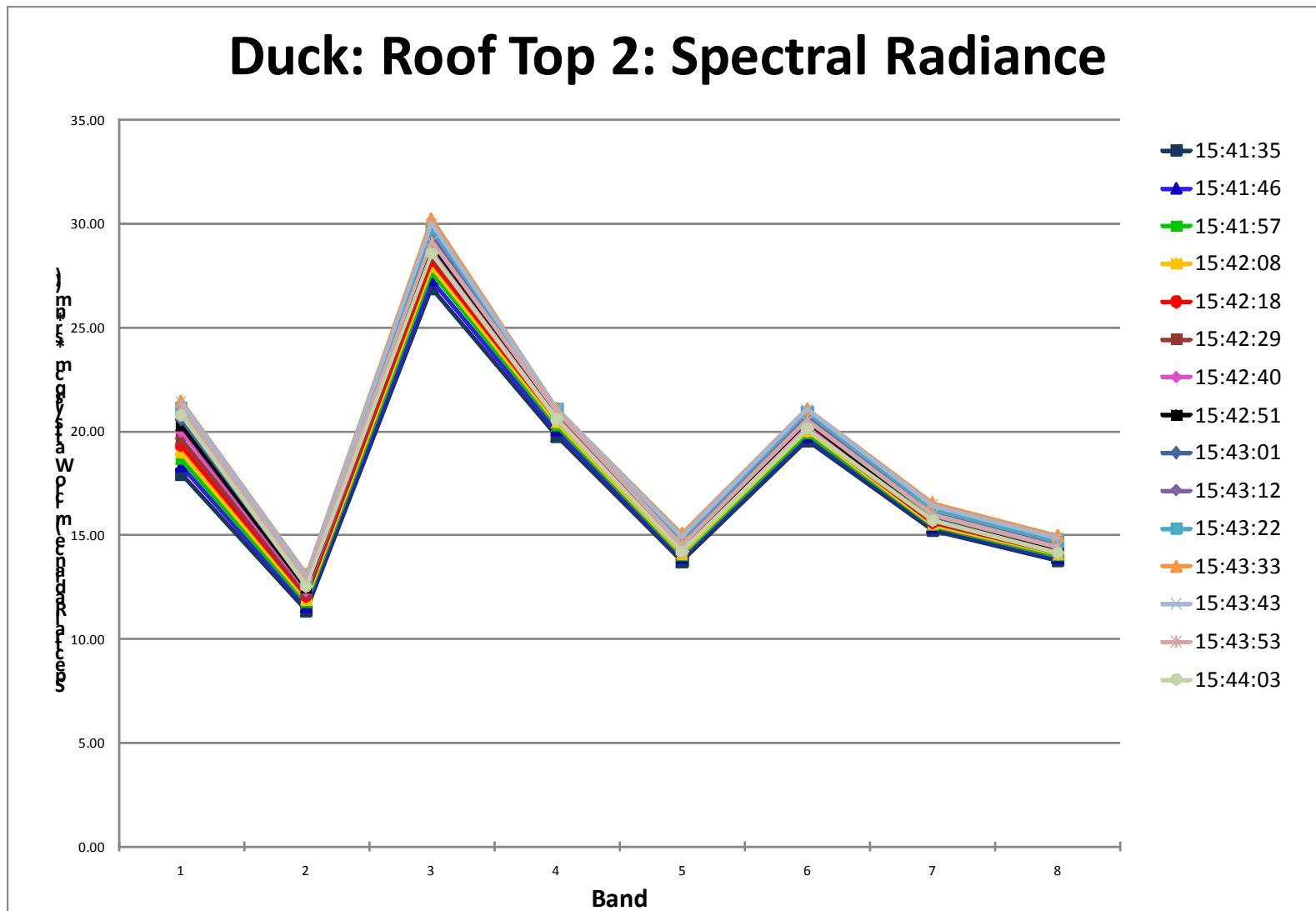


Figure 94. Spectral Radiance Displaying Variance with Wavelength and View Angle: Duck, NC (Roof Top 2 ROI)

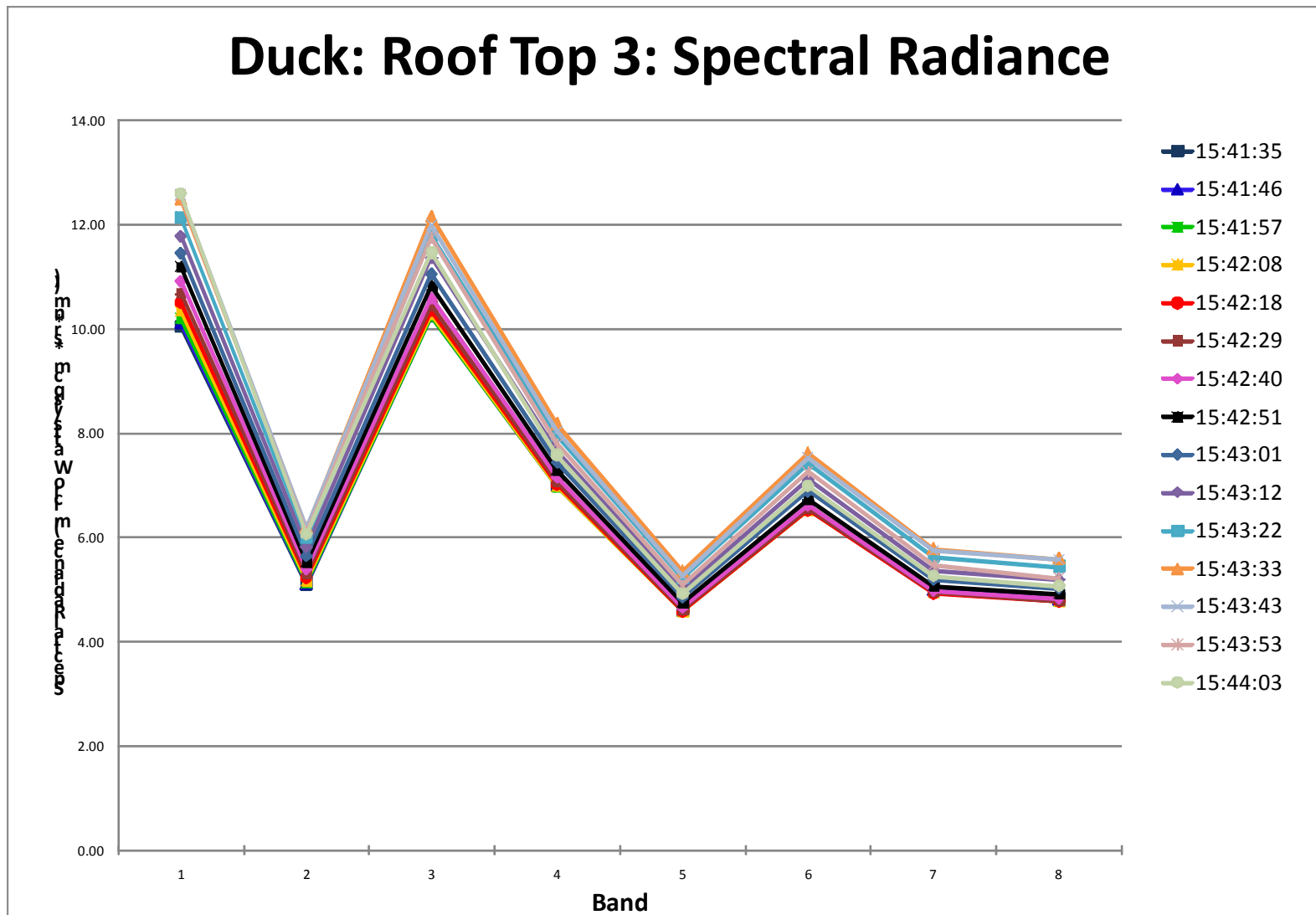


Figure 95. Spectral Radiance Displaying Variance with Wavelength and View Angle: Duck, NC (Roof Top 3 ROI)

G. SPECTRAL RADIANCE DISPLAYING VARIANCE WITH WAVELENGTH AND VIEW ANGLE (PENDLETON, CA)

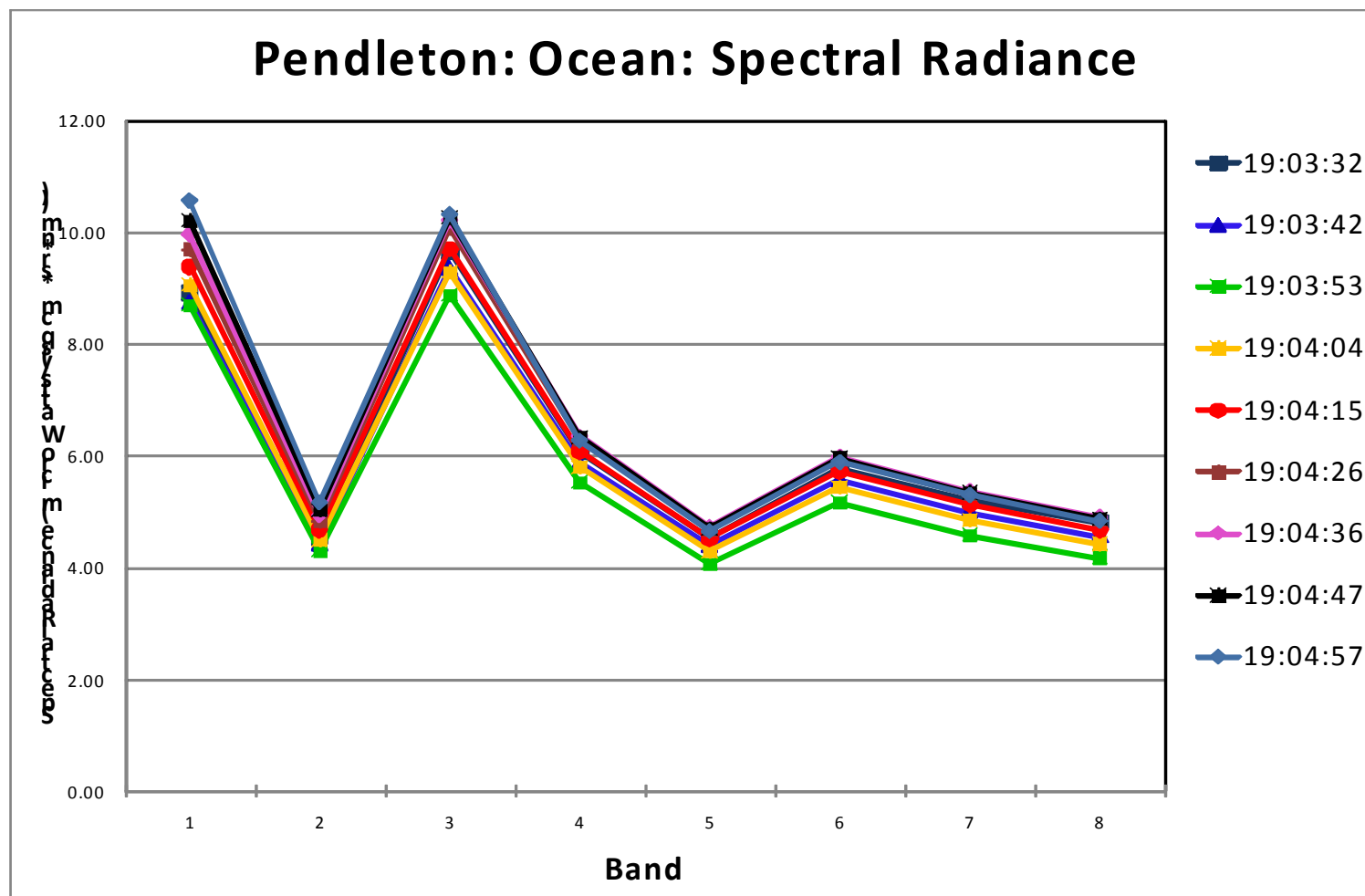


Figure 96. Spectral Radiance Displaying Variance with Wavelength and View Angle: Pendleton, CA (Ocean ROI)

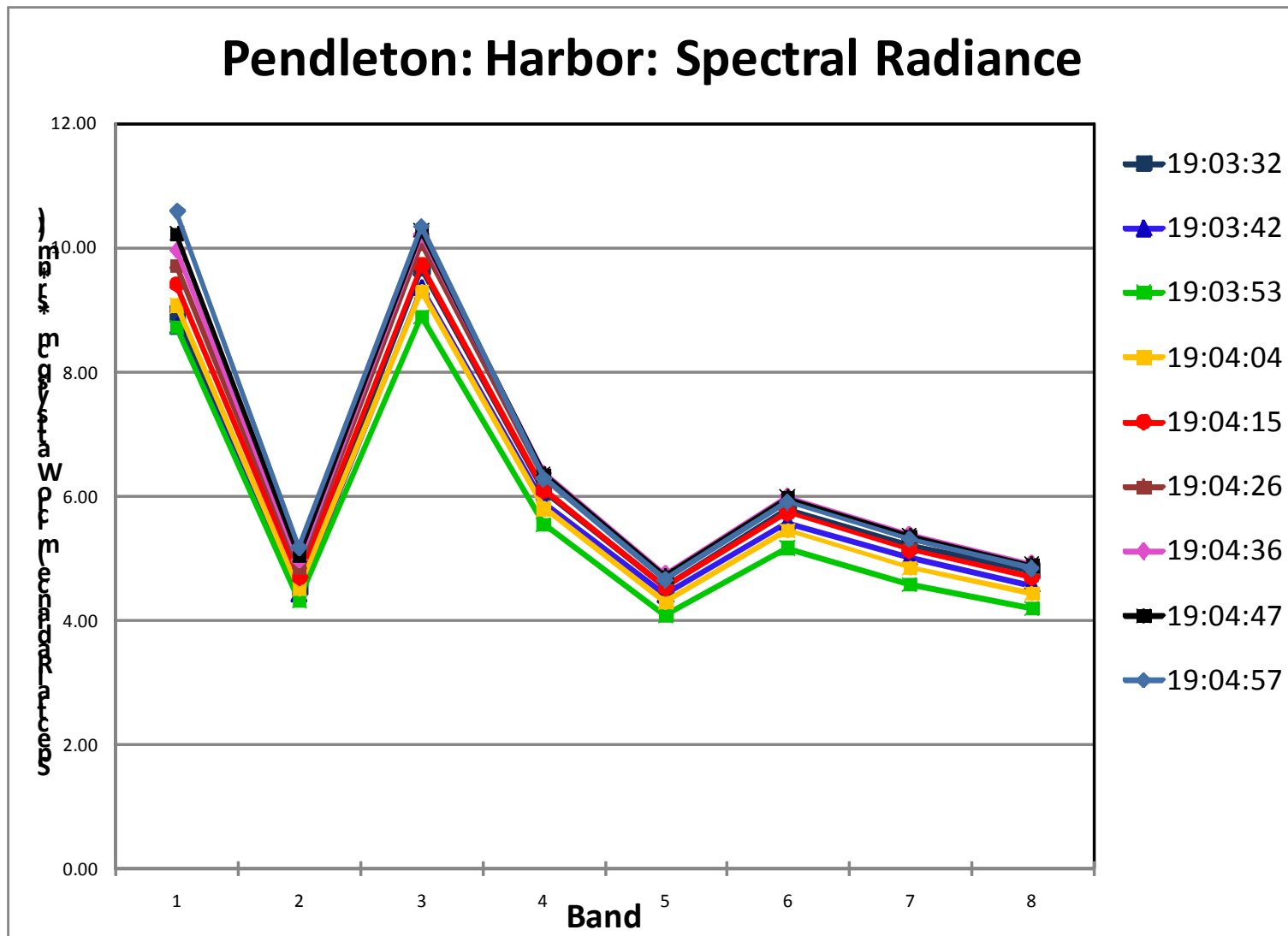


Figure 97. Spectral Radiance Displaying Variance with Wavelength and View Angle: Pendleton, CA (Harbor ROI)

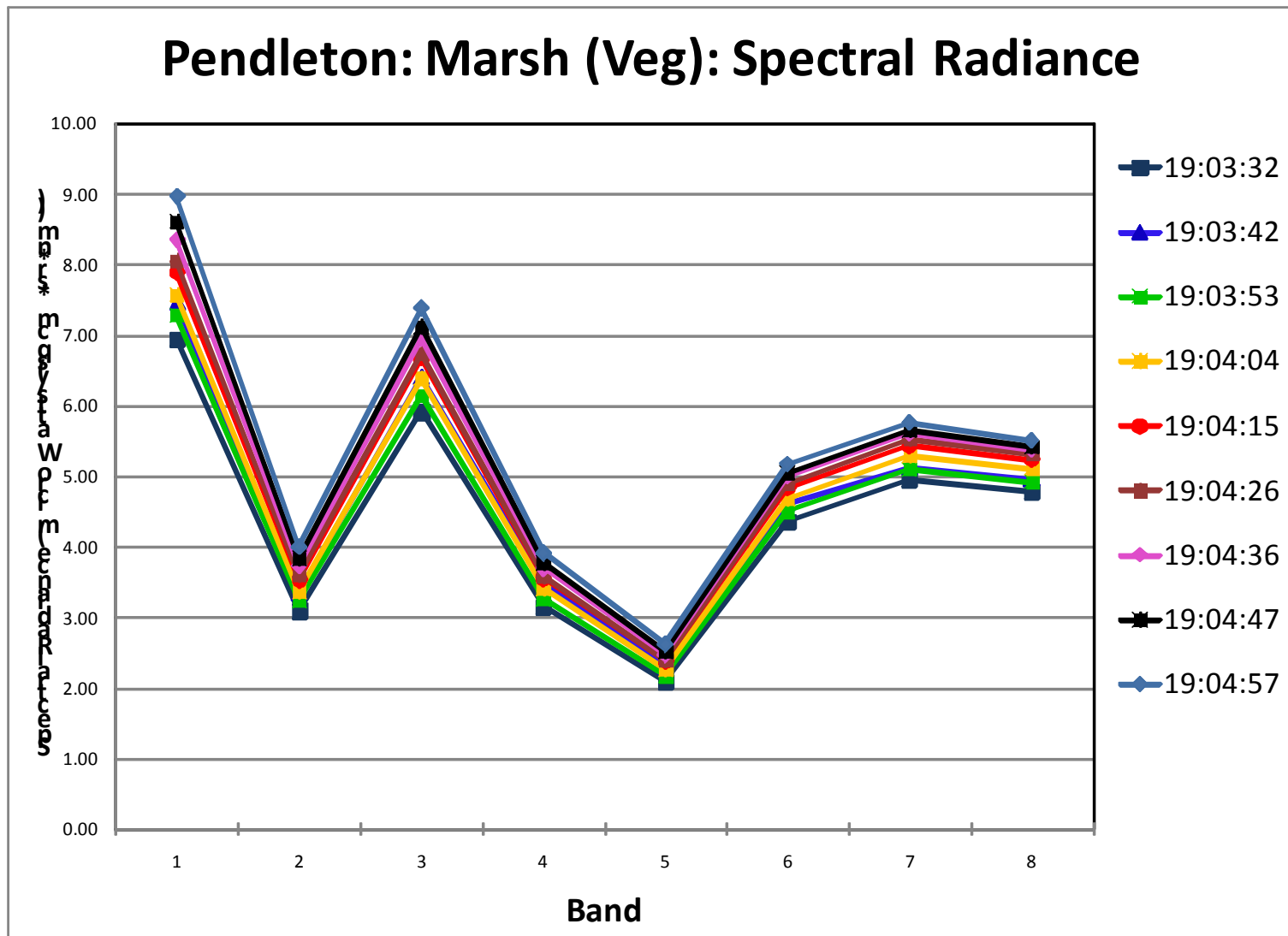


Figure 98. Spectral Radiance Displaying Variance with Wavelength and View Angle: Pendleton, CA (Marsh (Veg) ROI)

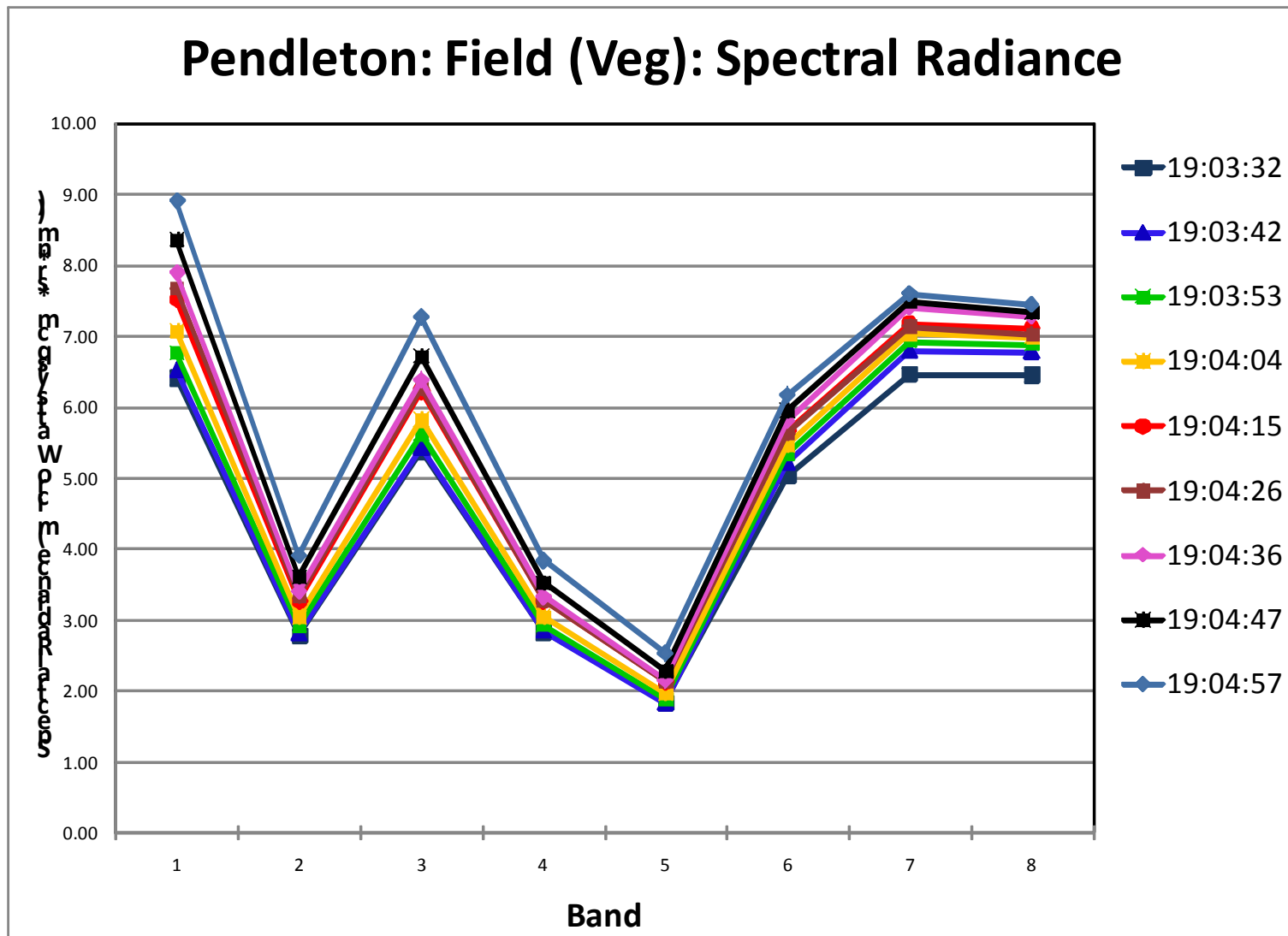


Figure 99. Spectral Radiance Displaying Variance with Wavelength and View Angle: Pendleton, CA (Field (Veg) ROI)

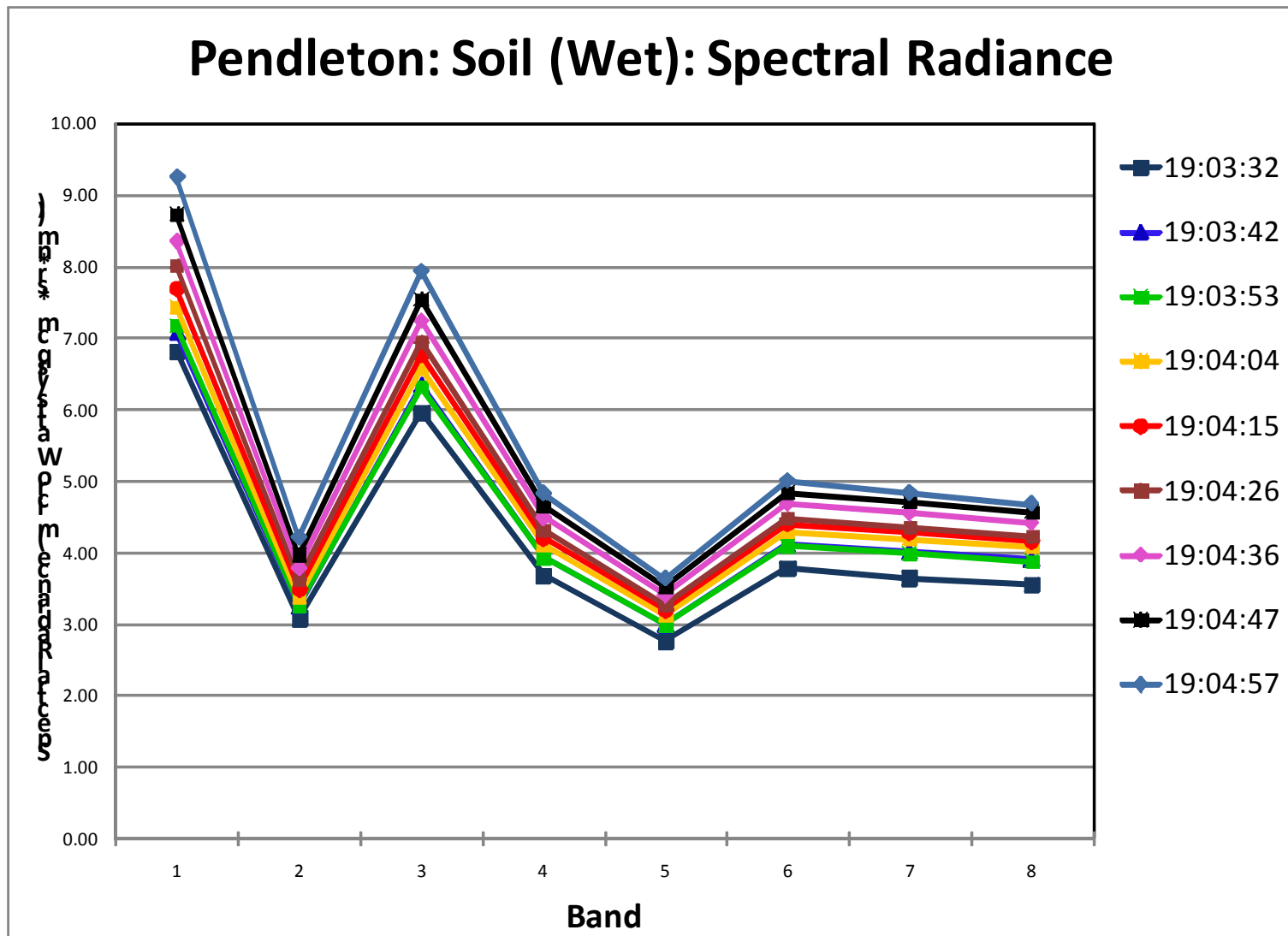


Figure 100. Spectral Radiance Displaying Variance with Wavelength and View Angle: Pendleton, CA (Soil (Wet) ROI)

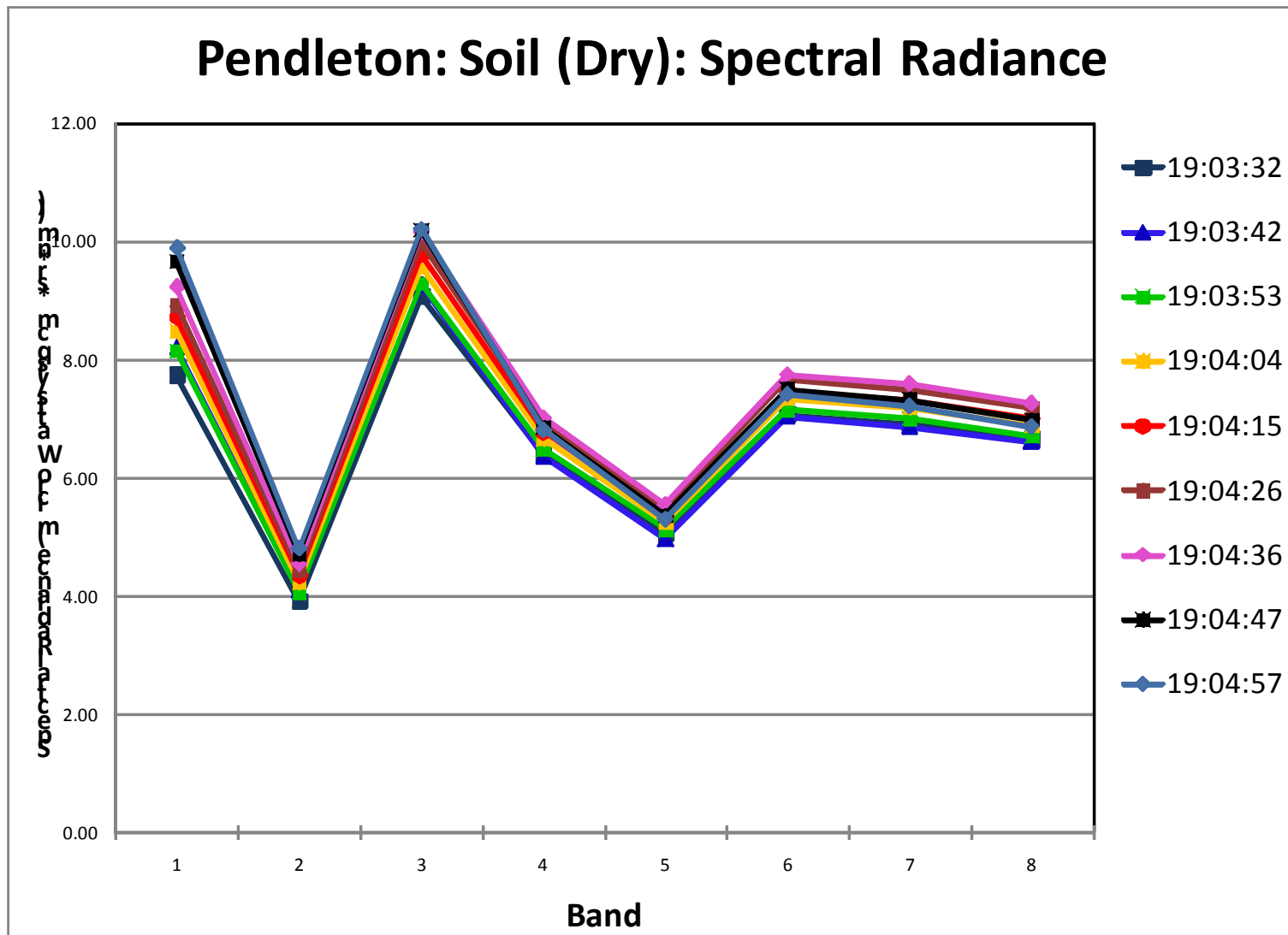


Figure 101. Spectral Radiance Displaying Variance with Wavelength and View Angle: Pendleton, CA (Soil (Dry) ROI)

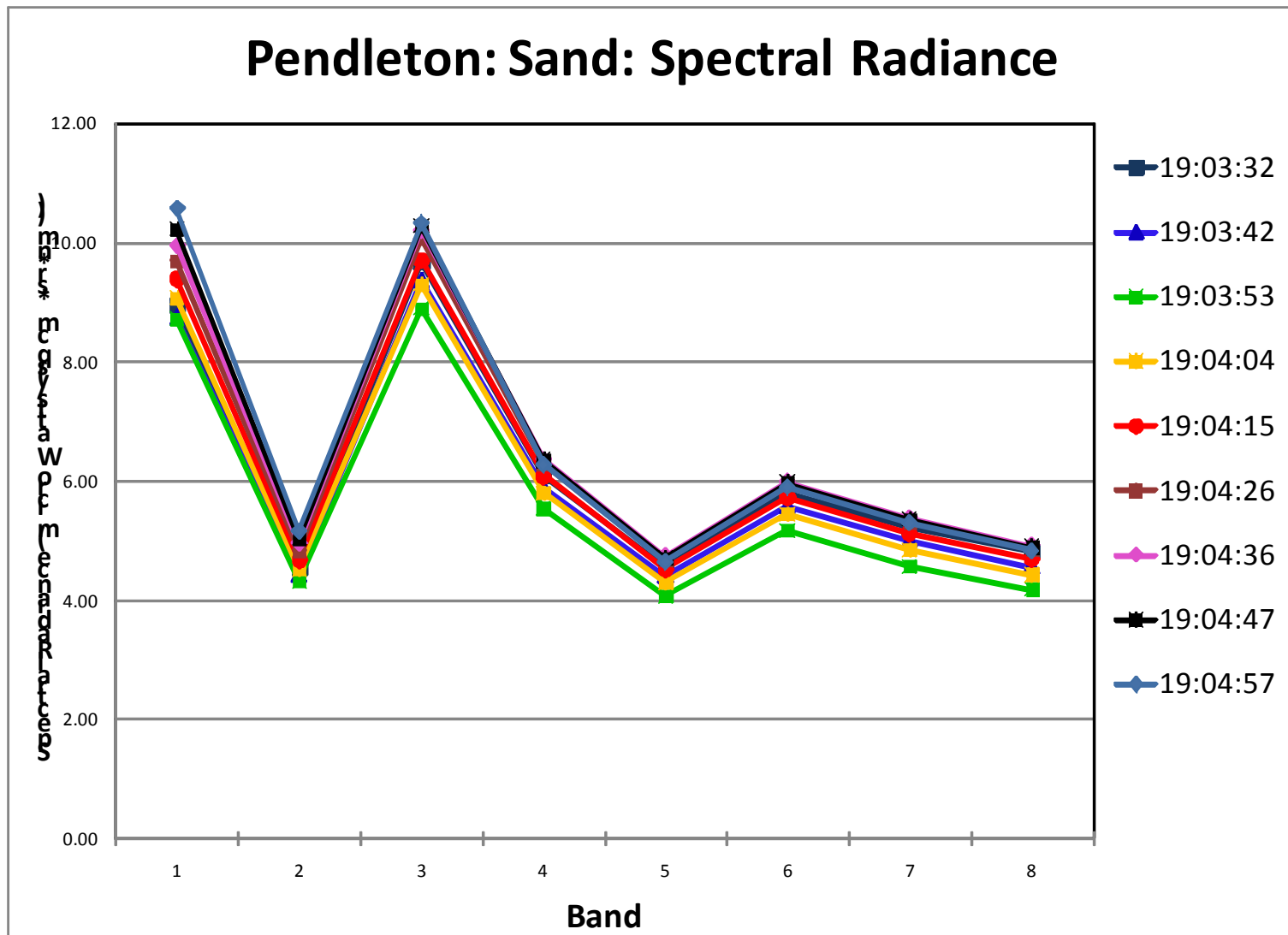


Figure 102. Spectral Radiance Displaying Variance with Wavelength and View Angle: Pendleton, CA (Sand ROI)

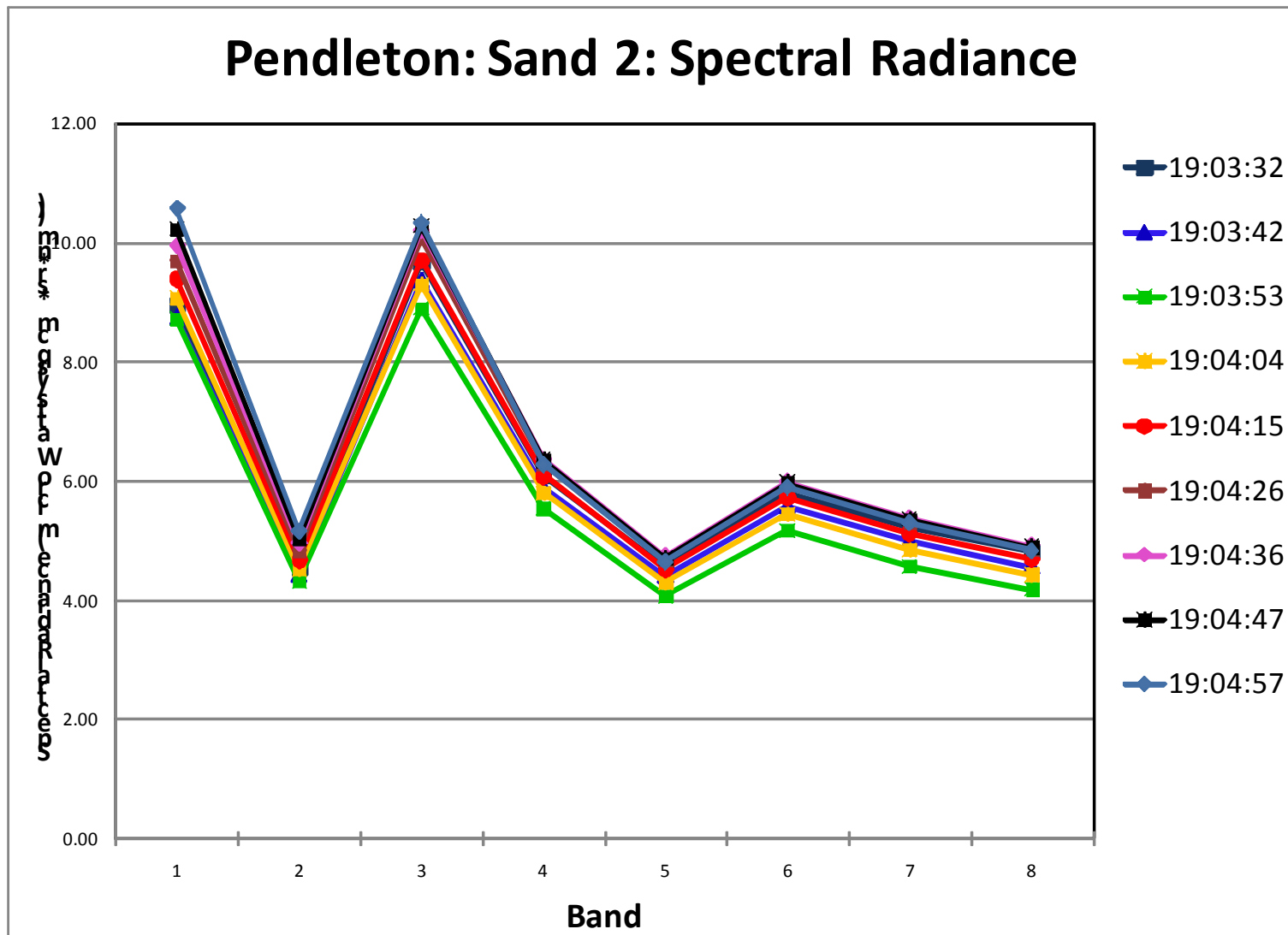


Figure 103. Spectral Radiance Displaying Variance with Wavelength and View Angle: Pendleton, CA (Sand 2 ROI)

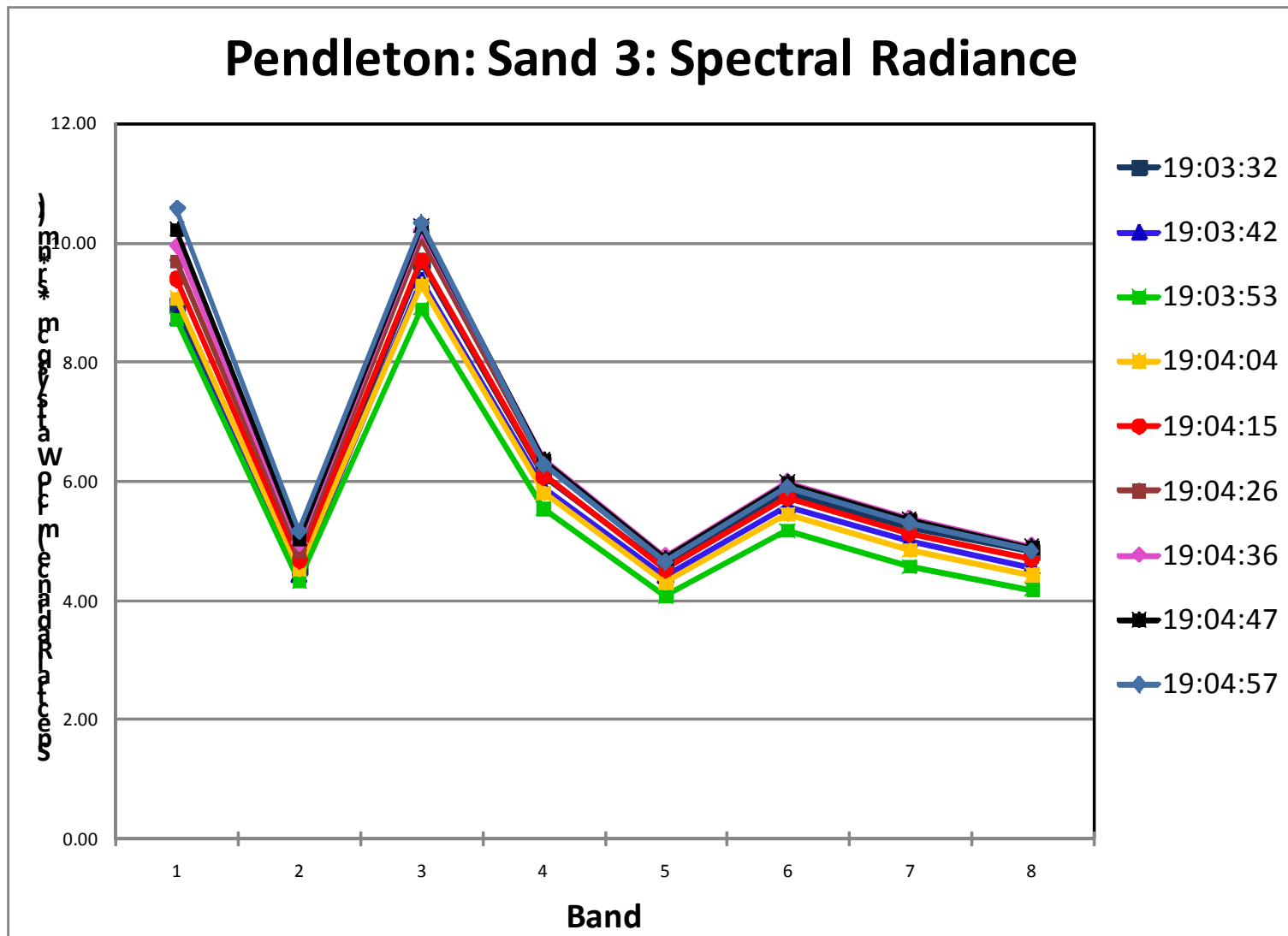


Figure 104. Spectral Radiance Displaying Variance with Wavelength and View Angle: Pendleton, CA (Sand 3 ROI)

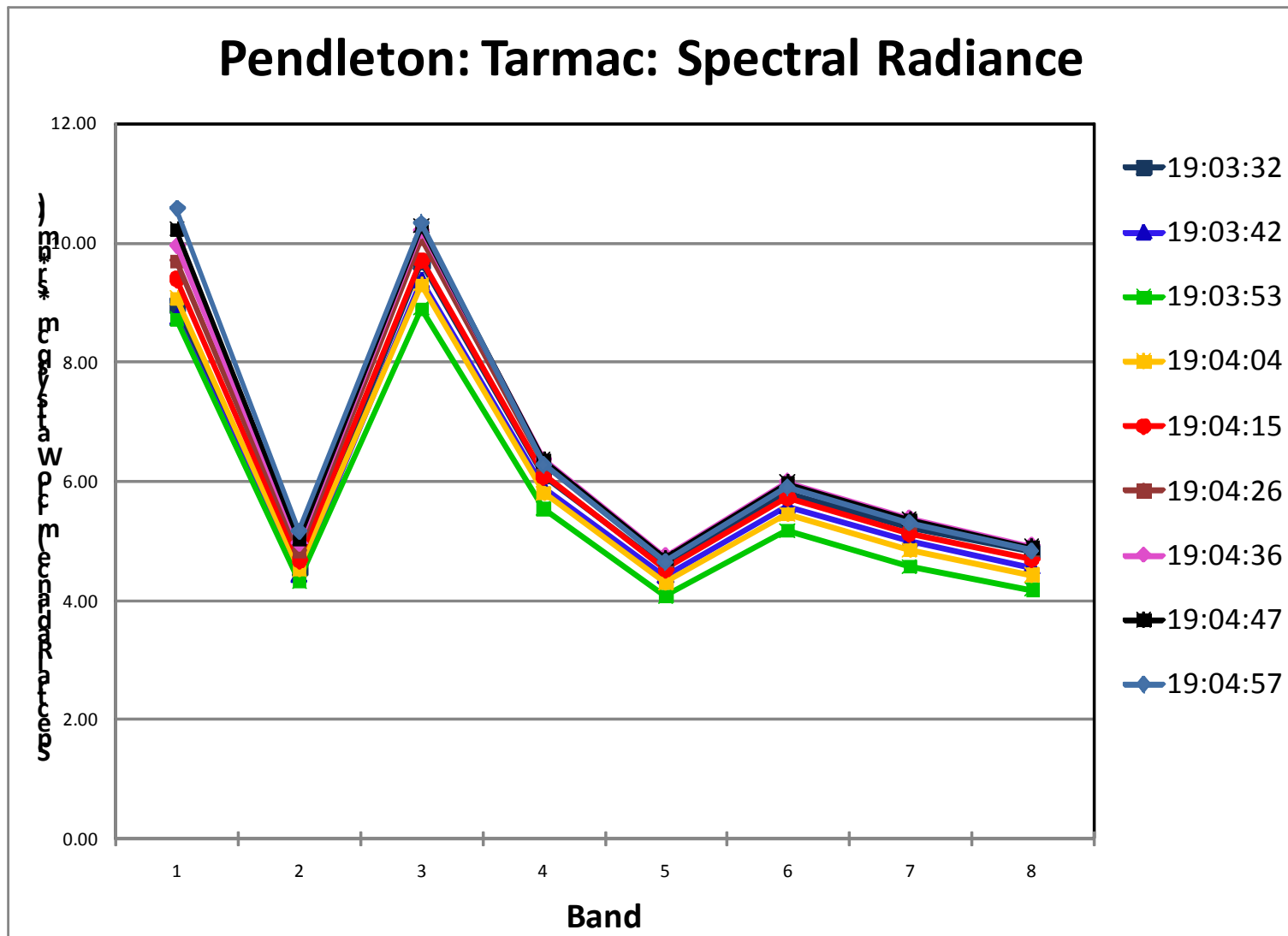


Figure 105. Spectral Radiance Displaying Variance with Wavelength and View Angle: Pendleton, CA (Tarmac ROI)

H. BRDF RESULTS BY SEPARATION ANGLE FOR REGIONS OF INTEREST (DUCK, NC)

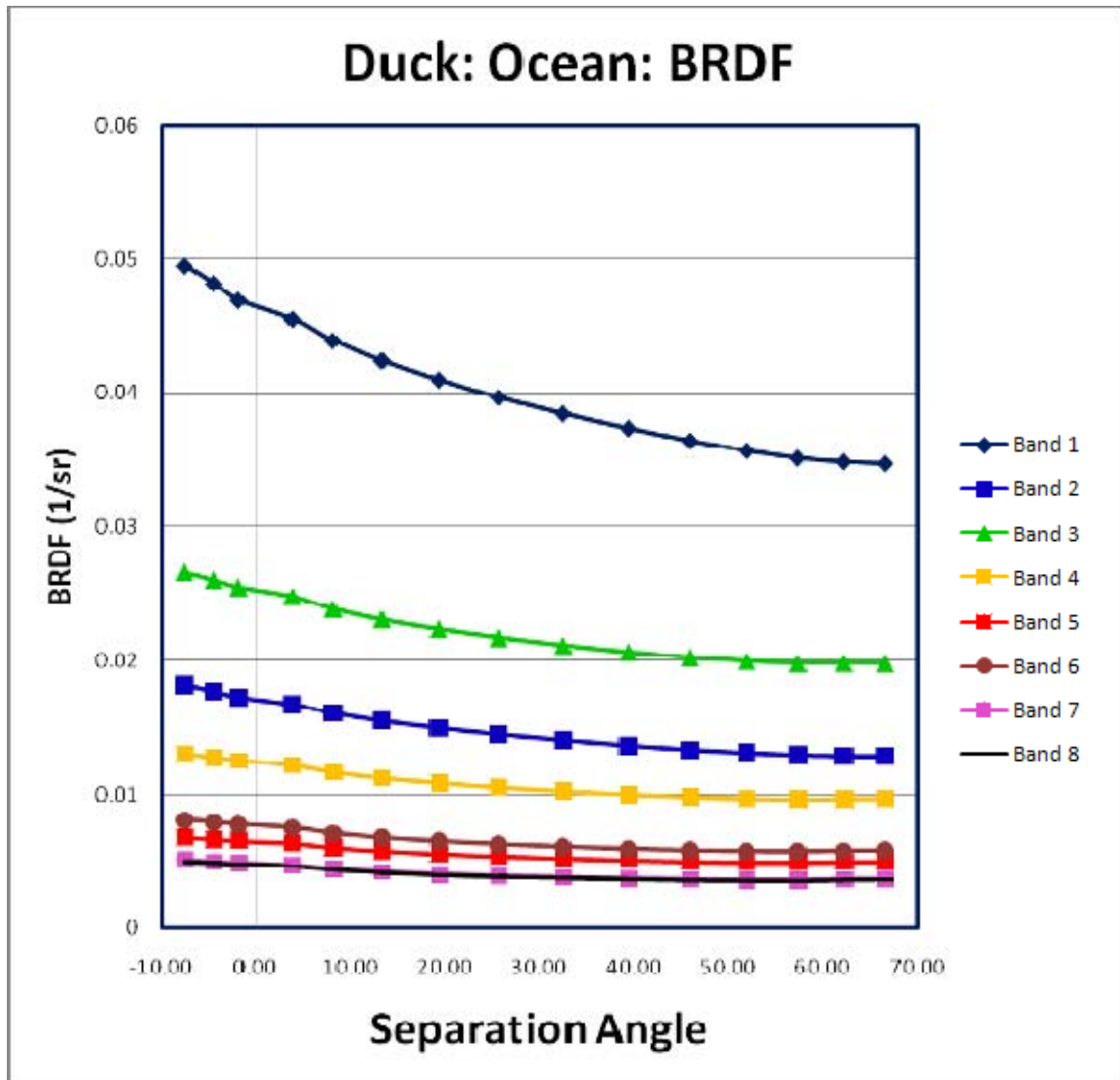


Figure 106. BRDF Results by Separation Angle: Duck, NC (Ocean ROI)

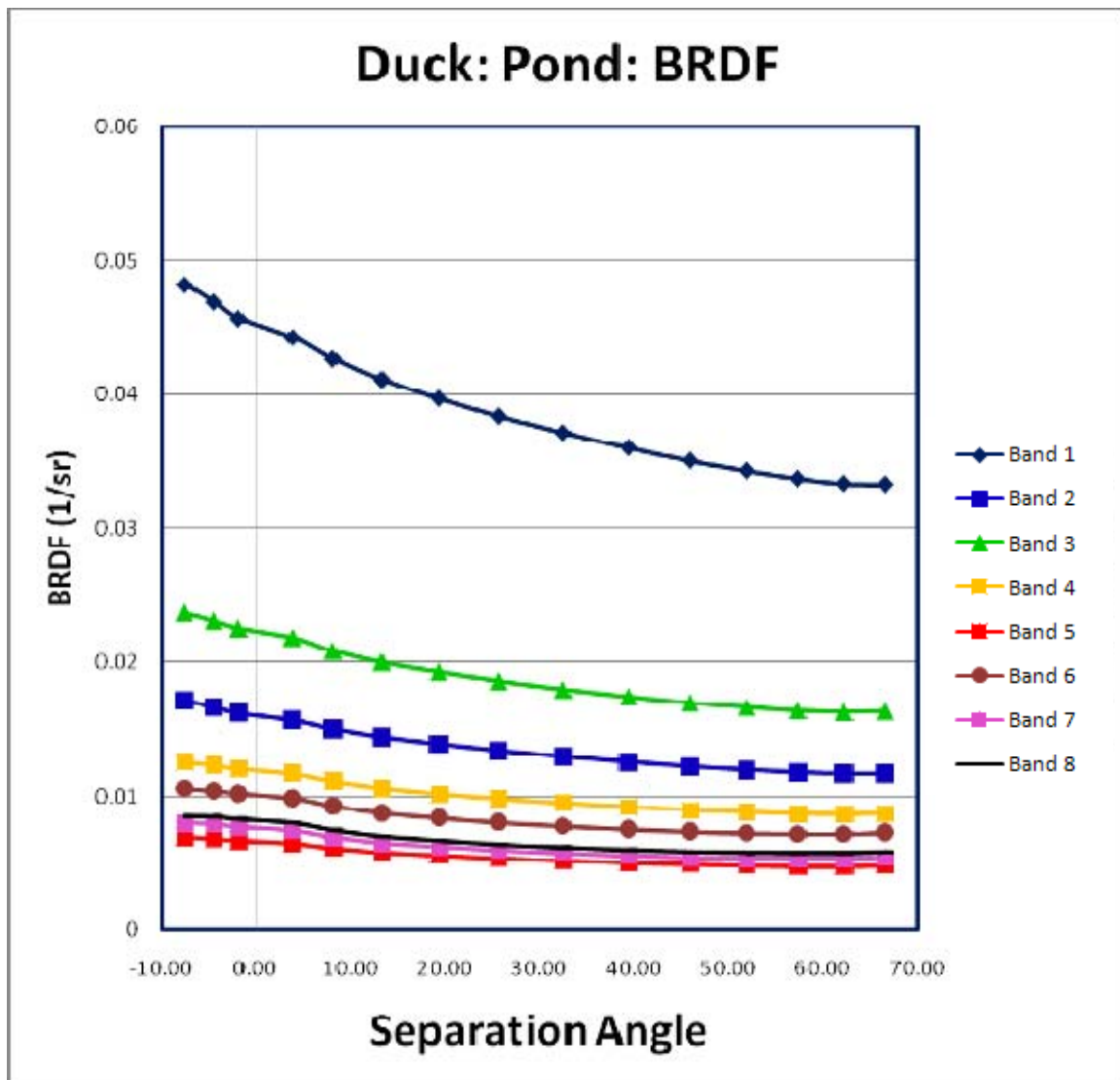


Figure 107. BRDF Results by Separation Angle: Duck, NC (Pond ROI)

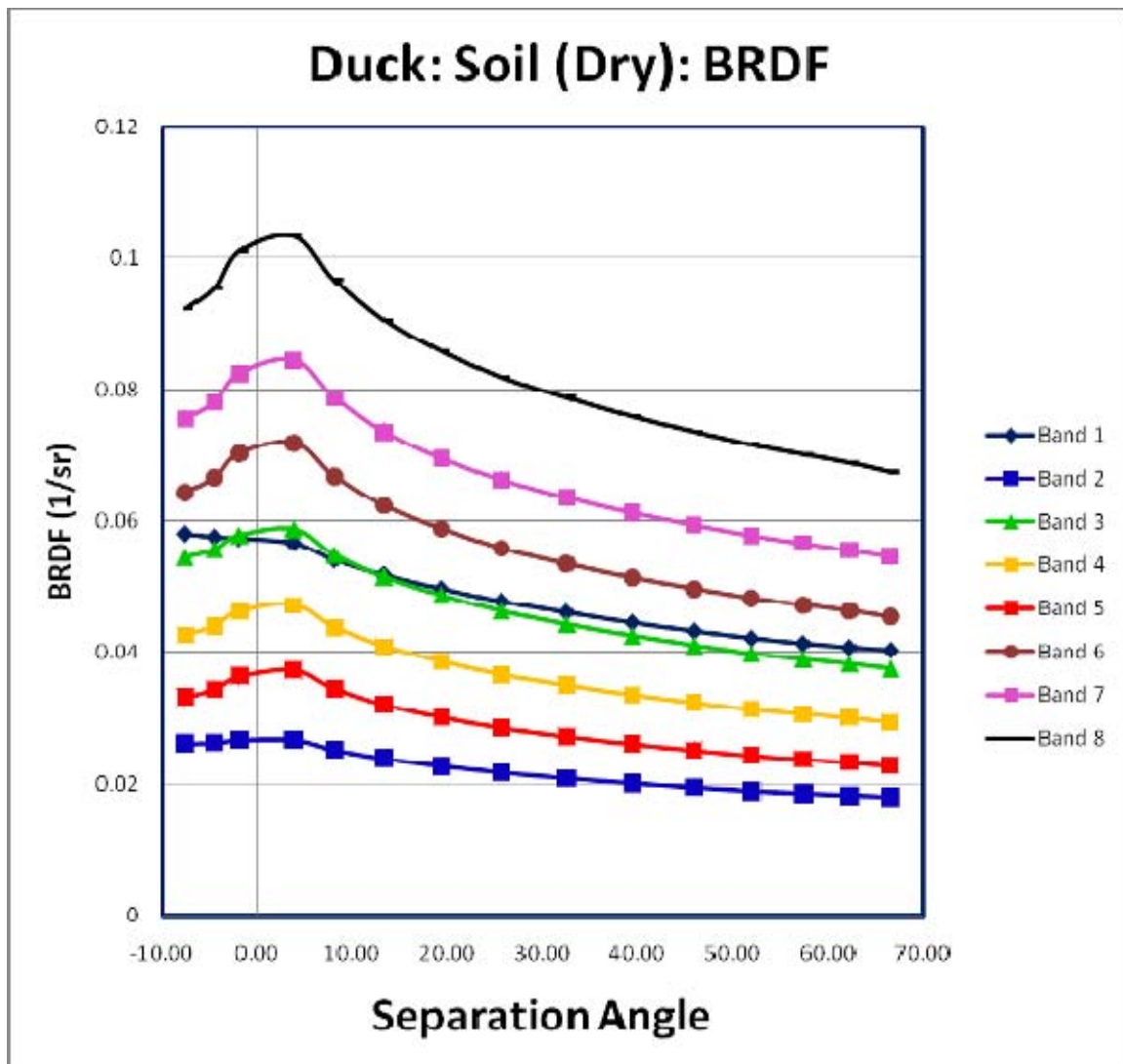


Figure 108. BRDF Results by Separation Angle: Duck, NC (Soil (Dry) ROI)

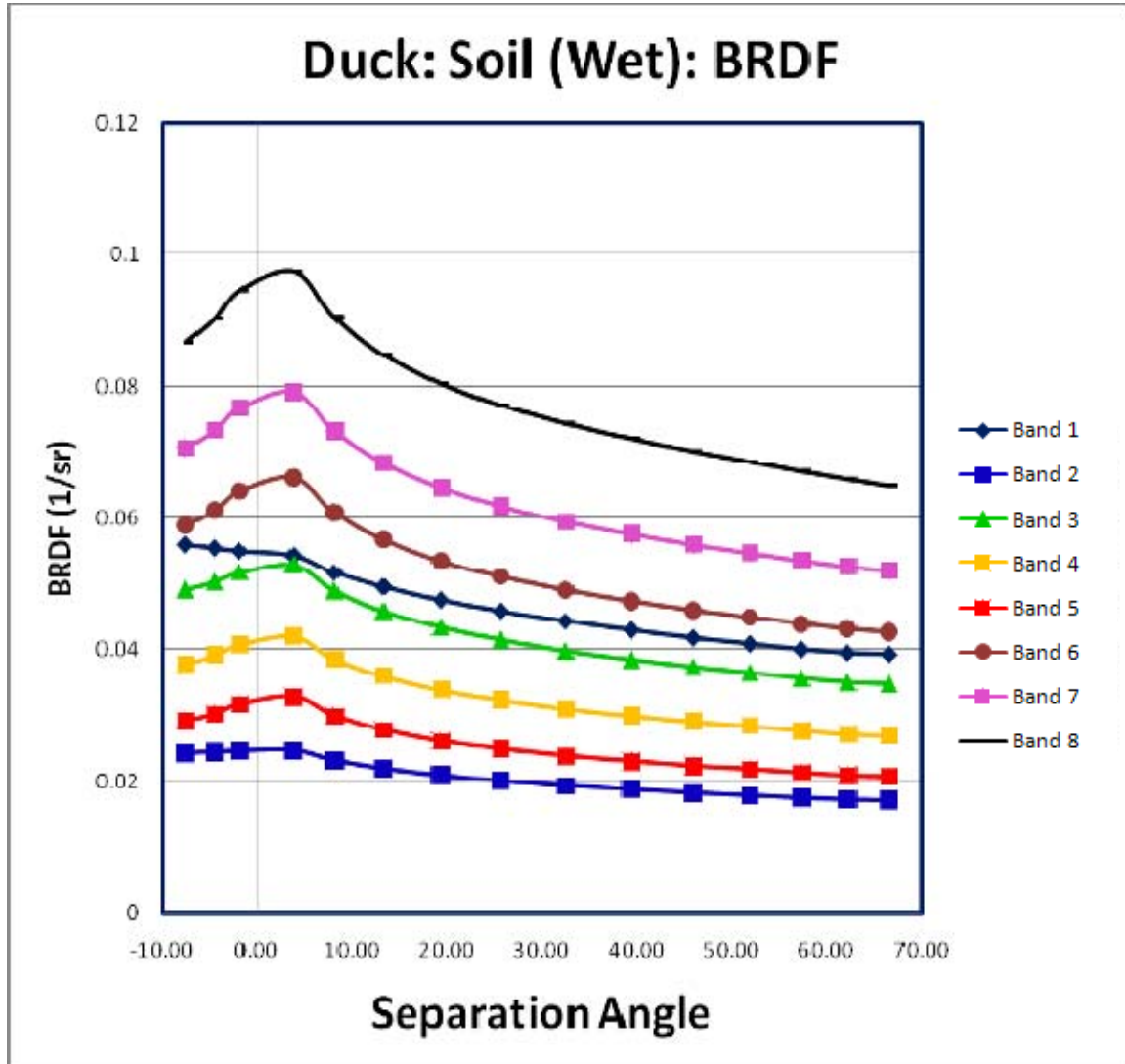


Figure 109. BRDF Results by Separation Angle: Duck, NC (Soil (Wet) ROI)

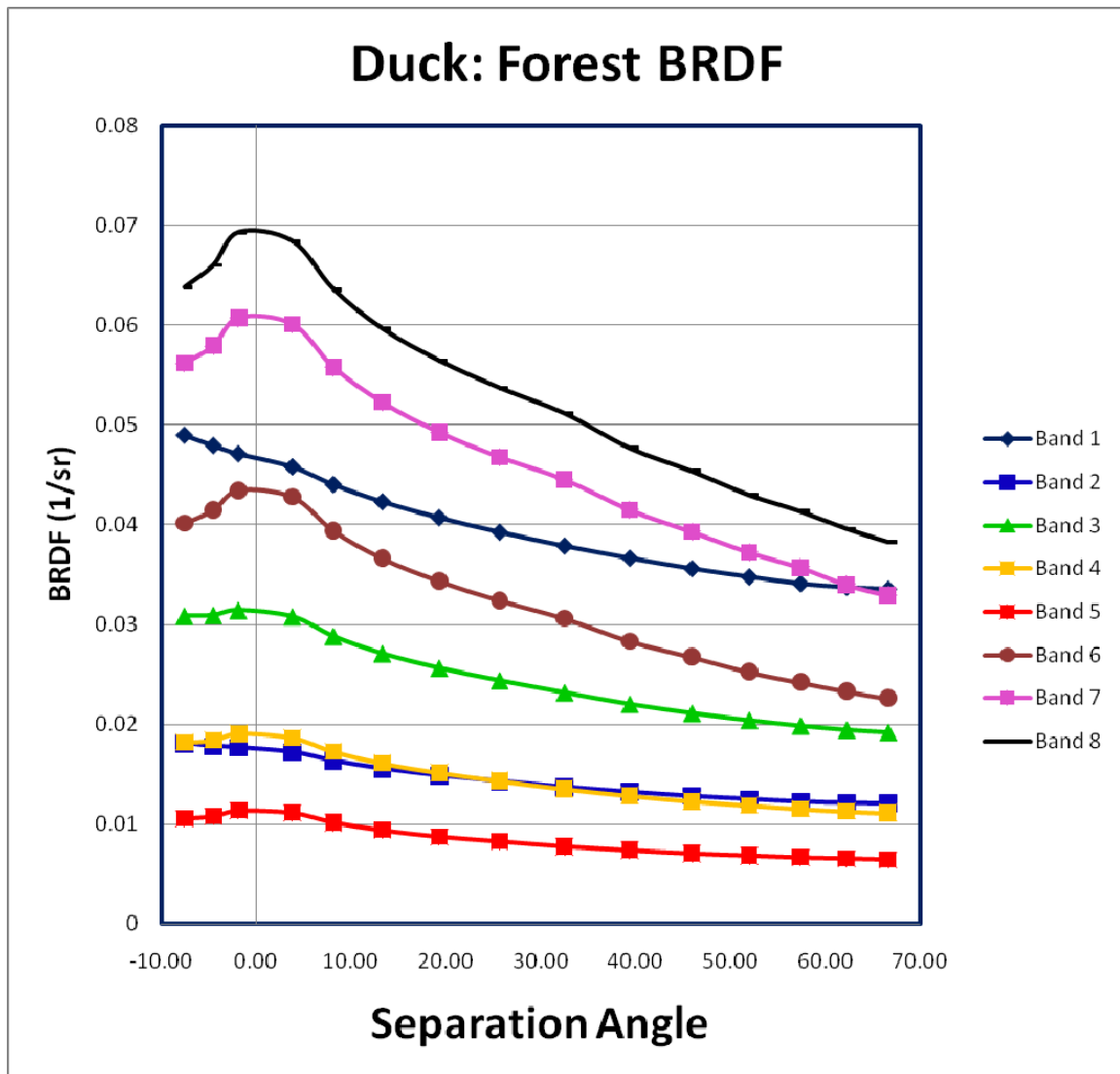


Figure 110. BRDF Results by Separation Angle: Duck, NC (Forest ROI)

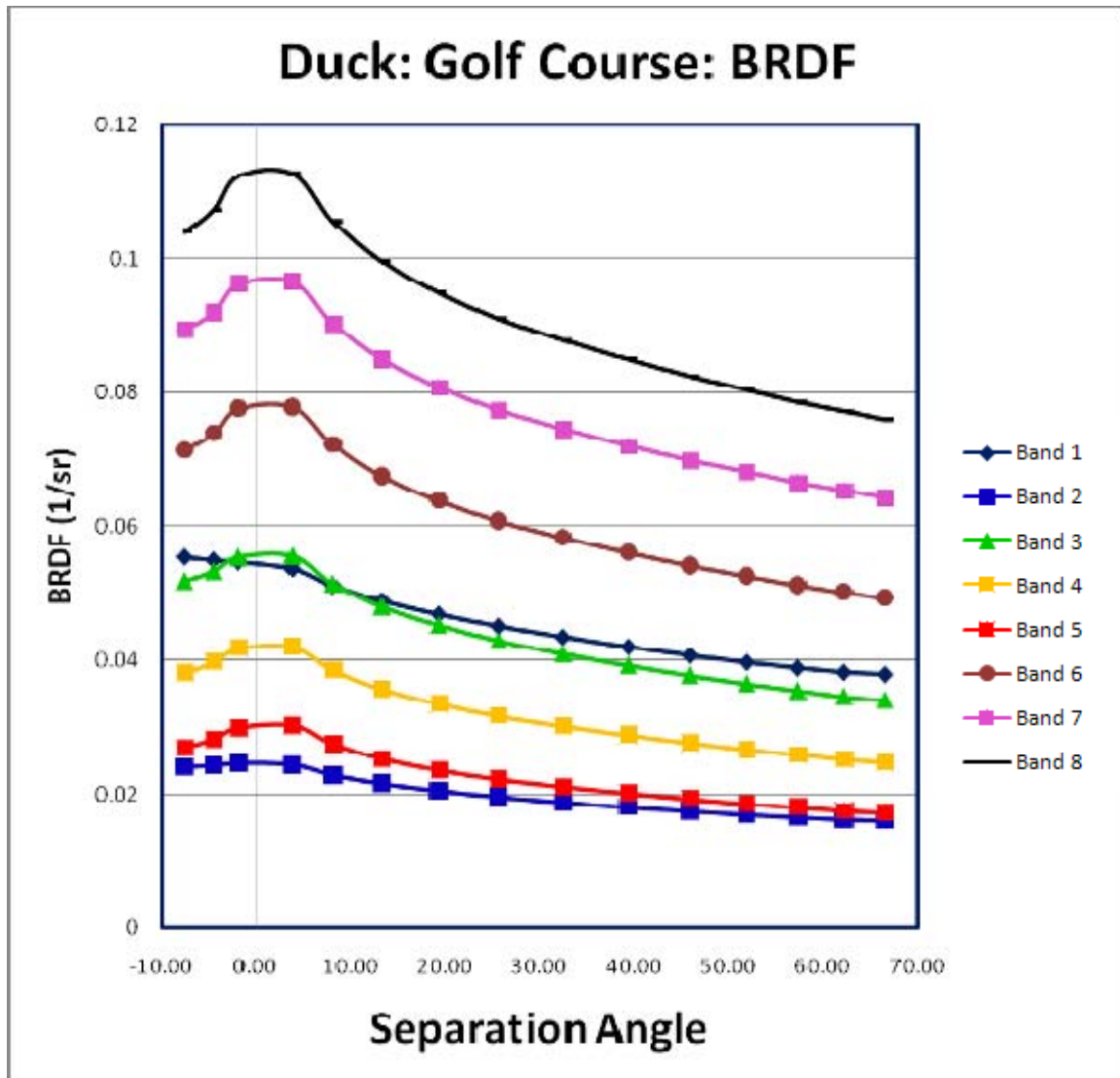


Figure 111. BRDF Results by Separation Angle: Duck, NC (Golf Course ROI)

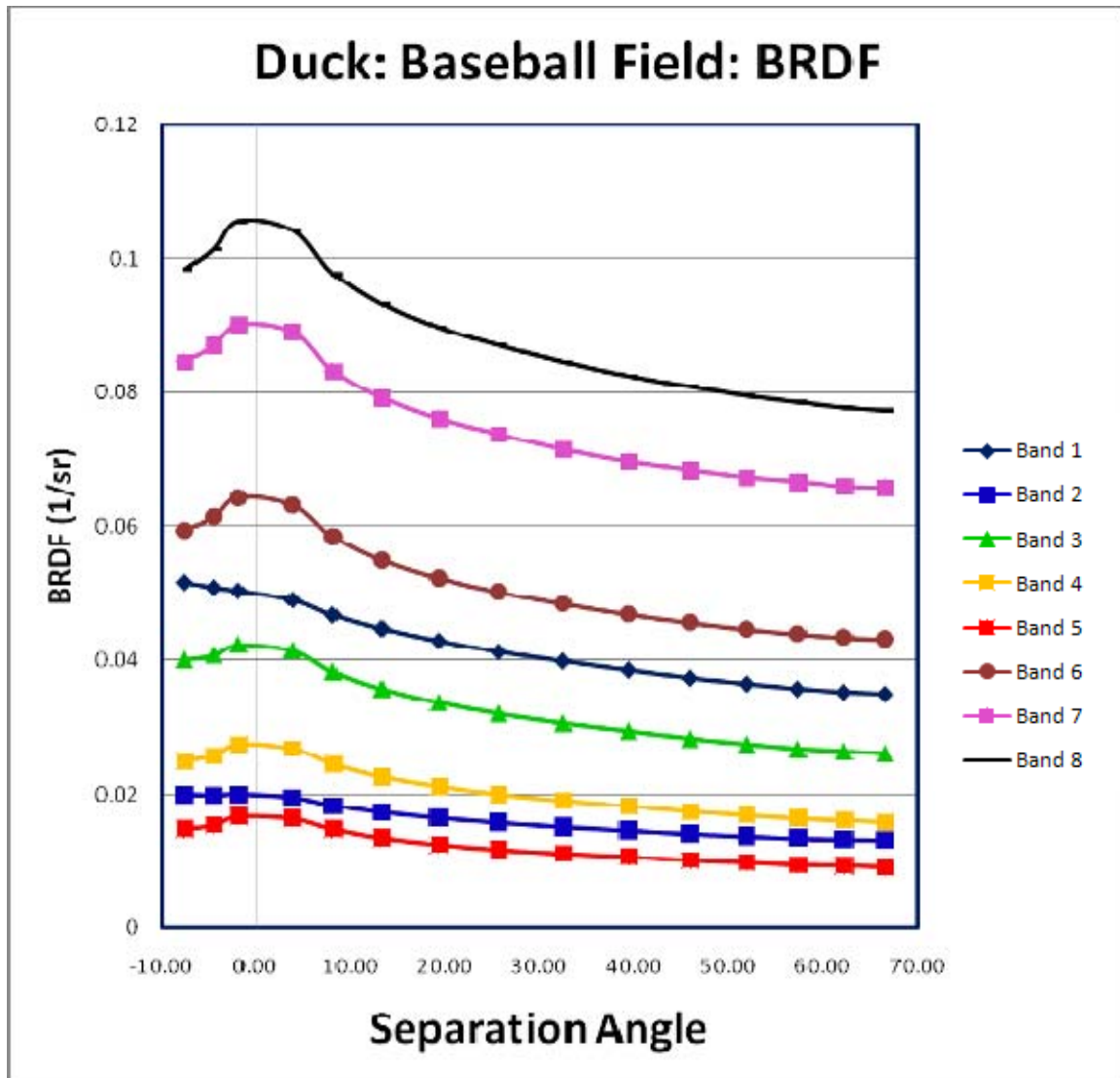


Figure 112. BRDF Results by Separation Angle: Duck, NC (Baseball Field ROI)

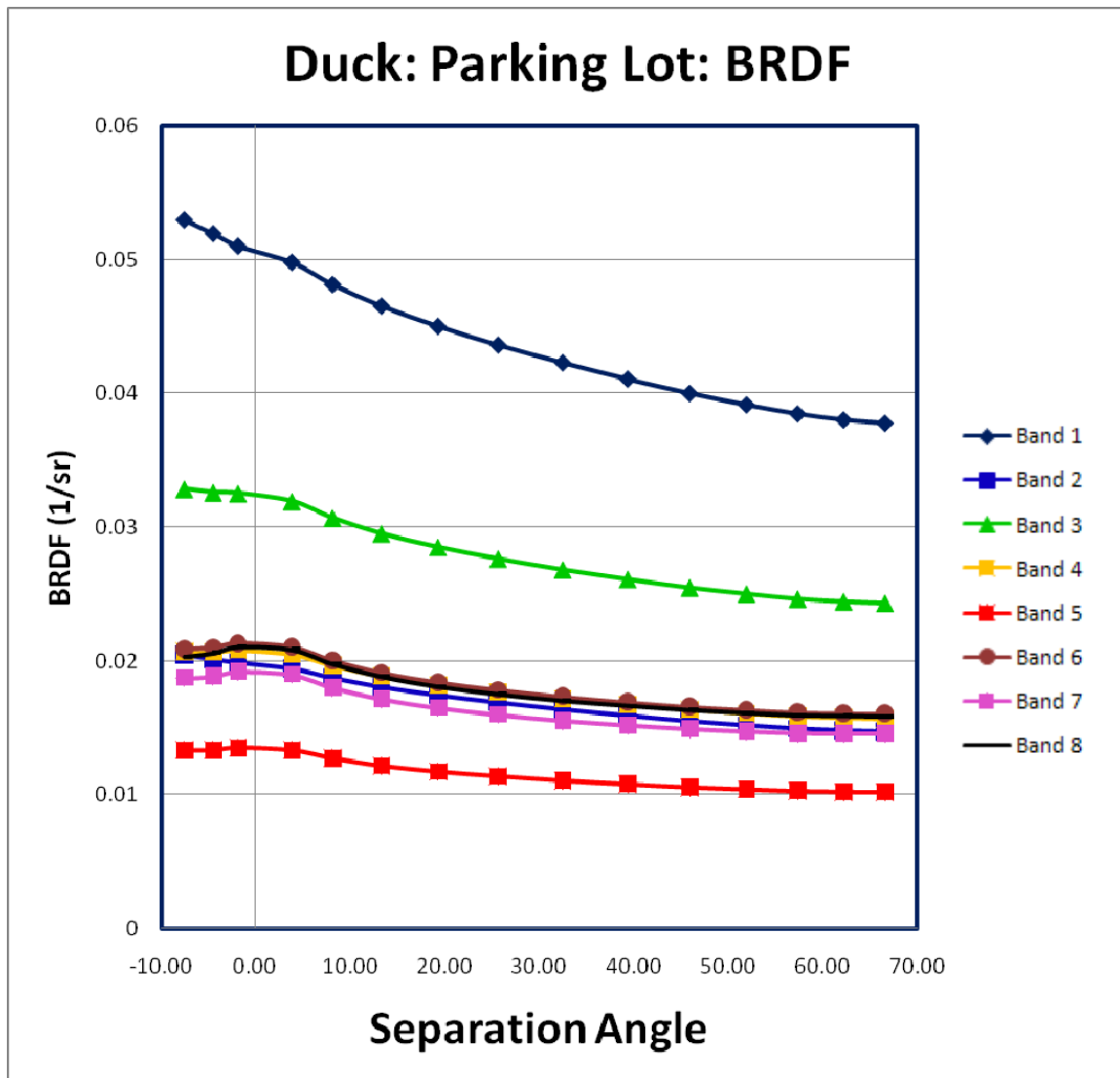


Figure 113. BRDF Results by Separation Angle: Duck, NC (Parking Lot ROI)

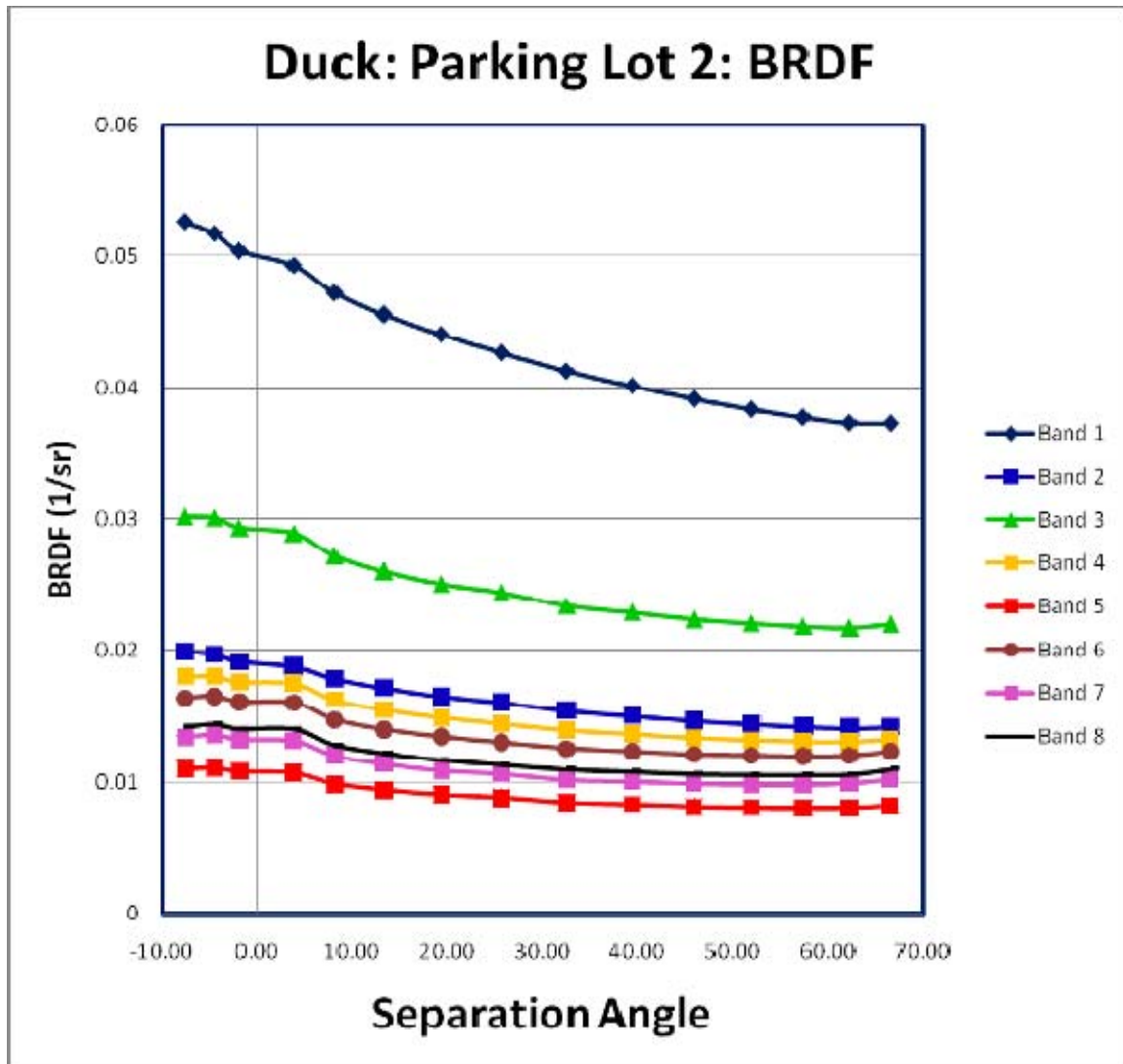


Figure 114. BRDF Results by Separation Angle: Duck, NC (Parking Lot 2 ROI)

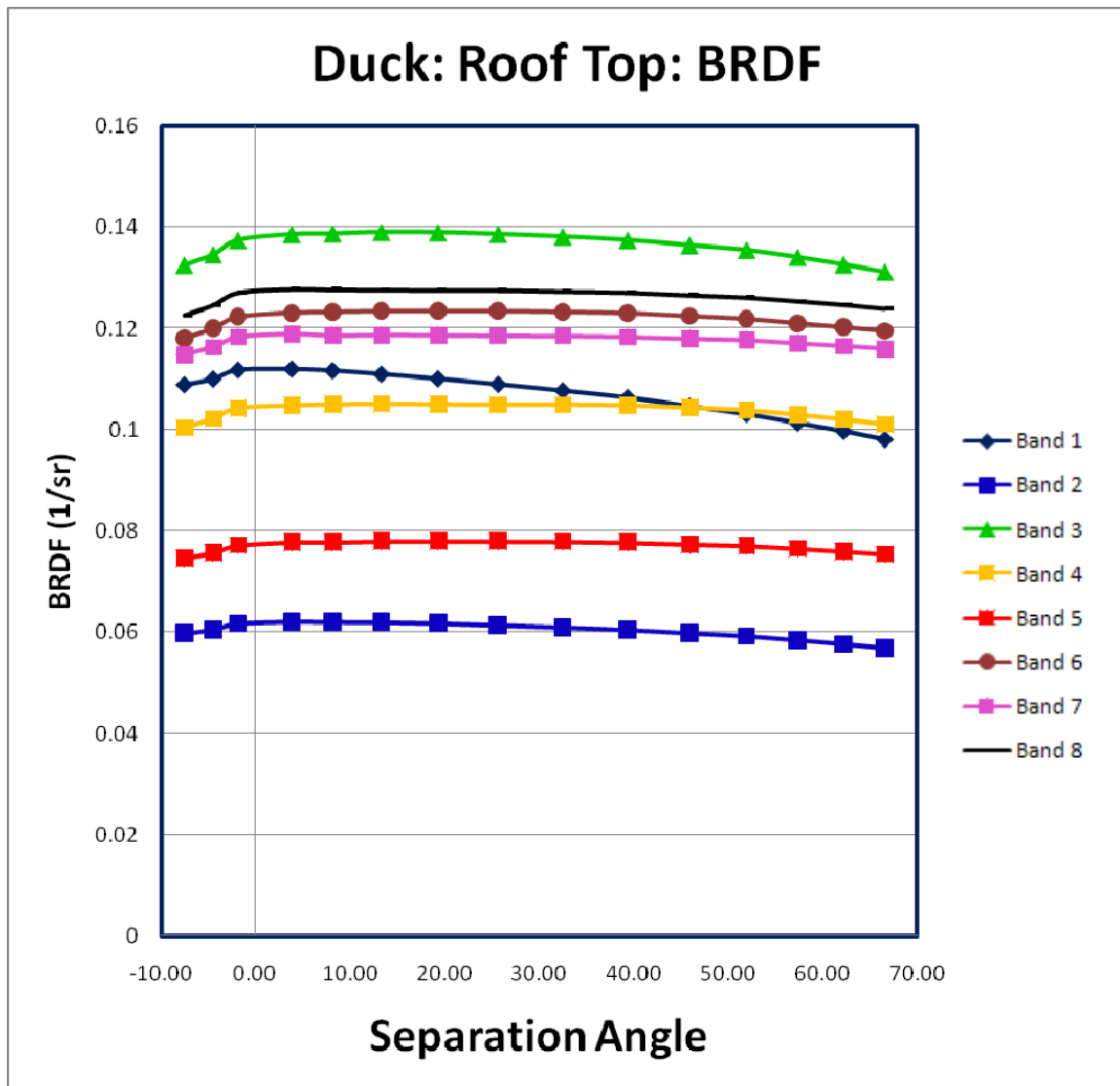


Figure 115. BRDF Results by Separation Angle: Duck, NC (Roof Top ROI)

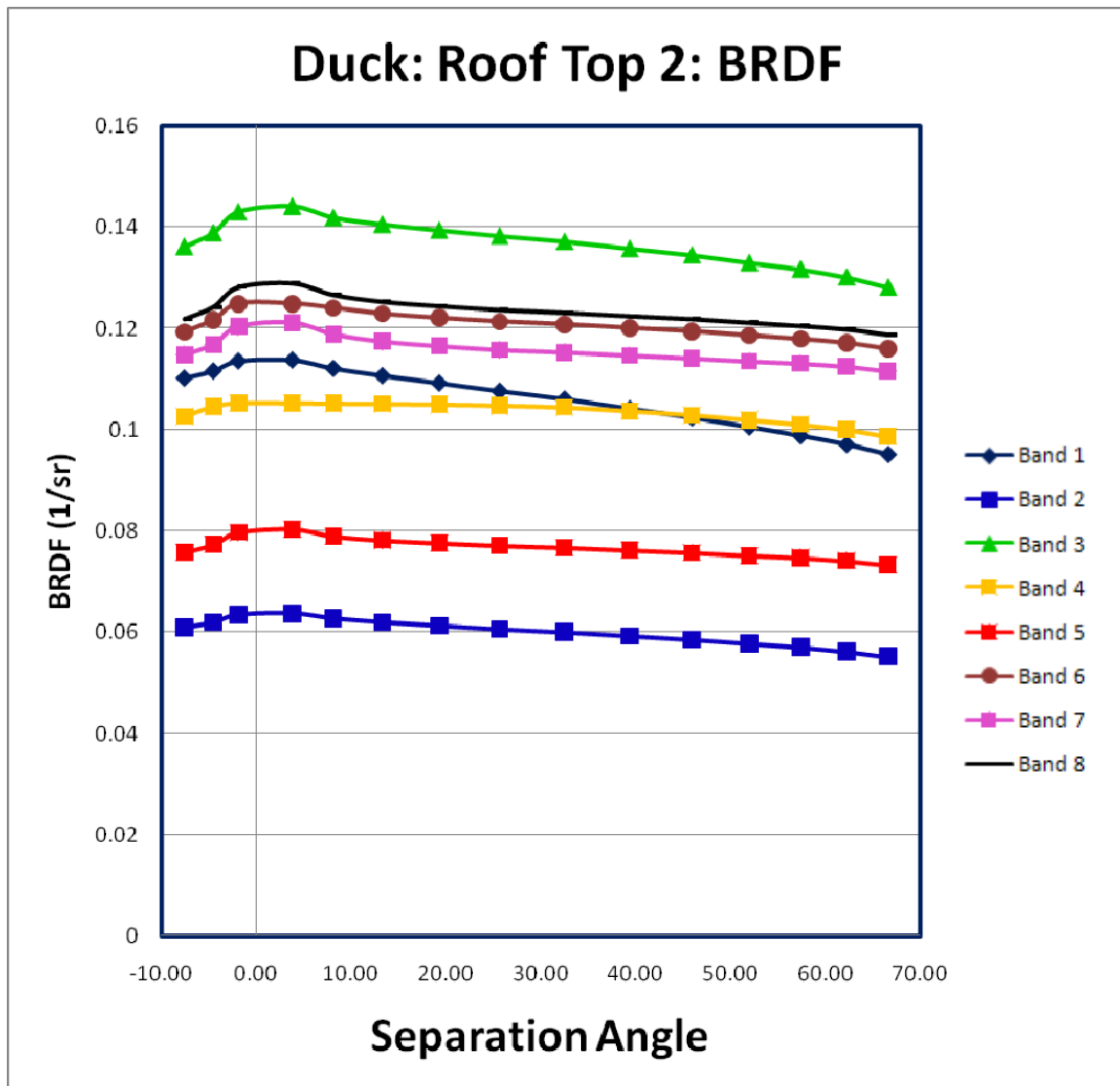


Figure 116. BRDF Results by Separation Angle: Duck, NC (Roof Top 2 ROI)

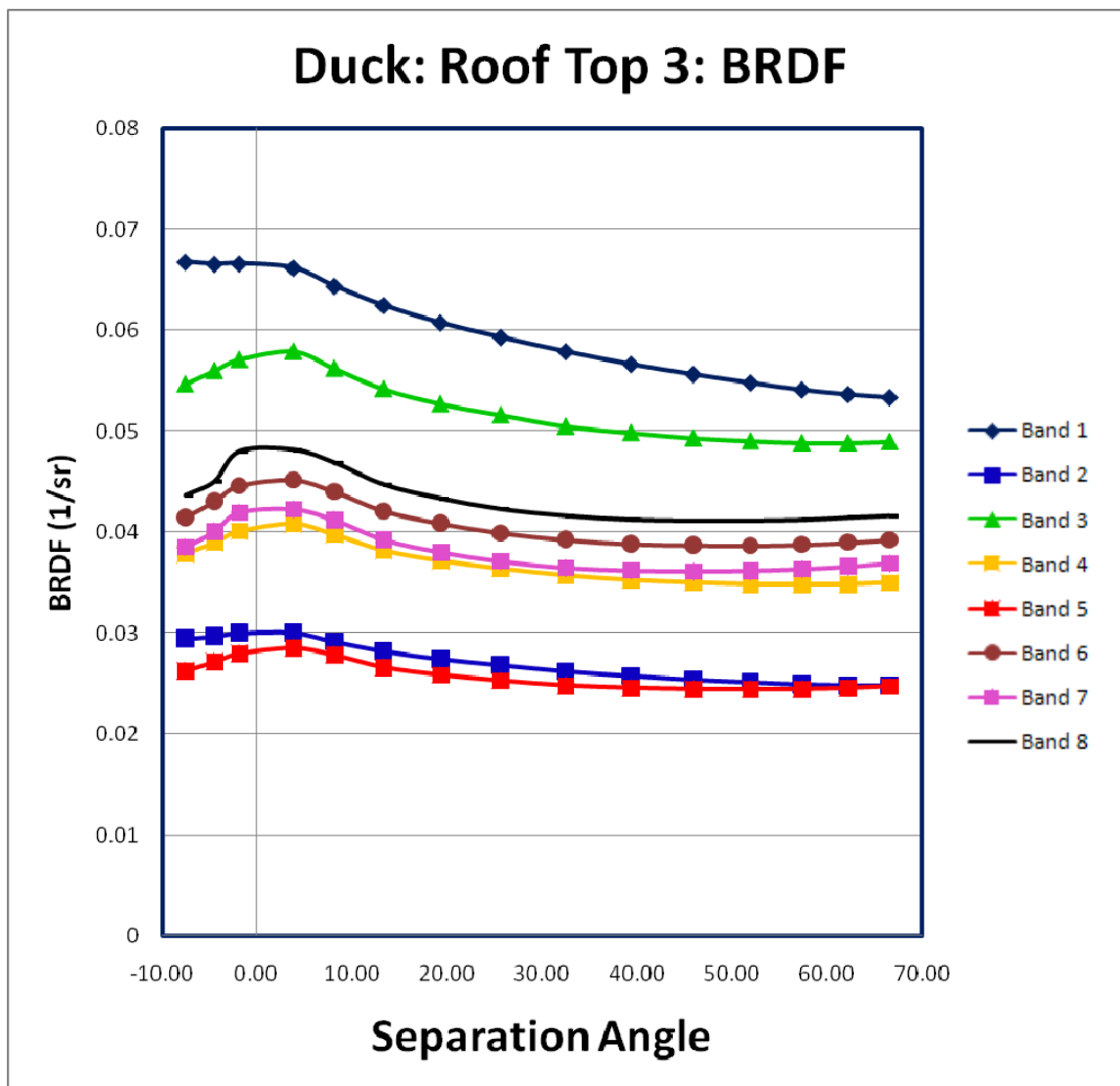


Figure 117. BRDF Results by Separation Angle: Duck, NC (Roof Top 3 ROI)

I. BRDF RESULTS BY SEPARATION ANGLE FOR REGIONS OF INTEREST (PENDLETON, CA)

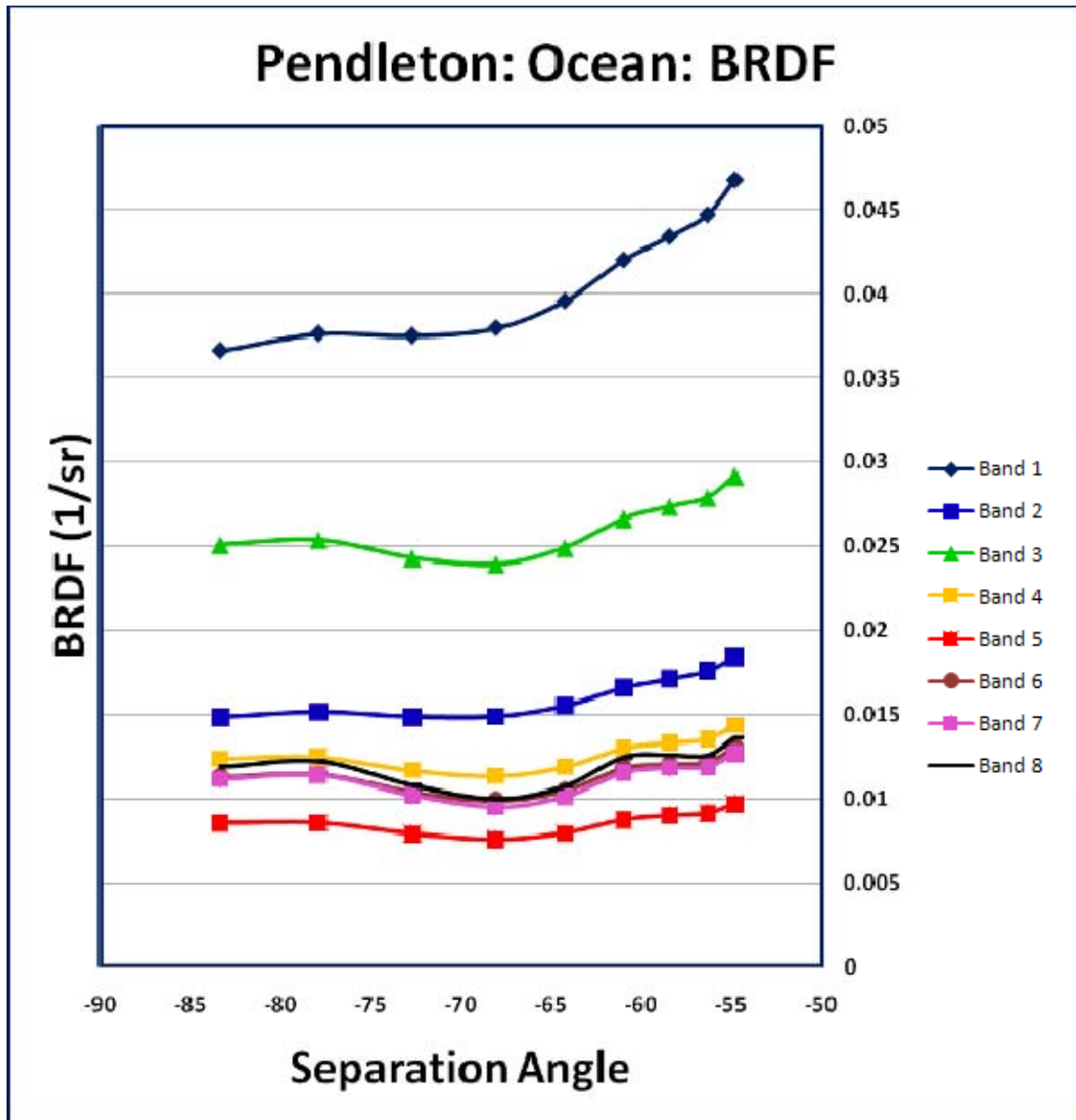


Figure 118. BRDF Results by Separation Angle: Pendleton, CA (Ocean ROI)

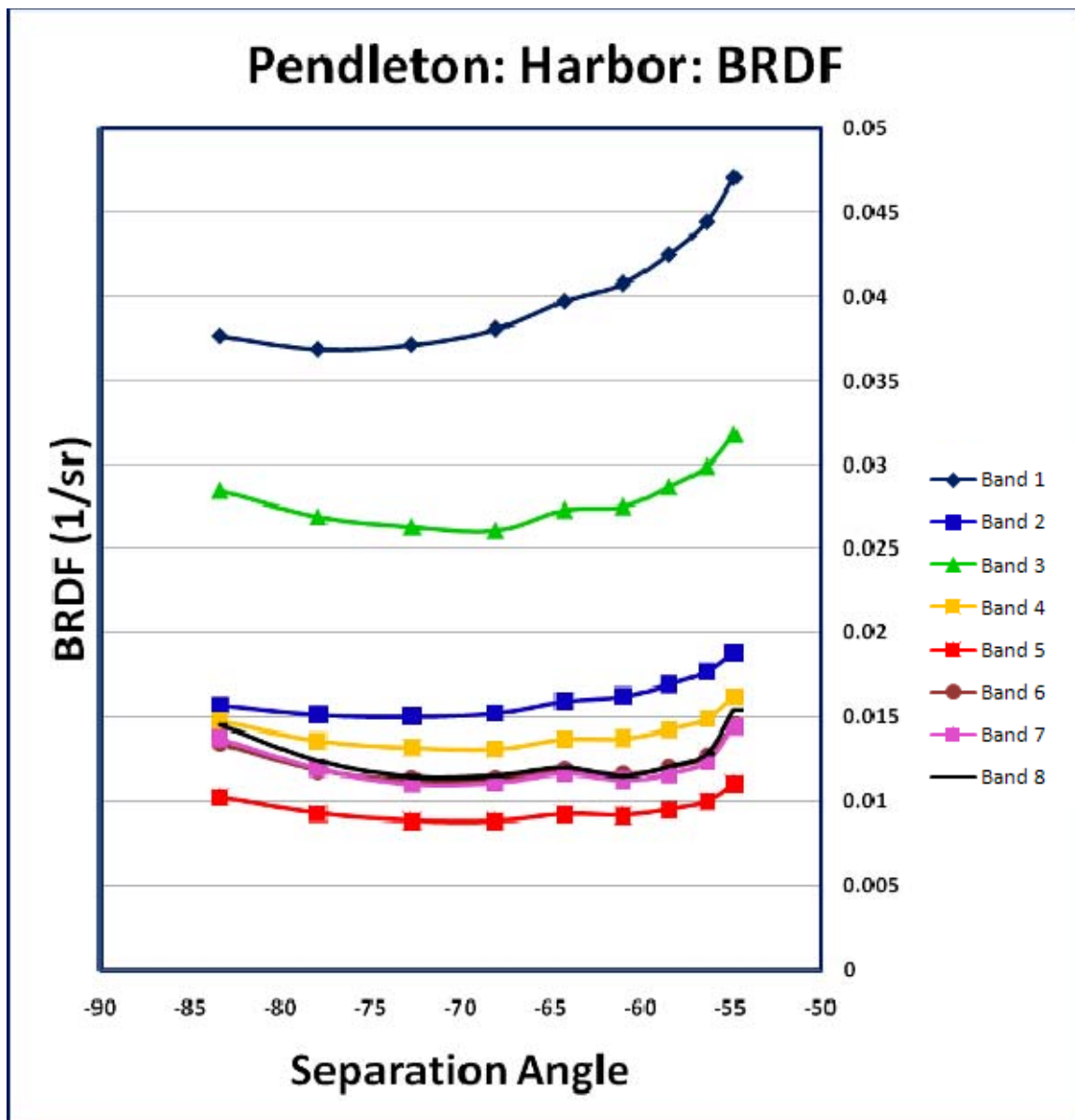


Figure 119. BRDF Results by Separation Angle: Pendleton, CA (Harbor ROI)

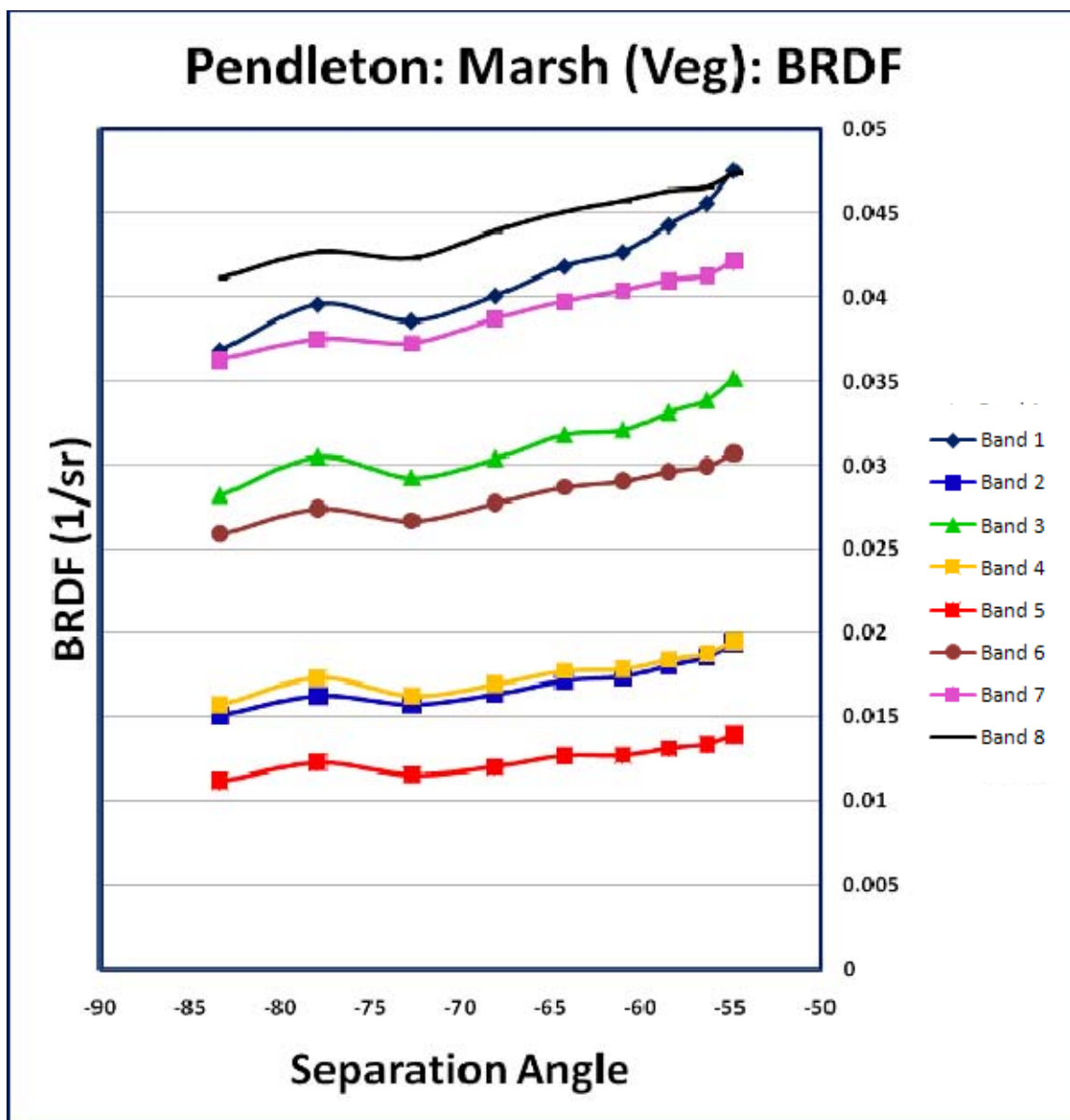


Figure 120. BRDF Results by Separation Angle: Pendleton, CA (Marsh (Veg) ROI)

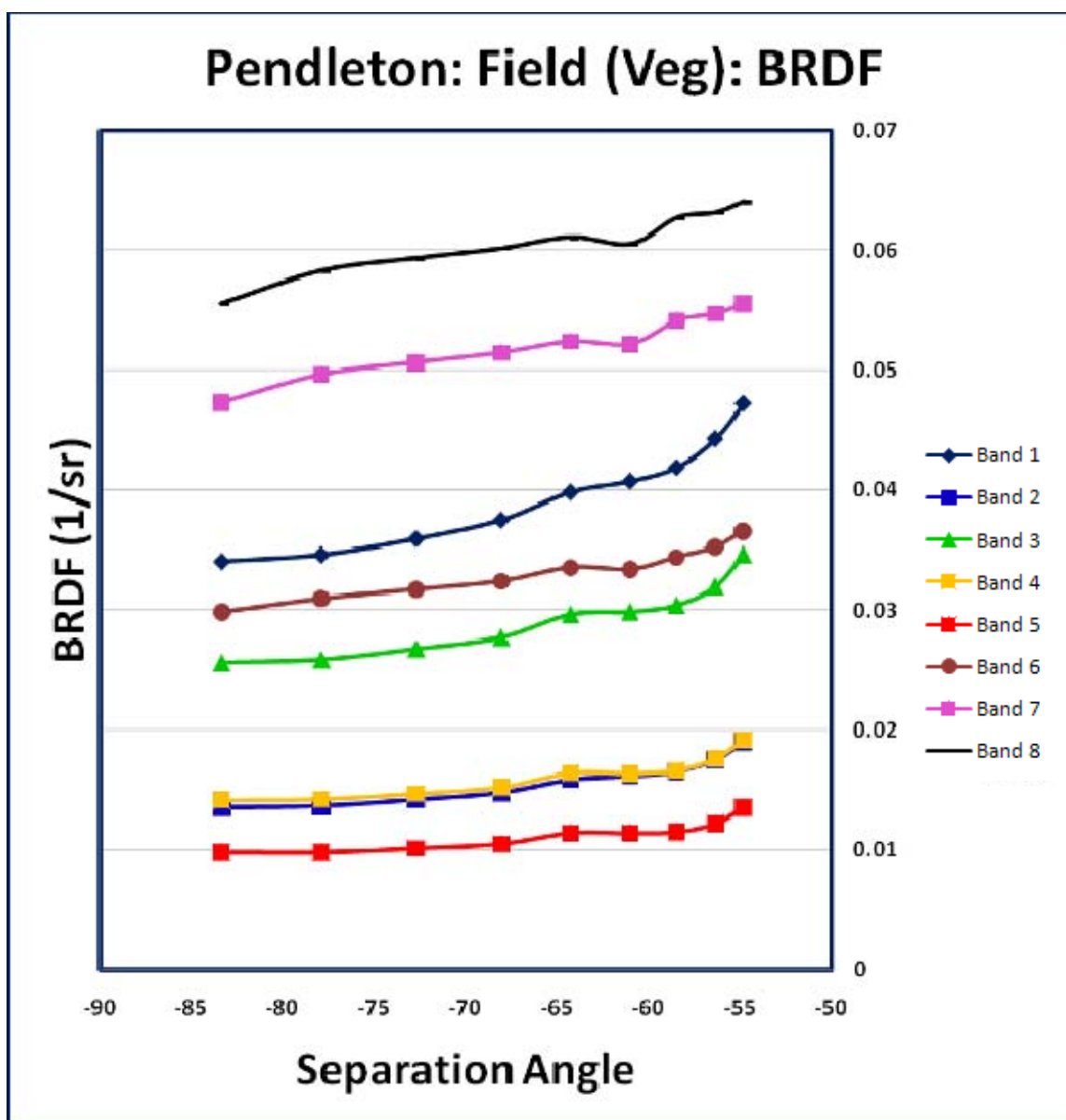


Figure 121. BRDF Results by Separation Angle: Pendleton, CA (Field (Veg) ROI)

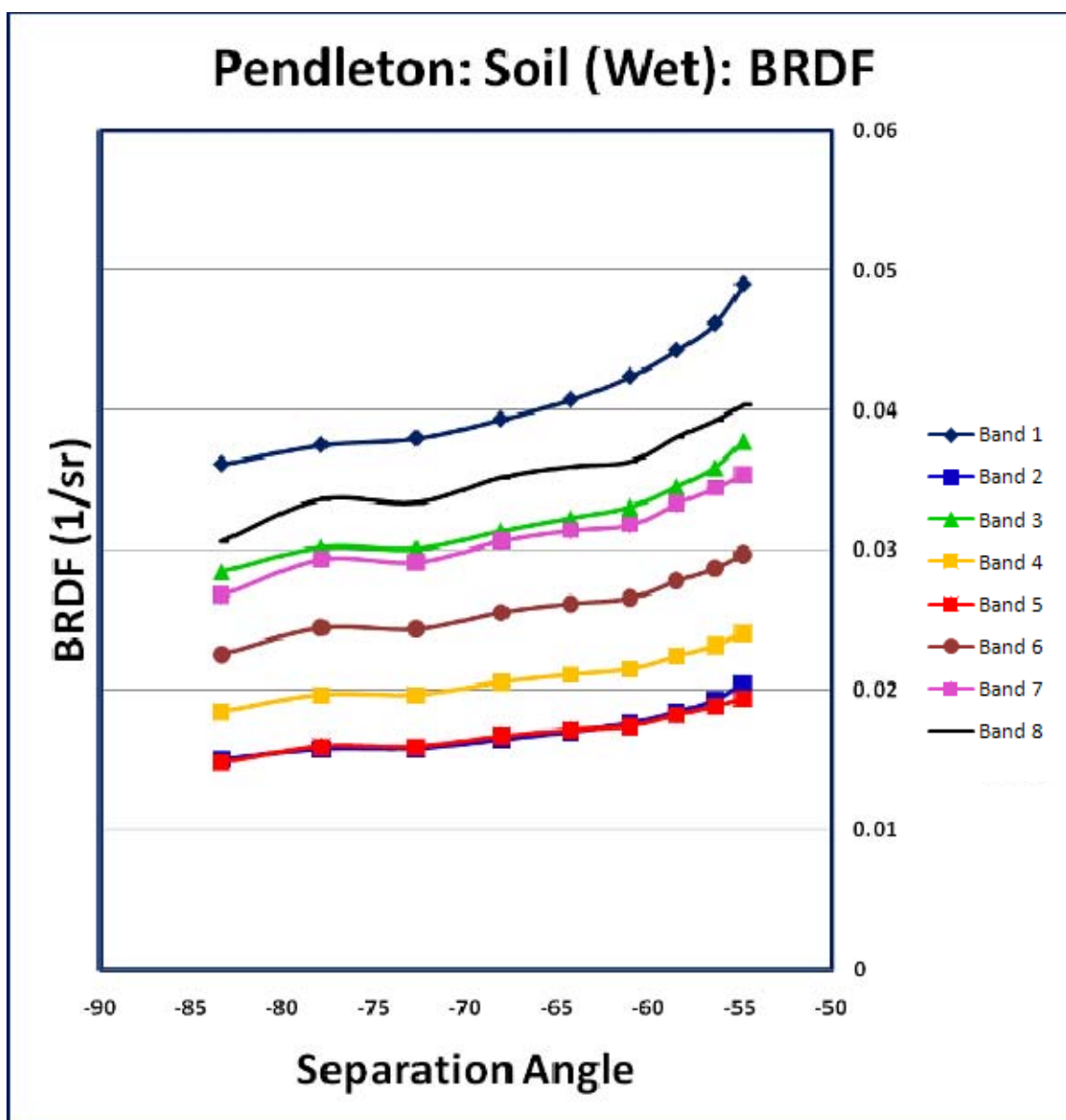


Figure 122. BRDF Results by Separation Angle: Pendleton, CA (Soil (Wet) ROI)

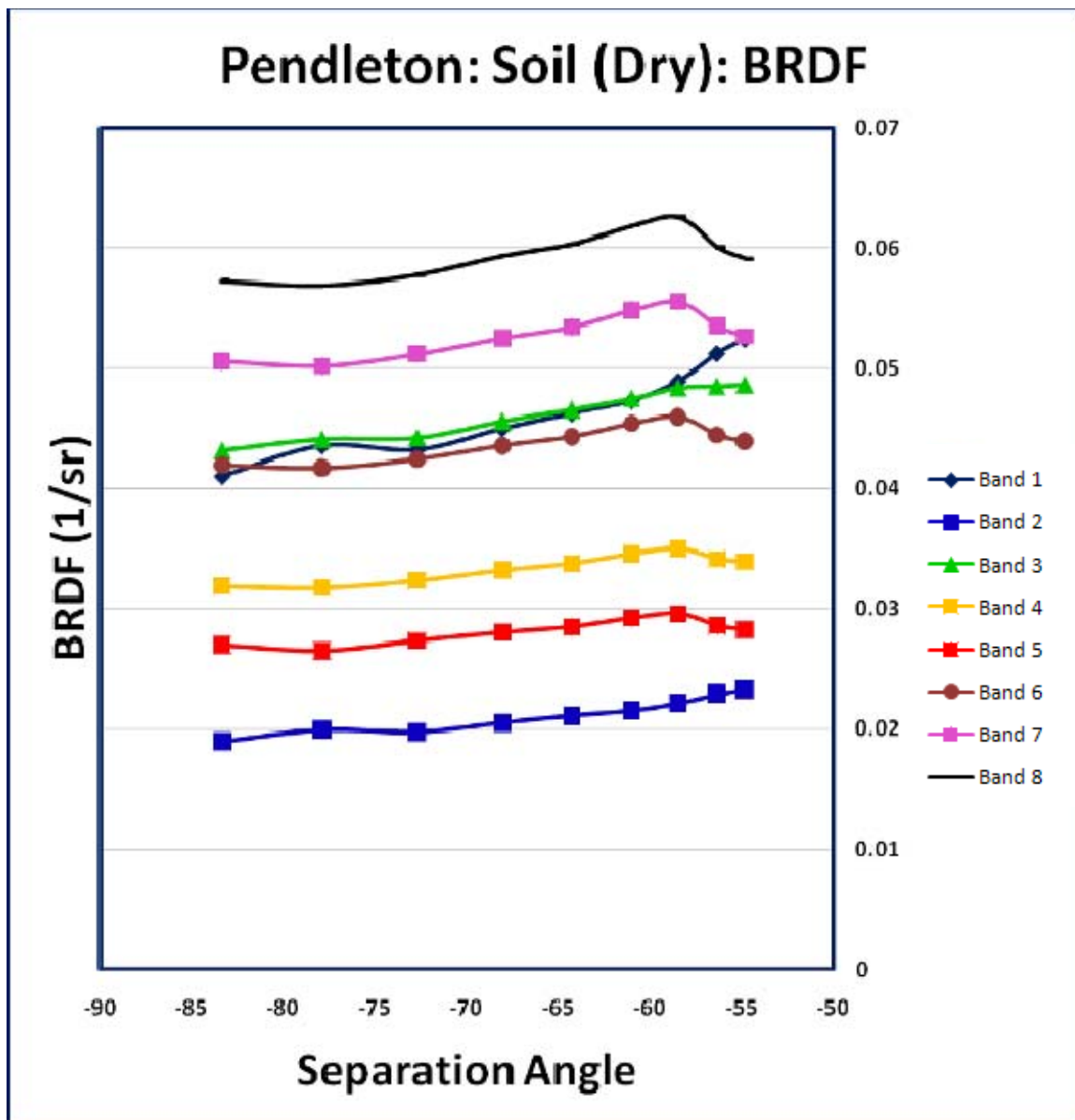


Figure 123. BRDF Results by Separation Angle: Pendleton, CA (Soil (Dry) ROI)

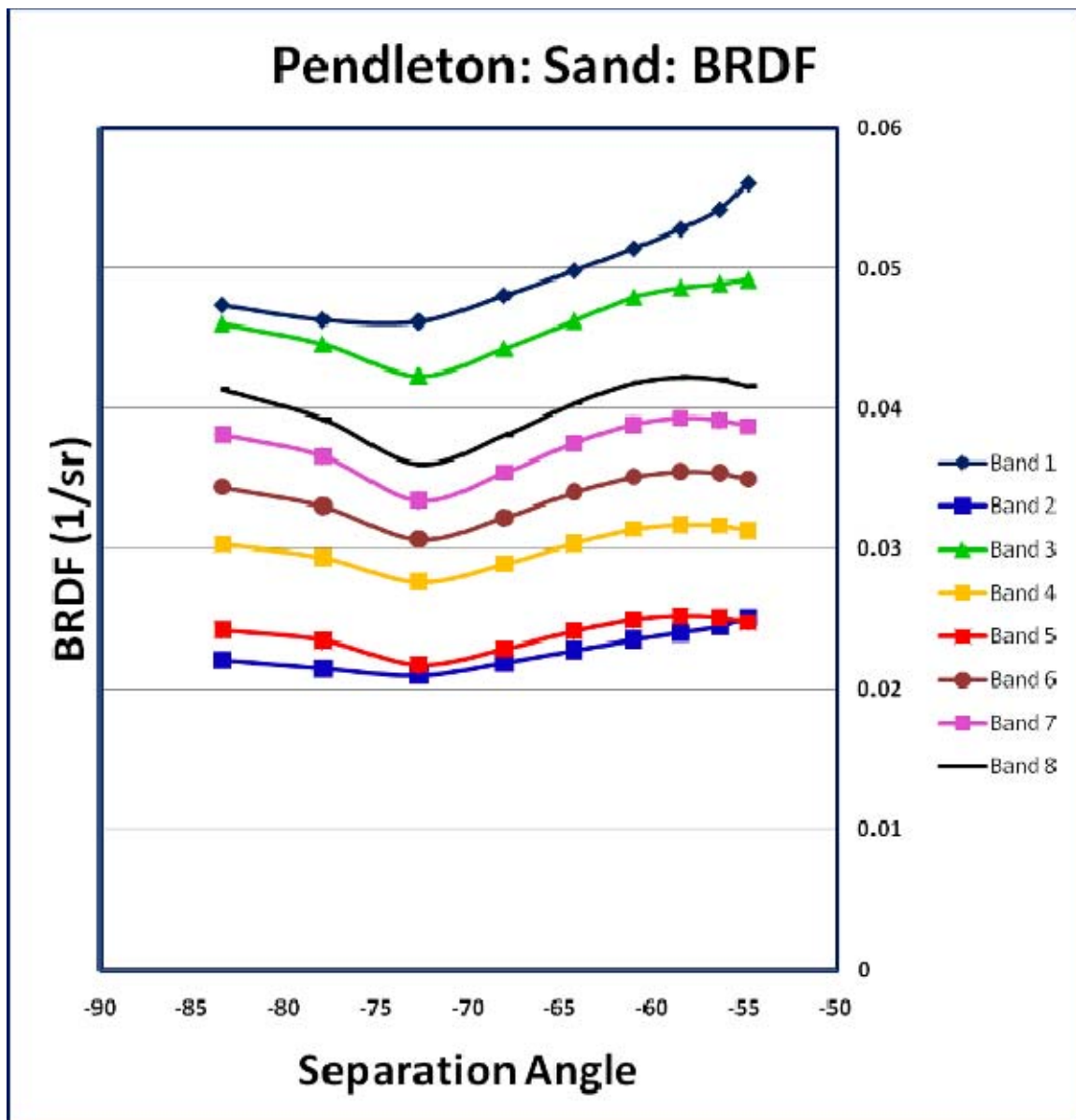


Figure 124. BRDF Results by Separation Angle: Pendleton, CA (Sand ROI)

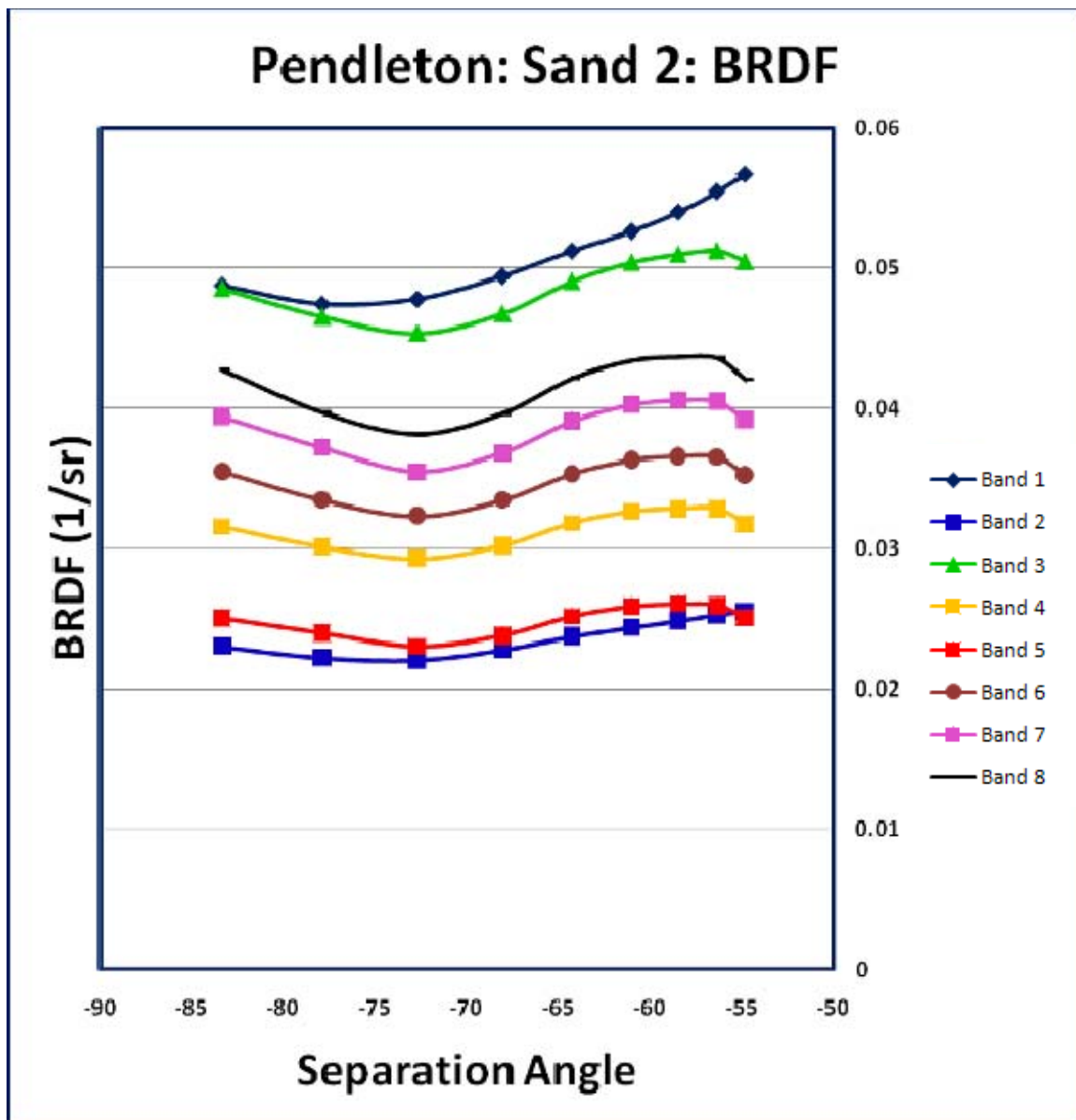


Figure 125. BRDF Results by Separation Angle: Pendleton, CA (Sand 2 ROI)

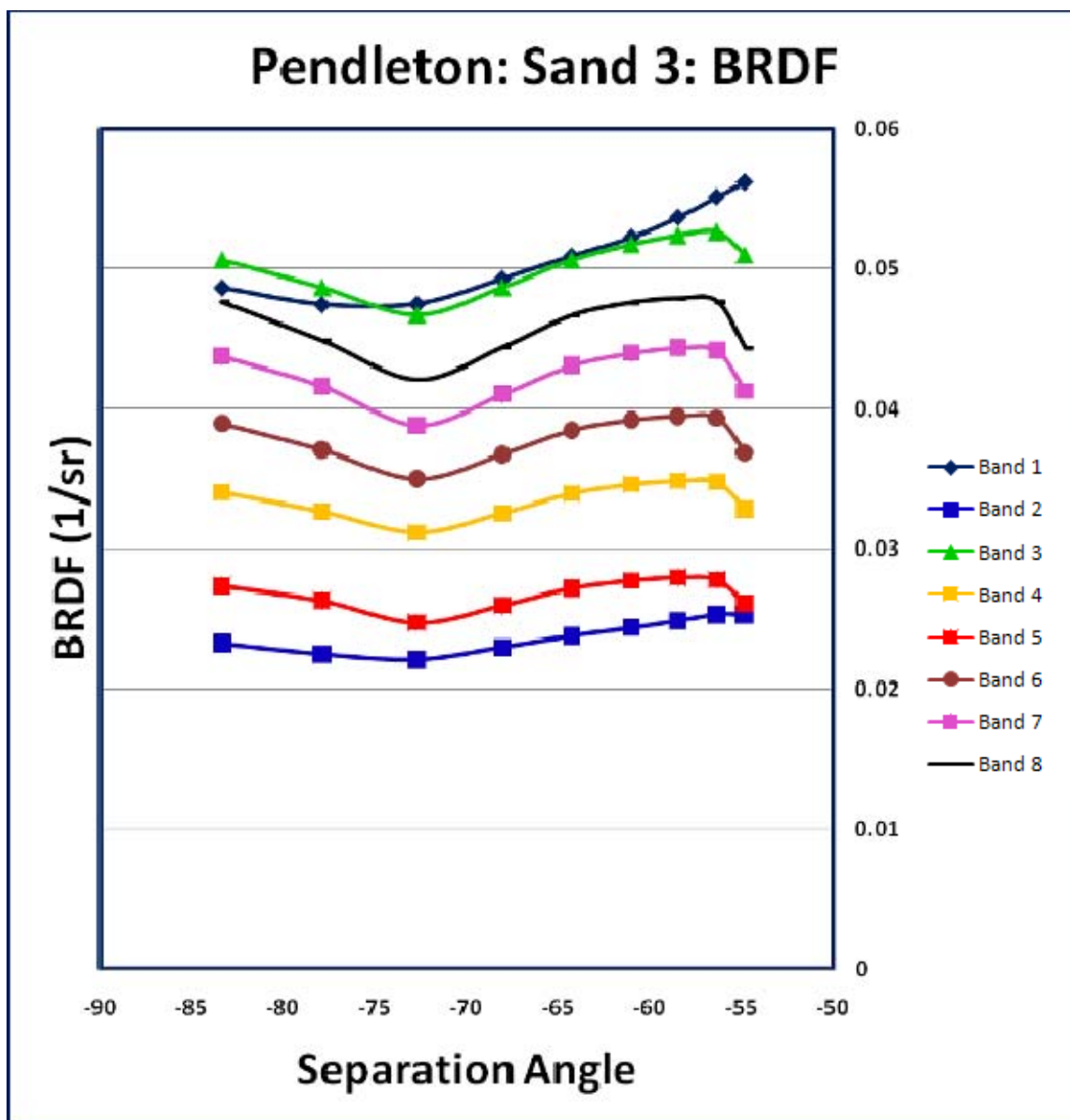


Figure 126. BRDF Results by Separation Angle: Pendleton, CA (Sand 3 ROI)

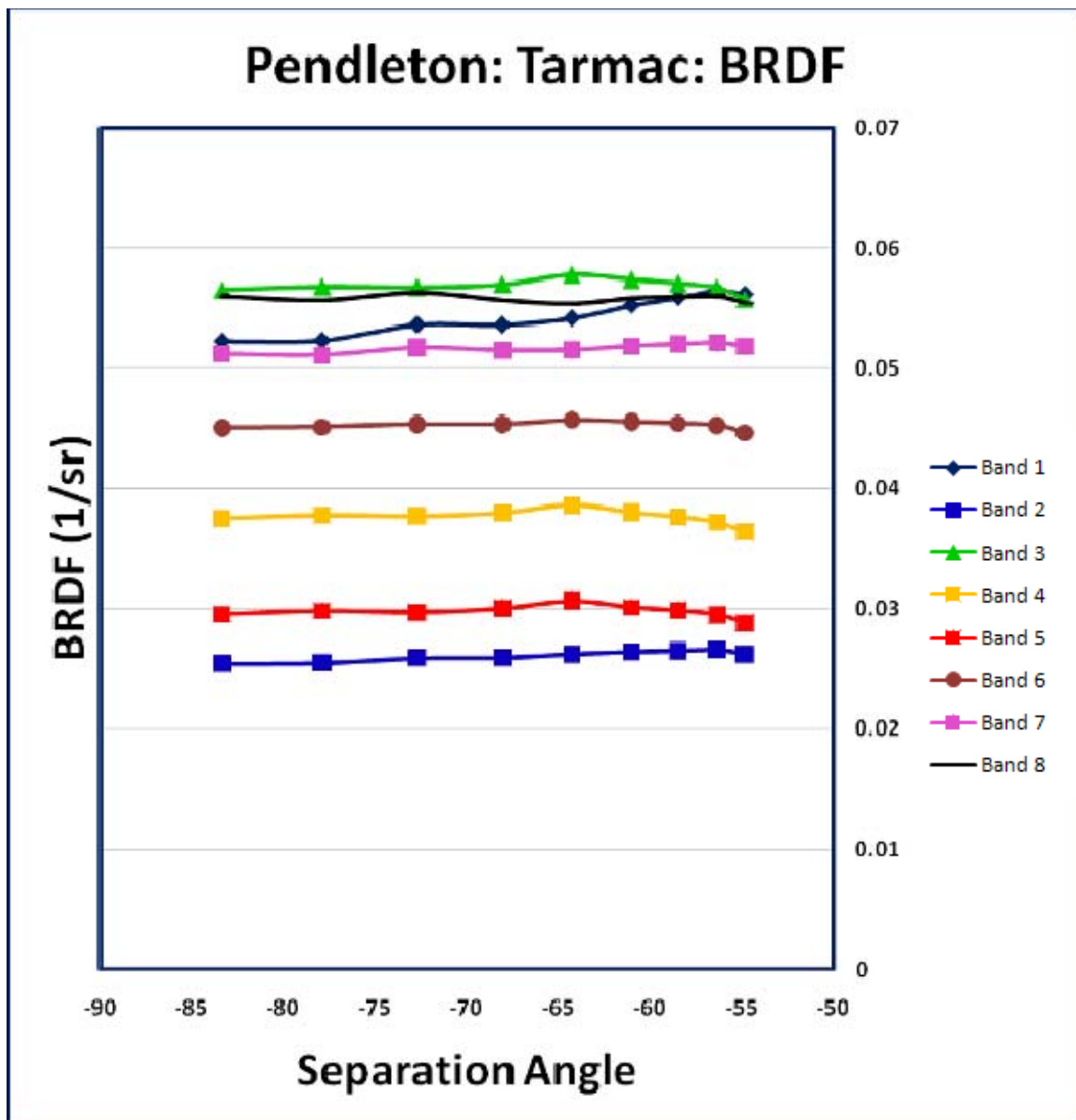


Figure 127. BRDF Results by Separation Angle: Pendleton, CA (Tarmac ROI)

INITIAL DISTRIBUTION LIST

1. Defense Technical Information Center
Ft. Belvoir, Virginia
2. Dudley Knox Library
Naval Postgraduate School
Monterey, California
3. Dr. Richard C. Olsen
Naval Postgraduate School
Monterey, California
4. Dr. James Newman
Naval Postgraduate School
Monterey, California